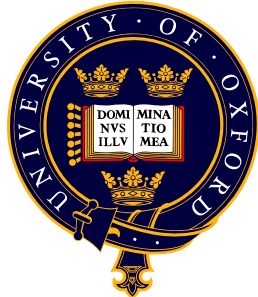


Strongly correlated one-dimensional systems of cold atoms in optical lattices



Stephen Richard James Franz Clark
Trinity College, Oxford

A thesis submitted to the Mathematical and Physical Sciences Division
for the degree of Doctor of Philosophy at the University of Oxford.

Trinity Term, 2007

Atomic and Laser Physics,
University of Oxford

*I dedicate this thesis to my mum, Barbara, who
passed away shortly before I began this work.
Much of what I have and will achieve is only possible
through the enduring influence of her love and kindness.*

Strongly correlated one-dimensional systems of cold atoms in optical lattices

Stephen Richard James Franz Clark
Trinity College, Oxford

Abstract

When the constituents of a many-body system have significant interactions between them the properties of the system often exhibit strong correlations. Such strongly-correlated systems frequently arise in condensed matter physics (CMP). In recent years systems of cold atoms in optical lattices have shown great potential as a versatile experimental tool for studying CMP model systems. Moreover, since there exists a detailed understanding of the microscopic dynamics of these systems, and an extensive ability to manipulate them with external fields, optical lattices permit the experimental investigation of coherent many-body dynamics. This capability naturally lends itself to numerous promising applications for quantum information processing (QIP).

In this thesis we consider a variety of one-dimensional (1D) strongly-correlated systems realisable with an optical lattice. To begin we analyse two seminal experiments by utilising recent advances in the numerical simulation of large 1D systems. The first is a study of the dynamical superfluid to Mott insulator transition in the 1D Bose-Hubbard model (BHM), analogous to the experiment by Greiner *et al.* [Nature **415**, 39 (2002)]. Our calculations show that for rapid transitions the build-up of single-particle coherence is faster than the timescale for single-atom hopping, consistent with the experimental findings. The second study analyses the excitation spectrum of the 1D BHM as revealed by a periodic modulation of the lattice equivalent to the experiment by Stöferle *et al.* [Phys. Rev. Lett. **92**, 130403 (2004)]. The results reproduce the broad response in the superfluid regime, and narrow discrete resonances in the Mott-insulator regime seen in the experiment. A central conclusion of both of these investigations is that BHM is sufficient to describe the experimental findings and represents an excellent model for the dynamics of cold atoms in optical lattices.

In the last part of this thesis we propose two new schemes for engineering useful many-body quantum states. The first scheme provides an efficient method for generating arbitrary graph states which are a vital resource for QIP. This is done by exploiting the special *mirror-inverting* dynamics of a so-called entangling bus. We discuss a possible implementation using an optical lattice and find that the scheme is realistic in its requirements even in the presence of noise. In the second scheme we propose to create twin-Fock states in an optical lattice by dynamically melting a two-component Mott insulator with two atoms per lattice site into a superfluid. The resulting twin-Fock state could potentially be used for Heisenberg-limited quantum metrology. Importantly, we find that in 1D near-adiabatic melting can be achieved in a time that does not scale with the system size thereby making the scheme experimentally feasible.

Supervisor: Dr. Dieter H. Jaksch, University of Oxford.
DPhil Examination occurred at 2:00pm on Monday 1st October 2007.
Internal Examiner: Prof. Christopher J. Foot, University of Oxford.
External Examiner: Prof. Martin B. Plenio, Imperial College London.

ACKNOWLEDGEMENTS

I am indebted to numerous people for all the help and support I have received over the past 4 years in Oxford. First and foremost, I would like to thank my supervisor Dieter Jaksch. It is hard to recognise, let alone quantify, quite how much I have learnt from him about how to do research. I have been both challenged by his exacting standards, and inspired by his insightful approach to physics. It has been a pleasure to work with such an extraordinary individual.

Over the course of my research I have had the opportunity to collaborate with many colleagues on a number of interesting projects. In particular I want to thank my co-authors, Alexander Klein, Martin Bruderer, Benoit Vaucher, Uwe Dorner, Carolina Mora Alves, Mirta Rodriguez, Andrew Daley, Andi Griessner and Peter Zoller. I would like to thank Peter Zoller especially for giving me two opportunities to visit Innsbruck. On both occasions I was shown much hospitality and benefited greatly from fruitful discussions with his group. I also thank Andrew Daley for giving me his thesis template which this manuscript is based on.

I extend a special thanks to Alexander Klein, Martin Bruderer and Karl Surmacz. As my office mates for most of the duration of my studies they showed great tolerance to my occasional frivolous interruption of their work. They also put a valiant effort into proof-reading and commenting large parts of this thesis and thereby considerably reducing the number of errors in it.

I must also express my sincerest gratitude to Trinity College for not only providing a wonderfully stimulating academic and social environment over the last 4 years, but also for allowing me to meet my wife and marry her in its beautiful chapel.

I share a big thanks to my brothers, Daniel and Adam, and their families for their unfailing support and for giving me a homely retreat from Oxford when needed. Last, but by no means least I give a heartfelt thanks to my loving wife, Kyla. Despite having very little interest in cold-atom physics and taking many opportunities to distract me from my work, she has nonetheless played an immensely important role in everything I have done in the past few years.

Stephen Clark, Oxford 2007

CONTENTS

I Background	1
Chapter 1. Introduction	3
1.1 Cold atoms and optical lattices	3
1.2 One dimensional systems and simulations	5
1.3 Thesis overview	6
Chapter 2. Dynamical simulation of one-dimensional many-body quantum systems	11
2.1 One-dimensional quantum systems	11
2.1.1 Definition and exact description	11
2.1.2 Generic properties of 1D quantum systems	13
2.1.3 Schmidt decompositions	16
2.2 Matrix product representation	18
2.2.1 Definition	18
2.2.2 Examples	20
2.2.3 Schmidt decompositions and canonical forms	21
2.2.4 Exhaustiveness of the matrix product representation	24
2.3 Calculations and manipulations	26
2.3.1 Matrix product states	26
2.3.2 Density matrices and correlation functions	26
2.3.3 Properties of correlation functions	29
2.3.4 Application of two-site gates	30
2.3.5 Quantum number conservation	33
2.4 Time Evolving Block Decimation	35
2.4.1 Time evolution via a Suzuki-Trotter expansion	35
2.4.2 Suzuki-Trotter sweeps	37
2.4.3 Preparing initial states	39
2.4.4 Errors in TEBD	40
Chapter 3. Ultra-cold atoms in optical lattices	45
3.1 Atom-light interaction	45
3.1.1 Two-level atom	45
3.1.2 Lattice geometry	49
3.1.3 Spontaneous emission	51

3.2	Single-particle physics	52
3.2.1	Bloch states	52
3.2.2	Wannier states	55
3.2.3	Non-interacting system	56
3.3	Many-body physics	58
II	Dynamics of the Bose-Hubbard model	63
Chapter 4.	Properties of the Bose-Hubbard model	65
4.1	Weakly interacting limit - superfluid	66
4.1.1	The $U = 0$ limit	66
4.1.2	The Bogoliubov approximation	68
4.1.3	Superfluidity	75
4.2	Strongly interacting limit - Mott Insulator	80
4.2.1	The $J = 0$ limit	80
4.2.2	Gutzwiller ansatz and decoupled mean-field theory	86
4.3	Refinements for one-dimension	92
4.4	Trapped systems	93
Chapter 5.	<i>Publication: Dynamics of the Superfluid to Mott-insulator transition in one dimension</i>	99
5.1	Introduction	99
5.2	Model and Numerical Method	101
5.2.1	Model	101
5.2.2	Numerical method	101
5.3	Ground states of the BHM	106
5.3.1	Comparison of exact and simulated ground states	106
5.3.2	MI and SF states with a superimposed magnetic trap	107
5.4	Dynamics of the BHM	110
5.4.1	Slow dynamics	112
5.4.2	Fast dynamics	117
5.5	Conclusion	120
Chapter 6.	<i>Publication: Signatures of the Superfluid to Mott-insulator transition in the excitation spectrum of ultracold atoms</i>	123
6.1	Introduction	123
6.2	Probing the system	125
6.2.1	Optical lattices and the Bose-Hubbard model	125
6.2.2	Lattice modulation excitation scheme	126
6.3	Analysis	127
6.3.1	Linear response	127
6.3.2	Numerical method	128
6.4	Results	129
6.4.1	Exact calculation for a small system	129

6.4.2	Large system in a box	133
6.4.3	Large harmonically trapped system	135
6.5	Conclusions	138
III	Quantum State Engineering	143
Chapter 7.	Quantum State Engineering with Optical Lattices	145
7.1	State-dependent optical lattices	145
7.2	Entanglement generation	147
7.3	Engineering spin chains Hamiltonians	151
7.4	Two-atom manipulation	154
Chapter 8.	<i>Publication: Efficient generation of Graph states for quantum computation</i>	159
8.1	Introduction	159
8.2	Non-interacting fermionic system	162
8.2.1	Mirror inversion on a lattice	162
8.2.2	Entanglement of fermionic modes	163
8.2.3	Generalisations	164
8.3	Entanglement generation scheme	164
8.4	Implementations	165
8.4.1	Optical lattice realisation	165
8.4.2	Optical lattice imperfections	167
8.4.3	Alternative implementations	169
8.5	Conclusions	169
Chapter 9.	<i>Publication: Generation of twin-Fock states via two-component Mott insulating to Superfluid transition</i>	173
Chapter 10.	Summary and conclusions	183

Part I

Background

CHAPTER 1

INTRODUCTION

1.1 Cold atoms and optical lattices

For more than a decade now the experimental realisation of Bose-Einstein condensation (BEC) [1] with dilute weakly-interacting alkali gases has provided unique opportunities for exploring the coherent quantum properties of a macroscopically sized system [3, 2]. Amongst other things this has led to the remarkable demonstration of matter wave interference [4] and Josephson-like effects, as well as quantised vortex lattices [5, 6] and solitons [7]. This was achieved due to the extensive control over a BEC that is possible with optical and magnetic trapping, and the ability to perform detailed density measurements after ballistic expansion. The creation of BEC's has also aided, via sympathetic cooling, in the realisation of degenerate Fermi gases and this has led to a number of similar experiments with them [9, 8]. Currently the influence of fermions as an impurity in Bose-Fermi mixtures is receiving a lot of attention [10, 11]. A prominent feature of many of these experiments with BEC's is that they are very successfully described by the Gross-Pitaevskii equation and Bogoliubov mean-field theories in which many-body quantum correlations are either neglected or treated perturbatively [3, 2]. In more recent experiments efforts have been made to enhance the role of interactions giving rise to strongly-correlated systems where this approach is no longer valid. This has been true, for example, in the fermion experiments which utilise a Feshbach resonance [12] to tune the interactions from a diatomic molecular BEC regime to a Bardeen-Cooper-Schrieffer (BCS) like superfluid of atom pairs bound in momentum space, via a so-called BEC-BCS crossover [13, 14]. Another possibility of entering the strongly correlated regime is through the introduction of an optical lattice, and this forms a central theme of this thesis.

An optical lattice is constructed from a far-off resonance standing wave laser field in which neutral atoms are trapped in the regular periodic array of intensity maxima (or minima) due to the optical dipole force [15]. By adiabatically superimposing an optical lattice on a BEC of ultra-cold neutral atoms it was predicted that the atomic motion would give a near-perfect realisation of the Bose-Hubbard model (BHM) [16]. A crucial property of this setup is that the experimenter has an unprecedented control of the parameters of the microscopic Hamiltonian via the corresponding laser intensities. Once trapped within an optical lattice the ratio of the interaction energy (on-site repulsion) to the kinetic energy (inter-site hopping) of the atoms can be significantly

increased with the depth of the lattice. When the interaction starts to dominate the Gross-Pitaevskii approach fails and the resulting many-body system becomes strongly correlated. The BHM has long been considered a useful toy model in condensed matter physics since it possesses an archetypal superfluid to Mott-insulator transition [17]. This transition has now been observed with cold alkali atoms in an optical lattice in a seminal experiment by Greiner *et al.* [18]. The acute controllability of optical lattices has also enabled low-dimensional quantum systems to be realised [19], and this is of particular importance for the work in this thesis. Very recently this permitted the unambiguous manifestation of the long sought after Tonks-Girardeau gas where the motion of atoms is restricted along a pipeline of one spatial dimension (1D) formed by an optical lattice [20].

A crucial property of neutral atoms in optical lattices is their isolation from the environment which allows them to display coherent dynamics on a timescale that far exceeds those required for the experimental manipulation of the system [21]. This situation differs considerably from genuine condensed matter systems and allows, for the first time, the clean unitary quantum dynamics of a strongly interacting many-body system to be explored experimentally. Given that the stationary properties of condensed matter systems have been extensively studied for the last 40 years, and are still far from being completely understood, the novelty of this situation cannot be overestimated.

The range of systems which are realisable can be significantly extended by trapping several internal states of the same atomic species in an optical lattice. As we shall discuss in chapter 7 these can then be independently manipulated with the polarisation of the lasers. By additionally exploiting effects such as Raman transitions or Feshbach resonances an extremely versatile “toolbox” of techniques becomes available in which more complex spin and lattice model Hamiltonians can be engineered and accurately controlled [21]. This has led to proposals for using optical lattices to simulate a variety of other important condensed matter systems such as the fractional quantum Hall effect [22], the Hofstadter butterfly [23], and spin chains [25, 24]. In addition to this the model Hamiltonians realised in optical lattices can often be explored in parameter regimes far beyond those easily accessible in genuine condensed matter systems. For a comprehensive overview of the systems realisable see the recent review papers by Lewenstein *et al.* [26] and Bloch *et al.* [27]. Neutral atoms in optical lattices have also shown to be a very promising candidate for implementing scalable quantum computing since they allow for the controlled creation of entangled states via collisional [29, 28] or dipole-dipole interactions [30], or tunnelling between neighbouring sites [31]. In this thesis we investigate engineering useful many-body quantum states with schemes which combine aspects of the direct manipulation techniques and the implementation of condensed matter models.

1.2 One dimensional systems and simulations

The central theme of this work is on 1D strongly correlated systems in optical lattices. Our focus is on 1D systems for several reasons. Quite generally 1D quantum systems are in themselves very intriguing since their properties often deviate heavily from their higher dimensions counterparts due to the increased influence of quantum fluctuations [32]. A good example of the uniqueness of 1D is that since particles cannot pass each other (or exchange) without colliding their statistics and interactions become inseparably mixed. From a more practical perspective having a system composed of many parallel 1D chains is a convenient geometry for quantum information processing and we shall exploit this in chapter 8. Perhaps the most important reason for restricting ourselves to 1D comes from the nature of these model systems themselves. As mentioned optical lattice setups provide a means of creating controllable, strongly-correlated systems along with the ability to study their coherent many-body dynamics. The flip side of this capability is that to understand and analyse the experimental results presents a considerable theoretical challenge. This is because such systems rarely possess an analytical solution and moreover are often difficult to deal with, even approximately, using standard perturbative techniques. Focussing our attention on 1D comes with the advantage that in some limiting cases we are able to handle them analytically¹ and so gain much insight into the physics (see chapter 8, for example). More generally, in situations which are not accessible to analytical investigation, such as the BHM, we appeal to numerical calculations. From this perspective 1D systems possess a (currently) unique feature in that their dynamical evolution can be efficiently computed with near-exact precision for realistically sized cold-atom systems.

Quantum lattice systems in 1D have been amenable to accurate numerical calculations since the revolutionary formulation of the density matrix renormalisation group (DMRG) method by White in 1992 [33, 34]. The DMRG algorithm was devised to compute the ground states and low-lying excitations of 1D systems. Like other renormalisation procedures it works by allowing the system size to grow, in this case by one site at a time. In order to curtail the exponential growth in the size of the Hilbert space the description of the system is truncated. The significant insight in DMRG is that the reduced density matrix of one half of the system provides an optimal means of performing this truncation. Specifically, the Hilbert space of the newly enlarged system is described by a reduced basis spanned by only the most significant eigenstates of the reduced density matrix. In fact it was found (see reference [35] for a comprehensive review of DMRG) that only a relatively small fixed number of these states need be retained for the description to remain accurate. Following this over the past decade DMRG has provided unprecedentedly accurate calculation of the stationary properties of 1D quantum systems.

Several early attempts to generalise DMRG to include dynamical evolution began in 2002 [36, 37]. Their approach was to use DMRG to determine the ground state, along with its associated truncated Hilbert space, and then time evolve the state within this subspace. While for short times this method worked it ultimately suffered from

¹In terms of analytical solutions 1D systems represent most of the “rarely” just mentioned.

the fundamental limitation that the initial truncated Hilbert space did not necessarily provide an accurate description of the time-evolved state. Quite separate from this in 2003 Vidal developed methods to efficiently simulate weakly entangled quantum computations [38]. It was then quickly realised that the same algorithm, commonly called time-evolving-block-decimation (TEBD), can also be used to study the unitary dynamics of strongly correlated 1D systems such as spin chains and the BHM [39]. The majority of numerical calculations in this thesis were performed using TEBD and for this reason we describe it in detail in chapter 2. A principle feature of TEBD is that it acts directly on a matrix product state ansatz² [40] and provides an efficient method of updating this state after applying the time-evolution, so long as the Hamiltonian only couples nearest-neighbouring sites. In contrast to previous methods this approach optimally adapts the truncated Hilbert space describing the state at each time step so that it remains close to optimal [41]. Since its inception TEBD has become a very important theoretical tool which is ideally suited to ultra-cold atom physics since it provides insight not easily determined by other means. In this thesis we exploit this method heavily to achieve two goals. Firstly, to analyse and understand open questions raised by a number of optical lattice experiments performed so far. Secondly, to aid in the development of new schemes which exploit the dynamical properties of optical lattice setups to engineer useful multipartite quantum states.

1.3 Thesis overview

This thesis is divided into three parts and is composed of four articles, included here in their published form, as well as four other chapters containing relevant background information. The structure of this thesis is as follows.

- **Part I - Background.** In this part of the thesis we introduce important background information. It begins in chapter 2 with a detailed introduction to the TEBD algorithm which forms a substantial part of all the subsequent work presented. In chapter 3 we then review the theory of optical lattices, discussing in detail how at low temperatures the effective Hamiltonian of atoms trapped within them is well described by a Bose Hubbard-like model.
- **Part II - Dynamics of the Bose Hubbard Model.** This part of the thesis is dedicated to investigating the dynamical properties of the BHM which is of particular relevance to recent optical lattice experiments. In chapter 4 we begin by elaborating in some detail on the equilibrium properties of the BHM. By employing a variety of standard analytical and numerical methods we systematically reveal the essential properties of its superfluid and Mott insulating phases. We then construct its mean-field phase diagram and describe some of the peculiarities of the BHM in 1D. This is then followed by two publications which study the dynamical behaviour of the 1D BHM. The first, in chapter 5, investigates the

²This is the same ansatz for the many-body state which underlies DMRG.

dynamical freezing of an initial superfluid ground state of the BHM into the Mott insulating regime, and the opposite case of dynamical melting of an initial Mott insulator. This situation is analogous to the one implemented experimentally by Greiner *et al.* [18]. By studying these processes for a slow (near-adiabatic) ramp and a rapid ramp we reveal that the build-up of single-particle coherence is faster than the timescale for single-atom hopping consistent with the experimental findings. In the second publication in chapter 6, we present a detailed analysis of the dynamical response of atoms in a one-dimensional optical lattice subjected to a periodic modulation of the lattice depth, equivalent to the experiment by Stöferle *et al.* [19]. We were able to determine the excitation spectrum for harmonically trapped systems comparable in size to those in the experiment for depths ranging from the Mott insulator to the superfluid regime. Our results agree well with the experiment, most significantly showing a broad response in the superfluid regime, and narrow discrete resonances in the Mott insulating regime. We have identified several signatures of the superfluid-Mott insulator transition that are manifested in the spectrum as it evolves from one limit to the other. These fully dynamical calculations both demonstrate that the BHM is sufficient to describe the experimental findings and represents an excellent model for the dynamics of cold atoms in optical lattices. Confirmation of the applicability of the BHM is essential for the results presented in part III which utilise the BHM in non-equilibrium situations.

- **Part III - Quantum State Engineering.** In this part of the thesis we propose two schemes for engineering particular types of quantum states useful for quantum information processing and quantum metrology, respectively. We begin in chapter 7 by describing some of the essential “tools” for quantum state engineering in optical lattices which are exploited in the rest of this part. This includes details of how state-dependent optical lattices can be created and shows how the two-component BHM describing this system can, under certain limits, implement an effective spin-chain Hamiltonian. Additionally, we outline the remarkable experimental progress in coherently manipulating two-atom states in the MI phase. Chapter 8 is then a publication where we describe a scheme for the controlled generation of a particular class of entangled states called graph states. This scheme is based on utilising a spin chain Hamiltonian that possess special mirror-inverting couplings, which we called an entangling bus (EB). The dynamics of the EB for a certain time implements a type of quantum circuit which is particularly suited to efficient graph state generation. In chapter 9 this is followed by another publication where we investigate the quantum melting of a two component Mott insulating state, with two atoms per lattice site, into a corresponding superfluid state. We identify two limiting cases where the resulting states are useful for quantum enhanced interferometry. Specifically, a twin Fock state realised from an initial doubly occupied Mott insulator with each site in a state $|ab\rangle$ (where a and b are the two internal states), and a multipartite GHZ state when each site is initialised in the entangled state $|aa\rangle + |bb\rangle$.

The thesis then concludes in chapter 10 with a summary of the main contributions of this work and an outline of future research directions.

Finally, I note that in compiling this thesis I have chosen to include only a portion of the work I have been involved in during my doctoral studies. The selection I have made is based primarily on those pieces of work I contributed most significantly to. However, the work which I have excluded does share some common themes with the contents of this thesis. In particular I have been involved in the development of cooling techniques [42, 43] for attaining the very low temperatures required for realising some condensed matter models in optical lattices. In [44] I helped investigate a scheme for initialising a quantum register with *addressable* atomic qubits in an optical lattice by dynamically doubling the lattice periodicity. In recent work [45] we used the mixed-state version of TEBD to analyse the robustness of the graph state generation scheme discussed in chapter 8 to local noise. Following the recent interest in Bose-Fermi mixtures I have also been involved in work [46, 47, 48] studying the behaviour of neutral atoms in an optical lattice which is immersed in a BEC and the associated formation of so-called polarons. Also the TEBD method used here has been utilised heavily in a numerical analysis of the single-atom-transistor proposal [49].

References

- [1] M. Anderson, J.R. Ensher, M.R. Matthews, C.E. Wieman, E.A. Cornell, *Science* **269**, 198 (1995).
- [2] C.J. Pethick, H. Smith, *Bose-Einstein Condensation in Dilute Gases* (Cambridge Univ. Press, Cambridge, 2002).
- [3] L. Pitaevskii, S. Stringari, *Bose-Einstein Condensation* (Oxford Univ. Press, Oxford, 2003).
- [4] M.R. Andrews, C.G. Townsend, H.J. Miesner, D.S. Durfee, D.M. Kurn, W. Ketterle, *Science* **275**, 637 (1997).
- [5] M.R. Matthews, B.P. Anderson, P.C. Haljan, D.S. Hall, C.E. Wieman, E.A. Cornell, *Phys. Rev. Lett.* **83**, 2498 (1999).
- [6] J.R. Abo-Shaeer, C. Raman, J.M. Vogels, W. Ketterle, *Science* **292**, 476 (2001).
- [7] J. Denschlag, J.E. Simsarian, D.L. Feder, C.W. Clark, L.A. Collins, J. Cubizolles, L. Deng, E.W. Hagley, K. Helmerson, W.P. Reinhardt, S.L. Rolston, B.I. Schneider, W.D. Phillips, *Science* **287**, 97 (2000).
- [8] G. Roati, F. Riboli, G. Modugno, M. Inguscio, *Phys. Rev. Lett.* **89**, 150403 (2002).
- [9] B. DeMarco, D.S. Jin, *Science* **285**, 1703 (1999).
- [10] K. Günter, T. Stöferle, H. Moritz, M. Köhl, T. Esslinger, *Phys. Rev. Lett.* **96**, 180402 (2006).
- [11] S. Ospelkaus, C. Ospelkaus, O. Wille, M. Succo, P. Ernst, K. Sengstock, K. Bongs, *Phys. Rev. Lett.* **96**, 180403 (2006).

- [12] E.A. Donley, N.R. Claussen, S.T. Thompson, C.E. Wieman, *Nature (London)* **417**, 529 (2002).
- [13] M. Greiner, C.A. Regal, D.S. Jin, *Nature (London)* **426**, 537 (2003).
- [14] T. Bourdel, L. Khaykovich, J. Cubizolles, J. Zhang, F. Chevy, M. Teichmann, L. Tarruell, S.J.J.M.F. Kokkelmans, C. Salomon, *Phys. Rev. Lett.* **93**, 050401 (2004).
- [15] P. Jessen, I. Deutsch, *Adv. At. Mol. Opt. Phys.* **37**, 95 (1996).
- [16] D. Jaksch, C. Bruder, J.I. Cirac, C.W. Gardiner, P. Zoller, *Phys. Rev. Lett.* **81**, 3108 (1998).
- [17] M.P.A. Fisher, P.B. Weichman, G. Grinstein, D.S. Fisher, *Phys. Rev. B* **40**, 546 (1989).
- [18] M. Greiner, O. Mandel, T. Esslinger, T.W. Hänsch, I. Bloch, *Nature (London)* **415**, 39 (2002).
- [19] T. Stöferle, H. Moritz, C. Schori, M. Köhl, T. Esslinger, *Phys. Rev. Lett.* **92**, 130403 (2004).
- [20] B. Paredes, A. Widera, V. Murg, O. Mandel, S. Fölling, J.I. Cirac, G.V. Shlyapnikov, T.W. Hänsch, I. Bloch, *Nature (London)* **429**, 277 (2004).
- [21] D. Jaksch, P. Zoller, *Ann. Phys. (N.Y.)* **315**, 52 (2005).
- [22] A.S. Sørensen, E. Demler, M.D. Lukin, *Phys. Rev. Lett.* **94**, 086803 (2005)
- [23] D. Jaksch, P. Zoller, *New J. Phys.* **5**, 56 (2003).
- [24] L.M. Duan, E. Demler, M.D. Lukin, *Phys. Rev. Lett.* **91**, 090402 (2003).
- [25] E. Jane, G. Vidal, W. Dür, P. Zoller, J.I. Cirac, *Quant. Inf. Comput.* **3**, 15 (2003).
- [26] M. Lewenstein, A. Sanpera, V. Ahufinger, B. Damski, A. Sen De, U. Sen, *Adv. in Phys.* **56**, 243 (2007).
- [27] I. Bloch, J. Dalibard, W. Zwerger, [arXiv:0704.3011](https://arxiv.org/abs/0704.3011).
- [28] O. Mandel, M. Greiner, A. Widera, T. Rom, T.W. Hänsch, I. Bloch, *Nature (London)* **425**, 937 (2003).
- [29] D. Jaksch, H.-J. Briegel, J.I. Cirac, C.W. Gardiner, P. Zoller, *Phys. Rev. Lett.* **82**, 1975 (1999).
- [30] G.K. Brennen, C.M. Caves, P.S. Jessen, I.H. Deutsch, *Phys. Rev. Lett.* **82**, 1060 (1999).
- [31] J.K. Pachos, P.L. Knight, *Phys. Rev. Lett.* **91**, 107902 (2003).
- [32] T. Giamarchi, *Quantum Physics in One Dimension* (Oxford Univ. Press, Oxford, 2004).
- [33] S.R. White, *Phys. Rev. Lett.* **69**, 2863 (1992).
- [34] S.R. White, *Phys. Rev. B* **48**, 10345 (1993).

- [35] U. Schollwöck, *Rev. Mod. Phys.* **77**, 259 (2005).
- [36] M.A. Cazalilla, J.B. Marston, *Phys. Rev. Lett.* **88**, 256403 (2002); *ibid* **91**, 049702 (2003).
- [37] H.G. Luo, T. Xiang, X.Q. Wang, *Phys. Rev. Lett.* **91**, 049701 (2003).
- [38] G. Vidal, *Phys. Rev. Lett.* **91**, 147902 (2003).
- [39] G. Vidal, *Phys. Rev. Lett.* **93**, 040502 (2004).
- [40] D. Perez-Garcia, F. Verstraete, M.M. Wolf, J.I. Cirac, [arXiv:quant-ph/0608197](https://arxiv.org/abs/quant-ph/0608197).
- [41] A.J. Daley, C. Kollath, U. Schollwöck, G. Vidal, *J. Stat. Mech.* P04005 (2004).
- [42] A. Griessner, A.J. Daley, S.R. Clark, D. Jaksch, P. Zoller, *Phys. Rev. Lett.* **97**, 220403 (2006).
- [43] A. Griessner, A.J. Daley, S.R. Clark, D. Jaksch, P. Zoller, *New J. Phys.* **9**, 44 (2007).
- [44] B. Vaucher, S.R. Clark, U. Dorner, D. Jaksch, *New J. Phys.* **9**, 221 (2007).
- [45] S.R. Clark, A. Klein, M. Bruderer, D. Jaksch, *New J. Phys.* **9**, 202 (2007).
- [46] M. Bruderer, A. Klein, S.R. Clark, D. Jaksch, *Phys. Rev. A* **76**, 011605(R) (2007).
- [47] A. Klein, M. Bruderer, S.R. Clark, D. Jaksch, *New J. Phys.* **9**, 411 (2007).
- [48] M. Bruderer, A. Klein, S.R. Clark, D. Jaksch, submitted to *New J. Phys.* (2007).
- [49] A.J. Daley, S.R. Clark, D. Jaksch, P. Zoller, *Phys. Rev. A* **72**, 043618 (2005).

CHAPTER 2

DYNAMICAL SIMULATION OF ONE-DIMENSIONAL MANY-BODY QUANTUM SYSTEMS

A central theme for the work presented in this thesis is the investigation and utilisation of the equilibrium and dynamical properties of one-dimensional (1D) quantum systems. An essential distinguishing feature of 1D quantum systems, which is heavily exploited in subsequent chapters, is that they permit near-exact simulation on a (classical) computer using the so-called time-evolving-block-decimation (TEBD) algorithm [1, 2, 3, 4]. In this background chapter we will give a detailed description why this is possible and how this is achieved.

2.1 One-dimensional quantum systems

2.1.1 Definition and exact description

To begin we consider a quantum system composed of M subsystems (or sites) each with an identical local finite d -dimensional Hilbert space \mathcal{H}_d spanned by states $|j\rangle$. The full state space of this system $\mathcal{H} = \mathcal{H}_d^{\otimes M}$ is then spanned by the product basis of these local states $|\mathbf{j}_{[1,M]}\rangle = |j_1\rangle \otimes |j_2\rangle \otimes \cdots \otimes |j_M\rangle$ and has dimension $D = d^M$ which grows exponentially with M . An arbitrary state $|\psi\rangle$ of the system can be expanded in this basis as

$$|\psi\rangle = \sum_{\mathbf{j}_{[1,M]}} c_{j_1 j_2 \cdots j_M} |\mathbf{j}_{[1,M]}\rangle,$$

with D complex amplitudes $c_{j_1 j_2 \cdots j_M}$. While we have imposed a sequential labelling to the subsystems we have not yet made any real constraint on the dimension of the system. Indeed, the actual geometry of the system is only truly revealed by the range and pattern (with respect to the labelling) of interactions between the underlying subsystems as determined by the Hamiltonian¹ of the system. Thus, to restrict our considerations to a genuine 1D quantum system the Hamiltonian \hat{H} governing the system must have short-ranged interactions only. Our case of interest is when the Hamiltonian \hat{H} is composed of arbitrary single-body $\hat{H}^{[1]}$ and two-body terms $\hat{H}^{[2]}$,

¹Note that any Hamiltonian acting between subsystems arranged in any number of dimensions can always be mapped to a 1D chain with an appropriate pattern of long-ranged interactions.

with the latter terms being restricted to act between nearest-neighbouring sites only, giving (note that we shall take $\hbar = 1$ throughout this chapter)

$$\hat{H} = \sum_{i=1}^M \hat{H}_i^{[1]} + \sum_{i=1}^{M-1} \hat{H}_{i,i+1}^{[2]}.$$

Despite placing a severe constraint on \hat{H} this class of Hamiltonians nonetheless includes many important models. For example, it includes several families of spin-chain Hamiltonians, such as those of Heisenberg form, and it also includes the Hubbard model which is often used to describe the motion of electrons in a crystal. Of particular relevance for the work presented here this class of Hamiltonian also contains the Bose-Hubbard model (BHM)

$$\hat{H}_{\text{BH}} = -J \sum_{i=1}^{M-1} (\hat{b}_i^\dagger \hat{b}_{i+1} + \text{h.c.}) + \frac{U}{2} \sum_{i=1}^M \hat{n}_i(\hat{n}_i - 1), \quad (2.1)$$

where each subsystem describes the occupancy² of a lattice site i by bosons via a creation operator \hat{b}_i^\dagger and number operator \hat{n}_i . A complete description of the properties of the BHM, including an explanation of the parameters J and U appearing Eq. (2.1), is given in chapter 4.

Exact calculations for this class of system typically proceed by exploiting the sparseness of the direct matrix representation of the Hamiltonian in the exponentially large product basis $|\mathbf{j}_{[1,M]}\rangle$. However, to hope to make any progress conserved quantities, such as the total particle number, must be taken into account. For the BHM this significantly reduces the Hilbert space dimension to

$$D_{\text{BH}}(N, M) = \frac{(M+N-1)!}{(M-1)!N!},$$

for N bosons in M lattice sites. Despite this reduction $D_{\text{BH}}(N, M)$ still represents an astronomical growth in the Hilbert space dimension with N and M . For unit commensurate filling where $N = M$ (which is interesting because the BHM displays a quantum phase transition as U/J is varied with this filling - see chapter 4 for details) we have $D_{\text{BH}}(8, 8) = 6435$, $D_{\text{BH}}(10, 10) = 92378$ and $D_{\text{BH}}(12, 12) = 1352078$. Moreover in the limit of $M = N \gg 1$ the Hilbert space dimensionality behaves as $D_{\text{BH}}(M, M) \approx \sqrt{2/\pi(M-1)} \exp[2M \ln(2) - \ln(2)]$ and so the growth remains exponential with M . This intractable scaling limits exact calculations of the BHM with current hardware³ to a small number of eigenstates of a $N = M = 12$ system.

²We note here that in principle d should be infinite, however the error incurred by introducing an occupancy cut off is well controlled and presents no practical limitations.

³At the time of writing a typical workstation might have a 3GHz processor and 1GB of RAM.

2.1.2 Generic properties of 1D quantum systems

An essential problem with the exact approach just described is that aside from the use of symmetries and sparseness it is still very generic and does not fully exploit essential features which are unique to 1D quantum systems⁴. Indeed, we shall demonstrate that by using knowledge of how entanglement is distributed within a 1D system a highly efficient parameterisation of the ground state and low-lying excitation for 1D quantum systems is possible [1, 2, 5].

In order to highlight some of the qualitative properties of 1D quantum systems we shall consider the 1D quantum Ising model with a transverse magnetic field

$$\hat{H}_{\text{Ising}} = -J \left(\sum_{i=1}^{M-1} \sigma_i^x \sigma_{i+1}^x + g \sum_{i=1}^M \sigma_i^z \right),$$

since it is exactly solvable [6, 7, 8]. The structure of the ground state $|\psi_{\text{gs}}\rangle$ of \hat{H}_{Ising} changes dramatically with the dimensionless parameter g and is separated into two distinct phases by a quantum phase transition [8] at $g = g_c = 1$, as shown in Fig. 2.1(a). We shall consider two important properties of the ground state. Firstly, the spin-spin correlations as a function of the distance between the spins ℓ which are of the form

$$C_\ell^{ab} = \langle \sigma_i^a \sigma_{i+\ell}^b \rangle - \langle \sigma_i^a \rangle \langle \sigma_{i+\ell}^b \rangle,$$

where $a, b \in \{x, y, z\}$ and $\langle \circ \rangle = \langle \psi_{\text{gs}} | \circ | \psi_{\text{gs}} \rangle$. Since correlation functions C_ℓ^{ab} vanish for all product spin states a change in their behaviour is a signature of a corresponding change in the structure of entanglement in the ground state. Secondly, we consider the entanglement entropy S_L of a contiguous block of L spins⁵, see Fig. 2.1(b), which is calculated from the block's reduced density matrix $\rho_L = \text{tr}_{M-L}(|\psi_{\text{gs}}\rangle \langle \psi_{\text{gs}}|)$ via the von-Neumann entropy

$$S_L = -\text{tr}(\rho_L \log_2 \rho_L),$$

and directly measures the amount of entanglement [9, 10] between the block and the rest of the chain.

In the regime where $g \gg g_c$ the transverse field dominates and the ground state becomes spin-polarised in the z -direction

$$|\psi_{\text{gs}}\rangle_{g \rightarrow \infty} \approx \prod_i |\uparrow\rangle_i.$$

This is the *paramagnetic* phase and corresponds to the magnetisation $\langle \sigma^x \rangle$ being zero. In the regime $g \ll g_c$ the nearest-neighbour spin-coupling dominates and the resulting ground state differs in a fundamental way from that in the $g \rightarrow \infty$ limit. In this case

⁴This is justified by the fact that the total number of sites M in any system that is accessible by exact calculation is not strongly dependent on the systems geometry or spatial dimension.

⁵The chain is taken to be translationally invariant so ρ_L depends only on L .

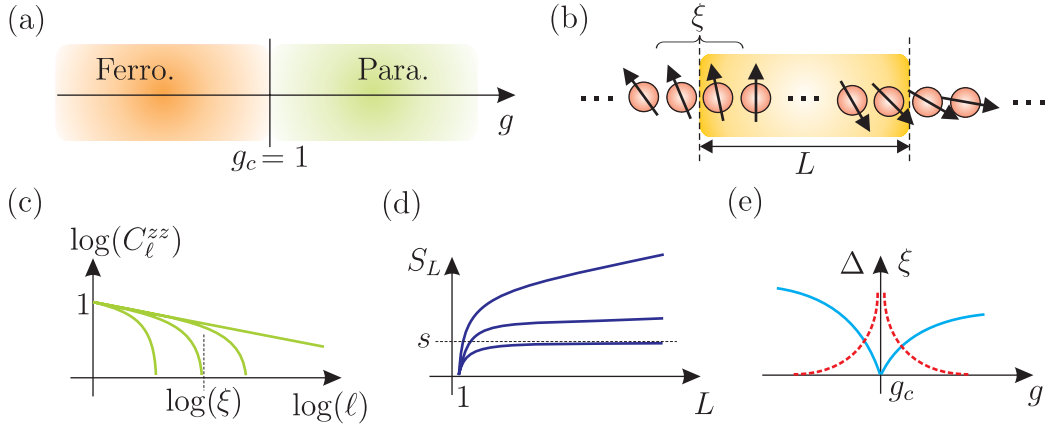


Figure 2.1. (a) The phase diagram of the 1D-Ising chain. For $g > g_c$ it is paramagnetic, while for $g < g_c$ is it ferromagnetic. (b) A distinguished region composed of L spins in a spin chain. The significant contribution to entanglement between the distinguished region and the rest of the chain is located within a correlation length ξ at the boundary. (c) A plot of the zz -correlation function. Away from criticality its long-distance behaviour is an exponential decay with a characteristic length scale of ξ . At criticality it decays as a power-law. (d) The entanglement entropy S_L of a block as a function of its length L . Away from criticality it eventually saturates at some value s . At criticality it increases logarithmically with L . (e) A plot of the gap Δ and correlation length ξ as a function of g . As $g \rightarrow g_c$ the gap Δ vanishes while ξ diverges.

the ground state is doubly degenerate and spanned by the product states with all spins polarised along the x -direction

$$|\psi_{\text{gs}}^+\rangle_{g \rightarrow 0} \approx \prod_i |\rightarrow\rangle_i \quad \text{or} \quad |\psi_{\text{gs}}^-\rangle_{g \rightarrow 0} \approx \prod_i |\leftarrow\rangle_i.$$

This degeneracy occurs because H_{Ising} possesses an exact global Z_2 symmetry generated by the phase flip transformation $U_P = \prod_i \sigma_i^z$, where $|\psi_{\text{gs}}^-\rangle_{g \rightarrow 0} \equiv U_P |\psi_{\text{gs}}^+\rangle_{g \rightarrow 0}$. This regime is known as the *ferromagnetic* phase and is characterised by the development of a non-zero magnetisation $\langle \sigma^x \rangle$ which breaks the Z_2 symmetry. This is commonly referred to as spontaneous symmetry breaking and is a key feature of a quantum phase transition in which the appearance of an order parameter, such as $\langle \sigma^x \rangle$, identifies a new phase.

Away from criticality, where $g \neq g_c$, in either of the two phases described above, the Ising chain has a non-zero energy gap Δ between the ground state and first excited state [5]. Related to this it is also found that the spin-spin correlations decay exponentially as $C_\ell^{ab} \sim e^{-|\ell|/\xi}$ and are characterised by a *correlation length* ξ , as schematically shown in Fig. 2.1(c). The block entropy S_L for a non-critical chain is found to be a growing function of L , but is upper-bounded by a saturation value $s \propto \log_2(\xi)$ as

depicted in Fig. 2.1(d). This value depends on g and increases as the critical point is approached. For a given fixed g the size of the block at the point where S_L approaches its saturation value is of the same order as the correlation length ξ . As a result for block sizes larger than ξ the entanglement between the block and the rest of an infinite chain has a fixed value. This is then entirely consistent with the so-called “area” law⁶ for entanglement scaling where the only significant contribution to the entanglement between a distinguished and exterior region comes from a finite width, given by ξ , around the boundary [11, 12, 13]. Since in 1D the boundary size is independent of block length L the entanglement should remain constant, and this implies that for large block sizes L the amount of entanglement per spin is negligible, i.e. $\lim_{L \rightarrow \infty} (S_L/L) = 0$ [5].

At criticality, when $g = 1$, the spectrum of the Ising chain becomes gapless with $\Delta = 0$ and the spin-spin correlation length ξ diverges, as depicted in Fig. 2.1(e). This is commonly expressed in terms of their scaling as a function of the deviation from the critical point as

$$\xi \sim |g - g_c|^{-\nu} \quad \text{and} \quad \Delta \sim |g - g_c|^{z\nu},$$

where ν and z are critical and dynamical exponents respectively. These are $\nu = z = 1$ for the Ising universality class. The divergence of ξ is symptomatic of a power-law scaling of the correlation functions $C_\ell^{ab} \sim |\ell|^{-q}$, where $q > 0$ at criticality, with $q = 2$ for the Ising model [5] (see Fig. 2.1(c)). For a critical chain the block entropy S_L is a growing function of L and asymptotically takes the form

$$S_L \sim \frac{1}{6} \log_2 L, \tag{2.2}$$

for the Ising model (c.f. with Fig. 2.1(d)). In contrast to a non-critical chain this indicates that the entanglement between a block of spins and the rest of the chain grows unboundedly with the size L of the block. However, despite this growth even at criticality the amount of entanglement in any block is exponentially smaller than the upper bound where S_L grows linearly with L (or with the “volume” of the block), and much like the non-critical case S_L/L becomes negligible for large L [5].

The discussion above has focussed on the 1D quantum Ising model. However, the general observations made have in fact been shown to hold for a very broad class of 1D quantum systems [14]. Early work [11, 15, 16, 17] in this area was motivated by the physics of black-holes and analysed the the block entropy of a 1+1 dimensional massless bosonic field⁷. From these studies the logarithmic divergence of the block entropy was found to violate the area law. Later from a quantum information perspective [5] several important spin-chain models, namely the XY model (containing the Ising and XX models) and XXZ model (containing the Heisenberg model) where

⁶The rationale for the area law is that since the entropies of the distinguished and exterior regions are identical (see section 2.1.3 for an explanation of this) the entropy should only depend on shared properties between the regions. The one property they have in common is their common boundary [11].

⁷This is essentially a system of coupled harmonic oscillators once an ultra-violet (finite lattice spacing or discretisation of space) and infra-red (finite system size) cut-off has been introduced.

examined numerically and also found to exhibit this behaviour. These findings were confirmed and greatly generalised in [18] where conformal field theory methods were applied to integrable lattice models (Ising and XXZ) for finite systems with open or periodic boundary conditions, finite temperatures, and disjoint partitions of the system. Analytical analysis also followed for the XY model [19, 20] and a variety of other models [21, 22, 23, 24, 25, 26]. A universal analytic result extending these findings to any gapless 1D system, such as the Hubbard model or Bose gas with a delta function interaction, was also obtained [27]. While the above studies dealt with homogeneous systems we also note that the logarithmic growth in the block entropy has been found for disordered 1D systems in the so-called random singlet phase [28].

For completeness we summarise here the body of knowledge acquired from these studies about critical and off-critical 1D systems [14]. For a system of length l_{ir} (IR cut-off) with periodic boundary conditions at criticality the entropy of a block of length L is given by

$$S_L = \frac{c}{3} \log_2 \left[\frac{1}{\pi} \frac{l_{\text{ir}}}{l_{\text{uv}}} \sin \left(\pi \frac{L}{l_{\text{ir}}} \right) \right] + A,$$

where c is the central charge of the underlying conformal field theory, l_{uv} is the lattice spacing (UV cut-off), and A is a non-universal constant. For the Ising model $c = \frac{1}{2}$, yielding Eq. (2.2) in the limit $l_{\text{ir}} \rightarrow \infty$, while for the Heisenberg chain $c = 1$. In the case where the system is gapped, or off-criticality, with a finite correlation length ξ the block entropy saturates to a finite value

$$S_L \sim \frac{c}{3} \log_2 \left[\frac{\xi}{l_{\text{uv}}} \right],$$

as $L \rightarrow \infty$. These results have important consequences for the nature of ground states of 1D systems. We shall now proceed to exploit this to devise a significantly more efficient description of the low-lying states of 1D systems than is possible with the general tensor of amplitudes $c_{j_1 j_2 \dots j_M}$ introduced earlier.

2.1.3 Schmidt decompositions

An essential mathematical tool we shall use to build a more efficient formulation is the Schmidt decomposition [9]. Starting from an arbitrary state $|\psi\rangle$ in the Hilbert space \mathcal{H} of an M -site system, we begin by bipartitioning this system into two subsystems A and B which are composed of some subset of m and $M - m$ sites respectively. By using some orthonormal basis $\{|i\rangle_A\}$ spanning the d^m -dimensional Hilbert space \mathcal{H}_A and similarly $\{|j\rangle_B\}$ spanning the d^{M-m} -dimensional Hilbert space \mathcal{H}_B this arbitrary state can be expressed as

$$|\psi\rangle = \sum_{i=1}^{d^m} \sum_{j=1}^{d^{M-m}} C_{ij} |i\rangle_A \otimes |j\rangle_B.$$

The amplitudes C_{ij} of this expansion can then be interpreted as the elements of a $(d^m \times d^{M-m})$ matrix C . We then perform a well-known operation from linear algebra, called the singular-value-decomposition (SVD)⁸, which breaks C up into the product $C = UDV$, where U and V are $(d^m \times d^m)$ and $(d^{M-m} \times d^{M-m})$ unitary matrices and D is a $(d^m \times d^{M-m})$ diagonal matrix whose elements are real and non-negative [9]. We denote the diagonal elements of D as $\lambda_\alpha = D_{\alpha\alpha}$, and the number of non-zero λ_α 's as χ . The value of χ is upper-bounded by $\min(d^m, d^{M-m})$ which is the maximum number of diagonal elements that the non-square matrix D can have. This operation then brings the expansion into the form of a Schmidt decomposition as

$$\begin{aligned} |\psi\rangle &= \sum_{\alpha=1}^{\chi} \lambda_\alpha \left(\sum_{i=1}^{d^m} U_{i\alpha} |i\rangle_A \right) \otimes \left(\sum_{j=1}^{d^{M-m}} V_{\alpha j} |j\rangle_B \right), \\ &= \sum_{\alpha=1}^{\chi} \lambda_\alpha |\phi_\alpha^{[A]}\rangle \otimes |\phi_\alpha^{[B]}\rangle. \end{aligned}$$

Since the unitary matrices U and V act solely on the corresponding subspaces, \mathcal{H}_A and \mathcal{H}_B , respectively, they have been used to construct the orthonormal bases, called Schmidt states, $\{|\phi_\alpha^{[A]}\rangle\}$ and $\{|\phi_\alpha^{[B]}\rangle\}$ which span χ -dimensional subspaces of \mathcal{H}_A and \mathcal{H}_B respectively. The diagonal elements λ_α are called the Schmidt coefficients which we take from now on as being arranged in descending order so $\lambda_\alpha > \lambda_{\alpha+1}$ and satisfy $\sum_\alpha \lambda_\alpha^2 = 1$, while χ is called the Schmidt rank.

The reduced density matrices for the two subsystems $\rho_A = \text{tr}_B(|\psi\rangle\langle\psi|)$ and $\rho_B = \text{tr}_A(|\psi\rangle\langle\psi|)$ then follow from the Schmidt decomposition as

$$\rho_A = \sum_{\alpha=1}^{\chi} \lambda_\alpha^2 |\phi_\alpha^{[A]}\rangle \langle \phi_\alpha^{[A]}| \quad \text{and} \quad \rho_B = \sum_{\alpha=1}^{\chi} \lambda_\alpha^2 |\phi_\alpha^{[B]}\rangle \langle \phi_\alpha^{[B]}|,$$

which immediately demonstrates that both ρ_A and ρ_B are diagonal in their respective Schmidt basis and have identical spectra [9]. Important physical quantities follow from the nature of the spectrum $\{\lambda_\alpha^2\}$. In particular it allows entanglement between the two subsystems to be measured via the entropy $S_{[A|B]}$, introduced earlier as S_L , which is computed via the Shannon entropy of spectrum⁹

$$S_{[A|B]} = - \sum_{\alpha=1}^{\chi} \lambda_\alpha^2 \log_2(\lambda_\alpha^2).$$

Thus, with the total system in a pure state, entanglement between the two subsystems appears as entropy (or mixed-ness) in the resulting reduced density matrices. Additionally, the spectrum allows the most relevant degrees of freedom for either subsystem to be identified as the Schmidt states $\{|\phi_\alpha^{[A]}\rangle\}$ or $\{|\phi_\alpha^{[B]}\rangle\}$ with the largest eigenvalue

⁸The SVD operation forms an important part of the forthcoming details on the numerical method.

⁹The spectrum of ρ_A is essentially a probability distribution $p_\alpha = \lambda_\alpha^2$ with $\sum_\alpha p_\alpha = 1$.

λ_α^2 . Both ρ_A and ρ_B can be approximated to an accuracy¹⁰ $1 - \epsilon$, where $0 \leq \epsilon \leq 1$, by retaining $\chi_m^\epsilon < \chi$ of these Schmidt states such that

$$\sum_{\alpha=1}^{\chi_m^\epsilon} \lambda_\alpha^2 \geq 1 - \epsilon.$$

The relevant degrees of freedom of either subsystem are then considered to be captured by this approximation if $\epsilon \ll 1$, and χ_m^ϵ is the effective Schmidt rank for a subsystem of m sites. A fundamental question, which we shall consider shortly, is whether this condition can be satisfied for $\chi_m^\epsilon \ll \chi$, thereby providing a means of compressing the description of the state. There are two extreme examples. When the system is in a product state $|\psi\rangle = |\phi_1^{[A]}\rangle \otimes |\phi_1^{[B]}\rangle$ it possess the minimum possible Schmidt rank $\chi = 1$ and no entanglement, $S_{[A|B]} = 0$, since its spectrum is $\lambda_1 = 1$. Evidently no compression is possible since each subsystem is already in a state of zero entropy. This is in contrast to a completely random state $|\psi\rangle \in \mathcal{H}$ where the spectrum is expected to be composed of a spread of exponentially many (i.e. $\chi = d^m$) roughly equal eigenvalues. In this case the system is in a state of maximum entropy and $S_{[A|B]}$ scales with the number of sites m (i.e. the volume of A). No compression is possible for such a highly entangled state and we are forced to use $\chi_m^\epsilon \sim d^m$.

In general, many physical states of interest arising from Hamiltonians with local interactions differ considerably from random states [5]. Indeed, for the case of 1D systems the most physically relevant bipartitions are those which involve splitting the system into two contiguous blocks (c.f. Fig. 2.2) with $L = m$. The results from the previous section for blocks of size L then provide some important observations. Firstly, for non-critical systems the saturation of $S_L \rightarrow s$ in Fig. 2.1(d) indicates a similar saturation of the effective Schmidt rank $\chi_L^\epsilon \rightarrow \chi^\epsilon$ for block sizes $L > \xi$. Secondly, numerical evidence shows that for the non-critical ground state of many 1D systems the spectrum decays roughly exponentially with the Schmidt index α . A consequence of this rapid decay is that only a very small number of these eigenvalues are relevant, and the vast majority, although being non-zero, sum to an insignificantly small overall weight. Thus, in spite of the exponential growth of the actual Schmidt rank χ of ρ_L with L , its effective Schmidt rank χ_L^ϵ remains small and leaves much scope for an accurate compression of non-critical states. Finally, for critical 1D systems there is no saturation in the χ_L^ϵ and we instead expect it to grow as some power of L [5].

2.2 Matrix product representation

2.2.1 Definition

Having seen that the ground states of 1D systems have a several unique properties we now come to the question of how to exploit these within a suitable framework. The

¹⁰This accuracy can be defined, for example, by the trace distance or fidelity.

approach that we shall pursue here is based on parameterising the state in the form

$$|\psi\rangle = \sum_{\mathbf{j}_{[1,M]}} f(\mathbf{A}^{[1]j_1} \mathbf{A}^{[2]j_2} \dots \mathbf{A}^{[M]j_M}) |\mathbf{j}_{[1,M]}\rangle, \quad (2.3)$$

where $\mathbf{A}^{[m]j_m}$ are a set of d complex matrices of dimension $(\chi_{m-1} \times \chi_m)$ labelled by the physical index j_m . Each site m of the system therefore has a matrix assigned to it dependent on which physical basis state $|j_m\rangle$ it is in. The full set of amplitudes $c_{j_1 j_2 \dots j_M}$ for the state are then encoded into specific products of such matrices and extracted by the function $f(\cdot)$ which maps $(\chi_0 \times \chi_M)$ matrices to scalars. For this reason Eq. (2.3) is called a matrix product representation [29, 30, 31, 32]. Notice that the matrix product $\prod_{m=1}^M \mathbf{A}^{[m]j_m}$ inherits its ordering from the underlying tensor-product basis $|\mathbf{j}_{[1,M]}\rangle$. The exact form of the function $f(\cdot)$ depends on the boundary conditions. In the case of periodic boundary conditions (PBC) the matrix product representation of a state is [31]

$$|\psi\rangle = \sum_{\mathbf{j}_{[1,M]}} \text{tr}(\mathbf{A}^{[1]j_1} \mathbf{A}^{[2]j_2} \dots \mathbf{A}^{[M]j_M}) |\mathbf{j}_{[1,M]}\rangle.$$

where the function $f(\cdot)$ is a conventional matrix trace. For open boundary conditions (OBC) the expansion is [31]

$$|\psi\rangle = \sum_{\mathbf{j}_{[1,M]}} \langle \Phi_0 | \mathbf{A}^{[1]j_1} \mathbf{A}^{[2]j_2} \dots \mathbf{A}^{[M]j_M} | \Phi_M \rangle |\mathbf{j}_{[1,M]}\rangle,$$

where $|\Phi_0\rangle$ and $|\Phi_M\rangle$ are boundary states in the vector spaces \mathbb{C}^{χ_0} and \mathbb{C}^{χ_M} , respectively¹¹. In this case the function $f(\cdot)$ is then equivalent to the scalar-product with these boundary states. It is important to note that the \mathbf{A} matrices can be completely general and this permits several intuitive physical interpretations of them which involve adding “virtual” sites to the system. The most notable examples of this are the bond-site [4, 31] and the projected entangled pair [33, 34] formulations. Here we shall take a more pragmatic approach and not explicitly use either of these interpretations. Instead we will build up a picture of how states are described in this representation by appealing to the Schmidt decomposition, and show that the dimensions χ_m of the \mathbf{A} matrices are directly related to the amount of block-wise entanglement in the state. The matrix product representation in Eq. (2.3) will therefore lead us to an efficient ansatz where χ_m is artificially fixed. Before pursuing this, however, we shall introduce some examples.

¹¹Note that for numerical calculation we can set $\chi_0 = 1$ and $\chi_M = 1$ for convenience.

2.2.2 Examples

Here we give five examples of many-body quantum states¹² which have particularly simple exact matrix product representations.

1. **Product states** : The class of site-wise factorised states $|\psi\rangle = \otimes_{m=1}^M |\vartheta^{[m]}\rangle$ possesses the most trivial matrix product representation possible. In this case, using OBC, we have that $\chi_m = 1$ for all m . The (1×1) “matrices” then follow directly from the expansion of each sites state in its local basis as

$$|\vartheta^{[m]}\rangle = \sum_{j_m=1}^d \mathbf{A}_{11}^{[m]j_m} |j_m\rangle.$$

The fact that the local dimensions χ_m reduce to unity in this case is a consequence of the lack of entanglement for this class of states. We shall make this connection more formal shortly.

2. **Affleck-Kennedy-Lieb-Tasaki** (AKLT) state : This state possesses perhaps the best-known non-trivial matrix product representation. It arises as the valence-bond ground state of the bilinear-biquadratic spin-chain Hamiltonian

$$\hat{H}_{\text{AKLT}} = \sum_{m=1}^M \left\{ \vec{S}_m \cdot \vec{S}_{m+1} + \frac{1}{3} \left(\vec{S}_m \cdot \vec{S}_{m+1} \right)^2 \right\},$$

where \vec{S}_m is the vector of spin-1 operators (so $d = 3$) for the m -th spin. Using PBC the ground state of \hat{H}_{AKLT} has a translationally invariant matrix product representation with $\mathbf{A}^{[m]j_m} = \mathbf{A}^{j_m}$ and $\chi_m = 2$ for all m . The matrices are then

$$\mathbf{A}^{j=1} = \sigma^z, \quad \mathbf{A}^{j=2} = \sqrt{2}\sigma^+, \quad \mathbf{A}^{j=3} = -\sqrt{2}\sigma^-,$$

where the σ 's are the usual Pauli matrices.

3. **Greenberger-Horne-Zeilinger** (GHZ) state : For a set of M spin- $\frac{1}{2}$ particles (so $d = 2$) these states have the form $|\psi\rangle = |\uparrow\uparrow\cdots\uparrow\uparrow\rangle + |\downarrow\downarrow\cdots\downarrow\downarrow\rangle$. Much like the AKLT state the GHZ state can be expressed in PBC as a translationally invariant matrix product representation with $\chi_m = 2$ for all m and matrices

$$\mathbf{A}^{j=\uparrow} = \frac{1}{2}(\mathbb{1} + \sigma^z), \quad \mathbf{A}^{j=\downarrow} = \frac{1}{2}(\mathbb{1} - \sigma^z).$$

In this case it is straightforward to see that any matrix product which contains factors of the form $\frac{1}{2}(\mathbb{1} - \sigma^z) \times \frac{1}{2}(\mathbb{1} + \sigma^z)$ yields a zero matrix. Similarly, the anti-ferromagnetic GHZ state $|\psi\rangle = |\uparrow\downarrow\cdots\uparrow\downarrow\rangle + |\downarrow\uparrow\cdots\downarrow\uparrow\rangle$ corresponds to the matrices $\mathbf{A}^{j=\uparrow} = \sigma^+$ and $\mathbf{A}^{j=\downarrow} = \sigma^-$.

¹²We shall ignore the normalisation of the states in this section.

4. **Cluster** state : In 1D a cluster state is the unique ground state of the three-body spin-chain Hamiltonian¹³

$$\hat{H}_{\text{CS}} = \sum_{m=1}^M \sigma_m^z \sigma_{m+1}^x \sigma_{m+2}^z.$$

With PBC we again obtain a translationally invariant matrix product representation with $\chi_m = 2$ for all m and matrices

$$\mathbf{A}^{j=\uparrow} = \sigma^- + \frac{1}{2}(\mathbb{1} - \sigma^z), \quad \mathbf{A}^{j=\downarrow} = \frac{1}{2}(\mathbb{1} + \sigma^z) - \sigma^+.$$

5. **W-state** : The W-state is an equal superposition of all translates of $|\downarrow\uparrow\cdots\uparrow\uparrow\rangle$ for M spin- $\frac{1}{2}$ particles. In contrast to the previous examples, despite this state possessing full permutation symmetry, there is no translationally invariant matrix product representation of a W-state with $\chi_m = 2$ for all m . Instead the simplest representation of a W-state uses OBC and so does not share its symmetries. More precisely, we choose matrices $\mathbf{A}^{[m]j_m}$ which are site dependent, but take $\chi_m = 2$ independent of m . The corresponding boundary states in \mathbb{C}^2 are then chosen to be $|\Phi_0\rangle = |\uparrow\rangle$ and $|\Phi_M\rangle = |\uparrow\rangle$. For the sites $m < M$ the matrices are then

$$\mathbf{A}^{[m]j_m=\uparrow} = \mathbb{1}, \quad \mathbf{A}^{[m]j_m=\downarrow} = \sigma^+,$$

while the last site $m = M$ has

$$\mathbf{A}^{[M]j_M=\uparrow} = \sigma^-, \quad \mathbf{A}^{[M]j_M=\downarrow} = \frac{1}{2}(\mathbb{1} + \sigma^z).$$

The W-state then arises from this since for every basis state of the type $|\downarrow\uparrow\cdots\uparrow\uparrow\rangle$ the matrix product becomes $\frac{1}{2}(\mathbb{1} + \sigma^z)$, whereas any other combination gives either a zero matrix or zero scalar-product with the boundary states. This example therefore illustrates the use of OBC and the subtle, but well-known, problems associated with matrix product representations with PBC [31].

2.2.3 Schmidt decompositions and canonical forms

As of yet we have made no constraints on the form of the matrices $\mathbf{A}^{[m]j_m}$. This not only makes this description difficult to interpret, it also makes them harder to handle numerically. The situation can be improved by exploiting the gauge freedom possessed by a matrix product representation. Specifically, this gauge freedom permits the insertion of any non-singular square ($\chi_m \times \chi_m$) matrix \mathbf{X} along with its inverse \mathbf{X}^{-1} into the matrix product since $\mathbf{A}^{[m]j_m} \mathbf{A}^{[m+1]j_{m+1}} = (\mathbf{A}^{[m]j_m} \mathbf{X}^{-1})(\mathbf{X} \mathbf{A}^{[m+1]j_{m+1}})$. In this section we shall sketch how to exploit this freedom to transform an unconstrained matrix product representation into a canonical form where all the contiguous Schmidt decompositions of the state are easily accessible.

¹³This Hamiltonian is simply the sum of the stabiliser operators that define a 1D cluster state.

To begin we consider a system with OBC and split it after site k into two contiguous blocks $L = \{1, \dots, k\}$ and $R = \{k+1, \dots, M\}$. Using the gauge freedom we redefine the matrix $\mathbf{A}^{[k]j_k}$ as $\mathbf{A}^{[k]j_k} \mapsto \mathbf{A}^{[k]j_k} \mathbf{D}^{-1}$ where \mathbf{D} is a diagonal $(\chi_k \times \chi_k)$ matrix with real elements λ_{α_k} , and correspondingly introduce it into the product as

$$\prod_{m=1}^M \mathbf{A}^{[m]j_m} \mapsto \left(\prod_{m=1}^k \mathbf{A}^{[m]j_m} \right) \mathbf{D} \left(\prod_{m'=k+1}^M \mathbf{A}^{[m']j'_m} \right).$$

By inserting the resolution of the identity $\sum_{\alpha_k} |\alpha_k\rangle \langle \alpha_k|$, for the vector space \mathbb{C}^{χ_k} , on both sides of the diagonal matrix \mathbf{D} the matrix product representation of $|\psi\rangle$ can then be readily split up into the form

$$|\psi\rangle = \sum_{\alpha_k=1}^{\chi_k} \lambda_{\alpha_k} |\varphi_{\alpha_k}^{[L]}\rangle |\varphi_{\alpha_k}^{[R]}\rangle, \quad (2.4)$$

where the states of the blocks L and R are

$$\begin{aligned} |\varphi_{\alpha_k}^{[L]}\rangle &= \sum_{\mathbf{j}_{[1,k]}} \langle \Phi_0 | \mathbf{A}^{[1]j_1} \cdots \mathbf{A}^{[k]j_k} | \alpha_k \rangle | \mathbf{j}_{[1,k]} \rangle, \\ |\varphi_{\alpha_k}^{[R]}\rangle &= \sum_{\mathbf{j}_{[k+1,M]}} \langle \alpha_k | \mathbf{A}^{[k+1]j_{k+1}} \cdots \mathbf{A}^{[M]j_M} | \Phi_M \rangle | \mathbf{j}_{[k+1,M]} \rangle. \end{aligned}$$

The corresponding scalar-products of these block states are then

$$\begin{aligned} \langle \varphi_{\alpha_k}^{[L]} | \varphi_{\beta_k}^{[L]} \rangle &= \sum_{\mathbf{j}_{[1,k]}} \langle \alpha_k | (\mathbf{A}^{[k]j_k})^\dagger \cdots (\mathbf{A}^{[1]j_1})^\dagger | \Phi_0 \rangle \langle \Phi_0 | \mathbf{A}^{[1]j_1} \cdots \mathbf{A}^{[k]j_k} | \beta_k \rangle, \\ \langle \varphi_{\alpha_k}^{[R]} | \varphi_{\beta_k}^{[R]} \rangle &= \sum_{\mathbf{j}_{[k+1,M]}} \langle \beta_k | \mathbf{A}^{[k+1]j_{k+1}} \cdots \mathbf{A}^{[M]j_M} | \Phi_M \rangle \langle \Phi_M | (\mathbf{A}^{[M]j_M})^\dagger \cdots (\mathbf{A}^{[k+1]j_{k+1}})^\dagger | \alpha_k \rangle. \end{aligned}$$

We now impose the following constraint on the boundary matrices

$$\sum_{j_1=1}^d (\mathbf{A}_{\leftarrow}^{[1]j_1})^\dagger | \Phi_0 \rangle \langle \Phi_0 | \mathbf{A}_{\leftarrow}^{[1]j_1} = \mathbb{1}, \quad (\text{lefthanded}), \quad (2.5)$$

$$\sum_{j_M=1}^d \mathbf{A}_{\rightarrow}^{[M]j_M} | \Phi_M \rangle \langle \Phi_M | (\mathbf{A}_{\rightarrow}^{[M]j_M})^\dagger = \mathbb{1}, \quad (\text{righthanded}), \quad (2.6)$$

which absorb the boundary states. Notice that the boundary \mathbf{A} matrices for the W-state introduced in the last section satisfy these constraints. To proceed and identify Eq. (2.4) as a genuine Schmidt decomposition of $|\psi\rangle$ we require the remaining \mathbf{A}

matrices to obey one of the following constraints¹⁴

$$\sum_{j_m=1}^d (\mathbf{A}_{\leftarrow}^{[m]j_m})^\dagger \mathbf{A}_{\leftarrow}^{[m]j_m} = \mathbb{1}, \quad (\text{lefthanded}), \quad (2.7)$$

$$\sum_{j_m=1}^d \mathbf{A}_{\rightarrow}^{[m]j_m} (\mathbf{A}_{\rightarrow}^{[m]j_m})^\dagger = \mathbb{1}, \quad (\text{righthanded}). \quad (2.8)$$

If Eq. (2.7) applies to all matrices $\mathbf{A}^{[m]j_m}$ with $1 < m \leq k$, then the orthonormality of the left block states $|\varphi_{\alpha_k}^{[A]}\rangle$ can be established, after using the boundary constraint Eq. (2.5), by its successive use. The same occurs for the right block states $|\varphi_{\alpha_k}^{[B]}\rangle$, after applying Eq. (2.6), if the constraint Eq. (2.8) applies to all matrices $\mathbf{A}^{[m]j_m}$ with $k < m < M$. Above we have introduced the notation \mathbf{A}_{\leftarrow} and \mathbf{A}_{\rightarrow} to signify when an \mathbf{A} matrix obeys the corresponding left or righthanded orthonormality constraint. Finally, we now require $|\psi\rangle$ to be normalised, which is equivalent to $\text{tr}(\mathbf{D}^2) = 1 = \sum_{\alpha_k} \lambda_{\alpha_k}^2 = 1$, allowing the diagonal matrix \mathbf{D} to be identified with the matrix of Schmidt coefficients $\sqrt{\Lambda^{[k]}}$. Now if these constraints on the matrices $\mathbf{A}^{[m]j_m}$ and the real parameters λ_{α_k} are simultaneously satisfied then the form of Eq. (2.4) precisely coincides with the Schmidt decomposition of $|\psi\rangle$ after site k .

In fact it can be proven [30] that any (unconstrained) matrix product can be reformulated in terms of matrices which obey a combination of Eq. (2.7) and Eq. (2.8). We shall not reproduce this proof here in full, but instead sketch the most important points. Suppose we have an unconstrained matrix product $\prod_{m=1}^M \mathbf{B}^{[m]j_m}$. The trick to this construction is to take the set of d matrices $\mathbf{B}^{[m]j_m}$ and build a single $(d \chi_{m-1} \times \chi_m)$ complex matrix \mathbf{B} out of them. This can be done by either (i) pairing the physical index j_m to α_{m-1} to form a row index, or by (ii) pairing j_m with α_m to form a column index. We then perform a SVD on the matrix \mathbf{B} and obtain the decompositions (i) $\mathbf{A} \mathbf{D} \mathbf{V}$ with \mathbf{A} a $(d \chi_{m-1} \times \chi_m)$ matrix or (ii) $\mathbf{V} \mathbf{D} \mathbf{A}$ with \mathbf{A} a $(\chi_{m-1} \times \chi_m d)$ matrix. In both cases matrix \mathbf{A} is unitary and this is the essential feature of this procedure. We then break up \mathbf{A} as a set of d $(\chi_{m-1} \times \chi_m)$ matrices $\mathbf{A}^{[m]j_m}$. For case (i) the unitary condition $\mathbf{A}^\dagger \mathbf{A} = \mathbb{1}$ is equivalent to the lefthanded orthonormality condition Eq. (2.7) for the new matrices $\mathbf{A}^{[m]j_m} = \mathbf{A}_{\leftarrow}^{[m]j_m}$. The opposite unitary condition then establishes righthanded orthonormality for case (ii). Thus the SVD has enabled an orthonormal matrix to be extracted from an initially unconstrained one. This procedure can be performed iteratively (passing on the left over \mathbf{D} and \mathbf{V} matrices to the next step) starting from the boundary matrices applying case (i) from the left and case (ii) from the right. If these left and right procedures meet at site L we have then transformed the original matrix product $\prod_{m=1}^M \mathbf{B}^{[m]j_m}$ into the form $(\prod_{m=1}^k \mathbf{A}_{\leftarrow}^{[m]j_m}) \sqrt{\Lambda^{[k]}} (\prod_{m=k+1}^M \mathbf{A}_{\rightarrow}^{[m]j_m})$ equivalent to a Schmidt decomposition after site k [30].

While this above procedure yields an orthonormalised matrix product equivalent to one particular Schmidt decomposition (depending on where the left and right proce-

¹⁴For the case where $\chi_0 = \chi_M = 1$ normalised boundary states are simply the scalar 1 and so the boundary constraints Eq. (2.5) and Eq. (2.6) are identical to Eq. (2.7) and Eq. (2.8), respectively.

dures meet) we have not yet constrained the \mathbf{A} matrices enough so that *all* contiguous Schmidt decompositions are easily accessible¹⁵. We therefore impose an additional “shifting” constraint

$$\begin{aligned} \sum_{j_m=1}^d \mathbf{A}_{\leftarrow}^{[m]j_m} \Lambda^{[m]} (\mathbf{A}_{\leftarrow}^{[m]j_m})^\dagger &= \Lambda^{[m-1]}, \quad (\text{lefthanded}), \\ \sum_{j_m=1}^d (\mathbf{A}_{\rightarrow}^{[m]j_m})^\dagger \Lambda^{[m-1]} \mathbf{A}_{\rightarrow}^{[m]j_m} &= \Lambda^{[m]}, \quad (\text{righthanded}). \end{aligned}$$

When all the \mathbf{A} matrices in the product obey an appropriate pair of orthonormality and shifting constraints we say that the representation is canonical. By obeying the shifting property the handedness of the \mathbf{A} matrices can be flipped trivially without recourse to an (expensive) SVD through

$$\mathbf{A}_{\leftarrow}^{[m]j_m} \sqrt{\Lambda^{[m]}} = \sqrt{\Lambda^{[m-1]}} \mathbf{A}_{\rightarrow}^{[m]j_m}.$$

This (cheap) flip operation can then be used repeatedly to bring a canonical matrix product representation into any desired contiguous Schmidt decomposition.

It is possible to show that any orthonormalised matrix product can be brought into canonical form [30]. Again, we will not reproduce the proof of this here and instead only sketch the important details. Similar to the orthonormalisation procedure the essential part of this process is to take an orthonormalised set of matrices $\mathbf{B}_{\rightarrow}^{[m]j_m}$ and diagonalise the positive matrix $\mathbf{M}^{[m]} = \sum_{j_m=1}^M (\mathbf{B}_{\rightarrow}^{[m]j_m})^\dagger \mathbf{B}_{\rightarrow}^{[m]j_m}$ formed from them. The unitary matrix extracted from this can then be used as a gauge transformation on $\mathbf{B}_{\rightarrow}^{[m]j_m}$ which establishes the appropriate shifting property while retaining its original orthonormality. By doing this iteratively from $m = 1$ to $m = M$ the entire matrix product can be made canonical [30].

2.2.4 Exhaustiveness of the matrix product representation

In this section we demonstrate that the matrix product representation is exhaustive and therefore can, in principle, describe any state [1, 30]. To proceed we split the system into two contiguous sets labelled as $L^{[m]} = \{1, \dots, m\}$ and $R^{[m]} = \{m+1, \dots, M\}$ and perform a Schmidt decomposition. This yields a set of Schmidt coefficients $\lambda_{\alpha_m}^{[m]}$, and corresponding Schmidt states $|L_{\alpha_m}^{[m]}\rangle$ and $|R_{\alpha_m}^{[m]}\rangle$, with a Schmidt rank χ_m . Repeating this for all m gives a set of $M - 1$ such Schmidt decompositions, as shown in Fig. 2.2.

While having precise knowledge of any one of these Schmidt decompositions completely describes the state $|\psi\rangle$, a canonical matrix product representation is in fact a recursive construction of scalar-products which utilises either $|L_{\alpha_m}^{[m]}\rangle$ or $|R_{\alpha_m}^{[m]}\rangle$ depending on the handedness of the matrices. For example, to build a completely lefthanded

¹⁵While we can obtain any Schmidt decomposition by applying sequences of SVD operations these are expensive operations and for this reason we do not consider them as being *accessible*.

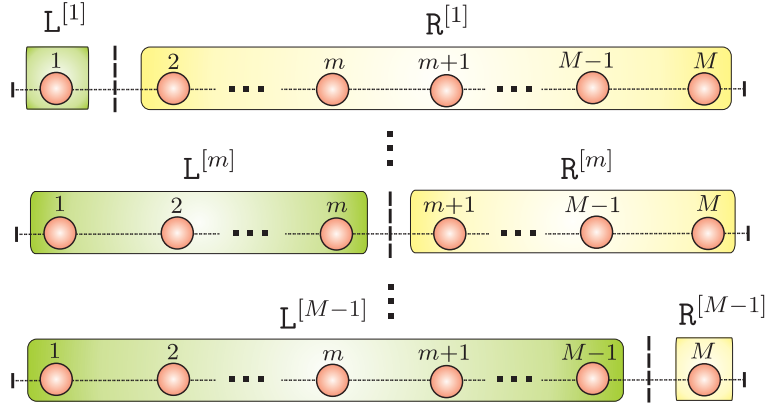


Figure 2.2. The sequence of $M - 1$ contiguous partitions (according to the labelling imposed) of the system in which the Schmidt decompositions are computed.

canonical representation start with $m = 1$ and expand $|L_{\alpha_1}^{[1]}\rangle$ in the basis $|j_1\rangle$ as¹⁶ $|L_{\alpha_1}^{[1]}\rangle = \sum_{j_1=1}^d A_{\alpha_1}^{[1]j_1} |j_1\rangle$. Moving to $m = 2$ we then expand $|L_{\alpha_2}^{[2]}\rangle$ in terms of $|L_{\alpha_1}^{[1]}\rangle$ and $|j_2\rangle$ as $|L_{\alpha_2}^{[2]}\rangle = \sum_{j_2=1}^d \sum_{\alpha_1=1}^{\chi_1} A_{\alpha_1\alpha_2}^{[2]j_2} |L_{\alpha_1}^{[1]}\rangle |j_2\rangle$. For a split after site m we perform the expansion $|L_{\alpha_m}^{[m]}\rangle = \sum_{j_m=1}^d \sum_{\alpha_m=1}^{\chi_m} A_{\alpha_{m-1}\alpha_m}^{[m]j_m} |L_{\alpha_{m-1}}^{[m-1]}\rangle |j_m\rangle$. For the last site $m = M$ the set $L^{[m]}$ contains all the sites leaving $|L_{\alpha_M=1}^{[M]}\rangle = |\psi\rangle$. We then take the tensors $A_{\alpha_{m-1}\alpha_m}^{[m]j_m}$ of expansion coefficients and form sets of matrices $\mathbf{A}_{\alpha_{m-1}\alpha_m}^{[m]j_m}$ for each m . These matrices are manifestly left-hand orthonormalised and canonical due to the fact that they were derived from Schmidt states [1]. Righthanded canonical matrices are then extracted by an analogous construction using expansions of the right Schmidt states $|R_{\alpha_m}^{[m]}\rangle$ instead.

We can draw two important conclusions from this construction. Firstly, a canonical matrix product representation naturally contains all the contiguous Schmidt decompositions of the state and the dimensions of the corresponding matrices χ_m are the Schmidt ranks. Secondly, for a matrix product representation to be exhaustive these dimensions χ_m can only be limited by the Hilbert space dimension of the smallest subsystem $L^{[m]}$ or $R^{[m]}$ involved. This leaves $\max(\chi_m) \leq d^{M/2}$ and, as expected, implies that the number of parameters within a matrix product representation can potentially grow exponentially with M if it is to describe arbitrary states exactly.

¹⁶This construction manifestly enforces $\chi_0 = \chi_M = 1$.

2.3 Calculations and manipulations

2.3.1 Matrix product states

A significant feature of the matrix product representation is that the dimensions of the \mathbf{A} matrices provide a natural means of constructing a class of states whose description possesses only a linear growth in parameters with M . Specifically, we define a matrix product state (MPS) ansatz as the class of states described by a matrix product representation with a maximum dimension $\max(\chi_m) \leq \chi$, where χ is a constant independent of M . As a result the scaling in the number of parameters is $O(d M \chi^2)$. We shall denote the set of states that can be described by an MPS ansatz with a given maximum dimension χ as \mathcal{S}_χ . An immediate consequence of the definition of MPS is that they have a fixed maximum Schmidt rank and therefore maximum entanglement entropy. For this reason MPS in \mathcal{S}_χ cannot describe states with a block entropy S_L which grows as some function of L such as the logarithmic growth seen earlier for critical 1D systems. However, off-criticality our earlier discussion about 1D quantum systems seems to suggest that MPS are a promising ansatz. Indeed this intuition has been confirmed by the enormous success of density matrix renormalisation group (DMRG) [31, 35, 36] which is essentially a variational method of constructing an MPS approximation to ground state and low-lying excitations of 1D systems [37, 38].

Another important property of any set \mathcal{S}_χ is that it is not a vector space. This is most easily demonstrated by a simple example. Consider the two product states $|\uparrow\uparrow\cdots\uparrow\uparrow\rangle$ and $|\downarrow\downarrow\cdots\downarrow\downarrow\rangle$ which are both members of \mathcal{S}_1 . The linear combination of them, however, is a GHZ state which as we saw earlier is a member of \mathcal{S}_2 and is entangled. More generally, suppose that we have two MPS, $|\psi_A\rangle$ and $|\psi_B\rangle$, described by matrices $\mathbf{A}^{[m]j_m}$ and $\mathbf{B}^{[m]j_m}$ each with maximum dimensions χ_A and χ_B respectively. The linear combination $|\psi_C\rangle = |\psi_A\rangle + |\psi_B\rangle$ can then be factorised into an MPS with corresponding matrices¹⁷ $\mathbf{C}^{[m]j_m} = \mathbf{A}^{[m]j_m} \oplus \mathbf{B}^{[m]j_m}$ and so the resulting maximum dimension increases to $\chi_C = \chi_A + \chi_B$. Importantly, the new MPS may not be normalised and will not be of canonical form, even if $\mathbf{A}^{[m]j_m}$ and $\mathbf{B}^{[m]j_m}$ were originally. The new MPS can be brought into a normalised canonical form following the procedures already outlined, and then have its Schmidt ranks χ_m optimally truncated back to χ if necessary.

2.3.2 Density matrices and correlation functions

When studying strongly-correlated systems there are several quantities which are typically of interest in characterising the system's state. These might include the reduced density operators of a small subset of sites, such as ρ_k for a single site k or ρ_{kl} for two sites k and l , and expectation values of the form $\langle\psi|O_1 \otimes O_2 \otimes \cdots \otimes O_M|\phi\rangle$, where $\{O_j\}_{j=1}^M$ are operators acting the Hilbert space \mathcal{H}_d for site j . The latter case not only enables n -point correlations to be calculate, but also enables overlaps $\langle\psi|\phi\rangle$ between

¹⁷At the boundaries, where $\chi_0 = \chi_M = 1$, the appropriate row or column vector additions are made.

different states to be computed. Here, we shall demonstrate that all these quantities can be efficiently computed whenever $|\psi\rangle$ and $|\phi\rangle$ are MPS.

For convenience the description given for the rest of this section utilises MPS with PBC and unconstrained matrices¹⁸. The modification to OBC involves replacing the $\text{tr}(\cdot)$ operation with an appropriate scalar-product of boundary states and is straightforward. To begin the full density operator $\rho = |\psi\rangle\langle\psi|$ of the system is given by

$$\rho = \sum_{\mathbf{j}_{[1,M]}} \sum_{\mathbf{i}_{[1,M]}} \text{tr} \left(\prod_{m=1}^M \mathbf{A}^{[m]j_m} \right) \text{tr} \left(\prod_{m=1}^M \mathbf{A}^{*[m]i_m} \right) |\mathbf{j}_{[1,M]}\rangle \langle \mathbf{i}_{[1,M]}|,$$

after using $\text{tr}(XYZ)^* = \text{tr}(X^*Y^*Z^*)$. The most useful form of this expression follows by combining the two traces over the separate matrix products as a single trace over the Kronecker tensor product¹⁹ of these matrix products. By applying the matrix identities $\text{tr}(X)\text{tr}(Y) = \text{tr}(X \otimes Y) = \text{tr}(Y \otimes X)$ and $(ABC) \otimes (XYZ) = (A \otimes X)(B \otimes Y)(C \otimes Z)$ we obtain a more compact form [30, 31]

$$\rho = \sum_{\mathbf{j}_{[1,M]}} \sum_{\mathbf{i}_{[1,M]}} \text{tr} \left(\prod_{m=1}^M \mathbf{E}^{[m]j_m i_m} \right) |\mathbf{j}_{[1,M]}\rangle \langle \mathbf{i}_{[1,M]}|,$$

where $\mathbf{E}^{[m]j_m i_m} = \mathbf{A}^{[m]j_m} \otimes \mathbf{A}^{*[m]i_m}$, as depicted in Fig. 2.3(a). The normalisation of the state is obtained by tracing out all the physical sites as $\text{tr}(\rho) = \langle\psi|\psi\rangle = \text{tr}(\prod_{m=1}^M \mathbf{I}^{[m]})$ where the contraction of the physical indices labelling the set of matrix $\mathbf{E}^{[m]j_m i_m}$ is called the “transfer” matrix and is denoted as $\mathbf{I}^{[m]} = \sum_{j_m=1}^d \mathbf{E}^{[m]j_m j_m}$. By leaving out one site k from this trace we obtain the reduced density operator

$$\rho_k = \sum_{j_k=1}^d \sum_{i_k=1}^d \text{tr} \left(\left[\prod_{m=1}^{k-1} \mathbf{I}^{[m]} \right] \mathbf{E}^{[k]j_k i_k} \left[\prod_{m'=k+1}^M \mathbf{I}^{[m']} \right] \right) |j_k\rangle \langle i_k|,$$

which is graphically represented in Fig. 2.3(b). Expressions for the reduced density operators of larger numbers of sites then follow a similar form as a trace of products of appropriate sets of $\mathbf{I}^{[m]}$ and $\mathbf{E}^{[m]j_m i_m}$ matrices [30, 31].

The computation of a general product operator expectation value follows a similar form as [30, 31]

$$\langle\psi|O_1 \otimes O_2 \otimes \cdots \otimes O_M|\psi\rangle = \text{tr} \left(\prod_{m=1}^M \mathbf{O}^{[m]} \right),$$

¹⁸In the next section we shall apply canonical constraints since it simplifies the analytical form of the correlation functions.

¹⁹The ordering of this tensor product is not important.

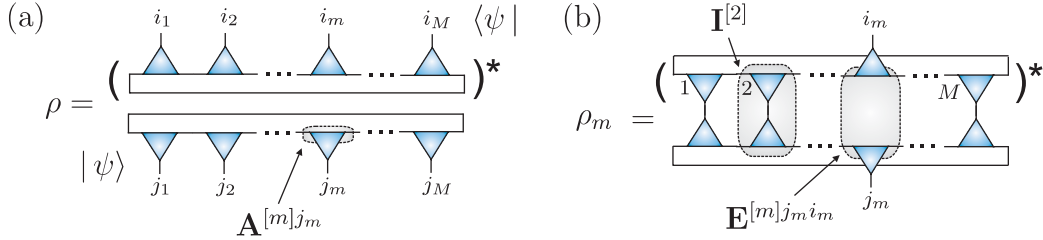


Figure 2.3. (a) The graphical representation of the full density matrix $\rho = |\psi\rangle\langle\psi|$ of the system with PBC. The shaded triangular object represents the matrices $\mathbf{A}^{[m]j_m}$. (b) Tracing out all sites, aside from site m , is equivalent to contracting (joining) all the appropriate physical indices. The remaining (uncontracted) indices i_m and j_m are then the rows and columns of the density matrix ρ_m . The shaded objects represent the matrices $\mathbf{E}^{[m]j_mi_m}$ and $\mathbf{I}^{[m]}$.

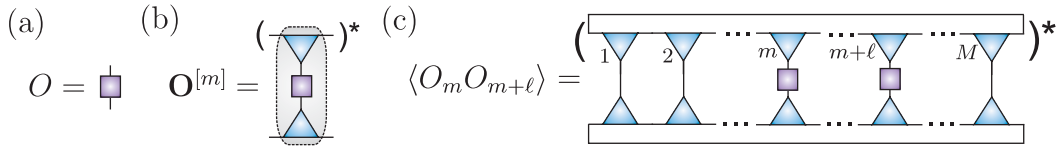


Figure 2.4. (a) An observable O acting on one site. (b) The graphical representation of the matrix $\mathbf{O}^{[m]}$ formed by contraction with O . (c) The contraction of indices required for the computation of $\langle O_m O_{m+\ell} \rangle$.

with the observable matrices being defined as

$$\mathbf{O}^{[m]} = \sum_{j_m=1}^d \sum_{i_m=1}^d \langle j_m | O_m | i_m \rangle \mathbf{E}^{[m]j_mi_m},$$

and noting that whenever $O_m = \mathbb{1}_m$ then $\mathbf{O}^{[m]} = \mathbf{I}^{[m]}$. To compute expectation values between two different states $\langle \psi | \cdots | \phi \rangle$ the same procedure is followed with only one difference. Given that the second state $|\phi\rangle$ is described by matrices $\mathbf{B}^{[m]}$ we now form matrices $\tilde{\mathbf{E}}^{[m]j_mi_m} = \mathbf{A}^{[m]j_m} \otimes \mathbf{B}^{[m]i_m}$ and then generate $\tilde{\mathbf{I}}^{[m]}$ and $\tilde{\mathbf{O}}^{[m]}$ out of these matrices correspondingly. It then follows that $\langle \psi | \phi \rangle = \text{tr}(\prod_{m=1}^M \tilde{\mathbf{I}}^{[m]})$.

From the above formalism it is apparent that these calculations can be performed efficiently for an MPS. In typical calculations, such as those for reduced density matrices or two-point correlation functions, the majority of the matrices involved are $\mathbf{I}^{[m]}$. Ignoring the small number of $\mathbf{E}^{[m]j_mi_m}$ or $\mathbf{O}^{[m]}$ matrices that are present it then requires time and storage which scales as $O(d\chi^4 M)$ to construct the matrices within the product. The calculations above then consist of additionally performing M multiplications of these matrices requiring $O(\chi^6 M)$ operations. Since χ is fixed (independent of M)

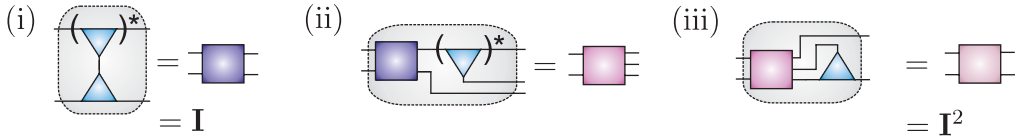


Figure 2.5. The sequence of contractions (i)-(iii) which implements the matrix multiplication $\mathbf{I} \times \mathbf{I}$. By exploiting the internal structure shown it can be done more efficiently than naively multiplying the full matrices.

within an MPS this ensures that these calculations have only polynomial scalings and therefore remain efficient with increasing M . In fact the naive approach outlined can be improved to give $O(d\chi^5 M)$ and $O(d\chi^3 M)$ performance for PBC and OBC respectively. This is achieved by exploiting the internal structure of the \mathbf{I} matrices, shown in Fig. 2.5, which allows the indices of the \mathbf{A} matrices to be contracted separately [39]. Additionally, we note that there are considerable benefits in having a canonical MPS with OBC. For example, in the computation of $\langle O_m O_{m+\ell} \rangle$ with OBC, analogous to Fig. 2.4(c), the total number of tensor contractions is of order ℓ since the Schmidt structure automatically provides terminating vectors representing the contribution of sites exterior to the region $m \leq j \leq m + \ell$.

2.3.3 Properties of correlation functions

As our discussion of the Ising chain illustrated earlier two point correlation functions of the form $C_\ell = \langle O_m O_{m+\ell} \rangle - \langle O_m \rangle \langle O_{m+\ell} \rangle$ are of particular interest. For simplicity we now consider an MPS with PBC and full translational invariance so all matrices \mathbf{A}^j and corresponding tensor product matrices \mathbf{E}^{ji} and \mathbf{I} , are site independent and square. In this case an MPS can only ever accommodate an exact description of all translationally invariant states in the limit $\chi \rightarrow \infty$. A general two-point correlation function for an MPS of a system with M sites can then be calculated as

$$\langle O_m O_{m+\ell} \rangle = \frac{\text{tr}(\mathbf{O} \mathbf{I}^{\ell-1} \mathbf{O} \mathbf{I}^{M-\ell-1})}{\text{tr}(\mathbf{I}^M)}.$$

The behaviour of two-point correlation functions obtained from an MPS are determined by the spectrum ν_γ of the transfer matrix \mathbf{I} . To help determine the properties of \mathbf{I} we shall apply canonical constraints onto the matrices \mathbf{A}^j . In the case of PBC and translational invariance the canonical constraints introduced in section 2.2.3 are related to the completely positive map $\mathcal{E}(x) = \sum_{j=1}^d \mathbf{A}^j x (\mathbf{A}^j)^\dagger$, and its dual $\mathcal{E}^*(x) = \sum_{j=1}^d (\mathbf{A}^j)^\dagger x \mathbf{A}^j$ which act on the space of $(\chi \times \chi)$ matrices. Indeed, the mapping $\mathcal{E}(x)$ represents right-multiplying the matrix \mathbf{I} by a vector x , while the dual $\mathcal{E}^*(x)$ is the corresponding left-multiplication. Without loss of generality we can take the spectral radius of \mathbf{I} as unity²⁰. Thus, for the matrices \mathbf{A}^j to form a righthanded canonical

²⁰This can always be enforced by rescaling all the \mathbf{A}^j matrices.

MPS these maps must possess the fixed points $\mathcal{E}(\mathbb{1}) = \mathbb{1}$ and $\mathcal{E}^*(\Lambda) = \Lambda$, which imply that $\mathbb{1}$ and Λ are the right and left eigenvectors of \mathbf{I} , respectively, with unit eigenvalue $\nu_1 = 1$ [29, 30]. We shall further assume that the eigenvalue $\nu_1 = 1$ is non-degenerate²¹, and that $|\nu_\gamma| < 1$ for any $\gamma > 1$ so no other eigenvalues of \mathbf{I} have unit modulus. Without the latter assumption $\text{tr}(\mathbf{I}^M)$ could be an oscillatory function of M leaving its value in the limit $M \rightarrow \infty$ undefined. Thus with these constraints the MPS is normalised in the thermodynamic limit as $\langle \psi | \psi \rangle = \lim_{M \rightarrow \infty} \text{tr}(\mathbf{I}^M) = 1$ [29, 30].

Although \mathbf{I} is a $(\chi^2 \times \chi^2)$ square matrix it is not necessarily diagonalisable. Here we shall assume it is diagonalisable²² as $\mathbf{I} = \sum_\gamma \nu_\gamma |r_\gamma\rangle \langle l_\gamma|$, where $|l_\gamma\rangle$ and $|r_\gamma\rangle$ are the corresponding left and right eigenvectors obeying the normalisation and phase convention $\langle l_\gamma | r_{\gamma'} \rangle = \delta_{\gamma,\gamma'}$. Under these assumptions the evaluation of a two-point correlation function attains the analytic form [31, 38]

$$C_\ell = \sum_{\gamma>1}^{\chi^2} \kappa_\gamma \left(\frac{\nu_\gamma}{|\nu_\gamma|} \right)^\ell \exp \left(-\frac{\ell}{\xi_\gamma} \right) + \mathcal{C}^2, \quad (2.9)$$

where the coefficients are $\kappa_\gamma = \langle l_1 | O | r_\gamma \rangle \langle l_\gamma | O | r_1 \rangle / \nu_\gamma$, and the constant is $\mathcal{C} = \langle l_1 | O | r_1 \rangle$. This demonstrates that C_ℓ is the sum of exponential decays with a sequence of decreasing correlation lengths $\xi_\gamma = 1/\ln |\nu_\gamma|$. For large distances $\ell \gg 1$ this will reduce to a single characteristic exponential decay with correlation length ξ_γ defined by the largest eigenvalue ν_γ with $\kappa_\gamma \neq 0$. In fact the expression Eq. (2.9) also applies in the more general and delicate case where \mathbf{I} is not diagonalisable and possesses other eigenvalues with unit modulus. In the situation where a second eigenvalue $|\nu_\gamma| \rightarrow 1$, a divergence in its corresponding correlation length ξ_γ occurs resulting in long-ranged two-point correlations. This has been likened to a type of quantum phase transition [40], but differs from the conventional type encountered in systems such as the Ising model since it is not possible for the matrix $\mathbf{I}^{\ell-1}$ to give rise to a power-law decay. Instead this demonstrates that correlations computed from an MPS, for a translationally invariant system or otherwise, are only either asymptotically constant/oscillatory (i.e. long-ranged) or exponentially decaying [30, 29]. This behaviour persists until $\chi \rightarrow \infty$ at which point any form of decay can be modelled. While this may appear to severely limit the usefulness of an MPS, from a practical viewpoint by choosing a sufficiently large χ for a finite-sized system an MPS can accurately reproduce power-law like decay of two-point correlations via a superposition of exponential decays for distances which are a substantial fraction of the system size M [29, 30, 31].

2.3.4 Application of two-site gates

Having established the properties of MPS and methods for computing a variety of useful quantities from them we now move on to the essential work-horse method of the TEBD algorithm, namely how to update them after applying two-site gates [1, 41]. For

²¹This is not always the case. For the GHZ state introduced in section 2.2.2 ν_1 is doubly degenerate.

²²We distinguish between left and right eigenvectors since \mathbf{I} is generally not a hermitian matrix.

reasons which will become clear in the next section we are interested in how to apply a two-site gate on two *adjacent* sites k and $k+1$. To begin we need only consider an MPS with the initial form

$$|\psi\rangle = \sum_{\mathbf{j}_{[1,M]}} \langle \Phi_0 | \left(\prod_{m=1}^{k-1} \mathbf{A}_{\leftarrow}^{[m]j_m} \right) \Xi^{j_k j_{k+1}} \left(\prod_{m'=k+2}^M \mathbf{A}_{\rightarrow}^{[m']j_{m'}} \right) |\Phi_M\rangle |\mathbf{j}_{[1,M]}\rangle,$$

where the \mathbf{A} matrices are orthonormalised, as indicated, but need not be canonical. The central set of matrices $\Xi^{j_k j_{k+1}}$ spanning the two sites is defined in one of three ways

$$\Xi^{j_k j_{k+1}} = \begin{cases} \sqrt{\Lambda^{[k-1]}} \mathbf{A}_{\rightarrow}^{[k]j_k} \mathbf{A}_{\rightarrow}^{[k+1]j_{k+1}} & (a) \text{ Left} \\ \mathbf{A}_{\leftarrow}^{[k]j_k} \sqrt{\Lambda^{[k]}} \mathbf{A}_{\rightarrow}^{[k+1]j_{k+1}} & (b) \text{ Centre} \\ \mathbf{A}_{\leftarrow}^{[k]j_k} \mathbf{A}_{\leftarrow}^{[k+1]j_{k+1}} \sqrt{\Lambda^{[k+1]}} & (c) \text{ Right} \end{cases} \quad (2.10)$$

depending on where the twist in the handedness is located. Since the remaining matrix products give orthonormalised left and right Schmidt states the state can be expressed in the basis

$$|\psi\rangle = \sum_{\mathbf{j}_{[k,k+1]}} \sum_{\alpha_{k-1}=1}^{\chi_{k-1}} \sum_{\alpha_{k+1}=1}^{\chi_{k+1}} \langle \alpha_{k-1} | \Xi^{j_k j_{k+1}} | \alpha_{k+1} \rangle | L_{\alpha_{k-1}}^{[k-1]} \rangle | j_k \rangle | j_{k+1} \rangle | R_{\alpha_{k+1}}^{[k+1]} \rangle.$$

The utility of this two-site-two-block form is that the physical basis of sites k and $k+1$ appear explicitly and we may now apply *exactly* an arbitrary transformation

$$\mathcal{G} = \sum_{\mathbf{j}_{[k,k+1]}} \sum_{\mathbf{i}_{[k,k+1]}} G_{i_k i_{k+1}}^{j_k j_{k+1}} | j_k \rangle | j_{k+1} \rangle \langle i_k | \langle i_{k+1} |,$$

on these two sites directly. This transformation mixes up the set of $\Xi^{j_k j_{k+1}}$ matrices as

$$\Theta^{j_k j_{k+1}} = \sum_{\mathbf{i}_{[k,k+1]}} G_{i_k i_{k+1}}^{j_k j_{k+1}} \Xi^{i_k i_{k+1}}, \quad (2.11)$$

giving the new state $|\psi'\rangle = \mathcal{G} |\psi\rangle$ in the same basis as

$$|\psi'\rangle = \sum_{\mathbf{j}_{[k,k+1]}} \sum_{\alpha_{k-1}=1}^{\chi_{k-1}} \sum_{\alpha_{k+1}=1}^{\chi_{k+1}} \langle \alpha_{k-1} | \Theta^{j_k j_{k+1}} | \alpha_{k+1} \rangle | L_{\alpha_{k-1}}^{[k-1]} \rangle | j_k \rangle | j_{k+1} \rangle | R_{\alpha_{k+1}}^{[k+1]} \rangle,$$

which is shown in Fig. 2.6(a). In a similar way to $\Xi^{j_k j_{k+1}}$ the new quantity $\Theta^{j_k j_{k+1}}$ is a set of d^2 ($\chi_{k-1} \times \chi_{k+1}$) matrices indexed by the two physical indices j_k and j_{k+1} . However, unlike $\Xi^{j_k j_{k+1}}$ this matrix does not, in general, manifestly factorise into any of the forms given in Eq. (2.10) and therefore represents a set of anomalous two-site matrices in our MPS, as depicted in Fig. 2.6(b). To bring the decomposition back into a standard MPS form we need to factorise $\Theta^{j_k j_{k+1}}$ [1, 41]. Crucially this can be

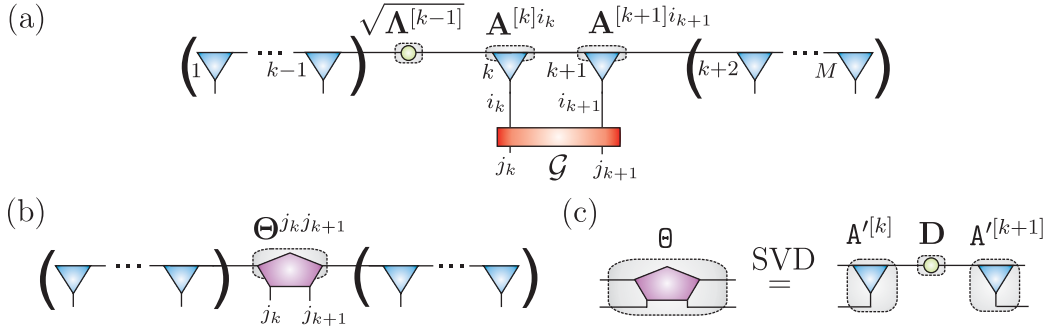


Figure 2.6. (a) A gate \mathcal{G} is applied to sites k and $k + 1$ of an MPS with the initial form $\sqrt{\Lambda^{[k-1]}} \mathbf{A}^{[k]} \mathbf{A}^{[k+1]}$ given in Eq. (2.10)(a). (b) This results in an anomalous set of matrices $\Theta^{j_k j_{k+1}}$ appearing in the product. (c) The state can be brought back into a standard MPS form by performing a SVD on the matrix Θ . In all cases the shaded parts indicates how the respective matrices are built up.

done by manipulating $\Theta^{j_k j_{k+1}}$ alone and is achieved by firstly reshaping it as a single $(d\chi_{k-1} \times d\chi_{k+1})$ complex matrix denoted as Θ and then once again employ the SVD operation [3, 41]. The result of the SVD, shown in Fig. 2.6(c), is then $\Theta = \mathbf{A}'^{[k]} \mathbf{D} \mathbf{A}'^{[k+1]}$ where $\mathbf{A}'^{[k]}$ is a $(d\chi_{k-1} \times \chi'_k)$ matrix, \mathbf{D} is a $(\chi'_k \times \chi'_k)$ real non-negative diagonal matrix, and $\mathbf{A}'^{[k+1]}$ is a $(\chi'_k \times d\chi_{k+1})$ matrix. Due to the respective column- and row-orthogonality of the matrices $\mathbf{A}'^{[k]}$ and $\mathbf{A}'^{[k+1]}$ it is possible (much like in section 2.2.3) to reform them as new sets of d matrices $\mathbf{A}'^{[k]j_k}$ and $\mathbf{A}'^{[k+1]j_{k+1}}$ which are correspondingly left- and right-hand orthonormalised. We have therefore performed the factorisation $\Theta^{j_k j_{k+1}} = \mathbf{A}'^{[k]j_k} \mathbf{D} \mathbf{A}'^{[k+1]j_{k+1}}$ and subsequently returned the description of the state back into a standard MPS. The computational cost of applying the gate \mathcal{G} in Eq. (2.11) scales as $O(d^4)$ while the SVD operation scales as $O(d^3\chi^3)$. Notice that regardless of the initial form for the $\Xi^{j_k j_{k+1}}$ matrix the SVD always factorises $\Theta^{j_k j_{k+1}}$ into the form similar to Eq. (2.10)(b). This implies that for the left Eq. (2.10)(a) and right Eq. (2.10)(c) initial forms the twist in the handedness of the \mathbf{A} matrices has been shifted one site to the right and left, respectively.

If the two-site gate \mathcal{G} is a unitary U then the above update procedure has some additional useful properties. Depending on the initial form of $\Xi^{j_k j_{k+1}}$ one of the new \mathbf{A}' matrices will be automatically canonical, in addition to being orthonormalised, even if the initial \mathbf{A} matrix wasn't. More precisely, for an initial form Eq. (2.10)(a) the matrices $\mathbf{A}'^{[k]j_k}$ are automatically canonical, whereas for Eq. (2.10)(c) the matrices $\mathbf{A}'^{[k+1]j_{k+1}}$ are. Regardless of the initial form of $\Xi^{j_k j_{k+1}}$ if both initial \mathbf{A} matrices are canonical then the unitarity of \mathcal{G} guarantees that both new matrices \mathbf{A}' will also be canonical. The preservation of the norm also means that $\text{tr}(\mathbf{D}^2) = 1$ and so allows us to immediately identify the diagonal matrix \mathbf{D} with the new Schmidt coefficients $\sqrt{\Lambda'^{[k]}}$ of the bipartition of the system after site k . Since the unitary U crosses this boundary the corresponding Schmidt rank $\chi'_k \leq \min(d\chi_{k-1}, d\chi_{k+1})$ may have changed, and will typically increase. For an MPS this potential increase in $\chi'_k \mapsto \chi_k$ may cause it to

exceed the fixed maximum χ . This circumstance is dealt with by retaining only the Schmidt states for the χ largest Schmidt coefficients giving a truncated MPS denoted as $|\psi'_{\text{tr}}\rangle$ whose norm will be less than unity²³. As shown earlier this truncation results in an overlap error for this gate operation give by

$$\epsilon = 1 - |\langle \psi' | \psi'_{\text{tr}} \rangle| = \sum_{\alpha_k=\chi+1}^{\chi_k} (\lambda_{\alpha_k}^{[k]})^2.$$

With respect to this error it follows from the definition of the Schmidt decomposition that $|\psi'_{\text{tr}}\rangle$ is the optimal²⁴ state with a Schmidt rank of χ approximating $|\psi'\rangle$. Thus, after performing this truncation we end up with a canonical MPS, which is the optimal projection of $|\psi'\rangle$ on to the set of states \mathcal{S}_χ [1, 4].

If the two-site gate \mathcal{G} is not unitary then we can only count on the orthonormality of the resulting matrices \mathbf{A}' and they will not in general be canonical. Moreover, because action of \mathcal{G} itself may not preserve the norm of the state we cannot immediately identify the diagonal matrix \mathbf{D} as Schmidt coefficients. In this case we may wish to renormalise the state by forcing $\text{tr}(\mathbf{D}^2) = 1$, after truncation to dimension χ if necessary, making $|\psi'_{\text{tr}}\rangle$ a properly normalised MPS. We shall see shortly that temporarily losing the canonical property of the \mathbf{A} matrices does not in fact present any major problems.

2.3.5 Quantum number conservation

Typically the system we consider will possess symmetries that lead to conservation of certain quantities. Recent work [42, 43] has shown that it is possible to take account of non-Abelian symmetries, such as those arising from $SU(2)$, within the matrix product representation. Here we shall only consider the simplest Abelian symmetries [4], such as $U(1)$, which result in the conservation of quantities like the total magnetisation or particle number. Abelian symmetries can be incorporated into the algorithm in a relatively straightforward way by attaching quantum numbers to all the indices, i.e. α_m, j_m, \dots , appearing within the matrix product representation.

Suppose we have some quantity Q associated to the operator $\hat{Q} = \sum_j \hat{Q}_j$ which is a sum of operators \hat{Q}_j for each site j . Initially we consider the state of the system as being an eigenstate $\hat{Q}|\psi\rangle = Q|\psi\rangle$ and therefore having a definite value for Q . The Schmidt decomposition of this state $|\psi\rangle = \sum_\alpha \lambda_\alpha |\mathbf{L}_\alpha\rangle |\mathbf{R}_\alpha\rangle$, for any bipartition, can then be chosen so that each pair of left and right Schmidt states are eigenstates of the sum of \hat{Q}_j 's in their respective subsystems as $\hat{Q}_\alpha^L |\mathbf{L}_\alpha\rangle = Q_\alpha^L |\mathbf{L}_\alpha\rangle$ and $\hat{Q}_\alpha^R |\mathbf{R}_\alpha\rangle = Q_\alpha^R |\mathbf{R}_\alpha\rangle$, such that $Q_\alpha^L + Q_\alpha^R = Q$. We have already seen that a canonical MPS is equivalent to all $M-1$ contiguous Schmidt decompositions, i.e. with partitions $\{1, \dots, k\} \{k+1, \dots, M\}$, so we can assign the quantum number $Q_{\alpha_k}^k$ from, say, the left subsystem to the Schmidt index α_k appearing in the MPS. We will now show that for an initial state possessing

²³Renormalising the state is somewhat against the spirit of the approximation since if it is ever *really* required then this is a signal that we have truncated too much.

²⁴The SVD is the optimal solution to the unconstrained linear optimisation of the overlap $\langle \psi' | \psi'_{\text{tr}} \rangle$.

such quantum numbers²⁵ the application of a \mathbf{Q} -conserving gate \mathcal{G} , unitary or otherwise, can be applied in such a way that \mathbf{Q} is manifestly conserved and the MPS retains quantum number labels for all its indices.

When updating an MPS after applying a two-site gate we describe the system at all times in the basis $|L_{\alpha_{k-1}}^{[k-1]}| i_k \rangle | i_{k+1} \rangle | R_{\alpha_{k+1}}^{[k+1]} \rangle$. The physical states $| i_k \rangle$ of each site k are chosen to be the eigenstates of \hat{Q}_k so that each basis state has a well-defined quantum number associated to it. This means that the only permissible states are those where the total quantum numbers satisfy $Q_{\alpha_{k-1}}^{k-1} + Q_{j_k} + Q_{j_{k+1}} + Q_{\alpha_{k+1}}^{k+1} = Q$, and we construct a list ℓ storing all these compatible indices $(\alpha_{k-1}, i_k, i_{k+1}, \alpha_{k+1})$ along with their corresponding quantum numbers. The only elements of $\Xi^{i_k i_{k+1}}$ which can be non-zero are stored within this list ℓ . Now if the gate \mathcal{G} applied in Eq. (2.11) is \mathbf{Q} -conserving it will only have non-zero matrix elements where $Q_{j_k} + Q_{j_{k+1}} = Q_{i_k} + Q_{i_{k+1}}$. Its action is therefore to mix up states within the list ℓ , and so the non-zero matrix elements of $\Theta^{j_k j_{k+1}}$ are also stored in this list. For this reason the computation of $\Theta^{j_k j_{k+1}}$ can already be optimised by replacing explicit sums over the physical and Schmidt indices with a single sum over the list ℓ instead.

The next step of the gate operation is to perform a SVD on the matrix Θ , and it is at this point where quantum numbers provide a significant speed-up. The list ℓ will generally include many pairs (α_{k-1}, i_k) with $Q_{\alpha_{k-1}}^{k-1} + Q_{j_k} = Q^L$ and similarly many pairs $Q_{j_{k+1}} + Q_{\alpha_{k+1}}^{k+1} = Q^R$ where $Q^L + Q^R = Q$. By reordering the elements of Θ according to these sets it will acquire a block diagonal form, with each block being labelled by the quantum number Q^L . Thus, instead of performing the SVD on Θ as a whole, we perform it on each block separately, and since these are typically much smaller in dimension than Θ this represents an enormous saving in computational time. The unitary matrices resulting from the SVD then contain the left and right singular vectors, which are used to form the new \mathbf{A} matrices, and these inherit the quantum number Q^L of their corresponding block. This means that quantum number labels for the state of the system are maintained and we can repeat this procedure of constructing block diagonal Θ matrices for any subsequent two-site gates. Importantly, by only applying the SVD on blocks we manifestly preserve the quantity \mathbf{Q} . In contrast, when the SVD is applied to the matrix Θ as a whole even if it possesses a block diagonal form initially numerical noise will soon mix up these blocks after only a few gates and inevitably break the underlying symmetry²⁶. In practise we have found that quantum number conservation has allowed a convenient working value of χ to increase from $\chi \sim 10$ to $\chi > 100$. In fact we found that much of our later work, some of which is included in this thesis, would not have been possible without using this optimisation.

²⁵Note that it is easy to construct a product state which fulfills this property by hand.

²⁶This is precisely the situation encountered in our earlier work [44] (see chapter 5) when we had not yet implemented quantum number conservation.

2.4 Time Evolving Block Decimation

2.4.1 Time evolution via a Suzuki-Trotter expansion

As stated at the beginning of this chapter we only consider Hamiltonians with short-range interactions. The most general form of Hamiltonian we shall consider is

$$\hat{H}(t) = \sum_{j=1}^M \sum_{\nu=1}^{k_1} c_j^\nu(t) \hat{h}_j^\nu + \sum_{j=1}^{M-1} \sum_{\nu=1}^{k_2} c_j^\nu(t) \hat{h}_{j,j+1}^\nu,$$

which is composed of a set of k_1 single-site terms \hat{h}_j^ν each with associated space- and time-dependent couplings $c_j^\nu(t)$, along with a set of k_2 two-site terms $\hat{h}_{j,j+1}^\nu$ and corresponding couplings $c_j^\nu(t)$. Crucially the two-site terms are restricted to acting between nearest-neighbouring sites only and we therefore have an explicit 1D geometry. The Hamiltonian $\hat{H}(t)$, and in turn all the couplings within it, are made dimensionless by dividing by some appropriate energy scale E as $\hat{H}(t) \mapsto \hat{H}(t)/E$. Additionally, this energy defines a time scale $\bar{t} = 1/E$ from which time is also be made dimensionless via $t \mapsto t/\bar{t}$. For OBC it is convenient both for notation and for calculations to reformulate $\hat{H}(t)$ in terms of time-dependent two-site operators as

$$\hat{H}_{j,j+1}(t) = \frac{1}{2} \sum_{\nu=1}^{k_1} c_j^\nu(t) \hat{h}_j^\nu + \sum_{\nu=1}^{k_2} c_j^\nu(t) \hat{h}_{j,j+1}^\nu + \frac{1}{2} \sum_{\nu=1}^{k_1} c_{j+1}^\nu(t) \hat{h}_{j+1}^\nu \quad \text{for } 1 < j < M-1,$$

which are defined symmetrically about site j , aside from at the boundaries where

$$\begin{aligned} \hat{H}_{1,2}(t) &= \sum_{\nu=1}^{k_1} c_1^\nu(t) \hat{h}_1^\nu + \sum_{\nu=1}^{k_2} c_1^\nu(t) \hat{h}_{1,2}^\nu + \frac{1}{2} \sum_{\nu=1}^{k_1} c_2^\nu(t) \hat{h}_2^\nu, \\ \hat{H}_{M-1,M}(t) &= \frac{1}{2} \sum_{\nu=1}^{k_1} c_{M-1}^\nu(t) \hat{h}_{M-1}^\nu + \sum_{\nu=1}^{k_2} c_{M-1}^\nu(t) \hat{h}_{M-1,M}^\nu + \sum_{\nu=1}^{k_1} c_M^\nu(t) \hat{h}_M^\nu, \end{aligned}$$

giving in total $\hat{H}(t) = \sum_{j=1}^{M-1} \hat{H}_{j,j+1}(t)$. The dynamical evolution of a system governed by $\hat{H}(t)$ and in an initial state $|\psi\rangle$ is determined by integrating the dimensionless time-dependent Schrödinger equation $i\partial_t |\psi(t)\rangle = \hat{H}(t) |\psi\rangle$. For the case of a time-independent Hamiltonian \hat{H} this equation admits a formal solution $|\psi(t)\rangle = \exp(-i\hat{H}t) |\psi\rangle$. Numerical calculations typically proceed by discretising the total time T into $T/\delta t$ steps where $\delta t < 1$ as $t_n = (n-1)\delta t$ with $n = \{1, \dots, T/\delta t\}$. So long as δt is sufficiently smaller than the characteristic time scale of the fastest varying coupling, the Hamiltonian $\hat{H}(t_n)$ can be well approximated as being piece-wise constant over these time-steps. This allows the time-evolution operator $\hat{U}(t)$ connecting $|\psi\rangle$ to the state $|\psi(t)\rangle$ at a later time t to be expressed as a time-ordered product of time-independent solutions $\hat{U}(t) = \mathcal{T}(\prod_{n=1}^T \hat{U}_n)$ with $\hat{U}_n = \exp[-i\hat{H}(t_n)\delta t]$. While this has broken up the time integration into simpler steps we are still left with computing a

unitary operator \hat{U}_n which acts over the full state space \mathcal{H} of the system and therefore this effort scales exponentially with M . Focussing on one time-step the computation of \hat{U}_n is further aided by 1D nearest neighbour form of the Hamiltonian $H(t)$. Specifically this enables $\hat{H}(t_n)$ to be summed up into two operators $\hat{H}(t_n) = \hat{F} + \hat{G}$ where

$$\hat{F} = \sum_{\text{odd } j} \hat{H}_{j,j+1}(t_n), \quad \text{and} \quad \hat{G} = \sum_{\text{even } j} \hat{H}_{j,j+1}(t_n),$$

leaving $\hat{U}_n = \exp[-i(\hat{F} + \hat{G})\delta t]$. Since no two terms within either \hat{F} or \hat{G} involve the same sites they all commute amongst themselves. This enables the exponentiation of either one of these operators alone to be calculated exactly as the product of unitaries which act exclusively on two neighbouring sites

$$e^{-i\hat{F}\delta t} = \prod_{\text{odd } j} e^{-i\hat{H}_{j,j+1}(t_n)\delta t}, \quad \text{and} \quad e^{-i\hat{G}\delta t} = \prod_{\text{even } j} e^{-i\hat{H}_{j,j+1}(t_n)\delta t}.$$

The complications in computing the unitary \hat{U}_n fully arise from the fact that \hat{F} and \hat{G} do not in general commute. To overcome this a Suzuki-Trotter expansion [45] is employed in which \hat{U}_n is approximated by a product of individual exponentiations of \hat{F} and \hat{G} . An important feature of a Suzuki-Trotter expansion is that it is a unitary approximation to the exact evolution operator (in contrast to say a power-series) and therefore preserves the norm of the state. The simplest such expansion follows by assuming \hat{F} and \hat{G} commute and constitutes a first-order expansion of \hat{U}_n in δt as $\hat{U}_n = \exp(-i\hat{F}\delta t) \exp(-i\hat{G}\delta t) + O(\delta t^2)$. If instead we define the symmetric product [45]

$$\mathbf{s}(\hat{F}, \hat{G}, y) = e^{-\frac{1}{2}i\hat{F}y} e^{-i\hat{G}y} e^{-\frac{1}{2}i\hat{F}y}$$

then a second-order expansion follows as $\hat{U}_n = \mathbf{s}(\hat{F}, \hat{G}, \delta t) + O(\delta t^3)$. A fourth-order expansion consists of a product of five second-order type terms as

$$e^{-i(\hat{F}+\hat{G})\delta t} = \prod_{l=1}^5 \mathbf{s}(\hat{F}, \hat{G}, q_l \delta t) + O(\delta t^5),$$

where the parameters q_l are defined as $q_1 = q_2 = q_4 = q_5 \equiv q = (4 - 4^{1/3})^{-1} > 0$ while $q_3 = 1 - 4q < 0$ represents evolution backwards in time [45]. Higher-order expansions are possible but are generally not practical since they are composed of increasingly larger numbers of operators. As will be discussed in section 2.4.4 the Trotter error is not the only source of error and in most cases is actually the least important. For this reason using higher-order expansions can even become counter-productive.

The approach pursued by the TEBD algorithm is to efficiently compute the dynamical behaviour of 1D strongly correlated systems by directly manipulating the matrix product representation. We now have all the ingredients for this algorithm. Specifically, we detailed earlier how to apply an arbitrary two-site gate between two neighbouring sites to an MPS and then systematically recast the resulting state back into an MPS of

a given dimension. In this section we have just shown that the application of a time-evolution operator \hat{U}_n can be well approximated by a Suzuki-Trotter expansion which is composed of a sequence of two-site unitary gates between nearest-neighbouring sites. The TEBD algorithm is then the combination of these two features applied to some initial MPS. In the next two sections we will describe how these features are combined in an efficient and stable way, as well as detailing how to construct initial states of interest.

2.4.2 Suzuki-Trotter sweeps

The Suzuki-Trotter decompositions introduced above require that two-site gates are applied to even sites and then to odd sites as shown in Fig. 2.7(a). In the formulation of the two-site gate update given earlier we assumed the twist in the handedness of the \mathbf{A} matrices was adjacent to the two sites of interest as in Eq. (2.10). If our initial state is canonical, and our gate is a unitary U (so they remain canonical) this limitation *appears* not be important. Specifically, we could take an initial state with some fixed canonical MPS, say entirely lefthanded $\mathbf{A}_{\leftarrow}^{[1]j_1} \mathbf{A}_{\leftarrow}^{[2]j_2} \dots \mathbf{A}_{\leftarrow}^{[M]j_M}$. Given that we also have all the Λ matrices for this state we can apply a unitary U to sites k and $k+1$ by constructing the $\Xi^{j_k j_{k+1}}$ matrix with the right form $\mathbf{A}_{\leftarrow} \mathbf{A}_{\leftarrow} \sqrt{\Lambda}$ even though the twist is not at site $k-1$. While the resulting updated matrix $\mathbf{A}'_{\leftarrow}^{[k]}$ can immediately be placed into the overall decomposition of the state, since it possesses the correct handedness, the updated matrix $\mathbf{A}'_{\rightarrow}^{[k+1]}$ cannot. However, because this matrix is canonical it can be flipped to $\mathbf{A}'_{\leftarrow}^{[k+1]}$ via a right division by $\sqrt{\Lambda^{[k+1]}}$ and a left multiplication by $\sqrt{\Lambda'^{[k]}}$. We then store the new Schmidt coefficients $\sqrt{\Lambda'^{[k]}}$ separately for convenience. In this way two-site unitaries can be applied to any adjacent pair of sites and the entire MPS can always be brought back into some fixed canonical form²⁷.

Despite its pleasing mathematical form the flip operation is numerically unstable²⁸ because it involves dividing by potentially very small numbers $\sqrt{\Lambda^{[k+1]}}$. Indeed if our MPS is to be accurate we expect that the last few Schmidt coefficients should be small. While performing a flip as a “one-off” operation presents no serious issues, concatenating it many times, as is the case for time evolution, will lead to numerical instability. Moreover, increasing the χ of the MPS, which should ordinarily increase the precision of the description, in fact only enhances this instability and is believed to be responsible for the pathological results seen in reference [46]. Another related problem which we mentioned earlier was that when applying non-unitary gates the resulting \mathbf{A} matrices are not canonical. In this case we cannot perform a flip operation and so applying two-site gates when the twist is not adjacent to the sites introduces problems with the handedness that can only be resolved by performing additional expensive SVD’s or diagonalisations.

Both of these problems can be solved by applying gates in a sequential *zip* through the system. For example, in the case of a second-order decomposition acting on a state

²⁷This is in fact how the TEBD algorithm was originally formulated.

²⁸This is not an uncommon situation in numerical linear algebra.

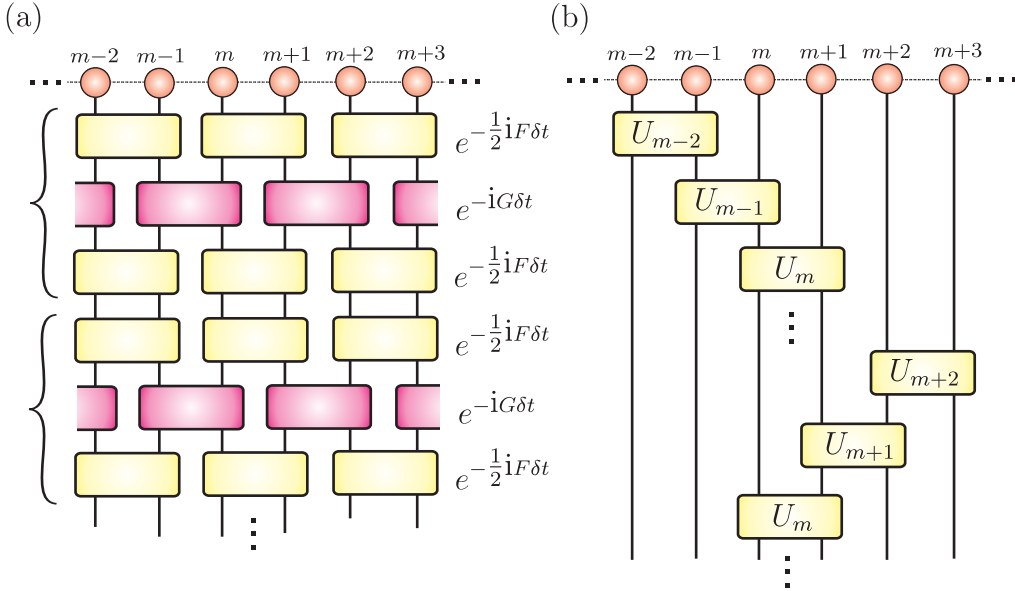


Figure 2.7. (a) The second-order Trotter gate sequence for one time-step δt where gates are first applied between even pairs $\exp(-\frac{1}{2}i\hat{F}\delta t)$, then odd pairs $\exp(-i\hat{G}\delta t)$, and finally even pairs $\exp(-\frac{1}{2}i\hat{F}\delta t)$ again. For practical implementations the two $\exp(-\frac{1}{2}i\hat{F}\delta t)$ sequences for adjacent time steps can be combined into one sequence, except when the computation of observables is required. (b) The second-order sweep where gates $\hat{U}_m = \exp(-\frac{1}{2}i\hat{H}_{m,m+1}\delta t)$ are applied to consecutive pairs from *left* \rightarrow *right* ($m = 1, \dots, M-1$), and then from *right* \rightarrow *left* ($m = M-1, \dots, 1$).

which is entirely lefthanded we apply the gates within $\exp(-\frac{1}{2}i\hat{F}\delta t)$ from left-to-right as

$$e^{-\frac{1}{2}i\hat{F}\delta t} = e^{-\frac{1}{2}i\hat{H}_{1,2}(t_n)\delta t} (\mathbb{1}_{2,3}) e^{-\frac{1}{2}i\hat{H}_{3,4}(t_n)\delta t} (\mathbb{1}_{4,5}) \cdots (\mathbb{1}_{M-2,M-1}) e^{-\frac{1}{2}i\hat{H}_{M-1,M}(t_n)\delta t}$$

where explicit identity operations $\mathbb{1}_{k,k+1}$ have been inserted in between the usual unitaries. The purpose of the identity operations is to shift the twist in handedness one site to the right making the decomposition compatible for the next gate. We then do precisely the same, but in the opposite direction, when applying $\exp(-i\hat{G}\delta t)$, and finally after applying the last zip $\exp(-\frac{1}{2}i\hat{F}\delta t)$ our MPS will be entirely righthanded. We remark here that this kind of zipping is very close to the finite-system sweeps used in DMRG. Similar constructions involving 11 zips can be used for the fourth-order decomposition.

In fact the second-order decomposition can be improved so that all the identity operations are removed and only 2 zips through the system are needed. As a bonus the even number of zips means that the MPS is always lefthanded after a complete time increment has been applied. This is done by using an alternative second-order

Suzuki-Trotter expansion

$$\begin{aligned} e^{-i\hat{H}(t_n)\delta t} &= \mathcal{P}_{M \rightarrow 1} \left(\prod_{j=1}^M e^{-\frac{1}{2}i\hat{H}_{j,j+1}(t_n)\delta t} \right) \times \mathcal{P}_{1 \rightarrow M} \left(\prod_{j=1}^M e^{-\frac{1}{2}i\hat{H}_{j,j+1}(t_n)\delta t} \right) + O(\delta t^3), \\ &= \overbrace{e^{-\frac{1}{2}i\hat{H}_{1,2}(t_n)\delta t} \dots e^{-\frac{1}{2}i\hat{H}_{M-1,M}(t_n)\delta t}}^{\text{Right zip}} \times \overbrace{e^{-\frac{1}{2}i\hat{H}_{M-1,M}(t_n)\delta t} \dots e^{-\frac{1}{2}i\hat{H}_{1,2}(t_n)\delta t}}^{\text{Left zip}} + O(\delta t^3), \end{aligned}$$

where \mathcal{P} denotes a path-ordered product. This 2nd order sweep Trotter sequence is shown explicitly in Fig. 2.7(b). For much of the work in this thesis the second-order sweep was utilised since it provides the simplest and fastest solution to both the problems raised above.

2.4.3 Preparing initial states

Having seen how to apply the time evolution operator to an MPS we now consider how one goes about preparing such an initial state. It is immediately clear that preparing states “by hand” will not be a useful strategy for anything but the most simple states such as product states or GHZ-type states. Typically the initial states of interest are related to the ground state of the system at time $t = 0$. There are three plausible methods of obtaining the ground state $|\Psi_{\text{gs}}\rangle$ of $\hat{H}(0)$.

1. **Adiabatic real time-evolution.** In this case we use the TEBD algorithm itself to construct an initial state. We define a time-varying Hamiltonian $\hat{H}(t)$ which smoothly interpolates between a Hamiltonian $\hat{H}(0)$ which has a product state $|\Psi_0\rangle$ as its ground state and Hamiltonian $\hat{H}(T)$ whose ground state $|\Psi_{\text{gs}}\rangle$ we desire. By performing sufficiently slow real time-evolution with $T \gg 1$, the state of the system $|\psi(t)\rangle$ will remain close to the instantaneous ground state of $\hat{H}(t)$ and will ultimately yield an approximation to $|\Psi_{\text{gs}}\rangle$. The accuracy will depend on whether the system was excited during this evolution.
2. **DMRG construction.** We mentioned earlier that DMRG is essentially an implicit scheme for variationally determining the best MPS approximation to the ground state (or low-lying excitations) of some 1D quantum lattice Hamiltonian [31]. The DMRG output can therefore be formulated as an MPS directly and used as an initial state for TEBD. This method has proven itself over the last decade to be a very efficient means of computing ground states in 1D.
3. **Imaginary time evolution.** The third option is to again use the TEBD algorithm to perform evolution, but in this case in imaginary time via the replacement $\delta t \mapsto -i\delta t$. The Suzuki-Trotter expansions above work regardless of this, only now they involve sequences of non-unitary gates. By using the 2nd-order sweep the non-unitarity of the gates presents no specific issues. Thus, we can apply imaginary time evolution to *decay* some initial product state $|\Psi_0\rangle$, which

is known to have a non-zero overlap with the desired ground state $|\Psi_{\text{gs}}\rangle$, as

$$|\Psi_\tau\rangle = \lim_{\tau \rightarrow \infty} \left(\frac{\exp(-\hat{H}\tau) |\Psi_0\rangle}{\|\exp(-\hat{H}\tau) |\Psi_0\rangle\|} \right), \quad (2.12)$$

This procedure is essentially another method of variationally minimising an MPS ansatz to the ground state of \hat{H} . If the \hat{H} displays a gap $\Delta > 0$ then the overlap $|\langle \Psi_\tau | \Psi_{\text{gs}} \rangle|$ can be shown [3] to grow with imaginary time τ as

$$|\langle \Psi_\tau | \Psi_{\text{gs}} \rangle| > 1 - O\left(\frac{e^{-2\Delta\tau}}{\zeta^2}\right),$$

where $\zeta = |\langle \Psi_0 | \Psi_{\text{gs}} \rangle|$. The use of quantum number conservation becomes especially important in this context since, in contrast to real time-evolution, symmetry breaking numerical noise gets amplified in imaginary time. As indicated by the denominator of Eq. (2.12) the renormalisation steps are essential in preventing the norm of the MPS from becoming vanishingly small and keeps the magnitude of its most significant amplitudes of order unity. Using imaginary time-evolution with a gradually decreasing δt for 10,000+ steps was primary method used in this thesis to obtain ground states. In order to make our final MPS canonical we applied a series of final sweeps through the system with trivial identity gates. While we found that this method generically worked well it is somewhat less efficient than DMRG. This efficiency becomes especially important for calculations involving more complex ladder or two-component BHM systems.

Once we have a ground state we then have the option of applying an additional discrete set of one-site or two-site gates (such as spin-flip operators) to create a variety of other useful (excited) initial states.

2.4.4 Errors in TEBD

In this final section we outline in slightly more detail the two primary sources of error in the TEBD algorithm which have been evident from our earlier discussion.

Trotter error

For any single time-step δt the Trotter error $\epsilon_{\delta t}$ will be of order $\epsilon_{\delta t} \sim (\delta t)^{p+1}$ for a p th-order expansion [2, 45]. To evolve the state to some final time T we need to perform $T/\delta t$ time steps, and denote the state after these steps as $|\psi_{\text{st}}\rangle$. If the exact time-evolved state is $|\psi(T)\rangle$ then the Suzuki-Trotter overlap error is $\epsilon_{\text{st}} = 1 - |\langle \psi(T) | \psi_{\text{st}} \rangle|$. It has been found from numerical evidence [2, 47] that $\epsilon_{\text{st}} \approx MT(\delta t)^p$ and therefore scales linearly with the overall evolution time T and the system size M . This error is controlled entirely by δt and so requires $\delta t \ll 1$.

Truncation error

After applying a two-site gate to sites m and $m + 1$ the resulting exact representation is the corresponding Schmidt decomposition of the state cut between these two sites. In practise the most serious error in TEBD is the truncation of this Schmidt decomposition to include only the χ Schmidt states with the largest Schmidt coefficients [4, 47, 31]. To gain some insight into the effect of truncation let us take a fixed state $|\psi\rangle$ and express its Schmidt decomposition after site m as $|\psi\rangle = |\psi_{\text{tr}}\rangle + |\psi_{\text{tr}}^\perp\rangle$, where $|\psi_{\text{tr}}\rangle = \sum_{\alpha_m=1}^{\chi} \lambda_{\alpha_m}^{[m]} |L_{\alpha_m}^{[m]}\rangle |R_{\alpha_m}^{[m]}\rangle$ and $|\psi_{\text{tr}}^\perp\rangle = \sum_{\alpha_m > \chi} \lambda_{\alpha_m}^{[m]} |L_{\alpha_m}^{[m]}\rangle |R_{\alpha_m}^{[m]}\rangle$ are the (un-normalised) contributions for the first χ Schmidt states and the orthogonal remainder, respectively. The error for this step is then $\epsilon_m = 1 - |\langle\psi|\psi_{\text{tr}}\rangle| = \sum_{\alpha_m > \chi} (\lambda_{\alpha_m}^{[m]})^2$. We now keep $|\psi_{\text{tr}}\rangle$ (without renormalising it) as our approximation to $|\psi\rangle$ and move on to the next site. By similarly Schmidt decomposing $|\psi_{\text{tr}}\rangle$ after site $m + 1$ we obtain $|\psi_{\text{tr}}\rangle = |\psi'_{\text{tr}}\rangle + |\psi'^\perp_{\text{tr}}\rangle$ after again dividing it into the contribution of the first χ Schmidt states and the rest. The new state $|\psi'_{\text{tr}}\rangle$ is then a truncation of $|\psi_{\text{tr}}\rangle$ with error $\epsilon_{m+1} = 1 - |\langle\psi_{\text{tr}}|\psi'_{\text{tr}}\rangle|$. Taking $|\psi'_{\text{tr}}\rangle$ as a further truncated approximation to $|\psi\rangle$ gives a total error $\epsilon = 1 - |\langle\psi|\psi'_{\text{tr}}\rangle| = 1 - |\langle\psi'_{\text{tr}}|\psi'_{\text{tr}}\rangle| = 1 - (1 - \epsilon_{m+1} - \epsilon_m)$. If we continue this process sweeping across all the contiguous Schmidt decompositions of the system from $m = 1$ to $m = M - 1$ targeting the fixed state $|\psi\rangle$ we obtain a truncation error $\epsilon_{\text{tr}} = \sum_{m=1}^{M-1} \epsilon_m$ which is additive in the individual truncation errors. In practise the degradation of the norm of the MPS is a good measure of the truncation error and we might tolerate it becoming $1 - 10^{-6}$.

The accumulation of the truncation error during a simulation results in an inevitable reduction in the precision of the dynamical evolution with TEBD. This was studied in detail in reference [47] where they found that after a certain time, which they called the *runaway time*, the precision drops by several orders of magnitude. The runaway time was empirically found to increase with χ , but decreases with the number of two-site gates applied (since truncation occurs at each of these) and with M . Obtaining an accurate simulation for a desired time therefore requires a careful balancing of δt and the order of the Suzuki-Trotter expansion used so as to minimise the number truncations actually applied [47].

References

- [1] G. Vidal, *Phys. Rev. Lett.* **91**, 147902 (2003).
- [2] G. Vidal, *Phys. Rev. Lett.* **93**, 040502 (2004).
- [3] G. Vidal, *Phys. Rev. Lett.* **98**, 070201 (2007).
- [4] A.J. Daley, C. Kollath, U. Schollwöck, G. Vidal, *J. Stat. Mech.* P04005 (2004).
- [5] J.I. Latorre, E. Rico, G. Vidal, *Quant. Inf. Comput.* **4**, 48 (2004).
- [6] P. Pfeuty, *Ann. Phys. (N.Y.)* **57**, 79 (1970).
- [7] E. Barouch, B.M. McCoy, *Phys. Rev. A* **3**, 786 (1971).

- [8] S. Sachdev, *Quantum Phase Transitions* (Cambridge Univ. Press, Cambridge, 2001).
- [9] M.A. Nielsen, I.L. Chuang, *Quantum Computation and Quantum Information* (Cambridge Univ. Press, Cambridge, 2000).
- [10] M.B. Plenio, S. Virmani, *Quant. Inf. Comput.* **7**, 1 (2007).
- [11] M. Srednicki, *Phys. Rev. Lett.* **71**, 666 (1993).
- [12] M.B. Plenio, J. Eisert, J. Dreissig, M. Cramer, *Phys. Rev. Lett.* **94**, 060503 (2005).
- [13] M. Cramer, J. Eisert, M.B. Plenio, J. Dreissig, *Phys. Rev. A* **73**, 012309 (2006).
- [14] L. Amico, R. Fazio, A. Osterloh, V. Vedral, [arxiv:quant-ph/0703044](http://arxiv.org/abs/quant-ph/0703044).
- [15] J. Cardy, I. Peschel, *Nucl. Phys. B* **300**, 377 (1988).
- [16] T.M. Fiola, J. Preskill, A. Strominger, S.P. Trivedi, *Phys. Rev. D* **50**, 3987 (1994).
- [17] C. Holzhey, F. Larsen, F. Wilczek, *Nucl. Phys. B* **424**, 44 (1994).
- [18] P. Calabrese, J. Cardy, *J. Stat. Mech.* P06002 (2004).
- [19] B.-Q. Jin, V.E. Korepin, *Phys. Rev. A* **69**, 062314 (2004).
- [20] A.R. Its, B.-Q. Jin, V.E. Korepin, *J. Phys. A* **38**, 2975 (2005).
- [21] V. Eisler, Z. Zimboras, *Phys. Rev. A* **71**, 042318 (2005).
- [22] J.P. Keating, F. Mezzadri, *Phys. Rev. Lett.* **94**, 050501 (2005).
- [23] I. Peschel, *J. Stat. Mech.* P12005 (2004).
- [24] V. Popkov, M. Salerno, *Phys. Rev. A* **71**, 012301 (2005).
- [25] R. Weston, *J. Stat. Mech.* L03002 (2006).
- [26] G. De Chiara, S. Montangero, P. Calabrese, R. Fazio, *J. Stat. Mech.* P03001 (2005).
- [27] V.E. Korepin, *Phys. Rev. Lett.* **92**, 096402 (2004).
- [28] N. Laflorencie, *Phys. Rev. B* **72**, 140408(R) (2005).
- [29] M. Fannes, B. Nachtergaele, R.F. Werner, *Comm. Math. Phys.* **144**, 3 (1992).
- [30] D. Perez-Garcia, F. Verstraete, M.M. Wolf, J.I. Cirac, *Quant. Inf. Comput.* **7**, 401 (2007).
- [31] U. Schollwöck, *Rev. Mod. Phys.* **77**, 259 (2005).
- [32] F. Verstraete, J. I. Cirac, *Phys. Rev. B* **73**, 094423 (2006).
- [33] F. Verstraete, J. I. Cirac, [arxiv:cond-mat/0407066](http://arxiv.org/abs/cond-mat/0407066).
- [34] F. Verstraete, D. Porras, J. I. Cirac, *Phys. Rev. Lett.* **93**, 227205 (2004).
- [35] S.R. White, *Phys. Rev. Lett.* **69**, 2863 (1992).
- [36] S.R. White, *Phys. Rev. B* **48**, 10345 (1993).
- [37] S. Östlund, S. Rommer, *Phys. Rev. Lett.* **75**, 3537 (1995).

- [38] S. Rommer, S. Östlund, *Phys. Rev. B* **55**, 2164 (1996).
- [39] J.J. Garcia-Ripoll, *New J. Phys.* **8**, 305 (2006).
- [40] M.M. Wolf, G. Ortiz, F. Verstraete, J.I. Cirac, *Phys. Rev. Lett.* **97**, 110403 (2006).
- [41] Y.-Y. Shi, L.-M. Duan, G. Vidal, *Phys. Rev. A* **74**, 022320 (2006).
- [42] S. Singh, H.-Q. Zhou, G. Vidal, [arXiv:cond-mat/0701427](https://arxiv.org/abs/cond-mat/0701427).
- [43] I.P. McCulloch, *J. Stat. Mech.* P10014 (2007).
- [44] S.R. Clark, D. Jaksch, *Phys. Rev. A* **70**, 043612 (2004).
- [45] M. Suzuki, *Phys. Lett. A* **146**, 6 (1990); *ibid*, *J. Math. Phys.* **32**, 2 (1991).
- [46] A.J. Daley, S.R. Clark, D. Jaksch, P. Zoller, *Phys. Rev. A* **72**, 043618 (2005).
- [47] D. Gobert, C. Kollath, U. Schollwöck, G. Schütz, *Phys. Rev. E* **71**, 036102 (2005).

CHAPTER 3

ULTRA-COLD ATOMS IN OPTICAL LATTICES

In chapter 1 we discussed the remarkable achievements in realising quantum degenerate Bose and Fermi gases. This has been possible, in no small part, due to the versatility of the laser as a tool for manipulating atoms. Indeed, laser cooling [1] has been instrumental in achieving the temperatures required for quantum degeneracy. In this chapter we shall focus on the ability to trap atoms with laser light via the purely conservative dipole force which it exerts [2]. If the lasers are arranged so as to produce a periodic intensity pattern atoms will experience, in certain limits, an optical lattice potential. By using the detailed microscopic understanding¹ of the Hamiltonian available for such systems we shall demonstrate the ultra-cold atoms in this lattice potential provide a near-perfect realisation of the Bose-Hubbard model (BHM) Hamiltonian [3]. Of the many distinguishing features of this setup we shall outline, perhaps the most important is that an optical lattice can be dynamically controlled via external fields on timescales much shorter than the decoherence time. This highly novel feature has permitted experimentalists to explore the coherent dynamical behaviour of a quantum many-body system. Understanding some of the results they find for 1D systems and proposing new ways to exploit this ability forms the central theme of this thesis.

3.1 Atom-light interaction

3.1.1 Two-level atom

Here we outline the basic theory of optical lattices by considering the idealisation of a two-level atom, possessing an internal ground state $|g\rangle$ and an excited state $|e\rangle$ separated by an energy $\hbar\omega_0$, whose motion is restricted to 1D [4]. For convenience we introduce atomic transition operators $\hat{\sigma}_+ = |e\rangle\langle g|$, $\hat{\sigma}_- = |g\rangle\langle e|$ and the inversion operator $\hat{\sigma}_3 = |e\rangle\langle e| - |g\rangle\langle g|$. The free atomic Hamiltonian is therefore

$$\hat{H}_{\text{atom}} = \frac{\hat{p}^2}{2m} + \frac{1}{2}\hbar\omega_0(\mathbb{1} + \hat{\sigma}_3),$$

where \hat{p} is the momentum operator along the x -axis, and m is the atomic mass. We now subject the atom, which is within a lossless 1d² cavity of length L , to a monochro-

¹This understanding allows a number of approximations to be justifiably applied to this system.

²In this chapter we shall use 1d to denote a one-dimensional laser configuration, and 1D to denote a one-dimensional system in order to avoid confusion.

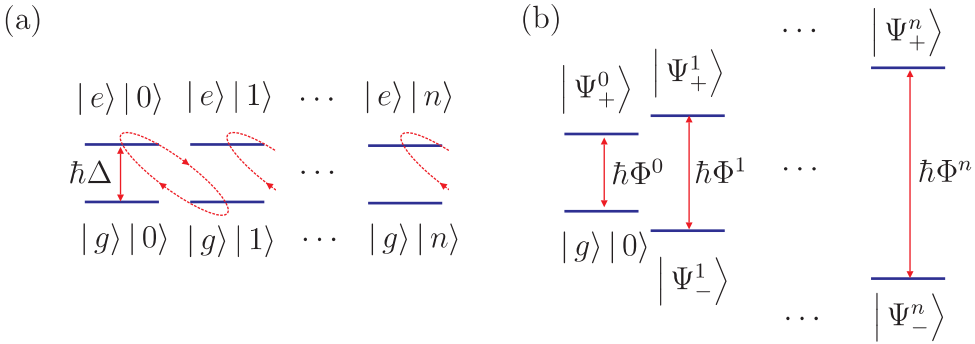


Figure 3.1. (a) When there is no interaction between the atom and light the states of the atom and field form two distinct degenerate manifolds separated by an energy $\hbar\Delta$ in the interaction picture. Since the field is quantised in the Jaynes-Cummings model the atom-light interaction couples pairs of states between these manifolds as denoted by the circles. (b) After solving the Jaynes-Cummings model the interaction modifies these manifolds by forming dressed states $|\Psi_{\pm}^n\rangle$ for each n which are separated by a spatially dependent energy $\hbar\Phi^n = \hbar\Delta + \hbar\sqrt{\Delta + 4|\kappa(x)|^2(n+1)}$. The states within these two manifolds are therefore split by the interaction. In the main text this result is considered in the far-detuned limit where $|\Delta| \gg |\kappa(x)|\sqrt{\langle n \rangle}$, where the splitting of the manifold around the dominant pairs of dressed states is much smaller than the separation between the manifolds. The upper ‘+’ manifold of (rapidly oscillating) states is then adiabatically eliminated.

magnetic electromagnetic field with polarisation \mathbf{e} and frequency ω (giving a wavelength $\lambda = 2\pi c/\omega$, a wavevector $k = 2\pi/\lambda$, and a recoil energy $E_R = \hbar^2 k^2/2m$). This field can be treated classically permitting all the relevant features of an optical lattice and spontaneous emission to be derived. However, here we shall ignore spontaneous emission in this section (it will be discussed in section 3.1.3) and instead consider the electric field as being quantised as [5]

$$\hat{\mathbf{E}}(x) = \mathcal{E}\mathbf{e} [\Theta(x)\hat{a}^\dagger + \Theta^*(x)\hat{a}],$$

where $\mathcal{E} = (\hbar\omega/2\epsilon_0 L)^{1/2}$, and possessing a free Hamiltonian $\hat{H}_{\text{field}} = \hbar\omega(\hat{a}^\dagger\hat{a} + \frac{1}{2})$. Here \hat{a} is the photon annihilation operator for the field mode $\Theta(x)$ whose precise form we shall specify shortly.

One property of the field mode $\Theta(x)$ we will assume is that the length scale of its spatial variation is much larger than the size of the atom. This enables the atom-light interaction to be adequately described by the dipole-approximation [5] as $\hat{H}_{\text{int}} = -\hat{\mathbf{d}} \cdot \hat{\mathbf{E}}(x)$ where $\hat{\mathbf{d}} = \mathbf{d}_{eg}(\hat{\sigma}_+ + \hat{\sigma}_-)$ is the atom dipole operator and \mathbf{d}_{eg} is the dipole

matrix element³ between $|g\rangle$ and $|e\rangle$. In total

$$\hat{H}_{\text{int}} = \hbar(\hat{\sigma}_+ + \hat{\sigma}_-) [\kappa(x) \hat{a}^\dagger + \kappa(x)^* \hat{a}],$$

where $\hbar\kappa(x) = \mathcal{E}\Theta(x) \mathbf{d}_{eg} \cdot \mathbf{e}$ and $\Theta(x)$ is the field mode evaluated at the atom's position x . By applying a time-dependent unitary $\hat{U}_1(t) = e^{i\omega_0\hat{\sigma}_3 t/2} e^{i\omega\hat{a}^\dagger\hat{a}}$ we transform to the interaction picture giving the complete Hamiltonian for the system as

$$\hat{H} = \frac{\hat{p}^2}{2m} + \hbar(\hat{\sigma}_+ e^{i\omega_0 t} + \hat{\sigma}_- e^{-i\omega_0 t}) \times [\kappa(x) \hat{a}^\dagger e^{i\omega t} + \kappa(x)^* \hat{a} e^{-i\omega t}]. \quad (3.1)$$

When the interaction in Eq. (3.1) is multiplied out it includes terms with an $\omega - \omega_0$ and $\omega + \omega_0$ time-dependence. If the detuning $\Delta = \omega - \omega_0$ satisfies $|\Delta| \ll \omega_0$ then the rapidly oscillating terms with a $\omega + \omega_0$ time-dependence can be dropped in what is called the rotating wave approximation [5]. This leaves the Hamiltonian

$$\hat{H}_{\text{jc}} = \frac{\hat{p}^2}{2m} + \hbar[\kappa(x)^* \hat{\sigma}_+ \hat{a} + \kappa(x) \hat{\sigma}_- \hat{a}^\dagger] + \frac{1}{2}\hbar\Delta(\mathbb{1} + \hat{\sigma}_3),$$

after performing one further unitary transformation $U_2(t) = e^{-i\Delta\hat{\sigma}_3 t/2}$. The part of \hat{H}_{jc} describing the internal atomic and photon degrees of freedom is the well-known Jaynes-Cummings model [4, 5]. This gives a physically sensible description of the atom-light interaction where the excitation or relaxation of the atom corresponds to the absorption or emission of a photon, respectively. The Jaynes-Cummings Hamiltonian couples pairs of “bare” states $|g\rangle |n+1\rangle$ to $|e\rangle |n\rangle$, where $|n\rangle$ is an n photon Fock state, and so for a fixed n its dynamics are completely confined to sets of two-dimensional subspaces. This allows it to be solved analytically in terms of so-called “dressed” states [5]. Here, however, we are interested in the far-detuned limit where $|\Delta| \gg |\kappa(x)|\sqrt{\langle n \rangle}$, with $\langle n \rangle$ being the average photon number for the state of the field. The dominant contribution to the dynamics will therefore be from pairs of bare states with (integer) n in the vicinity of $\langle n \rangle$. Being far-detuned allows the interaction terms for such values of n to be treated perturbatively giving the ground state to first-order as

$$|\Psi_-^n\rangle = |g\rangle |n+1\rangle - \frac{\kappa(x)\sqrt{n+1}}{\Delta} |e\rangle |n\rangle,$$

with an energy to second-order as

$$E_-^n = -\frac{\hbar|\kappa(x)|^2(n+1)}{\Delta}.$$

These results show that the population $P_e = |\kappa(x)|^2(n+1)/\Delta^2$ in the excited state $|e\rangle$ will be negligible in the far-detuned limit, and that the ground state population acquires an energy shift (or A.C. Stark shift) which has a spatial dependence governed by the mode function $\Theta(x)$. In light of this we derive an effective Hamiltonian (to

³We assume, without loss of generality, that \mathbf{d}_{eg} is real.

lowest order in $|\kappa(x)|/|\Delta|$ for the ground state manifold by applying the projection method [6]

$$\hat{H}_{\text{eff}} = \lim_{\varepsilon \rightarrow 0} \left[\mathbb{P} \hat{H}_{\text{jc}} \mathbb{P} - \mathbb{P} \hat{H}_{\text{jc}} \mathbb{Q} (\mathbb{Q} \hat{H}_{\text{jc}} \mathbb{Q} + \varepsilon \mathbb{I})^{-1} \mathbb{Q} \hat{H}_{\text{jc}} \mathbb{P} \right], \quad (3.2)$$

where \mathbb{P} is the projector onto the desired manifold of states, while $\mathbb{Q} = \mathbb{I} - \mathbb{P}$ is the projector onto the orthogonal subspace. We choose $\mathbb{P} = |g\rangle\langle g| \otimes \sum_n |n\rangle\langle n|$ so Eq. (3.2) yields an effective Hamiltonian in which the excited state manifold has been adiabatically eliminated

$$\hat{H}_{\text{eff}} = \frac{\hat{p}^2}{2m} - \frac{\hbar|\kappa(x)|^2}{\Delta} |g\rangle\langle g| \otimes \hat{a}^\dagger \hat{a}.$$

This Hamiltonian demonstrates that the electronic ground state of the atom experiences a conservative potential as a result of the coherent scattering of photons (i.e. $\hat{a}^\dagger \hat{a}$) from the field mode. Moreover, due to the projection the Hamiltonian \hat{H}_{eff} does not entangle the internal state of the atom with the field.

We now consider the field mode $\Theta(x)$ as arising from the superposition of two counter-propagating laser beams along the x -axis whose interference creates a standing wave mode $\Theta(x) = \sin(kx)$. Additionally, we describe the standing-wave laser field by a coherent state [5]

$$|\alpha\rangle = e^{-|\alpha|^2/2} \sum_{n=0}^{\infty} \frac{\alpha^n}{\sqrt{n!}} |n\rangle,$$

with an average photon number $\langle n \rangle = |\alpha|^2$ such that $\langle n \rangle \gg 1$ (high intensity). Taking the partial expectation value of \hat{H}_{eff} with respect to a fixed state $|g\rangle|\alpha\rangle$ for the internal and photon degrees of freedom gives an effective Hamiltonian for the motional degrees of freedom of the atom as

$$\begin{aligned} \langle g | \langle \alpha | \hat{H}_{\text{eff}} | g \rangle | \alpha \rangle &= \hat{H}_{\text{OL}}, \\ &= \frac{\hat{p}^2}{2m} - \frac{\hbar|\Omega(x)|^2}{4\Delta}, \end{aligned}$$

where $\Omega(x) = 2(\mathbf{d}_{eg} \cdot \mathbf{e}) \sin(kx) \sqrt{\hbar\omega\langle n \rangle / \epsilon_0 L}$ is the spatially-dependent Rabi frequency. For this Hamiltonian to be valid we require that the typical frequencies associated to the atomic motion are small compared to those characterising the internal and photon degrees of freedom, which culminates in the inequalities

$$\left\langle \frac{\hat{p}^2}{2m} \right\rangle \ll \hbar|\kappa(x)|\sqrt{\langle n \rangle} \ll \hbar|\Delta|.$$

We therefore require very low temperatures. When this is satisfied we find that overall a far-detuned standing wave laser field interacting with a two-level atom creates a conservative periodic potential along the x -axis $V_L(x) = V_0 \sin^2(kx)$ of depth $V_0 =$

$|\Omega(0)|^2/4\Delta$ and with a lattice spacing $a = \frac{1}{2}\lambda$. When $\omega > \omega_0$ ($\Delta > 0$) we have a blue detuned optical lattice where the potential minima coincide with the points of zero light intensity. Conversely when $\omega < \omega_0$ ($\Delta < 0$) we have a red detuned (bright) optical lattice where the potential minima match the points of maximum light intensity.

To achieve the requirements outlined above we specialise to the case where the atoms immersed in the laser field are a Bose-Einstein condensate (BEC) of weakly-interacting alkali atoms [7]. In this way the atoms are initially ultra-cold and the optical lattice potential is adiabatically superimposed on to the BEC thereby loading them into the optical potential. The simple two level model for an atom we have used above is certainly an approximation to real atoms [8]. Instead the actual optical potential felt by the atom will be given by a sum of contributions from all its internal states, however the underlying physics does not change. In practise for alkali atoms, in the far-detuned limit with an optical frequency laser, there will typically be a single dominant contribution, and in this way the two-level model is a good approximation to its influence.

3.1.2 Lattice geometry

So far we have restricted our discussion to 1d, however, periodic potentials in higher dimensions can also be created by superimposing additional laser beams. The simplest cases are a 2d square and 3d cubic lattice potential which are created by using two and three pairs of counter-propagating laser beams along orthogonal axes, respectively. In this case the lattice potential has a separable geometry and is simply a superposition of the 1D potential, which for a 3d cubic lattice is

$$V_{3d}(\mathbf{r}) = V_{0,x} \sin^2(kx) + V_{0,y} \sin^2(ky) + V_{0,z} \sin^2(kz), \quad (3.3)$$

where $V_{0,i}$ is the potential depth along the i -th direction which are independently controllable via the intensities of the corresponding laser pairs. The creation of such a potential requires that the beams from different pairs of lasers are independent and do not interfere with one another. This can be achieved by using orthogonal polarisations, or in the case of 3d, by slightly detuning each pair of lasers differently from a common frequency. Typically a negligible frequency difference, compared with the overall optical frequency, is required to achieve independence and to good approximation the lattice spacing can still be considered identical along all axes.

A major novelty of this setup is that it enables the dimensionality of the desired system to be controlled [9]. For 1d or 2d optical lattices with a very large depth (up to 100 kHz) tunnelling will be prohibited along the laser directions and the motion of the atoms will be restricted to one of an array of isolated planes or tubes, as shown in Fig. 3.2(a)(b). The very low temperatures thus prevent any excitations and freezes the motion along those lattice axes so genuine 1D and 2D systems can be realised. The motion within these regions will then be free aside from additional weak (typically 10-200 Hz) magnetic or optical trapping. With an additional third set of counter-propagating lasers a full 3d optical lattice is created. When the potential is deep in all

three directions then the motion of atoms is restricted to the potential minima of the simple cubic lattice sites, as depicted in Fig. 3.2(c). If we lower the depth along one or two axes then an anisotropic 3d lattice can be created as in Eq. (3.3). In this way atoms can move along tubes, or within planes, but are still subject to a periodic potential creating effective 1D / 2D lattice systems. The 1D lattice configuration formed from an anisotropic 3d cubic lattice is the main implementation considered in this thesis.

By confining atoms within a 3d periodic potential a close resemblance begins to emerge between ultra-cold atoms in optical lattices and conventional solid state crystals. However, optical lattices differ in several respect to solid crystals. Firstly, since the lattice structure is formed from light it is essentially defect free. Secondly, in the classical limit (i.e. a coherent state $|\alpha\rangle$ with $|\alpha| \gg 1$ for the field) the optical lattice does not possess lattice phonons like solid crystals. Although we note that in the quantum limit where the full Hamiltonian \hat{H}_{jc} is used phonon-like effects can occur [4]. Thirdly, the lattice spacing in optical lattices is several orders of magnitude larger than solid state crystals. Finally, the most important distinguishing feature is that the lattice potential can be controlled accurately and easily by changing the laser properties. More precisely, the potential depth can be changed by modifying the laser intensity, the lattice can be moved by changing the polarisation (see chapter 7), and the lattice geometry can be altered by changing the laser configuration [10, 11, 12]. Crucially all of these properties can be altered dynamically, and in some cases on timescales on the order of milliseconds.

For sufficiently deep lattices filled with cold atoms the wave-function of an atom localised at a single site, with a spatial extent much smaller than the lattice periodicity, can be approximated by the ground state of one potential minimum. If we expand the optical lattice potential in 1D about the centre of a minimum it gives a harmonic approximation

$$V_{\text{ho}}(x) = \frac{1}{2}m\omega_{\text{ho}}^2 x^2,$$

where $\omega_{\text{ho}} = 2\sqrt{V_0 E_R}$. The ground state for this effective harmonic potential is then

$$\psi_{\text{ho}}(x) = \sqrt{\frac{1}{\sqrt{\pi}a_{\text{ho}}}} e^{-x^2/2a_{\text{ho}}^2},$$

with the harmonic oscillator size $a_{\text{ho}} = \sqrt{\hbar/m\omega_{\text{ho}}}$. We may use $\psi_{\text{ho}}(x)$ to approximate the ground state of a trapped atom so long as $a_{\text{ho}} \ll a$. This is readily satisfied for the case of an anisotropic 3D lattice where $\psi_{\text{ho}}(x)$ can be taken as the part of the wave-function of an atom frozen in the tightly constrained direction. Generally the harmonic oscillator is very useful for obtaining analytical estimates for on-site properties, as we shall see shortly.

For completeness we note that wider classes of 2D and 3D lattices can be made by using additional lasers and non-orthogonal arrangement with the resulting geometries generally being non-separable [12]. For example, consider three laser beams propagating at angles $2\pi/3$ with respect to each other in the xy -plane and all polarised in the

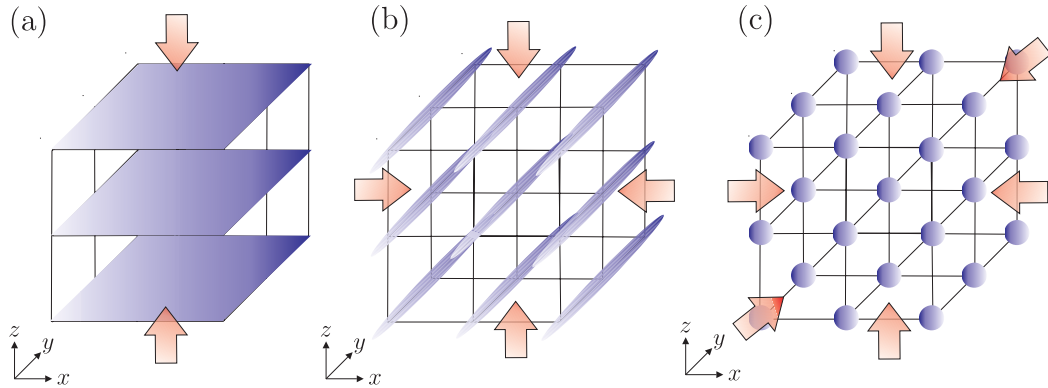


Figure 3.2. (a) A pair of counter-propagating lasers along the z -axis with sufficient intensity create a deep 1d optical lattice. The motion of atoms is then constrained to one of a set of xy planes. (b) With an additional pair of counter-propagating lasers along the x -axis a 2d optical lattice is created where the motion of atoms is constrained to one of a set of tubes along the y -axis. (c) Finally by adding another pair of counter-propagating lasers along the y -axis a full 3d optical lattice is generated which localises the atoms to one of the lattice sites. By lowering the intensities along one or two directions the 3d lattice becomes anisotropic allowing isolated 2D or 1D systems, similar to those shown (a) and (b), to be created, but with a non-zero lattice potential remaining within the weakly confined planes or tubes.

z -direction. The resulting lattice potential is then

$$V_{\text{tri}}(\mathbf{r}) \propto 3 + 4 \cos(3kx/2) \cos(\sqrt{3}ky/2) + 2 \cos(\sqrt{3}ky),$$

which is a triangular lattice in 2D [13]. Using similar methods more exotic geometries, such as Kagomé lattices [14], can be realised. Also, by using lasers with incommensurate wavelengths a pseudo-random super-lattice potential can be generated [15].

3.1.3 Spontaneous emission

In the above calculation we considered only the coherent interaction of an atom with the laser light and so implicitly assumed that the excited state $|e\rangle$ has an infinite lifetime. However, by introducing a light-matter interaction a dissipative contribution will unavoidably arise due to the spontaneous emission of photons from atoms in state $|e\rangle$ with an effective rate Γ_{eff} . Much of the physics in this thesis is based on coherent many-body dynamics of optical lattice systems and spontaneous emission constitutes one of the largest sources of decoherence. We can only ignore its effect if the experimental timescale is much smaller than $1/\Gamma_{\text{eff}}$. An estimate of Γ_{eff} can be made by taking the product of the lifetime $1/\Gamma$ of $|e\rangle$ and the probability of an atom occupying this internal state with its motional state approximated as $\psi_{\text{ho}}(x)$ of a potential minimum.

In the case of blue detuned optical lattices it is found⁴ that $\Gamma_{\text{eff}} \approx \Gamma\omega_{\text{ho}}/4\Delta$, whereas for red detuned lattices it is $\Gamma_{\text{eff}} \approx -\Gamma V_0/\hbar\Delta$ [16, 13]. Since $V_0 \gg \hbar\omega_{\text{ho}}$ spontaneous emission will always be more significant in a red detuned optical lattice than in a blue detuned one.

To give some quantitative estimates we can use the typical parameters in experiments. For example, in a blue detuned optical lattice with $\lambda = 514$ nm for ^{23}Na atoms, operating between the $S_{1/2} \rightarrow P_{3/2}$ transition with $\lambda_{eg} = 589$ nm and $\Gamma = 2\pi \times 10$ MHz, the recoil energy is $E_R \approx 2\pi \times 33$ kHz and gives a detuning $\hbar\Delta \approx 2.3 \times 10^9 E_R$. For a lattice depth of $V_0 = 25E_R$, equivalent to $\hbar\omega_{\text{ho}} = 10E_R$, the effective spontaneous emission rate is $\Gamma_{\text{eff}} = 10^{-2}$ Hz corresponding to a timescale on the order of minutes [16]. For a typical red detuned optical lattice with $\lambda = 852$ nm for ^{87}Rb atoms, operating between the $S_{1/2} \rightarrow P_{1/2}$ transition with $\lambda_{eg} = 795$ nm and $\Gamma = 2\pi \times 6$ MHz, the recoil energy is $E_R \approx 2\pi \times 3.1$ kHz giving a detuning of $\hbar\Delta \approx -8.0 \times 10^9 E_R$. For a lattice depth of $V_0 = 25E_R$, equivalent to $\hbar\omega_{\text{ho}} = 10E_R$, the effective spontaneous emission rate is $\Gamma_{\text{eff}} = 0.2 \times 10^{-2}$ Hz again corresponding to a timescale on the order of minutes [16]. Since experiments with optical lattices are usually carried out in timescales shorter than 1 s in both cases an appropriate choice for Δ can suppress Γ_{eff} sufficiently such that spontaneous emission does not play a significant role. Indeed, this has been resoundingly confirmed in the numerous experiments with ultracold alkali atoms in optical lattices [10, 11, 9, 12].

3.2 Single-particle physics

3.2.1 Bloch states

The purpose of this section is to outline the behaviour of a non-interacting particle subject to a periodic potential familiar to solid state systems. For simplicity we shall again restrict our discussion to 1D since for separable geometries, which we exclusively consider, the findings generalise straightforwardly to higher dimensions. We begin with a Hamiltonian of the form

$$\hat{H}_0 = \frac{\hat{p}^2}{2m} + V_L(x), \quad (3.4)$$

where $V_L(x) = V_L(x + a)$ and represents a periodic potential with lattice spacing a . Since eigenstates $\phi_q(x)$ of \hat{H} are required to also be eigenstates of the lattice translation operator $\hat{T}f(x) = f(x + a)$, a well-known consequence, called Bloch's theorem [17], is that they have the form

$$\phi_q(x) = e^{iqx} u_q(x), \quad \text{with} \quad u_q(x) = u_q(x + a), \quad (3.5)$$

⁴The difference in the formulas for Γ_{eff} is due to the fact that for a red detuned lattice the atom in the motional ground state of a well resides at the intensity maximum, hence the V_0 , whereas for a blue detuned lattice the atom resides in the minimum.

which is a plane-wave with wave-vector q modulated by a function $u_q(x)$ with the same periodicity as the underlying lattice. In much the same way as momentum is the quantum number characterising the continuous translational symmetry of free-space, q is the quantum number (i.e. eigenvalue of \hat{T}) associated to the discrete translational symmetry of the periodic potential. To emphasise this similarity $\hbar q$ is often called the quasi-momentum or crystal momentum. A major difference between them is that the quasi-momentum q can always be confined to a finite range of values called the first Brillouin zone (BZ), which in 1D is $-\pi/a < q \leq \pi/a$.

After inserting the Bloch ansatz into the Schrödinger equation $\hat{H}_0\phi_q(x) = E_q\phi_q(x)$ we obtain an equation for $u_q(x)$ as

$$\hat{H}_q u_q(x) = E_q u_q(x), \quad \text{with} \quad \hat{H}_q = \frac{(\hat{p} + q)^2}{2m} + V_L(x). \quad (3.6)$$

Unlike the free-particle Hamiltonian $\hat{p}^2/2m$, which is diagonal in \hat{p} , we see that \hat{H} is only block-diagonal in q since Eq. (3.6) still possesses an infinite number of discrete⁵ solutions for each q . For this reason another quantum number, which we denote as $n = 0, 1, 2, \dots$, labels the eigenstates, giving $\phi_{q,n}(x)$, and $u_{q,n}(x)$, with corresponding energies $E_{q,n}$. The index n is called the band index and for each n the energy $E_{q,n}$ forms a continuous function of the quasi-momentum in the first BZ called the band structure [17].

The band structure is most easily determined from Eq. (3.6) by introducing the Fourier expansion over reciprocal lattice points $G_k = 2\pi k/a$ for both the potential $V_L(x)$ and the modulation function $u_q(x)$ as

$$V_L(x) = \frac{1}{\sqrt{2\pi}} \sum_{k=-\infty}^{\infty} v_k e^{ikx}, \quad u_q(x) = \frac{1}{\sqrt{2\pi}} \sum_{k=-\infty}^{\infty} c_{q,k} e^{ikx}.$$

After inserting these into Eq. (3.6) we obtain a system of linear equations for each Fourier coefficient $c_{q,k}$ as

$$\frac{1}{2m} (q - G_k)^2 c_{q,k} + \sum_{p=-\infty}^{\infty} v_{p-k} c_{q,p} = E_q c_{q,k}. \quad (3.7)$$

These equations can be solved numerically in a very straightforward manner. Firstly, we take the system as being composed of a finite number of sites M with periodic boundary conditions (so $M + 1 \equiv 1$). This then gives a discrete set of M quasi-momenta⁶ $\{q\} = \{-\pi/a + \delta q, \dots, \pi/a - \delta q, \pi/a\}$ in the first BZ with $\delta q = 2\pi/M$. Next we restrict⁷ the number of reciprocal lattice points in the Fourier expansion to R .

⁵The periodicity of $u_q(x)$ means that we may restrict this equation to a single unit cell of the lattice. Since this is a finite volume it is expected on general grounds to have a discrete spectrum.

⁶Note that $q = -\pi/a \equiv q = \pi/a$ since they are connected by a reciprocal lattice vector $G_1 = 2\pi/a$.

⁷Depending on the periodic potential this can typically be quite small, say on the order of 50.

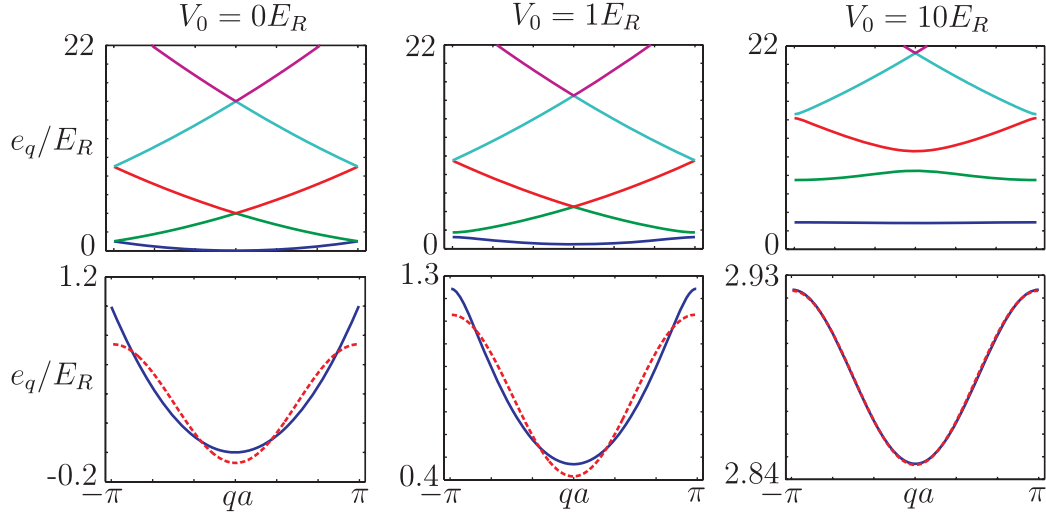


Figure 3.3. The top three panels show the five lowest bands for an optical lattice with $V_0 = 0, 1$ and $10E_R$, respectively. The bottom three panels show a zoomed in plot of the lowest band (solid line) and the tight-binding approximation (dashed line).

Then the set of equations Eq. (3.7) for fixed q can be recast as an eigenvalue problem

$$\mathbf{H}_q \vec{c}_q = E_q \vec{c}_q,$$

where \mathbf{H}_q is an $(R \times R)$ matrix and \vec{c}_q is an R -dimensional eigenvector of Fourier coefficients. Diagonalising \mathbf{H}_q then yields R eigenvectors $\vec{c}_{q,n}$, which define the functions $u_{q,n}(x)$, and eigenenergies $E_{q,n}$ which are labelled by the band index n . Repeating this calculation for each q then yields the numerical approximation to the band structure.

For the case of an optical lattice where $V_L(x) = V_0 \sin^2(kx) = \frac{1}{4}V_0(2 - e^{iG_1 x} + e^{-iG_1 x})$ the band structure can be solved analytically since the Schrödinger equation corresponds to the Mathieu equation [18]. However, it is also very simple to solve numerically since \mathbf{H}_q are tridiagonal matrices with $(\mathbf{H}_q)_{kk} = E_R(qa/\pi - 2k)^2 + \frac{1}{2}V_0$ and $(\mathbf{H}_q)_{kp} = \frac{1}{4}V_0$ for $|k - p| = 1$. The five lowest bands are plotted in the top panels of Fig. 3.3 for a variety of lattice depths. For $V_0 = 0$ the band structure is simply the quadratic free particle spectrum mapped into the first BZ and is characterised by the bands touching at the zone boundaries or centre. When $V_0 \neq 0$ it is roughly found that bands with $E_{q,n} < V_0$ have a sizable separation from one another (i.e. a band gap, see for example the lowest band for $V_0 = 1E_R$ in Fig. 3.3), whereas those with $E_{q,n} > V_0$ still form a continuum. In the bottom panels of Fig. 3.3 a zoomed-in plot of the lowest band is shown. Notice that when $V_0 \gg E_R$ the lowest band becomes cosinusoidal in shape, but with a very small band-width which makes it nearly flat.

3.2.2 Wannier states

While Bloch states $\phi_{q,n}(x)$ form a complete orthonormal basis for describing particles in any band, they are typically spatially extended functions over the entire system. To describe local interactions it would therefore be highly desirable to use an alternative orthonormal basis composed of states which are spatially localised on each lattice site. Such a localised basis is formed by the so-called Wannier states of the lattice [17].

To construct Wannier states we appeal to the fact that any function with a spread-out Fourier expansion is often equivalent to a localised real space function. Thus, we interpret, for fixed x and n , the continuous quasi-momentum q indexing $\phi_{q,n}(x)$ as resulting from the Fourier transform of some real-space function $w_n(x, y)$. Since $\phi_{q,n}(x)$ is a periodic function in reciprocal space (i.e. q is restricted to the first BZ) its Fourier expansion is over the corresponding real-space lattice with sites j at position x_j as

$$\phi_{q,n}(x) = \sum_j w_n(x, x_j) e^{iqx_j}.$$

Wannier functions are then extracted from the inverse as

$$w_n(x, x_j) = \nu_0^{-1} \int_{\text{bz}} dq e^{-iqx_j} \phi_{q,n}(x),$$

where the q integration is confined to the first BZ which has a volume (length) in reciprocal space of $\nu_0 = 2\pi/a$. Due to Bloch's theorem $w_n(x, x_j)$ is a function of $x - x_j$ as $w_n(x - x_j)$. If we define $w_n(x - x_j) = \langle x | w_{n,j} \rangle$ then the orthonormality of this set of states $\langle w_{n,j} | w_{n',j'} \rangle = \delta_{n,n'} \delta_{j,j'}$ follows from that of the Bloch states $\langle \phi_{q,n} | \phi_{q',n'} \rangle = \delta_{n,n'} \delta_{q,q'}$, as does their completeness [17].

One might hope that the Wannier functions $w_n(x - x_j)$ are well localised around each lattice site j and therefore provide a tight-binding orbital. However, this is by no means guaranteed by this construction. For a single isolated⁸ band n , the maximum localisation possible will depend on the band gap and band width. Loosely speaking they will be more localised for a narrow band separated from other bands by a large gap. To achieve the best possible localisation we encounter a subtle issue, namely that with the above prescription Wannier states are not unique [19]. For a single isolated band this manifests itself as a freedom in the choice of phases which can be attributed for each q to the Bloch state $\phi_{q,n}(x)$. Specifically, one can perform the transformation $\phi_{q,n}(x) \rightarrow e^{i\theta_{q,n}} \phi_{q,n}(x)$ where $\theta_{q,n}$ is a real function of q , and obtain an equally valid set of Bloch states. Such a transformation preserves the centres of the Wannier states $\langle x \rangle = \langle w_{n,j} | \hat{x} | w_{n,j} \rangle = x_j$, modulo a multiple of the lattice spacing, but alters its spatial spread $\sigma^2 = \langle x^2 \rangle - \langle x \rangle^2$ [20].

In 1D for an isolated band there is a unique choice of phases for the Bloch states where this spread is minimised and the resulting Wannier functions are maximally localised [19, 20]. Focussing on one band n we begin by computing the scalar-product

⁸An isolated band is one which is never degenerate at any point with any other bands.

matrix $S_q = \langle u_{q,n} | u_{q+\delta q,n} \rangle$ between the states⁹ $| u_{q,n} \rangle$ at neighbouring quasi-momenta q and $q + \delta q$. We compute the last element $S_{\pi/a}$ by wrapping around the BZ from $q = \pi/a$ to $q = -\pi/a$ using the relation $u_{-\pi/a,n}(x) = e^{2\pi i x/a} u_{\pi/a,n}(x)$. We then sum S_q over all q to give $\beta = \sum_q S_q$ and compute the band's so-called Berry phase as $\alpha = \beta/|\beta|$. Now starting from $q = -\pi/a + \delta q$ we adjust the phase of the neighbouring state $| u_{q+\delta q,n} \rangle$ such that $S_q = \alpha^{1/M}$, and continue until $| u_{\pi/a,n} \rangle$ has been adjusted. This process is said to minimise the Berry curvature of the band and the resulting Wannier states $w_n(x)$ are real symmetric (n even) / antisymmetric (n odd) functions which fall off exponentially with x as $|w_n(x)| \approx |x|^{-3/4} e^{-h_n x}$ with real $h_n > 0$, resulting in $\lim_{x \rightarrow \infty} |w_n(x)| = 0$ [20, 21]. On this basis these Wannier functions are said to be maximally localised.

In Fig. 3.4(a)(b) we plot the two lowest ($n = 0$ and $n = 1$) maximally localised Wannier states for $V_L(x) = V_0 \sin^2(kx)$ for a shallow $V_0 = 1E_R$ and deep $V_0 = 10E_R$ lattice. As expected the Wannier functions exhibit exponential localisation, as depicted in Fig. 3.4(c)(d), about their centres, with the localisation less pronounced for shallower lattice and higher bands. Within the central site Wannier functions bear a strong resemblance to eigenstates of the harmonic oscillator, especially for the deeper lattices, and following our earlier discussion this enables analytical estimates to be obtained for many on-site properties. However, at larger distances Wannier functions decay slower than the Gaussian envelopes of harmonic oscillator wave-functions, and moreover have oscillatory tails at neighbouring sites. The presence of nodes in the tail is essential for the precise orthogonality of Wannier functions and indicates that even in the deep lattice limit they do not precisely approach harmonic oscillator wave-functions. From a practical perspective, however, their overlap approaches unity sufficiently closely that this is not a serious difference.

For more complex super-lattice structures in 1D or general non-separable lattices in higher dimensions obtaining maximally localised Wannier states requires the introduction of *generalised* Wannier functions where Bloch states from different bands are mixed [20]. In all the situations considered in this thesis, however, the lattice will be taken as having a simple cubic geometry with Wannier states that are simply a product of maximally localised 1D Wannier states along each dimension as $w_{\mathbf{n}}(\mathbf{r} - \mathbf{r}_j) = w_{n_x}(x)w_{n_y}(y)w_{n_z}(z)$, where $\mathbf{r} = (x, y, z)$ and $\mathbf{n} = (n_x, n_y, n_z)$. An example of a 2D Wannier state for $V_0 = 1E_R$ is shown in Fig. 3.4(e).

3.2.3 Non-interacting system

In terms of bosonic field operators $\hat{\Psi}(\mathbf{r})$ the Hamiltonian for non-interacting particles moving in a lattice potential is

$$\hat{H}_0 = \int d\mathbf{r} \hat{\Psi}^\dagger(\mathbf{r}) \left(-\frac{\hbar^2}{2m} \nabla^2 + V_L(\mathbf{r}) \right) \hat{\Psi}(\mathbf{r}). \quad (3.8)$$

⁹Here $u_{q,n}(x) = \langle x | u_{q,n} \rangle$, and we use the discretisation of the quasi-momentum introduced earlier.

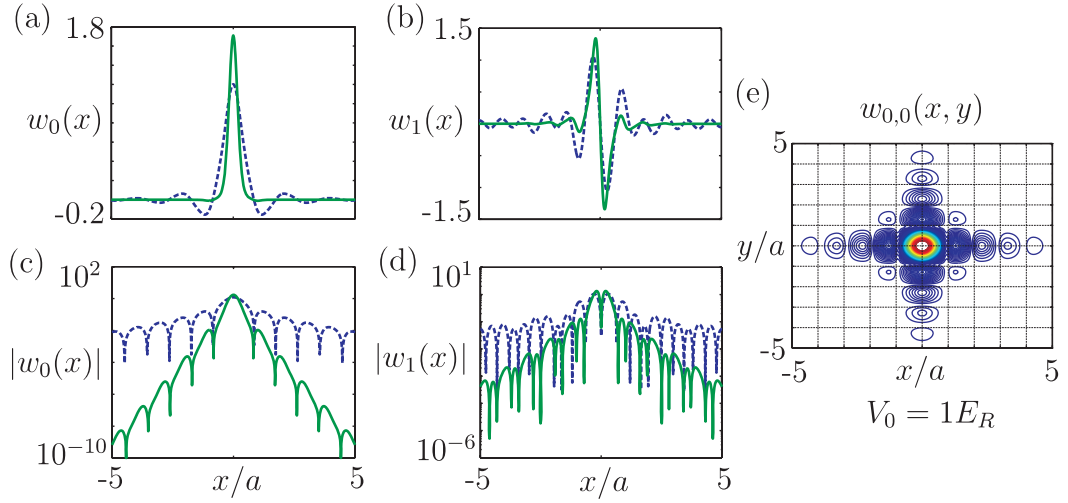


Figure 3.4. (a)-(b) The Wannier states for the lowest band $w_0(x)$ and first excited band $w_1(x)$ for $V_0 = 1E_R$ (dashed line) and $V_0 = 10E_R$ (solid line). (c)-(d) The same Wannier states as in (a) $|w_0(x)|$ and (b) $|w_1(x)|$ plotted on a logarithmic scale. For $V_0 = 10E_R$ notice the prominent exponentially decaying tails for both $|w_0(x)|$ and $|w_1(x)|$. (e) A contour plot of the Wannier state $w_{0,0}(x, y)$ for the lowest band of a 2D isotropic square lattice with $V_0 = 1E_R$.

We now expand the field operators in the complete orthonormal single-particle Wannier basis as

$$\hat{\Psi}(\mathbf{r}) = \sum_{j,\mathbf{n}} w_{\mathbf{n}}(\mathbf{r} - \mathbf{r}_j) \hat{b}_{\mathbf{n},j}, \quad (3.9)$$

where $\hat{b}_{\mathbf{n},j}$ is the bosonic annihilation operator for the Wannier state $w_{\mathbf{n}}(\mathbf{r} - \mathbf{r}_j)$. To expand \hat{H}_0 in terms of Wannier mode operators $\hat{b}_{\mathbf{n},j}$ we first compute the single-particle matrix elements

$$J_{\mathbf{n},\mathbf{n}'}(\mathbf{r}_j) = \langle w_{\mathbf{n},j} | \hat{H}_0 | w_{\mathbf{n}',0} \rangle,$$

describing the transition amplitude between a particle being in the Wannier state for band \mathbf{n} at $\mathbf{r} = \mathbf{r}_j$ and the Wannier state for band \mathbf{n}' at $\mathbf{r} = 0$. Using the fact that $\hat{H}_0 |\phi_{\mathbf{q},\mathbf{n}}\rangle = E_{\mathbf{q},\mathbf{n}} |\phi_{\mathbf{q},\mathbf{n}}\rangle$ it is found that

$$J_{\mathbf{n},\mathbf{n}'}(\mathbf{r}_j) = \delta_{\mathbf{n},\mathbf{n}'} \nu_0^{-1} \int_{\text{bz}} d\mathbf{q} e^{i\mathbf{q} \cdot \mathbf{r}_j} E_{\mathbf{q},\mathbf{n}},$$

and so the orthogonality of the Bloch states prohibits any inter-band coupling or hopping along directions other than the lattice axes. The non-zero amplitudes $J_{\mathbf{n},\mathbf{n}}(\mathbf{r}_j) = J_{\mathbf{n}}(\mathbf{r}_j)$ are simply the Fourier coefficients of the band structure $E_{\mathbf{q},\mathbf{n}}$ and therefore are

(somewhat counterintuitively) independent of the localisation properties of the Wannier states. Inserting the expansion Eq. (3.9) into Eq. (3.8) then gives

$$\hat{H}_0 = \sum_{i,j,\mathbf{n}} J_{\mathbf{n}}(\mathbf{r}_i - \mathbf{r}_j) \hat{b}_{\mathbf{n},i}^\dagger \hat{b}_{\mathbf{n},j}. \quad (3.10)$$

Again our case of interest is $V_L(\mathbf{r}) = V_{3D}(\mathbf{r})$ given in Eq. (3.3) describing an isotropic 3D simple cubic lattice. Along any single direction we have the 1D case which, as we saw earlier in Fig. 3.3, becomes increasingly cosinusoidal for deeper lattices. In the bottom panels of Fig. 3.3 the approximation to the band resulting from only taking the zeroth and first Fourier coefficients of the band structure is also plotted. The deviations seen at very shallow depths are a result of neglecting long-range hopping but are seen to become small for larger V_0 . For a perfect cosine band with band-width B as $E_{q,0} = -\frac{1}{2}B \cos(qa)$ we obtain $J_0(x_j) = -\frac{1}{4}B$ for $|x_j| = a$ and zero otherwise. Such a band is said to be tight-binding since the kinetic motion of a single particle is restricted to hopping between nearest neighbouring sites. This generalises straightforwardly for 3D so that the Hamiltonian describing just the lowest band reduces to

$$\hat{H}_0^{(0)} = \sum_{\langle i,j \rangle} J_0(a) \hat{b}_{0,i}^\dagger \hat{b}_{0,j}, \quad (3.11)$$

where $\langle i,j \rangle$ denotes summation over nearest neighbouring sites with $|\mathbf{r}_i - \mathbf{r}_j| = a$ only. Note that this result is purely a consequence of the band structure and would be true for any choice of Wannier states no matter how localised they are. We will see that the localisation of Wannier states becomes vitally important when interactions are included.

3.3 Many-body physics

So far we have only considered the single particle properties of atoms in optical lattices. In order to describe typical experimental situations where many atoms ($\approx 10^5$) from a BEC are loaded into the lattice we need to take account of the fact that the atoms will interact via a two-body interatomic potential $U_{\text{atom}}(\mathbf{r}_1 - \mathbf{r}_2)$. In general $U_{\text{atom}}(\mathbf{r}_1 - \mathbf{r}_2)$ will possess complicated short-range properties, such as supporting multiple bound states, and these are typically not well known [22]. However, in the limit of low energies the dominant contribution to two-body collisions is s -wave scattering which is completely specified by a corresponding scattering length a_s . In this case we may replace the actual interatomic potential by an effective pseudo-potential [23]

$$U_{\text{eff}}(\mathbf{r}_1 - \mathbf{r}_2) = \frac{4\pi\hbar^2 a_s}{m} \delta(\mathbf{r}_1 - \mathbf{r}_2) = g \delta(\mathbf{r}_1 - \mathbf{r}_2),$$

which describes a contact-interaction and gives the same asymptotic scattering if the actual (experimentally determined) a_s of the atoms is used [22]. This interaction is

then taken into account by the following term

$$\hat{H}_I = \frac{g}{2} \int d\mathbf{r} \hat{\Psi}^\dagger(\mathbf{r}) \hat{\Psi}^\dagger(\mathbf{r}) \hat{\Psi}(\mathbf{r}) \hat{\Psi}(\mathbf{r}), \quad (3.12)$$

which when added to \hat{H}_0 yields the full interacting many-body Hamiltonian $\hat{H} = \hat{H}_0 + \hat{H}_I$. Even for this contact potential when \hat{H}_I is expanded in terms of Wannier modes in Eq. (3.9) it will involve interactions between Wannier states in up to four different bands and four different sites. Significant simplifications are possible if we consider the system in the deep lattice limit. Specifically, we assume that $k_B T \ll \hbar\omega_{ho}$ and $g\langle n \rangle \ll \hbar\omega_{ho}$, where $\langle n \rangle$ is the average density of the system, so the thermal and mean interaction energy at a single site are much smaller than the separation between the lowest and first excited band. Thus, none of the relevant energies of the system, whether dynamical or in equilibrium, will cause significant excitation to the second band. We may therefore restrict our Wannier expansion to the lowest vibrational states where $\mathbf{n} = (0, 0, 0)$ [16]. For the case of a BEC loaded into an optical lattice these conditions are readily achieved.

With this restriction we are left with interaction matrix elements¹⁰ of the form

$$U_{ijkl} = g \int d\mathbf{r} w_0(\mathbf{r} - \mathbf{r}_i) w_0(\mathbf{r} - \mathbf{r}_j) w_0(\mathbf{r} - \mathbf{r}_k) w_0(\mathbf{r} - \mathbf{r}_l). \quad (3.13)$$

We shall focus on three specific terms, the on-site interaction U_{0000} , the nearest-neighbour density-density interaction U_{0101} , and the interaction induced hopping U_{0001} . It is at this point that the localisation of the Wannier states using the methods in section 3.2.2 plays a crucial role. From our earlier discussion, centred about Fig. 3.4(a)(c), we have seen that for lattices with $V_0 \approx 10E_R$ the Wannier functions $w_0(\mathbf{r} - \mathbf{r}_j)$ essentially decay within a single lattice constant. For deep lattices we therefore expect that the vanishingly small overlap between Wannier states on different sites should suppress off-site interaction terms, such as U_{0101} and U_{0001} , leaving the on-site term U_{0000} as the dominant contribution [16]. This intuition is indeed confirmed by numerical calculation of these matrix elements shown in Fig. 3.5(a). Even for $V_0 = 1E_R$ the on-site term U_{0000} is more than an order of magnitude larger than the most significant off-site terms. For deeper lattices this difference widens to several orders of magnitude and justifies our neglect of all but the term $U_{0000} = U$. Since the integral Eq. (3.13) for the on-site term is not very sensitive to the tails of the Wannier functions $w_0(\mathbf{r})$ we can approximate it by a product of ground states $\psi_{ho}(x)$ along each lattice axis giving an analytical expression

$$U = \sqrt{8\pi} \frac{a_s}{a} \left(\frac{V_0}{E_R} \right)^{3/4} E_R,$$

for an isotropic 3D lattice. This harmonic oscillator approximation for U is also plotted in Fig. 3.5(a) and seen to be a good approximation for deep lattices. Note that the

¹⁰Recall that the Wannier functions can be chosen to be real.

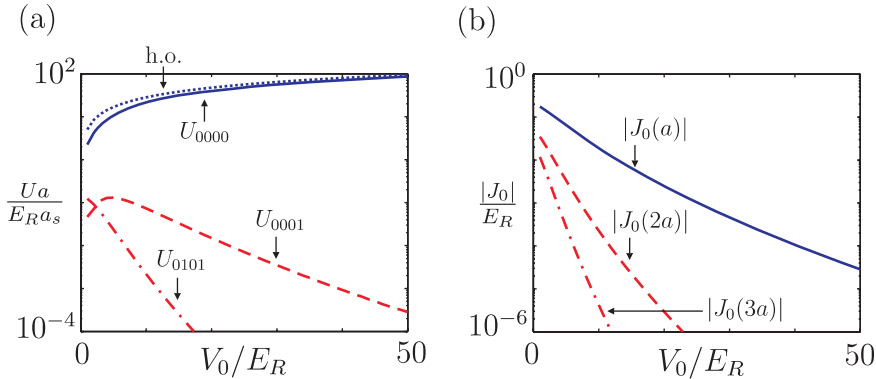


Figure 3.5. (a) The interaction matrix elements (in units of $a/E_R a_s$) U_{0000} (solid line), U_{0101} (dashed line) and U_{0001} (dashed-dotted line). The harmonic oscillator approximation to U_{0000} (dotted-line) labelled as h.o. is also shown. (b) The kinetic matrix elements along one of the lattice axes for first-neighbour hopping $J_0(a)$ (solid line), second-neighbour hopping $J_0(2a)$ (dashed line), and third-neighbour hopping $J_0(3a)$. All quantities are for the lowest band in an isotropic 3D lattice and are plotted against the lattice depth V_0 .

strength of U increases with V_0 due to the tighter squeezing of atoms in a lattice site.

As discussed for deep lattices the lowest band becomes increasingly close to a tight-binding band characterised by the zeroth and first Fourier coefficients of the actual band structure. This “closeness” can be quantified by also computing the second and third Fourier coefficients representing second-neighbour $J_0(2a)$ and third-neighbour $J_0(3a)$ kinetic terms, respectively. In Fig. 3.5(b) it is found that $J_0(2a)$ and $J_0(3a)$ are more than an order of magnitude smaller than $J_0(a)$ for depths $V_0 > 5E_R$ and thus may be neglected. The remaining nearest-neighbour tunnelling $J_0(a) = -J$ can be approximated by attributing it to the exact band-width found from the 1D Mathieu equation¹¹ [18]. This gives

$$J = \frac{4}{\sqrt{\pi}} \left(\frac{V_0}{E_R} \right)^{3/4} \exp \left[-2 \left(\frac{V_0}{E_R} \right)^{1/2} \right] E_R,$$

which is accurate to a few percent in deep lattices. This approximation shows that J decreases exponentially with potential barrier height V_0 as might be expected on general grounds.

After setting $\hat{b}_{0,j} \equiv \hat{b}_j$, we therefore arrive at an effective description of the quantised motion of atoms in an optical lattice that is the standard Bose-Hubbard model (BHM)

¹¹This can be done exactly with Mathematica for example.

Hamiltonian [3, 24]

$$\hat{H}_{\text{BH}} = -J \sum_{\langle i,j \rangle} \hat{b}_i^\dagger \hat{b}_j + \frac{U}{2} \sum_j \hat{n}_j (\hat{n}_j - 1) + \sum_j \epsilon_j \hat{n}_j,$$

where $\hat{n}_j = \hat{b}_j^\dagger \hat{b}_j$ is the number operator for site j . The last term has been included to describe an additional trapping $V_T(\mathbf{r})$, such as that provided by shallow magnetic or optical potentials, which varies slowly in space compared to the localisation of the Wannier states. Its matrix elements are given by

$$\epsilon_j = \int d\mathbf{r} |w_0(\mathbf{r} - \mathbf{r}_j)|^2 V_T(\mathbf{r}) \approx V_T(\mathbf{r}_j).$$

Analysing the ground state properties of the BHM in detail is the subject of the next chapter. An important feature we shall explore is the presence of a quantum phase transition between the so-called superfluid and Mott insulating phases which occurs at a critical ratio of U/J . In contrast to a genuine solid state system, in which the BHM is only ever a crude approximation, an optical lattice filled with ultracold bosonic atoms provides a near perfect¹² realisation of the BHM. Moreover, within an optical lattices realisation the ratio U/J , given here for a 3D lattice

$$\frac{U}{J} \approx \frac{a_s}{a} \exp \left[2 \left(\frac{V_0}{E_R} \right)^{1/2} \right],$$

increases exponentially with V_0 and means that the system can be tuned from the weak to strongly interacting regimes. Provided the average density $\langle \hat{n}_j \rangle \sim 1$, the presence of an optical lattice enhances the weak interaction between the atoms and has already enabled the superfluid and Mott insulator regimes to be experimentally measured [10]. In part II we investigate several aspects of the coherent dynamical evolution of the BHM. Comparison of these results with experiments further demonstrates that the BHM is indeed an excellent model for the motion of cold atoms in an optical lattice.

References

- [1] H. Metcalf, P. van der Straten, *Laser Cooling and Trapping* (Springer, New York, 1999).
- [2] P. Jessen, I. Deutsch, *Adv. At. Mol. Opt. Phys.* **37**, 95 (1996).
- [3] D. Jaksch, C. Bruder, J.I. Cirac, C.W. Gardiner, P. Zoller, *Phys. Rev. Lett.* **81**, 3108 (1998).
- [4] C. Maschler, H. Ritsch, *Phys. Rev. Lett.* **95**, 260401 (2005).

¹²Modulo the approximations discussed in this chapter.

- [5] S.M. Barnett, P.M. Radmore, *Methods in Theoretical Quantum Optics* (Oxford Univ. Press, Oxford, 2002).
- [6] C. Cohen-Tannoudji, J. Dupont-Roc, G. Grynberg, *Atom-Photon Interactions* (John Wiley & Sons, New York, 1998).
- [7] L. Pitaevskii, S. Stringari, *Bose-Einstein Condensation* (Oxford Univ. Press, Oxford, 2003).
- [8] C.J. Foot, *Atomic Physics* (Oxford Uni. Press, Oxford, 2005).
- [9] T. Stöferle, H. Moritz, C. Schori, M. Köhl, T. Esslinger, *Phys. Rev. Lett.* **92**, 130403 (2004).
- [10] M. Greiner, O. Mandel, T. Esslinger, T.W. Hänsch, I. Bloch, *Nature (London)* **415**, 39 (2002).
- [11] O. Mandel, M. Greiner, A. Widera, T. Rom, T.W. Hänsch, I. Bloch, *Nature (London)* **425**, 937 (2003).
- [12] S. Peil, J.V. Porto, B.L. Tolra, J.M. Obrecht, B.E. King, M. Subbotin, S.L. Rolston, W.D. Phillips, *Phys. Rev. A* **67**, 051603(R) (2003).
- [13] D. Jaksch, P. Zoller, *Ann. Phys. (N.Y.)* **315**, 52 (2005).
- [14] L. Santos, M.A. Baranov, J.I. Cirac, H.-U. Everts, H. Fehrmann, M. Lewenstein, *Phys. Rev. Lett.* **93**, 030601 (2004).
- [15] B. Damski, J. Zakrzewski, L. Santos, P. Zoller, M. Lewenstein, *Phys. Rev. Lett.* **91**, 080403 (2003).
- [16] D. Jaksch, *Bose-Einstein Condensation and Applications* (PhD. Thesis, Leopold-Franzens-Univ., Innsbruck, 1999).
- [17] N.W. Ashcroft, N.D. Mermin, *Solid State Physics* (Holt, Rinehardt and Winston, New York, 1976).
- [18] H.P. Büchler, G. Blatter, W. Zwerger, *Phys. Rev. Lett.* **90**, 130401 (2003).
- [19] W. Kohn, *Phys. Rev.* **115**, 809 (1959).
- [20] N. Marzari, D. Vanderbilt, *Phys. Rev. B* **56**, 12847 (1997).
- [21] L. He, D. Vanderbilt, *Phys. Rev. Lett.* **86**, 5341 (2001).
- [22] I. Bloch, J. Dalibard, W. Zwerger, [arXiv:0704.3011](https://arxiv.org/abs/0704.3011).
- [23] K. Huang, *Statistical Mechanics* (John Wiley & Sons, New York, 1987).
- [24] M.P.A. Fisher, P.B. Weichman, G. Grinstein, D.S. Fisher, *Phys. Rev. B* **40**, 546 (1989).

Part II

Dynamics of the Bose-Hubbard model

CHAPTER 4

PROPERTIES OF THE BOSE-HUBBARD MODEL

The Hubbard model [1] was originally devised as an approximate description of the motion of electrons within transition metals with the aim of better understanding quantum magnetic ordering. The prominent feature of this model is that the motion of electrons is confined to hopping between atoms on a regular lattice and the screened-coulomb interaction between electrons is truncated to a zero-range on-site interaction. Even with this approximation determining the properties of the Hubbard model in 2D/3D remains a subject of intense research today, especially given their potential relevance in revealing the fundamental mechanism of d -wave pairing in high- T_c superconductors [2].

In this chapter we shall study in some detail the properties of a simpler cousin of the Hubbard model, the Bose Hubbard model (BHM) [3], in which the spin- $\frac{1}{2}$ fermionic degrees of freedom are replaced by spin-less bosons. As a result of this replacement we are left with perhaps one of the simplest many-body Hamiltonians, which nonetheless possesses highly non-trivial properties. As we shall explore here the BHM in fact exhibits a richly structured phase diagram containing a quantum phase transition and is believed to capture much of the essential physics of strongly-interacting Bose systems. Moreover, according to Sachdev [4] much of our understanding of quantum phase transitions is based on the properties of two prototypical models, namely the para- to ferromagnetic transition in the Ising model (discussed briefly in chapter 2), and the superfluid to Mott-insulator transition in the BHM. For these reasons both models have been studied intensively for many years. As of late, interest in the BHM has undergone a major renaissance due to its near-perfect experimental realisation with ultra-cold atoms in optical lattices as discussed earlier in chapter 3.

The BHM Hamiltonian is composed of kinetic and interaction terms of the form (note that we shall take $\hbar = 1$ throughout this chapter)

$$\hat{H}_{\text{BH}} = -J \sum_{\langle i,j \rangle} \hat{b}_i^\dagger \hat{b}_j + \frac{U}{2} \sum_i \hat{n}_i (\hat{n}_i - 1),$$

where $\langle i,j \rangle$ denotes all nearest neighbouring sites for a D -dimensional regular lattice, while for the i -th site \hat{b}_i^\dagger (\hat{b}_i) is the bosonic creation (annihilation) operator and $\hat{n}_i = \hat{b}_i^\dagger \hat{b}_i$ is the number operator. Aside from the final section 4.4 we shall consider the system as homogeneous and we will assume periodic boundary conditions. As depicted in Fig. 4.1(a) the first term in \hat{H}_{BH} describes the hopping of bosons between

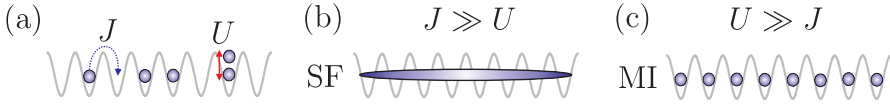


Figure 4.1. (a) A schematic depiction of the basic effects of the two terms, kinetic and interactions, which make up the BHM. The kinetic term causes the hopping of bosons between sites, while the interaction term causes an energy cost for multiple occupancies of a site. These effects lead to a simplistic picture of two different regimes of the BHM. (b) When the kinetic term dominates it causes the bosons to spread across the entire system. (c) When the interaction dominates, and the system is commensurately filled, it causes the bosons to be pinned to a lattice site.

nearest neighbouring sites with amplitude J , while the second describes a zero-range, on-site repulsion U which energetically suppresses multiple occupancies of any site. Competition between the tendencies of these contribution for itinerancy (Fig. 4.1(b)) and localisation (Fig. 4.1(c)) is responsible for the emergence of a quantum phase transition. Importantly we also see that $[\hat{H}_{\text{BH}}, \hat{N}] = 0$ where $\hat{N} = \sum_j \hat{n}_j$, and so the total number of bosons is a conserved quantity¹.

Despite its elementary appearance, however, the BHM is not exactly solvable for all U/J with any currently known analytical techniques in finite dimensions² [5, 6, 7]. This contrasts strongly with the conventional Hubbard model which is exactly solvable in 1D via the Bethe ansatz [8]. It is also somewhat surprising given that the continuum limit of the 1D BHM, where lattice sites are taken as discretising space, is the Lieb-Liniger model of bosons interacting via a contact potential which also exactly solvable [9] (again via the Bethe ansatz). To understand the BHM we will glean valuable insight from the two extreme limits ($U = 0$ and $J = 0$) where it is exactly solvable and then employ a number of analytical and numerical approximations to study quantum phase transition in between these limits.

4.1 Weakly interacting limit - superfluid

4.1.1 The $U = 0$ limit

To begin we examine the non-interacting limit of the BHM where the model is exactly solvable. In this case the Hamiltonian can be trivially diagonalised by a discrete Fourier transform to quasi-momentum space defined by the creation operator

$$\hat{c}_{\mathbf{k}}^\dagger = \frac{1}{\sqrt{M^D}} \sum_i \hat{b}_i^\dagger e^{-i\mathbf{k}\cdot\mathbf{r}_i},$$

¹The conservation of \hat{N} can also be seen as a consequence of \hat{H}_{BH} being invariant under the transformation $\hat{b}_j \mapsto \hat{b}_j e^{i\phi}$ and therefore possessing $U(1)$ symmetry.

²It is actually solvable in infinite-dimensions.

where \mathbf{r}_i is the coordinate of site i , \mathbf{k} is a wave-vector running over the first Brillouin zone and M^D is the total number of sites. The Hamiltonian then reads $\hat{H}_{\text{BH}} = \sum_{\mathbf{k}} \epsilon_{\mathbf{k}} \hat{c}_{\mathbf{k}}^\dagger \hat{c}_{\mathbf{k}}$ where the free-particle dispersion in a cubic lattice is $\epsilon_{\mathbf{k}} = -2J \sum_{d=1}^D \cos(k_d a)$ with lattice spacing a . When $|\mathbf{k}|a \ll 1$ this spectrum becomes quadratic as $\epsilon_{\mathbf{k}} \approx J(\mathbf{k}a)^2 - zJ$, where $z = 2D$ is the number of nearest-neighbours in D dimensions. Moreover, $\epsilon_{\mathbf{k}}$ is gapless³ in the thermodynamic limit where the set of available \mathbf{k} states becomes continuous. The ground state for N non-interacting bosons is when all particles are in the $\hat{c}_0 \equiv \hat{c}_{\mathbf{k}=0}$ mode as

$$|\Psi_{\text{gs}}\rangle = \frac{(\hat{c}_0^\dagger)^N}{\sqrt{N!}} |\text{vac}\rangle = \frac{1}{\sqrt{N!}} \left(\frac{1}{\sqrt{M^D}} \sum_{i=1}^M \hat{b}_i^\dagger \right)^N |\text{vac}\rangle, \quad (4.1)$$

where $|\text{vac}\rangle$ is the vacuum state and due to this macroscopic occupancy of a single-particle state the ground state is said to be Bose-condensed [10]. Since \hat{c}_0 is an equal superposition of the localised lattice modes \hat{b}_i this solution highlights that the kinetic term of \hat{H}_{BH} is minimised by delocalising the particles over the lattice.

Other important properties of the non-interacting limit can be deduced by computing the reduced density matrix ϱ of any single lattice site of the system. This is done by firstly performing a multinomial expansion of the bosonic operators⁴ as

$$\left(\sum_{i=1}^{M^D} \hat{b}_i^\dagger \right)^N = \sum_{\{n_1, n_2, \dots, n_M\}} \frac{N!}{n_1! n_2! \dots n_M!} (\hat{b}_1^\dagger)^{n_1} (\hat{b}_2^\dagger)^{n_2} \dots (\hat{b}_M^\dagger)^{n_M},$$

where the sum is over all partitions $\{n_1, n_2, \dots, n_M\}$ of non-negative numbers satisfying $\sum_{i=1}^{M^D} n_i = N$. Then after tracing⁵ out all but one site of $|\Psi_{\text{gs}}\rangle \langle \Psi_{\text{gs}}|$ we obtain a reduced density matrix $\varrho^{(1)}$ which is diagonal in the number basis

$$\varrho^{(1)} = \sum_{n=0}^N \frac{N!}{(N-n)! n!} \left(\frac{1}{M^D} \right)^n \left(1 - \frac{1}{M^D} \right)^{N-n} |n\rangle \langle n|,$$

with a binomial number distribution, and where $|n\rangle$ is a number state. Given that $|\Psi_{\text{gs}}\rangle$ is a pure state the mixedness of $\varrho^{(1)}$ reveals that the state of any single lattice site is entangled with the rest of the system independent of the dimension D . In the thermodynamic limit, where $N, M \rightarrow \infty$ while N/M^D is kept fixed, the on-site number statistics of the state becomes a Poisson distribution as

$$\varrho^{(1)} = \sum_{n=0}^{\infty} \frac{e^{-\langle n \rangle} \langle n \rangle^n}{n!} |n\rangle \langle n|,$$

³By ‘gap’ we mean a non-zero energy separation between the ground state and the first excited state which is independent of N or M and so remains in the thermodynamic limit.

⁴This expansion can be used straightforwardly since bosonic operators for different sites commute.

⁵Note that the sum of all multinomial coefficients for M^D terms raised to the power of N is M^{DN} .

with an average on-site occupancy $\langle n \rangle = N/M^D$ and corresponding number fluctuation $\Delta n = \sqrt{\langle n \rangle}$. A similar calculation can be performed for the reduced density matrix of any pair of sites $\rho^{(2)}$ and reveals that it is the identical for all pairs. This leaves expectation values such as the single-particle density matrix $\langle \hat{b}_i^\dagger \hat{b}_j \rangle = \langle n \rangle$ constant for all i and j , regardless of the distance $|i - j|$, indicating the presence of long-range order. These are characteristic properties of the non-interacting limit.

4.1.2 The Bogoliubov approximation

As originally devised by Einstein the concept of Bose-Einstein condensation is that a finite fraction $f_0 = N_0/N$ of the total number of particles N in the system occupy the same single-particle state below some critical temperature [11, 12, 13, 2]. Given that $f_0 = 1$ in the non-interacting limit at $T = 0$ this property represents an ideal starting point for approximating the effects of non-zero interactions. More precisely, we shall make the (non-trivial) assumption that the system remains Bose-condensed even in the presence of weak repulsive interactions resulting in the interacting ground state possessing a condensate fraction f_0 of order unity.

We begin by expressing the full BHM in terms of quasi-momentum operators as

$$\hat{H}_{\text{BH}} = \sum_{\mathbf{k}} \epsilon_{\mathbf{k}} \hat{c}_{\mathbf{k}}^\dagger \hat{c}_{\mathbf{k}} + \frac{U}{2M} \sum_{\mathbf{k}} \sum_{\mathbf{k}'} \sum_{\mathbf{q}} \hat{c}_{\mathbf{k}+\mathbf{q}}^\dagger \hat{c}_{\mathbf{k}'-\mathbf{q}}^\dagger \hat{c}_{\mathbf{k}} \hat{c}_{\mathbf{k}'}$$

On account of the two-body interaction terms it is clear that $|\Psi_{\text{gs}}\rangle$ is no longer an eigenstate which immediately indicates that quasi-momenta $\mathbf{k} \neq 0$ will be occupied in the interacting ground state. This feature is called quantum depletion of the condensate. The Bogoliubov approximation is based on the assumption that a Bose condensate exists, and moreover that it is only weakly depleted. We therefore restrict our attention to (superpositions of) momentum Fock states of the form $|N_0, \dots\rangle$ where $N > N_0 \gg N - N_0$ and N_0 is the occupancy of the $\mathbf{k} = 0$ state. To utilise this approximation and better understand the effects of the interaction terms we first break them up as⁶

$$\begin{aligned} \sum_{\mathbf{k}} \sum_{\mathbf{k}'} \sum_{\mathbf{q}} \hat{c}_{\mathbf{k}+\mathbf{q}}^\dagger \hat{c}_{\mathbf{k}'-\mathbf{q}}^\dagger \hat{c}_{\mathbf{k}} \hat{c}_{\mathbf{k}'} &= \hat{c}_0^\dagger \hat{c}_0^\dagger \hat{c}_0 \hat{c}_0 + \sum_{\mathbf{k} \neq 0} \left(\hat{c}_{\mathbf{k}}^\dagger \hat{c}_{-\mathbf{k}}^\dagger \hat{c}_0 \hat{c}_0 + 4 \hat{c}_{\mathbf{k}}^\dagger \hat{c}_{\mathbf{k}} \hat{c}_0^\dagger \hat{c}_0 + \hat{c}_0^\dagger \hat{c}_0^\dagger \hat{c}_{\mathbf{k}} \hat{c}_{-\mathbf{k}} \right) \\ &\quad + \sum_{\mathbf{k} \neq 0} \sum_{\mathbf{q} \neq 0} \left(2 \hat{c}_{\mathbf{k}+\mathbf{q}}^\dagger \hat{c}_{-\mathbf{q}}^\dagger \hat{c}_{\mathbf{k}} \hat{c}_0 + 2 \hat{c}_0^\dagger \hat{c}_{\mathbf{k}-\mathbf{q}}^\dagger \hat{c}_{\mathbf{k}} \hat{c}_{-\mathbf{q}} \right) \\ &\quad + \sum_{\mathbf{k} \neq 0} \sum_{\mathbf{k}' \neq 0} \sum_{\mathbf{q} \neq 0, \mathbf{k}, \mathbf{k}'} \hat{c}_{\mathbf{k}+\mathbf{q}}^\dagger \hat{c}_{\mathbf{k}'-\mathbf{q}}^\dagger \hat{c}_{\mathbf{k}} \hat{c}_{\mathbf{k}'}, \end{aligned} \tag{4.2}$$

so that the contributions involving the zero-momentum mode appear explicitly. In Fig. 4.2 these contributions are shown diagrammatically, and we see that due to momentum conservation there are no interaction terms involving three zero-momentum

⁶The coefficients of each term arises from the number of ways it is generated from the original sum.

operators. The dominant effect of the interaction can already be seen by applying it to the non-interacting ground state $|\Psi_{\text{gs}}\rangle$. As a result of the terms $\hat{c}_{\mathbf{k}}^\dagger \hat{c}_{-\mathbf{k}}^\dagger \hat{c}_0 \hat{c}_0$ pairs of zero-momentum bosons will be excited out of the condensate to momenta $\pm \mathbf{k}$ and the corresponding amplitude of this process will contain a bosonic enhancement factor of $\sqrt{N_0(N_0 - 1)}$. Since we have assumed weak depletion the interaction terms which involve only one or no zero-momentum operators (processes (6)-(8) in Fig. 4.2) will have much smaller amplitude in comparison owing to much less dramatic enhancement. We therefore drop these terms leaving a truncated Hamiltonian of the form

$$\hat{H}_{\text{trunc}} = \hat{H}_0 + \hat{H}_c + \hat{H}_{\text{ex}},$$

where H_0 acts only on the zero-momentum sector, H_{ex} is diagonal in the $\mathbf{k} \neq 0$ momentum sectors, while H_c describes the interaction coupling pairs of $\pm \mathbf{k}$ sectors to the $\mathbf{k} = 0$ state. Explicitly these contributions are

$$\begin{aligned}\hat{H}_0 &= -zJ\hat{c}_0^\dagger \hat{c}_0 + \frac{U}{2M}\hat{c}_0^\dagger \hat{c}_0^\dagger \hat{c}_0 \hat{c}_0, \\ \hat{H}_c &= \frac{U}{2M} \sum_{\mathbf{k} \neq 0} \left(\hat{c}_{\mathbf{k}}^\dagger \hat{c}_{-\mathbf{k}}^\dagger \hat{c}_0 \hat{c}_0 + 4\hat{c}_{\mathbf{k}}^\dagger \hat{c}_{\mathbf{k}} \hat{c}_0^\dagger \hat{c}_0 + \hat{c}_0^\dagger \hat{c}_0^\dagger \hat{c}_{\mathbf{k}} \hat{c}_{-\mathbf{k}} \right), \\ \hat{H}_{\text{ex}} &= \sum_{\mathbf{k} \neq 0} \epsilon_{\mathbf{k}} \hat{c}_{\mathbf{k}}^\dagger \hat{c}_{\mathbf{k}}.\end{aligned}$$

Importantly we see that H_{trunc} continues to conserve the total particle number \hat{N} . This truncation will be accurate in the weak interaction $U \rightarrow 0$ and/or low-density $N/M \rightarrow 0$ limit. In view of this we can intuitively expect that the interacting ground state will take the form [12, 14]

$$|\Psi_{\text{pair}}\rangle = \sum_{n_{\mathbf{k}}} \eta_{\{n_{\mathbf{k}}\}} \prod_{\mathbf{k}} (\hat{c}_{\mathbf{k}}^\dagger \hat{c}_{-\mathbf{k}}^\dagger \hat{c}_0 \hat{c}_0)^{n_{\mathbf{k}}} |\Psi_{\text{gs}}\rangle,$$

where $\eta_{\{n_{\mathbf{k}}\}}$ are the coefficients for all assignments of $\pm \mathbf{k}$ pair occupancies $\{n_{\mathbf{k}}\}$ and these are small for $\mathbf{k} \neq 0$. By exciting pairs of bosons out of the condensate the state $|\Psi_{\text{pair}}\rangle$ is likely to contain entanglement between quasi-momentum modes and this will manifest itself as quantum fluctuations between their occupancies.

It is possible to perform calculations with the Bogoliubov approximation using a state of the form $|\Psi_{\text{pair}}\rangle$ (and in some cases necessary, for example when describing an interferometer in chapter 9), though it entails a great many technical complications [12]. Instead we employ the standard (and simpler) approach which is to de-correlate the $\mathbf{k} = 0$ and $\mathbf{k} \neq 0$ contributions to the interacting ground state. The validity of this approach is justified by noting that the importance of the commutator of the zero-momentum operators

$$\frac{\langle [\hat{c}_0, \hat{c}_0^\dagger] \rangle}{\langle \hat{c}_0^\dagger \hat{c}_0 \rangle} = \frac{1}{N_0},$$

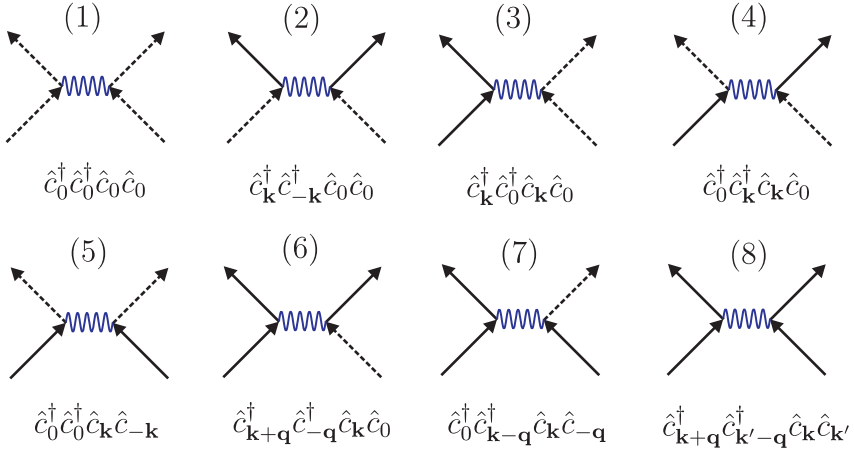


Figure 4.2. By singling out the contribution of the $k = 0$ condensate mode c_0 there are eight distinct processes of the interaction in momentum space: (1) Two condensate particles elastically scatter off each other. (2) Two particles are excited out of the condensate. (3) A condensate particle undergoes an elastic interaction with an excited particle. (4) The absorption of an excited particle into the condensate simultaneous with the a particle being excited out of it. In the case of a purely contact (on-site) interaction process (3) and (4) contribute to the same term. (5) Two excited particles are absorbed into the condensate. (6) A condensate particle undergoes an inelastic scattering with an excited particle resulting in it being excited out of the condensate. (7) Two excited particles inelastically scatter resulting with the absorption of one of them into the condensate. (8) Two excited particles elastically scatter of each other. Note that there are no processes involving three condensate particles due to momentum conservation.

with respect to an average $\langle \cdot \rangle$ over states of the form $|N_0, \dots\rangle$, vanishes in the thermodynamic limit $N, M \rightarrow \infty$, with N/M and $N_0/N = f_0$ fixed. This commutativity identifies the operators \hat{c}_0^\dagger and \hat{c}_0 (or more precisely their quadratures $\hat{X} = \frac{1}{2}(\hat{c}_0 + \hat{c}_0^\dagger)$ etc., in analogy with photons) as having weak quantum fluctuations, and suggests that we may replace them by (classical) c-numbers, $\hat{c}_0^\dagger \mapsto \langle \hat{c}_0^\dagger \rangle$, typical of a mean-field approach. Moreover since $N_0 \neq 0$ this means that $\langle \hat{c}_0^\dagger \rangle \neq 0$. Such a replacement has significant consequences to the underlying state which we now approximate the system with. Specifically, our ansatz for the ground state will be based on treating the zero-momentum contribution as *classically* as possible by using a state which minimises quantum fluctuations. To achieve this we do not permit any entanglement between the zero-momentum and excited states by using a product form $|\Psi_{\text{bog}}\rangle = |\Psi_0\rangle \otimes |\Psi_{\text{ex}}\rangle$, where $|\Psi_0\rangle$ is a state entirely within the zero-momentum sector, and $|\Psi_{\text{ex}}\rangle$ is a state in the remaining $\mathbf{k} \neq 0$ sectors. Secondly, to fully embody our requirement for classicality we choose the single-mode state $|\Psi_0\rangle$ to be a coherent state, which are well known to

possess $\langle \hat{c}_0^\dagger \rangle \neq 0$ and minimise (and also equalise) the quadrature fluctuations [14]. For the non-interacting case, where $N = N_0$, this approximates⁷ the ground state as [11]

$$\begin{aligned} |\Psi_{GP}\rangle &= \exp(-\frac{1}{2}N_0) \exp(\sqrt{N_0}\phi \hat{c}_0^\dagger) |\text{vac}\rangle, \\ &= \exp(-\frac{1}{2}N_0) \prod_{j=1}^M \exp(\sqrt{N_0/M}\phi \hat{b}_j^\dagger) |\text{vac}\rangle, \end{aligned} \quad (4.3)$$

and generates a non-zero average $\langle \hat{c}_0^\dagger \rangle = \sqrt{N_0}e^{i\phi}$. A non-trivial feature of this ansatz is that $\langle \hat{c}_0^\dagger \rangle \neq 0$ necessitates that $|\Psi_0\rangle$ is composed of a *coherent* superposition of different occupation numbers of the condensate which in turn makes $|\Psi_{\text{bog}}\rangle$ have an indefinite total particle number. Another entirely related consequence is that our description of the system is compelled to “choose” a phase ϕ and therefore break the $U(1)$ symmetry of the BHM⁸. These facts highlight that de-correlating comes at the expense of the conservation of the total number of bosons. From a practical viewpoint the introduction of states familiar to quantum optics [16] considerably simplifies the mathematics in comparison to explicitly particle-number conserving approaches. In the thermodynamic limit the predictions about the mean values of quantities from the conserving and non-conserving approach will agree since the fractional boson number fluctuations vanish. For the non-interacting case $|\Psi_{GP}\rangle$ can be seen to give equivalent results as the Fock ground state $|\Psi_{\text{gs}}\rangle$. Specifically, $\Delta \hat{n}_0 / \langle \hat{n}_0 \rangle = 1/\sqrt{N_0}$ and $|\Psi_{GP}\rangle$ is a product of site-wise coherent states giving $\langle \hat{n}_j \rangle = N_0/M = n_0$ and a Poisson number distribution for all sites j . Additionally, $|\Psi_{GP}\rangle$ likewise predicts that $\langle \hat{b}_i^\dagger \hat{b}_j \rangle = n_0$ is constant for all i and j .

Since we have dispensed with the conservation of the total boson number \hat{N} in order to keep the density of the system under control we constrain $\langle \hat{N} \rangle$ by introducing a Lagrange multiplier μ representing the chemical potential in the grand canonical ensemble. We then proceed to implement the factorisation of the interacting ground state by *freezing* the zero-momentum contribution in a coherent state

$$|\Psi_0\rangle = \exp(-\frac{1}{2}|\alpha|^2) \exp(\alpha \hat{c}_0^\dagger) |0\rangle,$$

where $|0\rangle$ is the zero-occupancy Fock state for mode \hat{c}_0 . The amplitude α and μ are related by minimising the energy function in the zero-momentum sector

$$\begin{aligned} E_0(\alpha) &= \langle \Psi_0 | \hat{H}_0 - \mu \hat{n}_0 | \Psi_0 \rangle, \\ &= (-zJ - \mu)|\alpha|^2 + \frac{U}{2M}|\alpha|^4. \end{aligned}$$

Upon minimising, and discarding the trivial $|\alpha| = 0$ solution, the relation between μ and the condensate density $n_0 = |\alpha|^2/M$ is established as $\mu = Un_0 - zJ$. This

⁷This is essentially the Gross-Pitaevskii approximation.

⁸The existence of a condensate phase has a great deal of phenomenological significance for a BEC’s superfluid and interference properties. However, the connection between the phase ϕ and that seen experimentally is not trivial. We shall take $\phi = 0$ without loss of generality [15].

expression has a sensible interpretation as the energy needed to add one particle to the condensate⁹. The energy of the system is increased due to interactions with the n_0 particles in each site already, and decreased due to the particle potentially hopping to one of the z nearest neighbours. As of yet we have not placed any constraints on the form of $|\Psi_{\text{ex}}\rangle$ and in particular our treatment of the zero-momentum state was special and cannot be similarly applied to any other momentum states. In fact to determine $|\Psi_{\text{ex}}\rangle$ we first form an effective quadratic Hamiltonian \hat{H}_{eff} defined over the $\mathbf{k} \neq 0$ momentum sectors by taking a partial expectation value (i.e. of the zero-momentum sector only) $\hat{H}_{\text{eff}} = \langle \Psi_0 | \hat{H}_{\text{trunc}} | \Psi_0 \rangle$ giving

$$\hat{H}_{\text{eff}} = -\frac{1}{2}U n_0 N_0 + \sum_{\mathbf{k} \neq 0} \left[(\bar{\epsilon}_{\mathbf{k}} - U n_0) \hat{c}_{\mathbf{k}}^\dagger \hat{c}_{\mathbf{k}} + \frac{1}{2}U n_0 \left(\hat{c}_{\mathbf{k}}^\dagger \hat{c}_{-\mathbf{k}}^\dagger + 4\hat{c}_{\mathbf{k}}^\dagger \hat{c}_{\mathbf{k}} + \hat{c}_{\mathbf{k}} \hat{c}_{-\mathbf{k}} \right) \right],$$

once the expression for μ has been inserted and $\bar{\epsilon}_{\mathbf{k}} = \epsilon_{\mathbf{k}} + zJ$ is defined. As expected from this formalism the H_{eff} contains non-particle-conserving terms like $\hat{c}_{\mathbf{k}} \hat{c}_{-\mathbf{k}}$. We then proceed to diagonalise \hat{H}_{eff} using the well known Bogoliubov transformation [11, 17]. This begins by introducing a new set of creation and annihilation operators for $\mathbf{k} \neq 0$

$$\begin{aligned} \hat{a}_{\mathbf{k}} &= u_{\mathbf{k}} \hat{c}_{\mathbf{k}} - v_{\mathbf{k}} \hat{c}_{-\mathbf{k}}^\dagger, \\ \hat{a}_{\mathbf{k}}^\dagger &= u_{\mathbf{k}} \hat{c}_{\mathbf{k}}^\dagger - v_{\mathbf{k}} \hat{c}_{-\mathbf{k}}, \end{aligned} \quad (4.4)$$

which are a judicious admixture of our original creation and annihilation operators with quasi-momentum \mathbf{k} and $-\mathbf{k}$ described by real symmetric amplitudes $u_{\mathbf{k}}$ and $v_{\mathbf{k}}$. We firstly demand that this transformation is canonical so the new operators $\hat{a}_{\mathbf{k}}$ continue to obey bosonic commutation relations. This imposes the constraint

$$u_{\mathbf{k}}^2 - v_{\mathbf{k}}^2 = 1,$$

and implies that we can express these amplitudes in terms of a single parameter $\beta_{\mathbf{k}}$ as $u_{\mathbf{k}} = \cosh(\beta_{\mathbf{k}})$ and $v_{\mathbf{k}} = \sinh(\beta_{\mathbf{k}})$. Next, we insert the new operators into the effective Hamiltonian and choose the parameter $\beta_{\mathbf{k}}$ such the effective Hamiltonian takes on the diagonal form

$$\hat{H}_{\text{eff}} = \sum_{\mathbf{k} \neq 0} \omega_{\mathbf{k}} \hat{a}_{\mathbf{k}}^\dagger \hat{a}_{\mathbf{k}} + \varepsilon_0,$$

with an excitation spectrum $\omega_{\mathbf{k}}$ and ground state energy ε_0 . In this case the new operators $\hat{a}_{\mathbf{k}}$ describe non-interacting quasi-particle¹⁰ excitations of the system. The ground state $|\Psi_{\text{ex}}\rangle$ of H_{eff} is then by definition the state which contains no quasi-

⁹This agrees with the formal definition $\mu = (\partial E / \partial N)_{S,V}$ since the system remains in a pure state, so its entropy S is not changed from zero, and the volume V is kept constant.

¹⁰The prefix *quasi* signifies that the new creation operators $\hat{a}_{\mathbf{k}}^\dagger$ do not create a physical particle but instead create a collective excitation of the system in which many physical particles participate.

particles [11, 17]

$$\hat{a}_{\mathbf{k}} |\Psi_{\text{ex}}\rangle = 0, \quad \text{for all } \mathbf{k} \neq 0,$$

and therefore specifies the quasi-particle vacuum. Notice that whenever $v_{\mathbf{k}} \neq 0$ this property can only be fulfilled if $|\Psi_{\text{ex}}\rangle$ differs from the state with zero-occupancy for $\mathbf{k} \neq 0$ and hence must contain some depletion from the condensate. After using the identities $\cosh(2x) = \cosh^2(x) + \sinh^2(x)$ and $\sinh(2x) = 2\cosh(x)\sinh(x)$ we find that this diagonalisation is achieved when $\beta_{\mathbf{k}}$ satisfies

$$(\bar{\epsilon}_{\mathbf{k}} + Un_0) \sinh(2\beta_{\mathbf{k}}) + Un_0 \cosh(2\beta_{\mathbf{k}}) = 0,$$

giving the solution

$$\tanh(2\beta_{\mathbf{k}}) = -\frac{Un_0}{\bar{\epsilon}_{\mathbf{k}} + Un_0}.$$

Then, by solving the diagonal contribution

$$Un_0 \sinh(2\beta_{\mathbf{k}}) + (\bar{\epsilon}_{\mathbf{k}} + Un_0) \cosh(2\beta_{\mathbf{k}}) = \omega_{\mathbf{k}},$$

explicit expressions for the spectrum, amplitudes and ground state energy can be deduced as [11, 17]

$$\begin{aligned} \omega_{\mathbf{k}} &= \sqrt{\bar{\epsilon}_{\mathbf{k}}(\bar{\epsilon}_{\mathbf{k}} + 2Un_0)}, \\ u_{\mathbf{k}}^2 = v_{\mathbf{k}}^2 + 1 &= \frac{1}{2} \left(\frac{\bar{\epsilon}_{\mathbf{k}} + Un_0}{\omega_{\mathbf{k}}} + 1 \right), \\ \varepsilon_0 &= -\frac{1}{2} Un_0 N_0 - \frac{1}{2} \sum_{\mathbf{k} \neq 0} (\bar{\epsilon}_{\mathbf{k}} + Un_0 - \omega_{\mathbf{k}}). \end{aligned}$$

These results reveal that the gapless excitation spectrum seen in the non-interacting case in the thermodynamic limit persists in the presence of interactions. However, in contrast to the non-interacting case in the limit $|\mathbf{k}|a \ll 1$ it takes the linear form

$$\omega_{\mathbf{k}} \approx a\sqrt{J}|\mathbf{k}| \sqrt{Ja^2|\mathbf{k}|^2 + 2Un_0} \approx c|\mathbf{k}|.$$

These long-wavelength excitations correspond to quantised density waves in the compressible boson fluid, called phonons, which propagate at the speed of sound $c = a\sqrt{2Un_0J}$. As we shall discuss shortly it is expected that at unit filling in the strongly interacting regime (where $U/J \rightarrow \infty$) the system will become insulating, which is characterised by the system becoming incompressible and having a gapped spectrum. Since the Bogoliubov spectrum permits excitations with an arbitrarily small energy regardless of the value of U/J it is already clear that it cannot describe an insulator [17]. Despite this the essential features of the Bogoliubov approximation, namely the existence of a depleted condensate and phonon-like excitations, are expected to persist beyond its range of applicability as the insulating phase is approached.

As already mentioned a significant new feature of the Bogoliubov approach is the quantum depletion of the condensate. While the population of $\mathbf{k} \neq 0$ states increases the kinetic energy of the system the expulsion of pairs from the condensate is energetically favourable since it reduces the overall interaction energy. The occupancy of the $\mathbf{k} \neq 0$ states in the interacting ground state is

$$\langle \Psi_{\text{bog}} | \sum_{\mathbf{k} \neq 0} \hat{b}_{\mathbf{k}}^\dagger \hat{b}_{\mathbf{k}} | \Psi_{\text{bog}} \rangle = \langle \Psi_{\text{bog}} | \sum_{\mathbf{k} \neq 0} v_{\mathbf{k}}^2 \hat{a}_{\mathbf{k}} \hat{a}_{\mathbf{k}}^\dagger | \Psi_{\text{bog}} \rangle = \sum_{\mathbf{k} \neq 0} v_{\mathbf{k}}^2,$$

and thus the total particle number N is set by

$$N = N_0 + \frac{1}{2} \sum_{\mathbf{k} \neq 0} \left(\frac{\bar{\epsilon}_{\mathbf{k}} + U n_0}{\omega_{\mathbf{k}}} - 1 \right). \quad (4.5)$$

The condensate density n_0 can then be obtained by solving Eq. (4.5) for a fixed value of N . In Fig. 4.3(a)-(b) we plot the numerically determined condensate fraction f_0 for a unit filled lattice with a weak interaction $U/J = 0.1$. These results show that for a 1D lattice, in Fig. 4.3(a), f_0 decreases monotonically to zero with the systems size M , whereas for a 2D lattice of size $M \times M$ lattice f_0 saturates to a finite value close to unity with increasing M . This behaviour can be confirmed more rigourously [17] by taking the thermodynamic limit where the sum in Eq. (4.5) is replaced by an integral. It can then be shown that for 1D this integral exhibits an infrared divergence¹¹ for any $U/J > 0$, while in 2D it always converges to a finite value [17]. This result indicates that in the thermodynamic limit a Bose condensed ($n_0 \neq 0$) solution exists for a 2D lattice, but not for a 1D one, in accordance with the Mermin-Wagner-Hohenberg theorem [18, 19]. In Fig. 4.3(c) the condensate fraction f_0 is evaluated numerically for a large unit-filled 2D lattice with increasing U/J . The onset of an insulating phase is characterised by the complete depletion of the condensate and a phase transition should then appear as f_0 vanishing at some finite value of U/J . In Fig. 4.3(c) f_0 is seen to be non-zero even in the strongly interacting regime. Indeed the asymptotic behaviour of the 2D integral shows that $\lim_{U/J \rightarrow \infty} f_0 = 0$ and therefore confirms our earlier suspicions that the Bogoliubov approximation does not predict a phase transition [17].

Finally, we now complete our description of the structure of the ground state within this approximation [14]. Following the decoupling of the zero-momentum sector the Bogoliubov ground state can be expressed as $|\Psi_{\text{bog}}\rangle = \hat{U}_0 \otimes \hat{U}_{\text{ex}} |\text{vac}\rangle$ where \hat{U}_0 and \hat{U}_{ex} are unitary transformations acting on the $\mathbf{k} = 0$ and $\mathbf{k} \neq 0$ momentum sectors respectively. Since $|\Psi_0\rangle$ was fixed as a coherent state \hat{U}_0 is simply a displacement transformation [16]. The form of \hat{U}_{ex} follows from the requirement of the Bogoliubov ground state to be the quasi-particle vacuum $\hat{a}_{\mathbf{k}} |\Psi_{\text{bog}}\rangle = 0$. For this to be satisfied \hat{U}_{ex} must be the same unitary as that which implements the Bogoliubov transformation in Eq. (4.4) through $\hat{a}_{\mathbf{k}} = \hat{U}_{\text{ex}} \hat{c}_{\mathbf{k}} \hat{U}_{\text{ex}}^\dagger$ and subsequently diagonalises \hat{H}_{eff} . This then fixes

¹¹This illustrates the importance of the long-wavelength contributions in 1D.

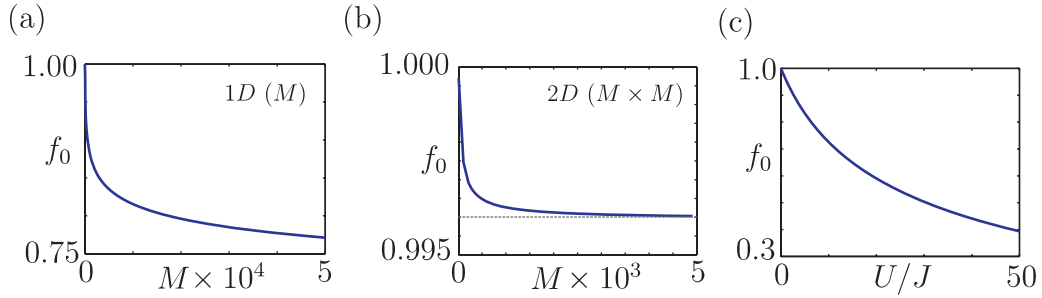


Figure 4.3. (a) For a 1D lattice of length M with $U/J = 0.1$ and unit filling the condensate fraction f_0 is plotted with increasing M . A monotonic decrease in f_0 with M is observed. (b) The same calculation as (a) but with a 2D lattice of size $M \times M$. Here only a very moderate depletion is seen and f_0 saturates to a non-zero value with increasing M . (c) For a unit filled 2D lattice of size 1000×1000 f_0 is plotted with increasing U/J . No critical point, where $f_0 = 0$, is observed within this approximation.

Bogoliubov ground state as [14]

$$|\Psi_{\text{bog}}\rangle = \exp(-\frac{1}{2}|\alpha|^2) \exp(\alpha \hat{c}_0^\dagger) \otimes \prod_{\mathbf{k} \neq 0} \exp\left(\frac{1}{2}\zeta_{\mathbf{k}} \hat{c}_{\mathbf{k}}^\dagger \hat{c}_{-\mathbf{k}}^\dagger\right) |\text{vac}\rangle, \quad (4.6)$$

where $\zeta_{\mathbf{k}} = \tanh(\beta_{\mathbf{k}})$ and the factor of $\frac{1}{2}$ accounts for \mathbf{k} and $-\mathbf{k}$ contributions within the product. On this basis the form of \hat{U}_{ex} in Eq. (4.6) coincides with a product of two-mode squeezing transformations between pairs of momentum states $\pm\mathbf{k}$, well known from quantum optics [16]. For two generic modes \mathbf{a} and \mathbf{b} the action of this operator is

$$\exp[-\tanh(r)\hat{\mathbf{a}}^\dagger \hat{\mathbf{b}}^\dagger] |0_{\mathbf{a}}, 0_{\mathbf{b}}\rangle = \text{sech}(r) \sum_{n=0}^{\infty} [-\tanh(r)]^n |n_{\mathbf{a}}, n_{\mathbf{b}}\rangle.$$

Thus, a sensible feature of two-mode squeezing, in the context of momentum conservation, is that it generates an entangled state between the modes \mathbf{a} and \mathbf{b} through the superposition of states only where both modes contain the same number of bosons.

The weakly interacting limit is said to be the superfluid phase of the BHM. Before moving on to the strongly interacting limit we now take a minor digression into the properties of superfluidity in order to shed some light onto this identification.

4.1.3 Superfluidity

Superfluidity is not really a single phenomenon but rather it is several complex inter-related phenomena. Much of the quantitative understanding of superfluidity follows from Landau's two-fluid theory which postulates that the superfluid component carries zero entropy and flows irrotationally, while the normal component behaves like

a conventional viscous fluid [20]. This essential phenomenology of superfluidity is now attributed to the presence of a BEC described by a complex order parameter $\chi(\mathbf{r}) = |\chi(\mathbf{r})|e^{i\theta(\mathbf{r})}$. The corresponding superfluid velocity for bosons of mass m is then defined as $m\mathbf{v}_s(\mathbf{r}) = \nabla\theta(\mathbf{r})$ which is manifestly irrotational ($\nabla \times \mathbf{v}_s = 0$), and the macroscopic occupancy of a single-particle state provides a zero-entropy component. Since the phase $\theta(\mathbf{r})$ must be single-valued modulo 2π this leads to the Onsager-Feynman quantisation condition $\oint \mathbf{v}_s \cdot d\mathbf{s} = n/(2\pi m)$, with n a non-negative integer, for superfluid circulation within a non-simply-connected geometry (such as a ring) [11, 20]. There are a large number of important physical consequences of these properties, however, here we limit our focus to the two conceptually simplest properties, namely a non-classical rotational inertia and the metastability of superflow.

Non-classical rotational inertia

Let us imagine that we have a fluid trapped in a ring of radius R between two cylinders which are synchronously rotating at some small angular frequency ω . A normal fluid will come to equilibrium with a velocity ωR with an angular momentum $I_{\text{cl}}\omega$ where $I_{\text{cl}} = NmR^2$ is the classical rotational inertia, due to viscosity and friction with the container walls. If we now cool the fluid¹² to below its critical point T_c a non-zero superfluid component appears and moves with velocity \mathbf{v}_s . However, \mathbf{v}_s is constrained by the quantisation condition and in general cannot take the value ωR . Instead it takes a circulation quantum n which is the closest integer to ω/ω_c , where $\omega_c = 1/mR^2$ is the angular frequency corresponding to $n = 1$. For $\omega \ll \omega_c$ this is evidently zero and the superfluid component no longer contributes to the circulating current. This phenomenon appears as a reduction in the fluid's angular momentum (i.e. non-classical rotational inertia) which can be *reversibly* altered with temperature T and tends to zero as $T \rightarrow 0$ [21, 22]. The superfluid fraction f_s is then defined as the fraction of the fluid's mass which is not rotating with the container [20, 14]. A remarkable consequence of this quantised circulation is the Hess-Fairbank effect where for larger ω , say $\omega = \frac{3}{4}\omega_c$, the apparent velocity of the fluid may actually exceed that of the containers.

To relate this situation to the BHM let us now consider a 1D lattice connected in a ring geometry as shown in Fig. 4.4(a). If we rotate this ring at a frequency ω the BHM becomes “twisted” due to the appearance¹³ of so-called Peierls phase factors on the kinetic terms [23, 24, 25]

$$\hat{H}_{\Delta\theta} = -J \sum_{j=1}^M \left(e^{i\Delta\theta} \hat{b}_j^\dagger \hat{b}_{j+1} + e^{-i\Delta\theta} \hat{b}_{j+1}^\dagger \hat{b}_j \right) + \frac{1}{2}U \sum_i \hat{n}_i(\hat{n}_i - 1), \quad (4.7)$$

where $M\Delta\theta = 2\pi R^2 m \omega$. The twisted BHM therefore encodes the response of the system to a small rotational perturbation [26, 27, 28, 29]. Given the above description

¹²This could be done before or while it is rotating. The latter would ensure we remain in equilibrium.

¹³Physically these phase factors arise from the $\vec{\omega} \times \vec{r}$ vector potential acquired after moving to the frame rotating with the lattice. This is analogous to the Aharonov-Bohm effect for charged particles when a magnetic flux penetrates the ring.

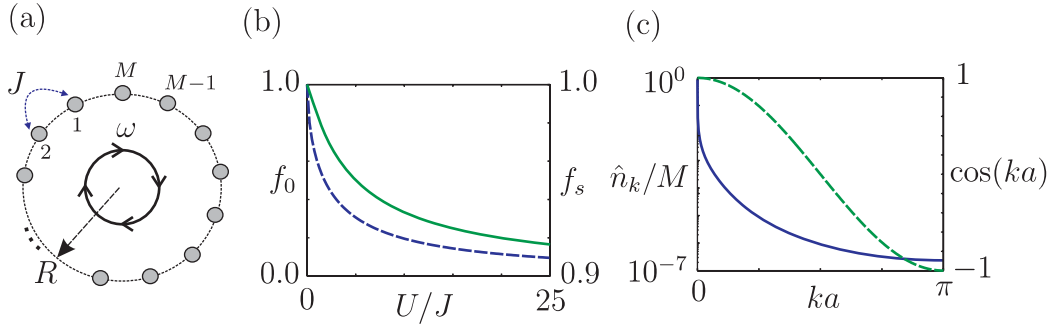


Figure 4.4. (a) A 1D lattice with M sites arranged as a ring which is then rotated at a frequency ω . (b) For a $M = 1000$ ring the condensate fraction f_0 (dotted line, left axis) and superfluid fraction f_s (solid line, right axis) are plotted against U/J . Note the differing scales on these two axes. (c) For $U/J = 0.1$ the momentum-density distribution \hat{n}_k/M (solid line, left axis) and $\cos(ka)$ (dashed line, right axis) are plotted against the quasi-momentum ka .

it is sensible to attribute the difference between the resulting ground state energies $E_{\Delta\theta} - E_0$ of the twisted and uniform system, respectively, for small twists $M\Delta\theta \ll \pi$, to the kinetic energy of a superfluid component [26]. Specifically we set

$$E_{\Delta\theta} - E_0 = \frac{1}{2}Nf_s m v_s^2.$$

We now assume that the superfluid accommodates this phase twist by having a phase $\theta(\mathbf{r})$ which varies linearly across the ring as $\theta_j = j\Delta\theta$, and consequently gives rise to a uniform superfluid velocity $m v_s = \Delta\theta/a$. Using $J \equiv 1/(2ma^2)$ the basic relation for the superfluid fraction is [24]

$$f_s = \frac{1}{M} \frac{E_{\Delta\theta} - E_0}{J(\Delta\theta)^2}.$$

This then gives a very appealing definition of the superfluid fraction as the “rigidity” of the system to a phase twist [26]. After expanding phase factors in Eq. (4.7) to 2nd order in $\Delta\theta$ the twisted Hamiltonian is approximately given by

$$\hat{H}_{\Delta\theta} \approx \hat{H}_{\text{BH}} + \Delta\theta \hat{J} - \frac{1}{2}(\Delta\theta)^2 \hat{T},$$

where $\hat{J} = iJ \sum_j (\hat{b}_j^\dagger \hat{b}_{j+1} - \hat{b}_{j+1}^\dagger \hat{b}_j)$ is the current operator for bosons in the lattice, while $\hat{T} = -J \sum_j (\hat{b}_j^\dagger \hat{b}_{j+1} + \hat{b}_{j+1}^\dagger \hat{b}_j)$ is the standard kinetic operator in the BHM. By evaluating the energy difference $E_{\Delta\theta} - E_0$ using second-order perturbation theory, and retaining

terms up to second-order in $\Delta\theta$, the superfluid fraction can be expressed¹⁴ as [23, 24]

$$\begin{aligned} f_s &= f_s^{(1)} - f_s^{(2)}, \\ f_s^{(1)} &= -\frac{1}{2MJ} \left(\langle \Psi_0 | \hat{T} | \Psi_0 \rangle \right), \\ f_s^{(2)} &= \frac{1}{MJ} \left(\sum_{\nu \neq 0} \frac{|\langle \Psi_\nu | \hat{J} | \Psi_0 \rangle|^2}{E_\nu - E_0} \right). \end{aligned} \quad (4.8)$$

Here $|\Psi_0\rangle$ is the ground state of the BHM while $|\Psi_\nu\rangle$ with ($\nu = 1, 2, \dots$) are its excited states with energy E_ν . Since $f_s^{(2)}$ depends intricately on the excitation spectrum and the nature of the excited states it is not simply a ground state calculation. Evidently to evaluate Eq. (4.8) we must employ further approximations. Within the Bogoliubov approximation for a translationally invariant system $f_s^{(2)}$ vanishes and we are left with the compact expression [24, 30]

$$f_s = f_s^{(1)} = \frac{M}{N} \left[n_0 + \frac{1}{M} \sum_k v_k^2 \cos(ka) \right]. \quad (4.9)$$

For the two most obvious limits this expression gives physically sensible results. Specifically for a non-interacting system, where $v_k^2 = 0$ for all k , the superfluid fraction and condensate fraction coincide as $f_s = n_0 = 1$. In the opposite case¹⁵ where all quasi-momentum states are equally occupied so $v_k^2 = 1$ for all k (giving a uniformly filled band) solving Eq. (4.5) yields $n_0 = 0$ and the $\cos(ka)$ contributions in Eq. (4.9) cancel perfectly giving $f_s = 0$. This shows that Eq. (4.9) correctly predicts an insulator in this limit. In Fig. 4.4(b) the condensate fraction f_0 and superfluid fraction f_s are plotted together for increasing interaction strength U/J . This shows that within this approximation the presence of depletion has weaker effect on the superfluidity and exemplifies the fact that these two fractions represent genuinely distinct quantities¹⁶. This is certainly consistent with the archetypal superfluid, ${}^4\text{He}$, which due to strong interactions exhibits depletion on the order of 90% while nearly all the atoms contribute to its superfluidity. As can be seen in Fig. 4.4(c) the difference between the two fractions for weak-interactions arises because the depletion populates quasi-momentum states close to $k = 0$ and these states continue to make a positive contribution to f_s due to the $\cos(ka)$ factor in Eq. (4.9). While at stronger interactions the contributions from large quasi-momenta, where $\cos(ka)$ is negative, will reduce f_s the Bogoliubov approximation can never induce the perfect cancellation seen for an insulator consistent with our earlier discussions.

¹⁴Note that \hat{J} never contributes to the 1st order correction since all ground states of the (non-twisted) BHM have zero current. Also since the contribution of \hat{T} is of order $(\Delta\theta)^4$ it is not included.

¹⁵We note here that technically we should use both $f_s^{(1)}$ and $f_s^{(2)}$ to examine the insulator limit. Indeed, insulating behaviour is manifested by the strong cancellation of these two contributions.

¹⁶Indeed, by including sufficiently strong on-site disorder in the BHM superfluidity can be completely suppressed while leaving a non-zero condensate fraction [31].

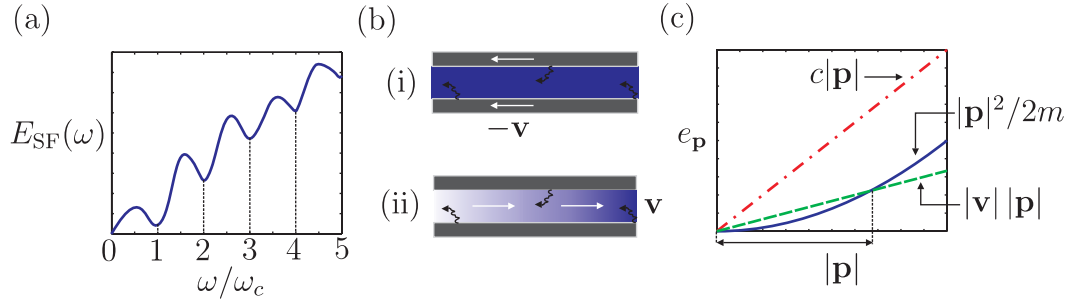


Figure 4.5. (a) A schematic plot of the energy $E_{SF}(\omega)$ of a superfluid circulating with an angular frequency ω . The presence of minima at multiples of the critical angular frequency ω_c results in the metastability of superflow. (b) A superfluid flowing through a narrow tube (i) in the fluid's rest frame and (ii) in the laboratory frame. The wavy lines represent quasi-particle excitations caused by scattering off the walls. (c) A plot of the Bogoliubov spectrum ω_p (dashed-dotted line), non-interacting spectrum ϵ_p (solid line) and $\mathbf{p} \cdot \mathbf{v}$ (dashed line) for $|\mathbf{v}| = \frac{1}{3}c$. Notice that for the non-interacting spectrum for any $|\mathbf{v}| > 0$ a finite range of $|\mathbf{p}|$ exists in which $\mathbf{p} \cdot \mathbf{v}$ is larger than ϵ_p , showing that the generation of excitations is always energetically favourable. In contrast this only occurs for the Bogoliubov spectrum when $|\mathbf{v}| \geq c$.

An important point about the rigidity property of superfluidity is that we have characterised it by examining the nature of the system in thermodynamic equilibrium (for $T = 0$ above) under new slowly rotating (twisted) condition. However, by using purely equilibrium quantities a non-vanishing f_s cannot say anything about the dynamical stability of superflow with a non-zero superfluid velocity v_s . It is on this basis that we move to the second superfluid property, which is an intrinsically dynamical non-equilibrium phenomenon.

Metastability of superflow

Perhaps the most familiar characteristic of superfluidity is the persistence of circulation showing dissipation-less flow. To set up such a current we again rotate a normal fluid and then cool it below T_c . This time, however, we rotate much faster with $\omega \gg \omega_c$ and as such the superfluid component will possess a sizable quantum of circulation. Finally, still keeping the temperature below T_c , we stop the rotation of the container. Since the state of the system in thermal equilibrium has zero current, the circulating superfluid corresponds to an excited state. What is found experimentally is that the superfluid preserves its circulation, despite not being in equilibrium, for what is effectively an infinite time. The circulating superfluid states must therefore be separated from the state with vanishing current by energy barriers, as shown in Fig. 4.5(a), which are much larger than the relevant thermal energy making them metastable [20, 14].

Unlike the superfluid fraction f_s there is no general formalism for determining if metastable superflow is possible. However, we may motivate why superfluids exhibit

dissipation-less flow by appealing to an ingenious phase-space argument by Landau [11, 13]. Suppose we have a fluid of mass M flowing at velocity \mathbf{v} through a narrow tube. A normal fluid experiences excitations, corresponding to friction, as a result of random scattering of fluid particles off the (atomically) rough walls. When the fluid is in its ground state and viewed from its rest-frame as in Fig. 4.5(b)(i), its energy is E_g^0 and its momentum is $\mathbf{P}_0 = 0$. Moving to the laboratory frame¹⁷, shown in Fig. 4.5(b)(ii), its energy and momentum become $E_g = E_g^0 + \frac{1}{2}M\mathbf{v}^2$ and $\mathbf{P} = M\mathbf{v}$, respectively. In the rest-frame the walls of the tube will appear as a time-dependent perturbation which may create quasi-particle excitations with energy e_p and momentum \mathbf{p} in the fluid. If one such quasi-particle is formed then the energy becomes $E^0 = E_g^0 + e_p$ and $P_0 = \mathbf{p}$. Back in the laboratory frame the energy and momentum of the excited fluid are

$$E = E_g^0 + e_p + \mathbf{p} \cdot \mathbf{v} + \frac{1}{2}M\mathbf{v}^2, \quad \text{and} \quad \mathbf{P} = \mathbf{p} + M\mathbf{v},$$

from which we identify the excitation energy in the laboratory frame as $\Delta E = e_p + \mathbf{p} \cdot \mathbf{v}$. Evidently the fluid flow will be unstable to the creation of quasi-particle excitations if $\Delta E < 0$. The $\mathbf{p} \cdot \mathbf{v}$ contribution has its largest negative value when \mathbf{p} and \mathbf{v} are antiparallel so the excitation retards the flow, and this occurs whenever $|\mathbf{v}| > e_p/|\mathbf{p}|$. The critical velocity of flow v_c is then

$$v_c = \min_{|\mathbf{p}|} \left(\frac{e_p}{|\mathbf{p}|} \right),$$

and depends delicately on the precise form of the excitation spectrum. For the non-interacting BHM, which has a quadratic spectrum $\epsilon_p = Ja^2|\mathbf{p}|^2 - zJ$, this yields $v_c = 0$, which may seem surprising given that we found that $f_s = 1$. This can be seen to be a pathology of the non-interacting limit since for any $U > 0$ the Bogoliubov spectrum $\omega_p = c|\mathbf{p}|$ yields a non-zero critical velocity $v_c = c$, with $c \rightarrow 0$ as $U \rightarrow 0$. These results are summarised graphically in Fig. 4.5(c). Thus, combined with $f_s \approx 1$ the weakly interacting limit of the BHM can be seen to possess the essential properties of superfluidity.

Finally, we note that from a more phenomenological perspective one might further include the occurrence of quantised vortices as a signature of superfluidity. Under this definition a bona fide superfluid can only exist in two dimensions and higher, however we shall continue to use the term superfluidity in the sense laid out above which does apply to 1D.

4.2 Strongly interacting limit - Mott Insulator

4.2.1 The $J = 0$ limit

We now examine the corresponding limit of strong interactions where $J/U \rightarrow 0$. In this case the BHM decouples as a sum of identical single-site Hamiltonians which are

¹⁷We change our reference frame by performing a Galilei transformation.

diagonal in the number basis. In the grand-canonical ensemble¹⁸ the non-degenerate ground state is easily deduced as a number state $|g\rangle$, where g is an integer valued function of μ/U defined as

$$g(\mu/U) = \begin{cases} 0, & \text{for } \mu/U < 0, \\ 1, & \text{for } 0 < \mu/U < 1, \\ 2, & \text{for } 1 < \mu/U < 2, \\ & \vdots \\ g, & \text{for } g-1 < \mu/U < g. \end{cases}$$

Notice that the definition of $g(\mu/U)$ excludes when μ/U is exactly equal to a positive integer. For reasons which will become clear shortly these values are called degeneracy points. For $g-1 < \mu/U < g$ the ground state of the system is the Fock state¹⁹

$$|\psi_{g\text{-gs}}^{(0)}\rangle = \prod_{j=1}^M \frac{1}{\sqrt{g!}} (\hat{b}_j^\dagger)^g |\text{vac}\rangle = |g, g, \dots, g\rangle, \quad (4.10)$$

with precisely the same number of bosons g on every site and an energy $E_{\text{gs}}^{(0)} = \frac{U}{2} Mg(g-1) - \mu Mg$. The number g jumps discontinuously whenever μ/U passes through a degeneracy point, whereupon we have regions where

$$\frac{\partial \langle \hat{N} \rangle}{\partial \mu} = 0,$$

signalling that the density does not change under variations of the chemical potential. For this reason the state is incompressible²⁰ [3] and since this property is caused by strong interactions, as opposed to energy bands, it is called a Mott insulator (MI).

The lowest-lying excitations of the MI state are those which change the overall particle number by either adding or removing a particle from the system called particle and hole excitations respectively [32, 33]. Each type of excitation is M -fold degenerate and has the general form

$$\begin{aligned} |\psi_{g\text{-p}}^j\rangle &= \frac{1}{\sqrt{g+1}} \hat{b}_j^\dagger |\psi_{g\text{-gs}}^{(0)}\rangle, \\ |\psi_{g\text{-h}}^j\rangle &= \frac{1}{\sqrt{g}} \hat{b}_j |\psi_{g\text{-gs}}^{(0)}\rangle, \end{aligned} \quad (4.11)$$

possessing energies $E_p = Ug - \mu$ and $E_h = U(1-g) + \mu$, with μ in the range $g-1 \leq \mu/U \leq g$. Consequently these excitations are separated from the ground state by a

¹⁸We add the chemical potential term $-\mu \sum_j \hat{n}_j$ to \hat{H}_{BH} when using the grand-canonical ensemble.

¹⁹For the ground state only we introduce a superscript (0) to signify that it is both a $J=0$ solution and the zeroth-order approximation in J/U to the exact ground state for small non-zero J .

²⁰This is definition compressibility arises from what is called the “electronic compressibility” which is used to describe the metallic-insulator transition in solid-state systems.

gap which vanishes when μ/U hits a degeneracy point. As this name suggests when $\mu/U = g$ the states $|\psi_{g\text{-p}}\rangle$, $|\psi_{g+1\text{-h}}\rangle$ and $|\psi_{g\text{-gs}}^{(0)}\rangle$ are degenerate and the resulting ground state is compressible²¹.

The lowest-lying excitations of the MI state, which conserve the total particle number, are Fock states with $g + 1$ bosons at one site i and $g - 1$ bosons at another site j , with all other sites having g bosons as

$$|\psi_{g\text{-ph}}^{ij}\rangle = \frac{1}{\sqrt{g(g+1)}} \hat{b}_i^\dagger \hat{b}_j |\psi_{g\text{-gs}}^{(0)}\rangle.$$

These type of states are called particle-hole (ph) excitations [32, 33, 30] and there are $M(M-1)$ of them in total. In a translationally-invariant system they are all degenerate and possess an energy $E_{\text{ph}} = U$ above the ground state. The presence of this gap in the excitation spectrum is another characteristic property of the MI state. The overall structure of the (particle-number conserving) MI excitation spectrum, shown in Fig. 4.6(a), is a sequence of increasingly degenerate manifolds, sometimes called Hubbard bands, which are separated from the ground state by integer multiples of the interaction energy U . So, for example, the $2U$ manifold is composed of states with two separate ph-excitations, while the $3U$ manifold contains states with three separate ph-excitations as well as states with two-particle-hole excitations where both particles are on the same site, also depicted in Fig. 4.6(a).

Small J limit

Let us now consider the effects of a small non-zero hopping J and determine which of these properties are maintained. Since the kinetic energy term is a total-particle-number conserving perturbation which respects the translational invariance to first order it mixes the $|\psi_{g\text{-gs}}^{(0)}\rangle$ with the manifold of ph-excitations, giving the correction

$$|\psi_{g\text{-gs}}^{(1)}\rangle = \left(|\psi_{g\text{-gs}}^{(0)}\rangle + \frac{J}{U} \sqrt{2Mg(g+1)} |\mathbf{S}\rangle \right),$$

where $|\mathbf{S}\rangle$ is the normalised translationally invariant superposition of all ph-excitations with the particle and hole on adjacent sites, which in 1D is [30]

$$|\mathbf{S}\rangle = \frac{1}{\sqrt{2M}} \sum_{j=1}^M (|\psi_{g\text{-ph}}^{j-1,j}\rangle + |\psi_{g\text{-ph}}^{j,j+1}\rangle).$$

The perturbative parameter in the correction to the ground state is $\frac{Jg}{U}\sqrt{M}$ and so its validity becomes more restricted with increasing lattice size. Since the hopping terms are entirely off-diagonal in the number basis the first order correction to the ground state energy vanishes leaving a second order correction $E_{\text{gs}}^{(2)} = -\frac{2J^2M}{U}g(g+1)$.

²¹The system is compressible since the lowest-lying degenerate states differ in total particle number.

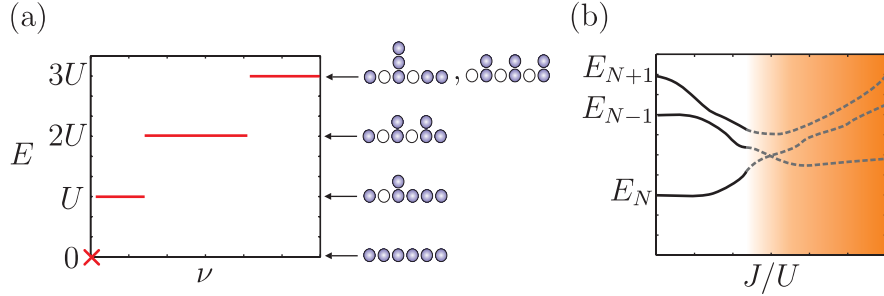


Figure 4.6. (a) The excitation spectrum of a perfect ($J = 0$) MI. The excited states ν form Hubbard bands separated by the interaction energy U . To the right a depiction of the type of excitations, particle-hole pairs etc., in each Hubbard band is shown. (b) The schematic evolution of the the ground state energies for N , $N + 1$ and $N - 1$ particles with increasing J/U . Due to the gap for a finite range of J/U there will be no level crossings between ground states with differing particle numbers for a finite (unshaded) region of J/U .

A number of important results are immediately available from $|\psi_{g\text{-gs}}^{(1)}\rangle$. The quasi-momentum distribution to first order is found to be

$$\langle \hat{n}_k \rangle = g + \frac{4J}{U} g(g+1) \cos(ka),$$

where k is the quasi-momentum. Notice that at zeroth order the quasi-momentum distribution of a MI is flat with all quasi-momentum states of the lowest band uniformly filled, in contrast to the superfluid regime where the bosons occupy quasi-momentum states around $\mathbf{k} = 0$. To first order in J/U particle-hole fluctuations are taken into account which generate short-ranged nearest-neighbour coherence in the MI ground state. The signature of these is the cosinusoidal modulation of the distribution. Importantly, because of the symmetrical form of the particle-hole fluctuations in $|\mathbf{S}\rangle$ the average occupancy of any site for $|\psi_{\text{gs}}^{(1)}\rangle$ continues to be $\langle \hat{n}_j \rangle = g$. Thus, perturbation theory indicates that the density pinning seen at $J = 0$ survives $J > 0$ to lowest order. In contrast to the $J = 0$ ground state, however, the on-site particle number fluctuations become non-zero to second order as [30]

$$\Delta n = \frac{4J^2}{U^2} g(g+1),$$

again signifying that the MI ground state is never a Fock state for $J > 0$. This highlights that it is the incompressibility property which is the defining characteristic of a MI and not the emergence of a Fock state [10].

Generic MI-superfluid phase diagram

The observations from perturbation theory can be expanded into an exact result which proves that the MI phase exists [3, 4]. Away from the degeneracy points at $J = 0$ the ground state is non-degenerate with a gap separating it from all other excited states. Depending on the value of μ , the closest excited state will be either a particle or hole excitation which change the total number of particles. By slowly turning on J the ground state will transform adiabatically and the presence of a gap guarantees that no level crossings will occur so long as J is sufficiently small, as depicted in Fig. 4.6(b). Since the ground state at $J = 0$ was an eigenstate of \hat{N} with eigenvalue $Mg(\mu/U)$ and the perturbation caused by the hopping term also commutes with \hat{N} it will remain an eigenstate with the precisely same eigenvalue even for small non-zero J . This proves that there exists of a finite region of the $\mu-J$ phase diagram where the expectation value of the density remains pinned at the quantised value g . These regions are called MI lobes and within them both the incompressibility and the energy gap to all excitations seen in the $J = 0$ limit persist [3, 4].

Quite generally the boundaries of the MI phase occur when the MI ground state becomes degenerate with its lowest-lying particle or hole excitations, since this point signifies the onset of compressibility and instability of the MI state [32, 33]. The lobe-like shape of the MI phase can be understood by using the zeroth order ($J = 0$) approximation to the MI ground state and its excitations for all $J > 0$. This amounts to fixing the MI ground state within the lobe to be $|\Psi_{g\text{-gs}}\rangle = |\psi_{g\text{-gs}}^{(0)}\rangle$ and in turn makes its energy expectation value independent of J . For non-zero J the resulting mobility breaks most of the M -fold degeneracy in the particle- and hole-excitation manifolds²² resulting in the lowest-lying excitations of both manifolds being non-degenerate as

$$|\Psi_{g\text{-p}}\rangle = \frac{1}{\sqrt{M}} \sum_{j=1}^M |\psi_{g\text{-p}}^j\rangle \quad \text{and} \quad |\Psi_{g\text{-h}}\rangle = \frac{1}{\sqrt{M}} \sum_{j=1}^M |\psi_{g\text{-h}}^j\rangle.$$

The nature of these excitations demonstrate that when $J \neq 0$ the mobility of the additional particle or hole causes them to Bose condense into the $k = 0$ Bloch state of the lattice. This is equivalent to treating the particle or hole as a non-interacting boson completely delocalised on top of a frozen MI. The energies of these two excitations above the MI ground state are $E_p = Ug - \mu - zJ(g + 1)$ and $E_h = U(1 - g) + \mu - zJg$ where $z = 2d$ is the number of nearest neighbours in d -dimensions. Importantly these energies depend on J since they include the first-order contribution of the kinetic energy terms. The MI boundaries occur at points where either $E_p = 0$ or $E_h = 0$ which signifies that the kinetic energy gained by adding a Bose condensed particle or hole precisely balances the on-site interaction and potential energies. By using the phase rigidity definition of section 4.1.3 the states $|\Psi_{g\text{-p}}\rangle$ and $|\Psi_{g\text{-h}}\rangle$ can be shown to possess a non-zero superfluid fraction f_s and so degeneracy with these states is indicative of crossing into the superfluid phase. This approximation then predicts the particle and hole

²²Since the particle and hole excitations are degenerate we diagonalise the kinetic terms in these subspaces to determine the appropriate zeroth order combination to use.

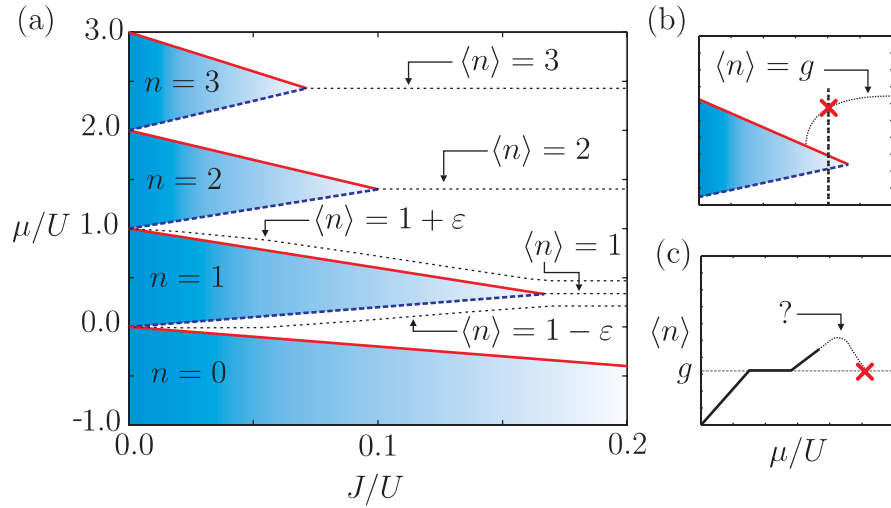


Figure 4.7. (a) The phase diagram of the BHM in 1D ($z = 2$) calculated to first-order in J/U . The shaded regions are the MI lobes labelled with their corresponding density, while the unshaded regions are SF. The lobes are delineated by (solid) particle-excitation boundaries, and (dashed) hole-excitation boundaries. The dotted lines schematically represent density contours. The tip of the $n = 1$ lobe is located at $zJ/U = \frac{1}{3}$. (b) A depiction of the situation if the $\langle n \rangle = 1$ contour intersected the MI lobe somewhere other than the tip. The dashed line represents a line of constant J/U through the vicinity of the tip of a MI lobe. (c) The density $\langle n \rangle$ as a function of μ conjectured to occur along the line shown in (b). Notice that the placement of the $\langle n \rangle = 1$ contour in (b) necessitates a negative compressibility.

branches²³ of the boundaries as

$$(\mu/U)_{\pm} = \frac{1}{2} \{2g - 1 - (zJ/U) \pm [1 - (2g + 1)(zJ/U)]\}.$$

The tip of the MI lobe occurs when the particle and hole branches of the phase boundary meet which for this approximation gives $(J/U)_c = 1/z(2g + 1)$. Despite its crudeness a number of important observations are already clear from this phase diagram. Firstly, the lobe-like shape occurs due to the decreasing width of the MI phase with increasing J . What's more the size of the lobes decreases with increasing g due to the bosonic enhancement of the kinetic energy of an additional hole or particle. The shape of the lobes is also slightly asymmetrical due to the intrinsic asymmetry between particles and holes seen in their definition Eq. (4.11). Notice also that these boundaries are correct to first order in J/U and therefore asymptotically correct as $J \rightarrow 0$. In the case of the boundary for the vacuum insulator, which is determined by a one particle calculation, the result is exact.

²³For convenience we shall signify particles by (+) and holes by (−) at several points from now on.

In addition to the MI lobes Fig. 4.7(a) also shows schematically the expected contours of constant density $\langle n \rangle$. At the MI phase boundary a non-zero compressibility is re-established and so the density $\langle n \rangle$ will change as a function μ . Compressibility must be non-negative so $\langle n \rangle$ must increase as the particle branch of the phase boundary is passed through, and correspondingly decrease through the hole branch. An immediate consequence of this is that all non-integer density contours must lie entirely within the superfluid phase, skirting around the MI lobes and terminating at an appropriate degeneracy point. Thus in a homogeneous system the superfluid-insulator transition only appears for commensurate filling of the lattice. Additionally this also indicates that away from integer densities the superfluid phase extends down to arbitrarily small J in the vicinity of the degeneracy points. Of particular importance are the lines of integer density $\langle n \rangle = g$ which are seen to meet the phase boundary at the tip of each MI lobe. It is straightforward to see that this has to be the case [3]. If instead the $\langle n \rangle = g$ contour intersected elsewhere on a lobe, as depicted in Fig. 4.7(b), then the density $\langle n \rangle$ as a function of μ taken through a cut at fixed J in the vicinity of the tip, as shown in Fig. 4.7(c), would necessarily yield a negative compressibility. No stable system can have a negative compressibility so the $\langle n \rangle = g$ must intersect the tip.

The density contours also reveal that there are two different MI to superfluid transitions [3]. At a generic point on the phase boundary the transition is driven by the addition or removal of particles from the MI resulting in a continuous change in density from an integer value as the superfluid phase is entered. This picture of the transition has formed the basis of our understanding of the phase diagram thus far. However, at the tip of the lobe the transition occurs at fixed density and is governed by quite different physics. Here the onset of superfluidity is instead driven purely by an increasing kinetic contribution to the energy. When J becomes sufficiently large the bosons can overcome the on-site interaction, breaking the localisation, and hop throughout the lattice. These differences are reflected in the fact that the transition at the tip belongs to the universality class of the $(D + 1)$ -dimensional XY model, whereas the generic transition does not [3]. In 1D, as we shall discuss in more detail in section 4.3, this means that the transition at the tip is a Berezinskii-Kosterlitz-Thouless (BKT) type transition.

4.2.2 Gutzwiller ansatz and decoupled mean-field theory

We have seen how working from the superfluid regime the Bogoliubov approach fails to predict a phase transition, while working from the MI regime a crude first-order estimation of the phase diagram can be constructed. Here we consider a computationally simple ansatz for the state of the system, and a corresponding mean-field theory, which does predict a phase transition and improves upon these earlier methods.

The Gutzwiller ansatz

The approach we take here is based on the observation that at $J = 0$ the MI ground state in Eq. (4.10) is a site-wise product, and similarly that at $U = 0$ the superfluid

ground state in Eq. (4.1) can be considered to be equivalent to a site-wise product of coherent states in Eq. (4.3). This suggests that it may be plausible to approximate the ground state of the system for arbitrary J/U in between these two limits by a translationally invariant site-wise product state of the form

$$|\Psi_{\text{GW}}\rangle = \prod_{j=1}^M \left(\sum_{n=0}^{\infty} c_n |n\rangle_j \right),$$

where c_n are the amplitudes for the on-site number states $|n\rangle$ [34, 35]. Restriction to this type of bosonic state is typically called a Gutzwiller ansatz due to its parallels with the fermionic Gutzwiller projection method. The best approximation within this ansatz for the ground state of the BHM is then found by treating the amplitudes c_n as variational parameters which are determined by minimising the energy function

$$\begin{aligned} E_{\text{GW}}(\{c_n\}) &= \frac{1}{M} \langle \Psi_{\text{GW}} | \hat{H}_{\text{BH}} - \mu \sum_j \hat{n}_j | \Psi_{\text{GW}} \rangle \\ &= -zJ|\Phi|^2 + \sum_n \left[\frac{U}{2}(n^2 - n) - \mu n \right] |c_n|^2, \end{aligned} \quad (4.12)$$

where we have defined the order parameter Φ as

$$\Phi = \langle \Psi_{\text{GW}} | \hat{b}_j | \Psi_{\text{GW}} \rangle = \sum_{n=1}^{\infty} c_{n-1}^* \sqrt{n} c_n.$$

This minimisation can be performed analytically [34, 35] by using some appropriate parameterisation of c_n , or numerically [36] with standard methods once an occupancy cut-off is introduced²⁴.

There are several important consequences which result from approximating the ground state of the BHM by an ansatz which completely neglects entanglement between different sites. The simplest is that the only states possessing a definite total particle number within this ansatz are Fock states. Moreover continuity with the $J = 0$ limit means that the entire MI phase is also described by a Fock state. Contrary to our earlier findings this correspondingly predicts vanishing number fluctuations throughout the MI phase. It is then clear that within this ansatz the phase transition will manifest itself through the sudden appearance of states which have an indefinite total particle number²⁵. These states violate the $U(1)$ symmetry of the original BHM and their presence is signalled by a non-zero order parameter Φ which can already be seen to play a crucial role in the energy function Eq. (4.12) above. Within this approximation the transition is also reflected in the local number distribution which changes sharply

²⁴While truncating the number basis does introduce an error in to the calculation it is easily controlled. Generally the cut-off will need to be larger for smaller U/J .

²⁵We can, of course, overcome this by projecting the resulting state $|\Psi_{\text{GW}}\rangle$ on to the subspace with fixed total particle number, but this makes the resulting calculations significantly more complicated.

from being Poissonian-like to a delta function (i.e. Fock state) which is contrary to the exact theory (in finite dimensions) where it is known that such local variables change smoothly through the transition [10, 37].

Another significant limitation of this description is that all p -point correlation functions factorise [37] so, for example, the single-particle density matrix is

$$\rho_{ij} = \langle \Psi_{\text{GW}} | \hat{b}_i^\dagger \hat{b}_j | \Psi_{\text{GW}} \rangle = \langle \Psi_{\text{GW}} | \hat{b}_i^\dagger | \Psi_{\text{GW}} \rangle \langle \Psi_{\text{GW}} | \hat{b}_j | \Psi_{\text{GW}} \rangle = |\Phi|^2,$$

and therefore cannot display any distance dependence. In this way the Gutzwiller ansatz embodies the simplest characterisation of a generic order-disorder transition. The MI is then the disordered phase described by symmetric states with $\Phi = 0$ yielding no off-diagonal correlations since $\rho_{ij} = 0$ for all $|i - j| \neq 0$. In contrast the superfluid is the ordered phase described by broken-symmetric states with $\Phi \neq 0$ so $\rho_{ij} = |\Phi|^2$, independent of $|i - j|$, resulting in long-range order. As we shall see shortly, while this description does describe a phase transition, it fails to capture some of the more subtle physics of the superfluid-Mott insulator transition.

Decoupled mean-field theory

The Gutzwiller ansatz is in fact entirely equivalent to special type of mean-field theory for the BHM. In contrast the Bogoliubov approach this mean-field theory treats the interaction exactly and instead approximates the kinetic energy terms of H_{BH} . To achieve this the kinetic energy terms are decoupled as²⁶

$$\hat{b}_i^\dagger \hat{b}_j = \langle \hat{b}_i^\dagger \rangle \hat{b}_j + \hat{b}_i^\dagger \langle \hat{b}_j \rangle - \langle \hat{b}_i^\dagger \rangle \langle \hat{b}_j \rangle = \Phi \hat{b}_i^\dagger + \Phi^* \hat{b}_j - |\Phi|^2,$$

with $\langle \cdot \rangle$ being (at $T = 0$) the ground state average. Notice that we have tacitly assumed that $\langle \hat{b}_i \rangle$ is non-zero and after assuming further that it is homogeneous the order parameter $\Phi = \langle \hat{b}_i \rangle$ enters the theory as a mean-field describing the influence of hopping between neighbouring sites. This decoupling then leaves an effective Hamiltonian $\hat{H}_{\text{eff}} = \sum_j \hat{H}_{\text{MF}}$ which is a sum of identical single-site Hamiltonians²⁷

$$\hat{H}_{\text{MF}} = -zJ(\Phi \hat{b}^\dagger + \Phi^* \hat{b}) + zJ|\Phi|^2 + \frac{U}{2}\hat{n}(\hat{n} - 1),$$

which continue to share the translational symmetry of the original BHM, however the introduction of Φ again signifies that the $U(1)$ symmetry is broken. The ground state $|\psi_{\text{eff}}\rangle$ of \hat{H}_{eff} is a site-wise product of the ground state $|\psi_{\text{MF}}(\Phi)\rangle$ of \hat{H}_{MF} with energy $E_{\text{MF}}(\Phi)$. The ground state $|\psi_{\text{MF}}(\Phi)\rangle$ can be determined very straightforwardly by numerical diagonalisation of \hat{H}_{MF} once an appropriate occupancy cut-off is introduced [38]. The value of Φ is then determined self-consistently by minimising $E_{\text{MF}}(\Phi)$

²⁶We note in passing that this decoupling has a rigorous basis within the functional integral representation of the BHM partition function. Here a complex field Φ is naturally introduced by performing a Hubbard-Stratanovich transformation on the kinetic terms and after assuming it is homogeneous and taking the saddle point approximation of the action the Hamiltonian H_{eff} is obtained [38, 3, 4].

²⁷We drop the site index j for this reason.

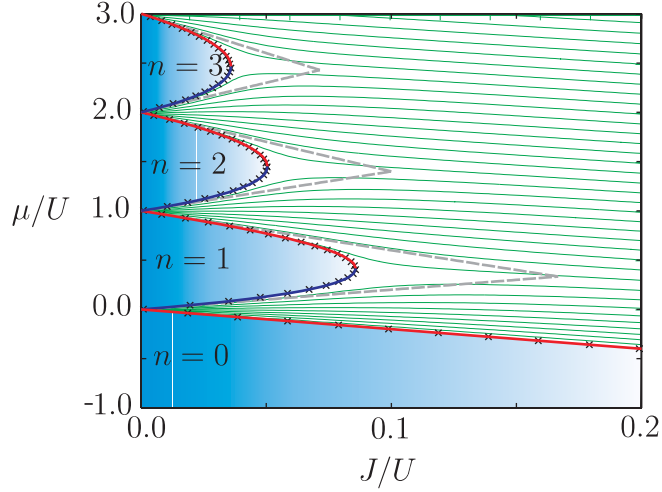


Figure 4.8. The mean-field phase diagram of the BHM in 1D ($z = 2$). The shaded regions are the MI lobes labelled with their corresponding density, while the unshaded regions are SF. The lobes are delineated by the analytical curves (solid) and by the numerically determined boundary points (\times). The first order estimation of the MI lobes are also included (dashed lines) for comparison. The fine lines in the background are lines of constant density. These are seen to skirt around the MI lobes and have a downwards slope. The tip of the $n = 1$ MI lobe is located at $zJ/U \approx 0.17$ in mean-field theory, which is roughly half that of the first-order calculation.

with respect to Φ . Notice that $|\psi_{\text{eff}}\rangle$ is precisely a Gutzwiller state so this minimisation could proceed by computing $\langle\Psi_{\text{GW}}|\hat{H}_{\text{eff}} - \mu \sum_j \hat{n}_j|\Psi_{\text{GW}}\rangle$. In fact the resulting energy function is identical to Eq. (4.12) found from the full BHM Hamiltonian \hat{H}_{BH} so the minimisation of the Gutzwiller ansatz state is equivalent to determining the ground state of the on-site Hamiltonian \hat{H}_{MF} in the number basis [38].

The advantage of the mean-field formulation is that a number of important properties can be determined analytically [17]. In particular the phase boundaries predicted by this mean-field theory can be found by applying second-order perturbation theory with respect to the order parameter Φ within \hat{H}_{MF} . Specifically, we take Φ as real (without loss of generality) and then set $\hat{H}_{\text{MF}} - \mu n = \hat{H}^{(0)} + \Phi \hat{H}_{\text{pert}}$ giving

$$\begin{aligned}\hat{H}^{(0)} &= zJ\Phi^2 + \frac{U}{2}\hat{n}(\hat{n} - 1) - \mu\hat{n}, \\ \hat{H}_{\text{pert}} &= -zJ(\hat{b}^\dagger + \hat{b}),\end{aligned}$$

where the mean-field contribution of hopping is treated as the perturbation. To zeroth order the ground state energy is identical to the $J = 0$ case considered earlier with $E_{\text{gs}}^{(0)} = \frac{U}{2}g(g-1) - \mu g$ and eigenstates of $\hat{H}^{(0)}$ are Fock states. Since \hat{H}_{pert} is off-diagonal in the number basis the first order correction vanishes. The second order correction is

composed of two contributions [17]

$$E_{\text{gs}}^{(2)} = \frac{zJg}{U(g-1) - \mu} + \frac{zJ(g+1)}{\mu - Ug},$$

reflecting the fact that \hat{H}_{pert} couples the ground state to excited states with one more or one less boson. Combining these results we now write the ground state energy as an expansion in Φ as

$$E_{\text{gs}}(\Phi) = a_0(g, U, \mu) + a_2(g, U, \mu)\Phi^2 + O(\Phi^4),$$

and following the Landau procedure minimise it with respect to Φ . With the usual ‘Mexican hat’ picture it is clear that if $a_2(g, U, \mu) > 0$ then $\Phi = 0$ is the minimum, whereas if $a_2(g, U, \mu) < 0$ the minimum has $\Phi \neq 0$. Thus, the boundary between the superfluid and insulator phases is equivalent to $a_2(g, U, \mu) = 0$. Solving this equation then gives the two branches of the boundary as [17]

$$(\mu/U)_{\pm} = \frac{1}{2} \left[2g - 1 - (zJ/U) \pm \sqrt{1 - 2(2g+1)(zJ/U) + (zJ/U)^2} \right].$$

The tip of the lobes is then given by equating the two boundary curves and is given by

$$(J/U)_c = \frac{1}{z(2g+1 + \sqrt{4g^2 + 4g})},$$

which is significantly reduced in comparison to our earlier first-order estimate. The phase diagram calculated with this mean field theory is shown in Fig. 4.8. From this we see that it results in MI lobes with rounded tips which lie squarely within the first-order MI lobes. Also by computing the density contours we find agreement with our earlier expectations, but do find in addition that lines of constant density slope downwards with increasing J . Overall we may interpret the fact that this particular mean-field theory predicts any transition as a sign that the interaction is the dominant contributor to it.

In addition to the phase boundaries by using functional integral methods [17] the particle and hole dispersions within this mean-field theory can be determined as

$$\Delta_{\mathbf{k}}^{\pm} = \frac{1}{2}U(2g-1) - \mu - \frac{1}{2}\epsilon_{\mathbf{k}} \pm \frac{1}{2}\sqrt{\epsilon_{\mathbf{k}}^2 - (4g+2)U\epsilon_{\mathbf{k}} + U^2}.$$

A first-order approximation of the dispersion of ph-excitations can be found by subtracting the two solutions [17]

$$\Delta_{\mathbf{k}} = \sqrt{\epsilon_{\mathbf{k}}^2 - (4g+2)U\epsilon_{\mathbf{k}} + U^2}.$$

In the limit $U/J \gg 1$ this gives a cosinusoidal ph-band $\Delta_k = U - 2J(2g+1) \cos(ka)$ in 1D, shown in Fig. 4.9(a), essentially describing free particle-hole pairs. This result is also consistent with that obtained by directly diagonalising the kinetic energy terms

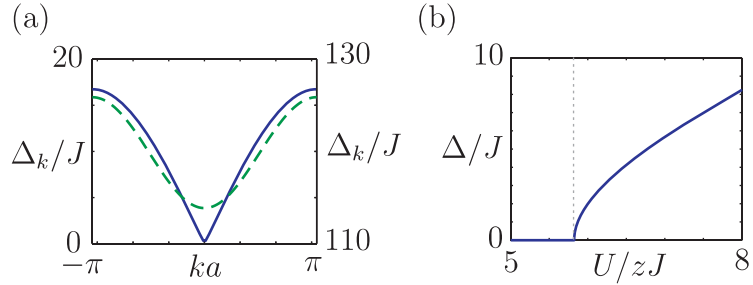


Figure 4.9. (a) The particle-hole dispersion Δ_k for a 1D system. The solid line (left axis) is for $U/J = 11.66$ which is very close to the mean-field transition, while the dotted line (right axis) is for $U/J = 120$ deep in the MI phase. (b) The gap $\Delta = \Delta_{k=0}$ between the MI ground state and lowest-lying particle-hole excitation as a function of U/zJ . Note that it vanishes (dotted line) at the mean-field critical point $U/zJ \approx 5.83$ as expected.

in the particle-hole subspace (i.e. first-order perturbation theory), and as expected $\Delta_k \rightarrow E_{\text{ph}} = U$ when $J \rightarrow 0$. As U/J becomes smaller the ph-band shape changes, also shown in Fig. 4.9(a), with the gap Δ between $k = 0$ state and the MI ground state closing. In Fig. 4.9(b) this gap is plotted as a function of U/J and seen to vanish precisely at the mean-field transition point found earlier. Overall this mean-field calculation reveals the expected picture that the MI possess a gap, and shows that the system does indeed go from a gapped to gapless phase at the mean-field critical point. From our analysis of the superfluid regime we then expect the dispersion relation below the transition to be linear, and therefore phonon-like.

We shall now comment on the general validity of this mean-field approach. Firstly, like all mean-field theories it becomes more accurate in higher dimensions as formally expressed in the Ginzburg criterion. The intuition behind this is that when more degrees of freedom are involved in the interaction (or in our case hopping) the relevant averaged quantities on any single site fluctuate less about their mean value. In fact the decoupled mean-field theory can be shown to be exact in the limit of infinite dimensions in the thermodynamic limit [3]. From a more practical perspective it is found that for the BHM in a 3D simple cubic lattice ($z = 6$) the predicted critical point $(U/J)_c \approx 35$ is reasonably close to the recently determined numerical result $(U/J)_c \approx 29.36$ which was calculated with Quantum Monte-Carlo methods to an accuracy of 0.1% [39]. There are, however, strong deviations from mean-field theory in lower dimensions, most especially in 1D. This failure of mean-field theory can be understood as a consequence of the significant quantum fluctuations (and at finite temperature thermal fluctuations also) present in low-dimensional system which destroy the ordered phase earlier than predicted. Despite this, however, the qualitative structure of the BHM phase diagram has been found to be well captured by this mean-field theory.

4.3 Refinements for one-dimension

We can obtain some quite general conclusions about the BHM in 1D by examining the continuum model of interacting bosons in the presence of a lattice potential. In the special case of 1D the boson field operators $\hat{\Psi}(x)$ of the continuum system can be uniquely expressed in terms of the density operator $\hat{\rho}(x)$ and phase operator $\hat{\Phi}(x)$ as $\hat{\Psi}(x) = \sqrt{\hat{\rho}(x)}e^{i\hat{\Phi}(x)}$ following Haldane's prescription for Luttinger liquids [40, 41]. Without a periodic potential the low-energy physics of this system is described by the basic Hamiltonian

$$\hat{H}_0 = \frac{1}{2\pi} \int dx \left\{ vK[\hat{\Pi}(x)]^2 + \frac{v}{K}[\partial_x \hat{\Phi}(x)]^2 \right\},$$

where $\hat{\Pi}(x)$ is the operator of density fluctuations, v is the speed of sound and K is the Luttinger parameter. One of the essential features of Luttinger liquid theory is that \hat{H}_0 is an effective low-energy description which is the fixed point of any gapless phase of bosons, regardless of the underlying microscopic Hamiltonian, provided the correct parameters v and K are used [41]. Thus \hat{H}_0 equally well describes the superfluid phase of the 1D BHM. Utilising the full machinery of this approach²⁸ reveals that the Luttinger parameter controls the decay of correlation functions. Of particular importance are the off-diagonal correlations in the one-particle density matrix which are found to exhibit power-law decay as

$$\langle \hat{b}_i^\dagger \hat{b}_j \rangle = A \left(\frac{\alpha}{|i-j|} \right)^{K/2} + \dots,$$

where A is a non-universal amplitude and α is the cut-off introduced to regularise the theory at short distances [41]. By exhibiting a power-law decay we see that an interacting superfluid in 1D does not possess long-range order, and is instead usually referred to as quasi-long-range order. For a non-interacting system $K = 0$ and off-diagonal-long-range order is reestablished. To describe the transition from this superfluid phase to a MI a periodic potential is added to H_0 via the term

$$\hat{H}_L = V \int dx \cos(2p \hat{\Phi}(x) - \delta x),$$

where V is the strength of the potential, p is the order of commensurability ($p = 1$ here) and δ is doping. The introduction of this term has a significant effect to the total Hamiltonian $\hat{H}_B = \hat{H}_0 + \hat{H}_L$ by making it non-quadratic. In the case where $\delta = 0$, so there is no doping and the system is commensurately filled, \hat{H}_B is equivalent to the sine-Gordon Hamiltonian [41]. The analysis of \hat{H}_B proceeds by varying the cut-off α to eliminate the short-range degrees of freedom. This yields a set of renormalisation equations which establish how K and V must vary in order for the long-distance physics to be invariant. As might be expected two regions of parameters arise in which either \hat{H}_0

²⁸We shall not do so here since this is beyond the scope of this thesis.

or \hat{H}_L is dominant and in this way a phase diagram for \hat{H}_B can be derived. Moreover, since the resulting renormalisation equations are identical [41, 3] to those of the 2D XY problem they reveal that \hat{H}_B contains a BKT transition at $T = 0$ driven by variations in K shown in Fig. 4.10(a). The BKT critical point is then found to occur at $K_c = \frac{1}{2}$, with the regime $K < K_c$ being superfluid, while above the critical point K jumps discontinuously from K_c to $K = \infty$ producing the incompressible MI phase with gap Δ and exponentially decaying correlations

$$\langle b_i^\dagger b_j \rangle = B e^{-|i-j|/\xi} + \dots,$$

where the correlation length $\xi = v/\Delta$. The phase diagram for \hat{H}_B is shown in Fig. 4.10(a) and depicts the transition found by following the density contour $\langle n \rangle = 1$ (or any other integer) in the full 1D BHM phase diagram. By including doping the commensurate to incommensurate transition can be described. Importantly the presence of a $\delta \neq 0$ breaks the equivalence of \hat{H}_B with the 2D XY model and so the resulting critical phenomenon is not of BKT form. Instead it is found that $K_c = 1$ for transitions across the boundaries of the MI lobe [41, 3].

By utilising these general features density-matrix-renormalisation-group (DMRG) calculations [42, 43] have been able to accurately locate the superfluid-MI phase boundary in 1D as the point at which the exponent of the power-law decay of correlations intersects with the critical values K_c given above. This has revealed that the MI lobes have a very long and narrow tip consistent with the exponential closing of the gap Δ for a BKT transition. This tip points downwards in agreement with the downward sloping density contours seen in the mean-field calculation earlier. This BKT-point is found to be located at $(U/zJ) = 1.68$. Thus as J is decreased from some initially large value we find that in 1D the superfluid is destabilised into a MI significantly earlier than mean-field theory predicts. In addition to this the resulting 1D phase diagram also displays a surprising feature not seen in higher dimensions, namely a reentrance phase transition [42, 43]. This can be understood by considering the density along a line of constant μ . If we now choose a μ not too far above the BKT point (see dashed line in Fig. 4.10(b)) and increase J from some point within the MI lobe a transition in the superfluid phase is made where the density $\langle n \rangle < 1$. If we continue $\langle n \rangle$ will eventually increase until it hits $\langle n \rangle = 1$ again, whereupon the MI phase is reentered and so paradoxically an increased kinetic energy has re-stabilised an insulator (see Fig. 4.10(c)). Increasing J further will lead to another transition to the superfluid phase, this time with $\langle n \rangle > 1$, and the density increases monotonically with J from there on. This reentrance transition is essentially a consequence of the long narrow tips of the 1D MI lobe and the downward slope of the density contours.

4.4 Trapped systems

Earlier we saw how the superfluid to MI transition in a homogeneous system only occurs for integer densities. This situation is not substantially altered by use of open (or box) boundary conditions rather than the periodic boundary we have consider up

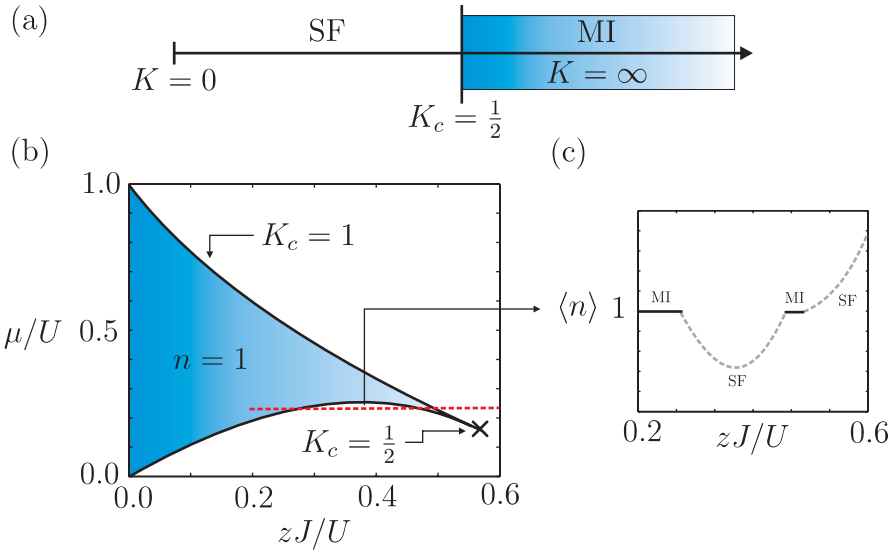


Figure 4.10. (a) The phase diagram of H_B , when commensurate, showing the essential feature of the BKT transition. (b) A schematic plot of the phase diagram around the $n = 1$ MI lobe for the 1D BHM adapted from DMRG calculations. A line of constant μ is drawn (dashed line) to illustrate a path in which the reentrance transition would occur. The BKT-point is depicted by the ‘ \times ’ and occurs at $zJ/U \approx 0.59$. Notice that following the $\langle n \rangle = 1$ density contour in (b) yields the phase diagram in (a). (c) The resulting change in the density $\langle n \rangle$ as zJ/U is increased along the path shown in (a). The reentrance transition is signalled by the appearance of the MI density plateaus twice.

to now. However, in the presence of harmonic trapping the nature of the ground state is dramatically altered and the realisation of the MI phase is far less restrictive. To include harmonic trapping the following term is added to \hat{H}_{BH}

$$\hat{H}_{\text{trap}} = \sum_{j=1}^M \epsilon_j \hat{n}_j + \frac{\Omega}{2} \sum_{j=1}^M (j - c)^2 \hat{n}_j,$$

where $\Omega = ma^2\omega_T^2$ with ω_T being the trap with frequency and c being the central site. The influence of this trapping can be determined by using a local density approximation where the trapping itself is combined with the overall μ to define a local chemical potential $\mu_j = \mu - \epsilon_j$. Suppose that at the centre μ_c is located in the $n = 2$ MI lobe. Now by moving towards the boundary of the trap μ_j decreases in value. The local density approximation then predicts that the characteristics of each site j will be determined by the phase in which μ_j is located in the mean field phase diagram. Thus a sequence of MI domains separated by superfluid regions is expected to occur as the trap potential is climbed. The incompressibility of the MI phase should then yield regions where the density remains constant despite the rising potential. In this way

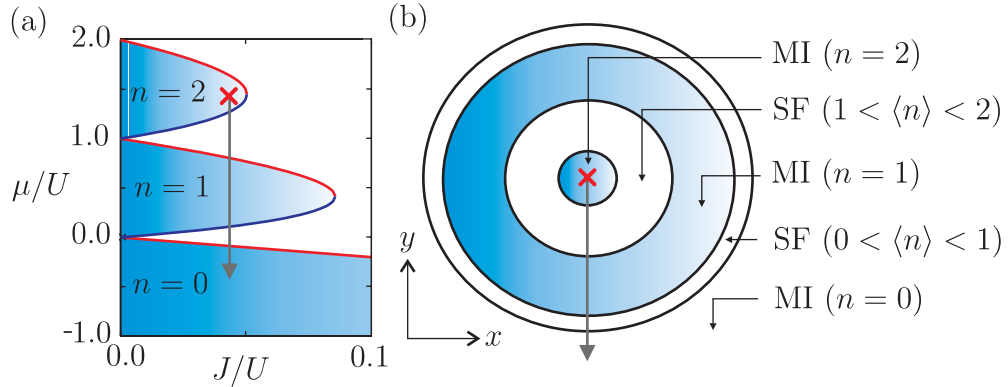


Figure 4.11. (a) The mean-field phase diagram introduced earlier with the addition of a line of constant zJ/U which represents the sequence of local chemical potentials μ_j encountered in a trapped system. (b) From the μ_j depicted in (a) the predicted wedding-cake 2D density profile composed of successive MI and superfluid phases in coexistence is shown.

the coexistence of different phases should be observed yielding a ‘wedding-cake’ density profile. The qualitative validity of this picture is supported by accurate DMRG [44] and quantum Monte-Carlo calculations [45, 46, 47, 48] in 1D and 2D/3D, respectively. In addition examples of trapped ground states in 1D will also be presented in the following two chapters.

Finally, we note that the presence of a trap modifies the Hubbard picture of excitations above the MI that was introduced earlier [30]. For example in 1D, at some appropriate U and μ the zeroth order ground state of a trapped system will be composed of a unit-filled central MI core of N boson as

$$|\psi_{\text{MI}}^{(0)}\rangle = |0, 0, \dots, \overbrace{1, 1, \dots, 1}^N, 1, \dots, 0, 0\rangle.$$

In this case the MI domain is surrounded by a ‘sea of holes’. As in the translationally invariant case the MI core possesses ph-exitations within the core of the form

$$|\psi_{\text{ph}}^{ij}\rangle = |0, 0, \dots, \underbrace{1, \dots, 2}_\text{MI core}, \dots, \underbrace{0, \dots, 1}_j, \dots, 0, 0\rangle,$$

however, in contrast even at zeroth order they are not completely degenerate and their associated Hubbard band is not flat. Instead the excitations are doubly degenerate and composed of equal superpositions of $|\psi_{\text{ph}}^{ij}\rangle$ with their mirror reflection. The energy of these excitations relative to the ground state is then $E_{\text{ph}}^{ij} = U + \frac{1}{2}\Omega[(i - c)^2 - (j - c)^2]$. A new feature introduced by trapping is an additional type of excitation. The vacuum

surrounding the MI core is essentially a reservoir of holes and so it is possible for a hole to hop to a site inside the core giving a hole-hopping (hh) excitation of the form [30]

$$|\psi_{\text{hh}}^{ij}\rangle = |0, \dots, \underbrace{1}_i, \dots, \underbrace{1, \dots, 0}_j, \dots, 1, \dots, 0, 0\rangle.$$

MI core

Since these excitations are caused by the transfer of holes they do not generate any double occupancies and so their energy above the ground state $E_{\text{hh}}^{ij} = \frac{1}{2}\Omega[(i - c)^2 - (j - c)^2]$ does not involve the interaction energy U . For this reason hh-excitations can have a lower energy than ph-excitations and in this case the trapping energy Ω defines the MI gap. In the following two chapters the properties of the BHM with harmonic trapping will be examined and we shall find that taking account of the general features discussed above becomes essential when assessing experimental results.

References

- [1] J. Hubbard, *Proc. Roy. Soc. Series A (London)* **276**, 238 (1963); *ibid*, **277**, 237 (1964).
- [2] A.J. Leggett, *Quantum Liquids* (Oxford Univ. Press, Oxford, 2006).
- [3] M.P.A. Fisher, P.B. Weichman, G. Grinstein, D.S. Fisher, *Phys. Rev. B* **40**, 546 (1989).
- [4] S. Sachdev, *Quantum Phase Transitions* (Cambridge Univ. Press, Cambridge, 2001).
- [5] W. Krauth, *Phys. Rev. B* **44**, 9772 (1991).
- [6] A.R. Kolovsky, A. Buchleitner, *Europhys. Lett.* **68**, 632 (2004).
- [7] E. Calzetta, B.L. Hu, A.M. Rey, *Phys. Rev. A* **73**, 023610 (2006).
- [8] E.H. Lieb, F.Y. Wu, *Phys. Rev. Lett.* **20**, 1445 (1968).
- [9] E.H. Lieb, W. Liniger, *Phys. Rev.* **130**, 1605 (1963); *ibid*, *Phys. Rev.* **130**, 1616 (1963).
- [10] I. Bloch, J. Dalibard, W. Zwerger, [arXiv:0704.3011](https://arxiv.org/abs/0704.3011).
- [11] L. Pitaevskii, S. Stringari, *Bose-Einstein Condensation* (Oxford Univ. Press, Oxford, 2003).
- [12] A.J. Leggett, *Rev. Mod. Phys.* **73**, 307 (2001).
- [13] J.F. Annett, *Superconductivity, Superfluids and Condensates* (Oxford Univ. Press, Oxford, 2004).
- [14] A. Lamacraft, *Cold Atoms for Condensed Matter Theorists*, Lecture Notes (2006): <http://www-thphys.physics.ox.ac.uk/user/AustenLamacraft/Lectures.pdf>.
- [15] S.M. Barnett, K. Burnett, J.A. Vaccaro, *J. Res. Natl. Inst. Stand. Tecnhol.* **101**, 593 (1996).

- [16] S.M. Barnett, P.M. Radmore, *Methods in Theoretical Quantum Optics* (Oxford Univ. Press, Oxford, 2002).
- [17] D. van Oosten, P. van der Straten, H.T.C. Stoof, *Phys. Rev. A* **63**, 053601 (2001).
- [18] P.C. Hohenberg, *Phys. Rev.* **158**, 383 (1967).
- [19] N.D. Mermin, H. Wagner, *Phys. Rev. Lett.* **17**, 11331136 (1966).
- [20] A.J. Leggett, *Rev. Mod. Phys.* **71**, S318-23 (1999).
- [21] A.J. Leggett, *Physica Fennica* **8**, 125 (1973).
- [22] A.J. Leggett, *J. Stat. Phys.* **93**, 927 (1998).
- [23] R. Roth, K. Burnett, *Phys. Rev. A* **67**, 031602(R) (2003).
- [24] A.M. Rey, K. Burnett, R. Roth, M. Edwards, C.J. Williams, C.W. Clark, *J. Phys. B* **36**, 825 (2003).
- [25] V. Vedral, [arXiv:quant-ph/0703129](https://arxiv.org/abs/quant-ph/0703129).
- [26] M.E. Fisher, M.N. Barber, D. Jasnow, *Phys. Rev. A* **8**, 1111 (1973).
- [27] B.S. Shastry, B. Sutherland, *Phys. Rev. Lett.* **65**, 243 (1990).
- [28] D.J. Scalapino, S.R. White, S. Zhang, *Phys. Rev. B* **47**, 7885 (1993).
- [29] W. Kohn, *Phys. Rev.* **113**, A171 (1964).
- [30] A.M. Rey, *Ultracold bosonic atoms in optical lattices* (PhD. Thesis, University of Maryland, 2003).
- [31] B. Damski, J. Zakrzewski, L. Santos, P. Zoller, M. Lewenstein, *Phys. Rev. Lett.* **91**, 080403 (2003).
- [32] J.K. Freericks, H. Monien, *Phys. Rev. B* **53**, 2691 (1995).
- [33] N. Elstner, H. Monien, *Phys. Rev. B* **59**, 12184 (1999).
- [34] W. Krauth, M. Caffarel, J.P. Bouchaud, *Phys. Rev. B* **45**, 3137 (1992).
- [35] D.S. Rokhsar, B.G. Kotliar, *Phys. Rev. B* **44**, 10328 (1991).
- [36] C. Schroll, F. Marquardt, C. Bruder, *Phys. Rev. A* **70**, 053609 (2004).
- [37] W. Zwerger, *J. Opt. B* **5**, 9 (2003).
- [38] K. Sheshadri, H.R. Krishnamurthy, R. Pandit, T.V. Ramakrishnan, *Europhys. Lett.* **22**, 257 (1993).
- [39] B. Capagrosso-Sansone, N.V. Prokof'ev, B. Svistunov, [arXiv:cond-mat/0701178](https://arxiv.org/abs/cond-mat/0701178).
- [40] F.D.M. Haldane, *Phys. Rev. Lett.* **48**, 569 (1982).
- [41] T. Giamarchi, *Quantum Physics in One Dimension* (Oxford Univ. Press, Oxford, 2004).
- [42] T.D. Kuhner, H. Monien, *Phys. Rev. B* **58**, R14741 (1998).
- [43] T.D. Kuhner, S.R. White, H. Monien, *Phys. Rev. B* **61**, 12474 (2000).

- [44] C. Kollath, U. Schollwöck, J. von Delft, W. Zwerger, *Phys. Rev. A* **69**, 031601 (2004).
- [45] V.A. Kashurnikov, N.V. Prokof'ev, B.V. Svistunov, *Phys. Rev. A* **66**, 031601 (2002).
- [46] S. Wessel, F. Alet, M. Troyer, G.G. Batrouni, *Phys. Rev. A* **70**, 053615 (2004).
- [47] G.G. Batrouni, V. Rousseau, R.T. Scalettar, M. Rigol, A. Muramatsu, P.J.H. Denteen, M. Troyer, *Phys. Rev. Lett.* **89**, 117203 (2002).
- [48] S. Bergkvist, P. Henelius, A. Rosengren, *Phys. Rev. A* **70**, 053601 (2004).

CHAPTER 5

PUBLICATION

Dynamics of the Superfluid to Mott-insulator transition in one dimension

S. R. Clark, and D. Jaksch

Clarendon Laboratory, University of Oxford, Parks Road, Oxford OX1 3PU, U.K.

Physical Review A **70**, 043612 (2004)¹

We numerically study the superfluid to Mott insulator transition for bosonic atoms in a one dimensional lattice by exploiting a recently developed simulation method for strongly correlated systems. We demonstrate this methods accuracy and applicability to Bose-Hubbard model calculations by comparison with exact results for small systems. By utilising the efficient scaling of this algorithm we then concentrate on systems of comparable size to those studied in experiments and in the presence of a magnetic trap. We investigate spatial correlations and fluctuations of the ground state as well as the nature and speed at which the superfluid component is built up when dynamically melting a Mott insulating state by ramping down the lattice potential. This is performed for slow ramping, where we find that the superfluid builds up on a timescale consistent with single atom hopping, and for rapid ramping where the build up is much faster than can be explained by this simple mechanism. Our calculations are in remarkable agreement with the experimental results obtained by M. Greiner, *et al.* [Nature **415**, 39 (2002)].

5.1 Introduction

Recent experiments on loading Bose-Einstein condensates into an optical lattice have allowed for the creation and study of strongly correlated systems of atoms [1, 2, 3, 4]. In particular the superfluid (SF) to Mott insulating (MI) transition first observed in a seminal experiment by M. Greiner *et al.* [1] has received a lot of attention since it impressively demonstrated a clean realisation of the Bose-Hubbard model (BHM) [5] which has long been considered a toy model in condensed matter physics. Furthermore, in the ideal MI state each atom is localised to a lattice site corresponding to a commensurate filling of the optical lattice with zero particle number fluctuations.

¹The appendices of this paper have been removed. The material that was covered there is dealt with in far greater detail in chapters 3 and 4.

These properties make MI states attractive candidates for several applications, most notably quantum memory, quantum computing [6, 7, 8, 9, 10, 11, 12], and quantum simulations of many-body quantum systems [13, 14].

The BHM Hamiltonian describes atoms loaded into a sufficiently deep optical lattice [15, 16]. It contains a kinetic energy term, with matrix element J , describing the hopping of particles from one site to the next and an interaction term, with matrix element U , which accounts for the repulsion of two atoms occupying the same site. The ratio U/J increases with the depth of the optical lattice and can be varied over several orders of magnitude by tuning the optical lattice parameters [15]. In particular by changing the intensity of the laser beams creating the optical lattice it is possible to vary J and U on time scales much smaller than the decoherence time of the system. This opens up the possibility of directly studying the dynamics of the BHM during the quantum phase transition at temperature $T = 0$ [1, 17]. According to Mean Field (MF) theory this phase transition occurs at $u_c = U/zJ \approx 5.8$, where z is the number of nearest neighbor sites in the lattice [5, 18, 19] and is easily accessible in an optical lattice.

In [1] the dynamics of atoms in a 3D optical lattice ($z = 6$) was studied while more recently optical lattice setups where the motion of the atoms was restricted to 1D ($z = 2$) [2] were investigated. These experiments revealed some striking properties of the quantum phase transition. In particular a feature which is yet to be fully understood is the timescale over which coherence is built up throughout the atomic system when going from the MI to the SF limit [1]. Indeed it cannot be easily explained using MF theory and numerical studies of this dynamical effect were, until now, limited to small systems of approximately ten atoms. Recently, however, it has been shown that quantum computations on 1D systems of qubits which do not give rise to strong entanglement can be efficiently simulated on a classical computer via the so called time-evolving block decimation (TEBD) algorithm [20]. An immediate application of this discovery is to the simulation of the time evolution of many-body 1D quantum systems which are governed by a nearest neighbor Hamiltonian [21]. The BHM is one of many important model Hamiltonians which fall into this class [22]. The simulation method is efficient for all such 1D model Hamiltonians due to a universal property of 1D systems that their ground state and lowest lying excitations tend to contain only a small amount of entanglement [21].

In this paper we restrict our attention to the 1D BHM with our physical motivation being to study the the nature and speed at which the superfluid component is built up as the system is dynamically driven through the SF-MI transition. By exploiting the efficient scaling of the TEBD algorithm with the size of the system we are able to investigate this phenomenon for setups which are of comparable size to those studied in experiments [2]. First, in Sec. 5.2, we introduce the 1D BHM for describing atoms in optical lattices and briefly introduce the TEBD algorithm as used in this paper. In Sec. 5.3 we then demonstrate the applicability of the TEBD to the BHM by comparison with exact numerical calculations for small systems. This is then followed by an investigation of SF and MI ground states of larger lattice setups concentrating on their spatial correlations and occupation number fluctuations together with a comparison to

MF results. We then study the dynamics of the MI to SF transition in Sec. 5.4 when changing the lattice depth on two different time scales. Most notably for rapid MI to SF ramping we find that the width of the central interference peak, as observed after releasing the atoms from the lattice, shrinks with an increasing total ramping time with the same functional dependence found in [1]. This result is discussed in Sec. 5.4B. Finally, we summarise our results in Sec. 5.5.

5.2 Model and Numerical Method

In this section we introduce the BHM describing bosonic atoms in an optical lattice where the motion is restricted to 1D, and give a short overview of the numerical method used in our simulations.

5.2.1 Model

By confining an ultra-cold bosonic gas in a 3D optical lattice with a large depth in the two orthogonal directions y and z it is possible to create an array of effective 1D systems in the x direction [2, 8, 23]. The dynamics of these systems is governed by the external trapping and the optical lattice potential along the x -axis. The optical lattice then has a depth V_0 proportional to the laser intensity and a lattice period $a = \lambda/2$, where λ is the wavelength of the laser light. The Hamiltonian describing each 1D system reduces to the 1D BHM (for details see chapter 3) [15] (taking $\hbar = 1$ throughout)

$$H = \sum_m -J(b_m^\dagger b_{m+1} + \text{h.c.}) - \mu_m b_m^\dagger b_m + \frac{U}{2} b_m^\dagger b_m^\dagger b_m b_m, \quad (5.1)$$

where the operators b_m (b_m^\dagger) are bosonic destruction (creation) operators for a bosonic particle in site m , centered at $x_m = ma$, obeying the standard canonical commutation relations. The grand canonical Hamiltonian then has $\mu_m = \mu - V_T(x_m)$ as the local chemical potential for site m , where V_T is the external trapping potential. The parameters U and J can be determined in terms of the Wannier functions $w(x)$ as shown in chapter 3, and under the assumptions outlined are independent of the lattice site m [15]. Their ratio can be varied over a wide range by dynamically changing the depth V_0 of the optical lattice. For all the systems considered here we take the wavelength of the light used to form the optical lattice as $\lambda = 826$ nm, and the atomic species trapped as ^{87}Rb , where $a_s = 5.1$ nm.

5.2.2 Numerical method

In this paper we exploit the recently devised TEBD simulation algorithm [20, 21] which allows the dynamics of 1D systems with nearest neighbor interactions, such as the BHM, to be computed accurately and efficiently. The TEBD algorithm has been shown to be closely related to density matrix renormalisation group (DMRG) [24, 25].

Over the past decade DMRG has provided enormous insight into the static and dynamic equilibrium properties of 1D systems. Although originally devised as a ground state method it has been extended to yield accurate low energy spectra [26], and also to calculations of the real time evolution of 1D systems [27] which is of particular importance here. The approach of [27] is to take the DMRG ground state $|\psi(0)\rangle$ obtained for the initial Hamiltonian and use it to define a decimation of the Hilbert space in which the Schrödinger equation is numerically integrated. The key assumption, and most severe approximation, within this scheme is that this static subspace defined by $|\psi(0)\rangle$ is adequate to approximate $|\psi(t)\rangle$ with reasonable accuracy for all times. In general this will only be true for short periods of time. Novel methods have been devised [28] which can maintain the accuracy over longer periods by ‘targeting’ other states in addition to the ground state, but in doing so the efficiency of the computation is significantly reduced [29]. In contrast the TEBD algorithm can maintain typical DMRG accuracies whilst remaining efficient. Despite their differing origins it has recently been shown that TEBD and DMRG algorithms share some crucial conceptual and formal similarities [22, 29]. Indeed both methods search for an approximation to the true wave-function within a restricted class of wave-functions which are described by matrix product states [30, 31], and do so with identical decomposition and truncation procedures. The essential difference, which we shall emphasise shortly, is that the TEBD algorithm updates the matrix product decomposition directly and in such a way that the resulting decimated subspace in which the time evolution is computed is optimally adapted at each step [22].

Here we briefly outline the essential features of the TEBD algorithm, with specific attention to its application to the BHM. Let us consider a 1D BHM composed of M sites. An arbitrary state of this system can be expanded in the Fock basis

$$|\psi\rangle = \sum_{n_1=0}^{\infty} \cdots \sum_{n_M=0}^{\infty} c_{n_1 \dots n_M} |n_1, \dots, n_M\rangle, \quad (5.2)$$

where $|n_m\rangle$ denotes the Fock state of n_m particles in site m . For the purpose of simulating this system the number of Fock basis states per lattice site must be cut-off to some upper limit n_{\max} . In all the numerical calculations we performed $n_{\max} = 5$. This is sufficient to avoid any cut-off effects in the bosonic occupation, so long as only small filling factors of the lattice are used and the on-site interaction energy U is sufficiently large compared to the hopping energy J .

Now suppose we split the system into two contiguous parts A_m composed of the first m sites and B_m composed of the last $M - m$ sites. We can think of this partitioning as cutting the m -th bond situated between sites m and $m + 1$. For any state $|\psi\rangle$ a Schmidt decomposition (SD) can be performed which renders the state in the form

$$|\psi\rangle = \sum_{\alpha=1}^{\chi_m} \lambda_{\alpha}^{[m]} |\phi_{\alpha}^{A_m}\rangle |\phi_{\alpha}^{B_m}\rangle, \quad (5.3)$$

where χ_m is the Schmidt rank of the SD, $\lambda_{\alpha}^{[m]}$ are the Schmidt coefficients and $|\phi_{\alpha}^c\rangle$, with

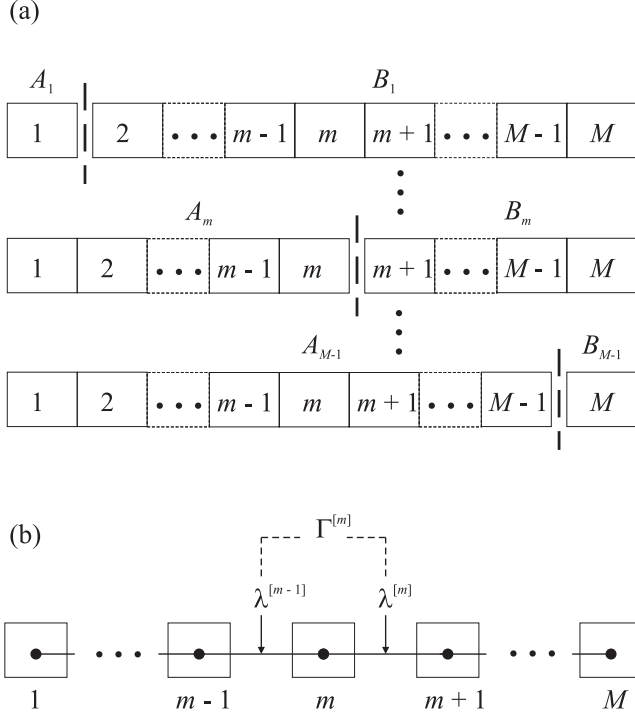


Figure 5.1. (a) The sequence of contiguous partitions of the system in which the SD are computed. The coefficients and states from these SD are then used to form the Γ and λ tensors. (b) A depiction of the Γ tensors associated to lattice sites and λ tensors associated to bonds between those sites.

$c \in \{A_m, B_m\}$, are the corresponding Schmidt states of the respective subsystems. The Schmidt rank χ_m is a useful measure of the entanglement between the two subsystems A_m and B_m [20]. Given any state $|\psi\rangle$ a set of $(M - 1)$ SD can be performed according to a sequence of such partitions of the system with $m \in \{1 \cdots M - 1\}$, as depicted in Fig. 5.1(a).

Using the $\lambda_\alpha^{[m]}$ and states $|\phi_\alpha^s\rangle$ for each subsystem obtained from these SD it is possible [20] to construct a set of Γ and λ tensors which are equivalent to a matrix product decomposition of the expansion coefficients $c_{n_1 \dots n_M}$ of $|\psi\rangle$ in the fixed Fock basis [22]. Specifically one finds

$$c_{n_1 \dots n_M} = \sum_{\alpha_1, \dots, \alpha_{M-1}} \Gamma_{\alpha_1}^{[1]n_1} \lambda_{\alpha_1}^{[1]} \Gamma_{\alpha_1 \alpha_2}^{[2]n_2} \lambda_{\alpha_2}^{[2]} \dots \lambda_{\alpha_{M-1}}^{[M-1]} \Gamma_{\alpha_M}^{[M]n_M}, \quad (5.4)$$

where n_m is the occupation number of site m , and α_m are the Schmidt indices of the m -th partition, each of which sums from 1 to its respective Schmidt rank χ_m . With reference to Fig. 5.1(b) we note that each $\lambda_{\alpha_m}^{[m]}$ is labelled by the bond between sites m and $m + 1$, along with the corresponding Schmidt index α_m , whereas each $\Gamma_{\alpha_{m-1} \alpha_m}^{[m]n_m}$ is labelled by a site m which resides between the two bonds $m - 1$ and m , and so also possess the Schmidt indices, α_{m-1} and α_m , of these bonds.

Under the circumstances described the expansion Eq. (5.4) is exact and as such the number of parameters stored could grow exponentially with the size of the system. However it is a general feature of 1D systems that their ground state and low-lying excitations have only a small amount of entanglement [21]. Indeed it can be shown that the entanglement of a block of size ℓ with the rest of the system remains finite as $\ell \rightarrow \infty$ in 1D systems or at worst grows logarithmically with ℓ at criticality [22]. Consequently the entanglement between the blocks of any of the $(M-1)$ SD illustrated in Fig. 5.1(a) are typical saturated by a small Schmidt rank. It is this fact that accounts for the success of DMRG in 1D systems. Similarly within TEBD it allows the maximum possible Schmidt rank used in the matrix product decomposition Eq. (5.4) to be fixed to some value χ , thereby truncating it to the most significant contributions. For an appropriate choice of χ this approximation will be accurate with the error proportional to the sum of the discarded eigenvalues in the SD [21]. This clear interpretation of the central numerical parameter χ within TEBD is very useful. Once a value of χ is found to saturate the entanglement of the ground state and low lying excitations of a system then this a direct measure of the role of entanglement in the dynamics of the system. Now the scaling in the number of parameters within the expansion Eq. (5.4) is quadratic in χ and linear in the size of the system M and in n_{\max} . So upon fixing χ , and thus preventing its possible exponential dependence on M , the description becomes efficient. As with DMRG this decomposition of a state generates, for all practical purposes, an optimal $\chi \times \chi$ matrix product state [22]. A noteworthy limit of this is the approximation is where $\chi = 1$, which forces the description of the system to be of product form with respect to all sites. Using the TEBD algorithm under this severe restriction is in fact equivalent to MF theory and the Gutzwiller ansatz [5, 18, 32, 33, 17].

Another crucial advantage of the TEBD algorithm is that once a state is expressed in the matrix product form Eq. (5.4) one and two site unitary transformations can be applied directly and exactly to the system such that the resulting state can be efficiently returned to a matrix product form [22]. Indeed, given a partitioning of the system into two blocks two sites configuration $[1 \cdots m-1][m \ m+1][m+2 \cdots M]$, the application of a two site unitary to sites m and $m+1$ only requires updates to be performed on the tensors *local* to those sites, namely $\Gamma_{\alpha_{m-1}\alpha_m}^{[m]n_m} \lambda_{\alpha_m}^{[m]} \Gamma_{\alpha_m\alpha_{m+1}}^{[m+1]n_{m+1}}$. The major computational effort of this update is limited to the re-diagonalisation of the reduced density matrix of one of the adjacent site and block subsystems, such as sites $[m+1][m+2 \cdots M]$, which is of dimension $(\chi n_{\max}) \times (\chi n_{\max})$ at most [20]. The crucial feature here is that a DMRG-style truncation to only the most relevant eigenstates of this reduced density matrix occurs in an optimal way at each application of a two site unitary. This is in contrast with time-dependent DMRG methods where the basis states which make up the matrix product decomposition is fixed at the start [27, 22]. The number of basic operations required to perform this update scales as $\mathcal{O}(\chi^3)$ [20].

To compute the action of the time-evolution unitary $\exp(-iH\delta t)$, for a time step δt , we first make the observation that for Hamiltonians with nearest neighbor interactions, which are composed of two-site operators at most, terms can be separated into a sum

of those involving odd sites, F , and those involving even sites, G ,

$$F = \sum_{n \text{ odd}} F_{n,n+1}, \quad (5.5)$$

$$G = \sum_{n \text{ even}} G_{n,n+1}, \quad (5.6)$$

$$H = F + G. \quad (5.7)$$

Given that no terms within F involve the same lattice sites they all commute amongst themselves. Thus the action of $\exp(-iF\delta t)$ can be computed exactly as

$$e^{-iF\delta t} = \prod_{n \text{ odd}} e^{-iF_{n,n+1}\delta t}. \quad (5.8)$$

Since each term in this product is a two site unitary they can be applied individually to the state with the method detailed in [20], and the same is also true for G . The complications in computing the time-evolution arise from the fact that F and G do not in general commute, and hence we approximate the unitary time evolution operator $\exp(i(F+G)\delta t)$ using a Trotter expansion. Ignoring their non-commutativity would constitute a 1-st order expansion. If we define

$$s_2(F, G, y) = e^{-iFy/2} e^{-iGy} e^{-iFy/2}, \quad (5.9)$$

then the 2-nd order expansion follows when $y = \delta t$. For the numerical simulations performed in this paper the 4-th order expansion [34] was used, which has the form

$$e^{-i(F+G)\delta t} = \prod_{l=1}^5 s_2(F, G, q_l \delta t) + \mathcal{O}(\delta t^5), \quad (5.10)$$

where the parameters q_l are defined as

$$q_1 = q_2 = q_4 = q_5 \equiv q = \frac{1}{(4 - 4^{1/3})} \text{ and } q_3 = 1 - 4q. \quad (5.11)$$

A detailed analysis of the errors and computational cost of TEBD is given in [21], where it is shown that the Trotter error propagates quadratically with the simulated time and so the accuracy of the method can be maintained for long periods with appropriate choices of the parameters.

The pure TEBD implementation we employ here can be improved further by combining the advantageous features of TEBD outlined with the well established optimisations of DMRG such as good quantum numbers and White's 'State prediction' method. In doing so an adaptive time-dependent DMRG algorithm is obtained [22, 29] illustrating the extremely close relationship between these two methods. Finally we note the very recent advances in generalising TEBD/DMRG to describe mixed state dynamics and generic master equation evolution of 1D systems with nearest neighbor

coupling [35, 36]. This opens up the possibility of simulating finite temperature effects, decoherence and dissipation.

5.3 Ground states of the BHM

We first investigate the ground state of the BHM and compare the numerical results with the exact ground states for a small homogeneous system. Then we consider a larger system in the presence of a shallow magnetic trap V_T superimposed on the lattice, and compare the results to those predicted by MF theory. In all cases the numerical ground state was computed with the TEBD algorithm using continuous imaginary time evolution from a simple product state, as detailed in [21].

5.3.1 Comparison of exact and simulated ground states

To investigate the accuracy of the numerical simulation and its applicability to the BHM we first consider a small system in which an exact solution can be found readily. Specifically we use an optical lattice composed of $M = 7$ sites, a trapping potential of $V_T = 0$ with box boundary conditions, and a total number of particles $N = 7$. The ground state is then calculated numerically and exactly for $U/2J = 2, 6$ and 20 , corresponding to the SF, intermediate and MI regimes respectively. The numerical simulation was performed for $\chi = 3, 5$ and 7 in each case.

The one-particle density matrix $\rho_{m,n} = \langle b_m^\dagger b_n \rangle$ obtained for each regime for the numerical and exact calculations are visually indistinguishable in all cases. In order to highlight the extent of the agreement we present a number of other plots. Specifically in the SF regime the comparisons of the spatial correlation of the central site $|\rho_{4,4+d}|$ as a function of the distance d are shown in Fig. 5.2(a)(b) between the exact and numerical calculations using $\chi = 3$ and $\chi = 5$. Identical comparisons of the standard deviation of the site occupation $\sigma(\rho_{m,m}) = ((\langle N_m^2 \rangle - \langle N_m \rangle^2)^{1/2}$, where $N_m = b_m^\dagger b_m$, and the spectrum of the one-particle density matrix e_γ (normalised with $\text{tr}(\rho) = N$) are shown in Fig. 5.2(c)(d) and Fig. 5.2(e)(f) respectively. These results show that although there is qualitative agreement between exact and $\chi = 3$ calculation almost all expectation values have a maximum deviation from the exact calculation improved by an order of magnitude with $\chi = 5$. As expected for a SF ground state the one-particle density matrix spectrum in Fig. 5.2(f) is dominated by one eigenvalue of order N . However given that the lattice still has a non-zero depth this state deviates from that of a pure SF, where $|\psi_{\text{SF}}\rangle \propto (\sum_m b_m^\dagger)^N |\text{vac}\rangle$, since the sum of the remaining eigenvalues (in descending order) is $\sum_{\gamma=2}^7 e_\gamma \approx 2.5$, and so represents a significant quantum depletion of the SF.

For the intermediate and MI regime a similar factor of improvement can be obtained, however in this case the $\chi = 3$ calculation already yields excellent agreement with the exact calculation. Specifically we find the infidelity between the numerical and exact many-body state is $1 - F = 1 - |\langle \psi_0 | \psi'_0 \rangle| \approx 10^{-5}$, where $|\psi_0\rangle$ ($|\psi'_0\rangle$) is the numerical (exact) ground state, and the temperature corresponding to the difference in their

ground state energy as $\Delta T \approx 10^{-2}$ nK. The comparisons of the spatial correlation, site occupancy standard deviation, and one-particle density matrix spectrum for $U/2J = 6$ and $U/2J = 20$, with $\chi = 3$, are shown in Fig. 5.3.

These plots, along with those where $\chi = 5$ for the SF regime, illustrate the onset of increasing MI characteristics in the ground states. In particular the rapidly decreasing spatial correlations and fluctuations in occupancy, as well as the change in the spectrum from being dominated by one single-particle state to having 7 almost equally occupied orbitals. These indicate that the MI ground state obtained is a very close approximation to that of a pure MI, where $|\psi_{\text{MI}}\rangle \propto \prod_m b_m^\dagger |\text{vac}\rangle$, representing a commensurate filling of the lattice. However given that the lattice is not infinitely deep deviations with this pure MI state exist and are evident from the persistence of small off-diagonal correlations visible at $d = 1$ in Fig. 5.3(b), and the spread of the spectrum about unity in Fig. 5.3(f).

As expected we find that the agreement between the numerical and exact calculations for a given value of χ improves with increasing $U/2J$ in line with the decrease in off-diagonal correlations. In all cases the $\chi = 7$ results gave excellent agreement with the exact calculation. The worst case being in the SF regime where an infidelity of $1 - F \approx 10^{-4}$, and a deviation in ground state energy of $\Delta T \approx 10^{-2}$ nK was obtained.

We note here that the exact calculation was performed with the canonical Hamiltonian with $N = 7$, whereas the numerical simulations used the grand canonical Hamiltonian. With an appropriate choice of the chemical potential μ the average particle number can be fixed to $N = 7$ enabling the comparisons above. Indeed for the calculations performed the worst absolute value of the projection of the simulated state outside the $N = 7$ Fock subspace was $\langle \psi_0 | \mathcal{P}_{N \neq 7} | \psi_0 \rangle \approx 10^{-13}$. Hence our results confirm the agreement of these approaches for small systems, and we assume the agreement holds for the larger systems.

5.3.2 MI and SF states with a superimposed magnetic trap

To consider systems closer to those studied in experiments [2] we use a lattice with $M = 49$ sites and made the system inhomogeneous by superimposing a harmonic trap potential $V_T(x_m) = m_A \omega^2 x_m^2 / 2$, where ω is the trapping frequency and m_A is the mass of an atom. As with the smaller system the ground states for the SF, intermediate and MI regimes were calculated. The lattice was loaded with a total number of particles $N = 40$ by choosing an appropriate chemical potential μ in each regime. For all cases a trapping frequency of $\omega = 2\pi \times 70$ Hz was used and found to be sufficient in eliminating any occupation at the boundaries of the system.

The inhomogeneity caused by a spatially varying confining potential can result in the coexistence of spatially separated SF and MI regions. Such properties have been confirmed experimentally [1, 2] and have received intense theoretical study with numerical calculations. In particular through Gutzwiller ansatz/MF theory [15, 37], Quantum Monte Carlo (QMC) [38, 39] and DMRG [40] simulations in 1D, as well as calculations using QMC [41, 42] and numerical renormalisation group [43] for 2D and 3D systems. Here we explore the SF-MI coexistence features of BHM ground states in

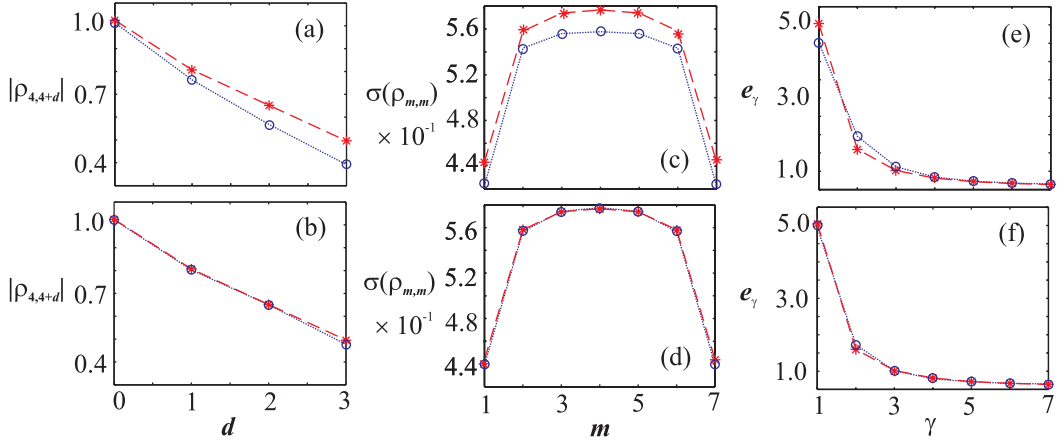


Figure 5.2. Comparisons of the numerical ‘o’ and exact ‘*’ calculations with $U/2J = 2$ for: spatial correlations $|\rho_{4,4+d}|$ with the central site $m = 4$ obtained for (a) $\chi = 3$ and (b) $\chi = 5$, the standard deviation of the site occupation $\sigma(\rho_{m,m})$ obtained for (c) $\chi = 3$ and (d) $\chi = 5$, and the spectrum e_γ of the one-particle density matrix obtained for (e) $\chi = 3$ and (f) $\chi = 5$. The dashed and dotted curves shown are to guide the eye.

order to confirm the physical picture arising from our numerical calculation for the large inhomogeneous system. Specifically we make comparisons of the mean site occupancy and its standard deviation between the numerical results and those obtained by MF theory for each regime (see chapter 4 for details of the MF calculation) [37, 33].

The one-particle density matrix of the resulting SF ground state is shown in Fig. 5.4(a). Important features of this state are outlined in Fig. 5.5(a)-(d), where it can be seen that the system is entirely SF. The MF results for the site occupancy and its standard deviation, are also shown in Fig. 5.5(a)(b), and as expected there is good agreement between the curves in both cases. For the intermediate regime, whose one-particle density matrix is shown in Fig. 5.4(b), we see a system possessing alternating regions of coherent SF and incoherent MI phases [40, 38]. The pattern of these regions starts with a central SF region with a mean occupancy exceeding unity, which then becomes a singly occupied MI, a SF region with mean occupancy less than unity, and finally the vacuum MI. In Fig. 5.5(e)(f) we see that the MI region in Fig. 5.5(e) coincides with suppressed fluctuations in occupancy shown in Fig. 5.5(f). The MF curves also plotted show general agreement with these phase identifications, however the MF curve in Fig. 5.5(f) predicts a significantly greater suppression of the particle number fluctuations for the MI regions than the numerical results. Such deviations are consistent with the fact that MF theory predicts a sharp and well pronounced SF-MI phase transition [37, 33]. Whilst these predictions are known to be accurate for infinite homogeneous systems, for small inhomogeneous systems we see that the role of correlations is important and that the transition between the SF and MI regions is not established with

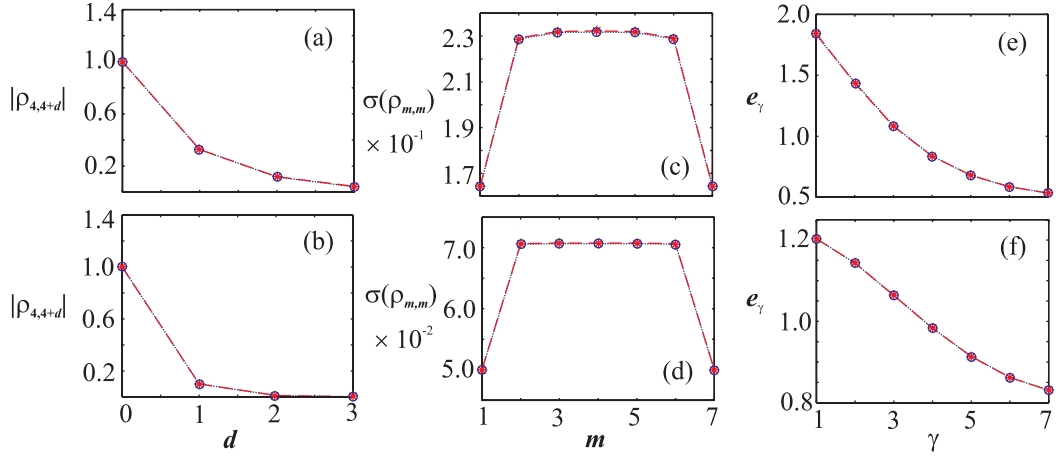


Figure 5.3. Comparisons of the numerical ‘o’ and exact ‘*’ calculations, where the numerics were all performed with $\chi = 3$, for: spatial correlations $|\rho_{4,4+d}|$ with the central site $m = 4$ obtained with (a) $U/2J = 6$ and (b) $U/2J = 20$, the standard deviation of the site occupation $\sigma(\rho_{m,m})$ obtained with (c) $U/2J = 6$ and (d) $U/2J = 20$, and the spectrum e_γ of the one-particle density matrix obtained with (e) $U/2J = 6$ and (f) $U/2J = 20$. Note the differing scales and that the dashed and dotted curves are shown only to guide the eye.

such definiteness.

Given that the ground state for the intermediate regime exhibits significantly sized SF regions which are separated by a MI, we investigated whether any correlations were present between these regions. Evidence of such correlations would be the presence of elongated peaks in the one-particle density matrix at the off-diagonal locations corresponding to the intersection of the rows m and columns n of the SF regions. To within the accuracy obtained with $\chi = 5$ no such correlation peaks were found in the one-particle density matrix of the ground state. This was confirmed with continuous imaginary time evolution not only for a product initial state used conventionally, but also with an initial state which already contained significant correlations. Our results suggest that if such SF correlations do exist within the ground state then they are extremely fragile. Despite this we shall see shortly that such correlations do occur readily in dynamical situations which cross the MI-SF transition, where the system does not necessarily remain in the ground state.

Lastly, the one-particle density matrix for the MI regime is shown in Fig. 5.4(c). It is clear from this and the corresponding plots in Fig. 5.5(i)(j) that the system is almost completely in the singly occupied MI phase, aside from the small SF regions at the far extremes before the vacuum. Their presence is typified by the two peaks in the occupancy standard deviation shown in Fig. 5.5(j). The MF calculation in this case gives the same identification of the regions, except for the very center of the trap, where a small SF region is predicted to exist, as evidenced by the central peak in the MF

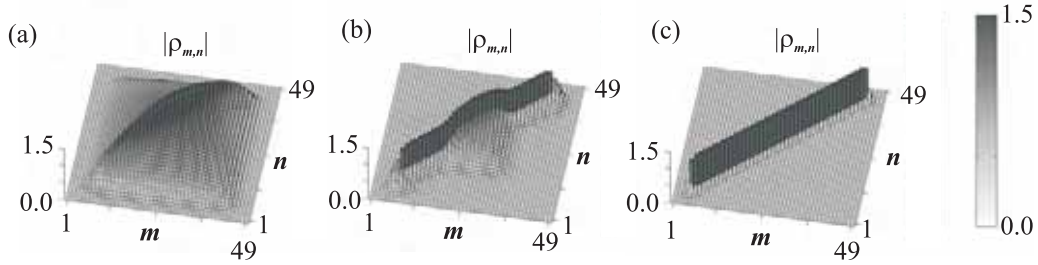


Figure 5.4. The absolute value $|\rho_{m,n}|$ of the one-particle density matrix as a function of site indices m, n for (a) $U/2J = 2$, (b) $U/2J = 6$, and (c) $U/2J = 20$.

occupancy standard deviation curve of Fig. 5.5(j). Again MF theory predicts a much greater suppression of occupancy fluctuations in the MI regions of the system than the numerical calculation. As with the smaller system the plots of Fig. 5.5 for the three ground states illustrate the transition from predominately SF to MI characteristics.

In all cases the ground state calculations were performed with $\chi = 5$. To ensure convergence the calculations were repeated for $\chi = 7$. The largest deviation between these two calculations was found in the SF regime where the estimated ground state energy differed by a temperature $\Delta T_{\chi=5 \rightarrow 7} \approx 0.2$ nK. We made a similar comparison between the $\chi = 5$ results and those of MF theory, which are equivalent to $\chi = 1$, where the largest deviation was found to be $\Delta T_{\chi=1 \rightarrow 5} \approx 3$ nk. Given the larger occupancy of the system the calculations were also repeated with larger values of n_{\max} confirming that no cut-off effects were encountered.

5.4 Dynamics of the BHM

The most novel feature of the TEBD algorithm is its capacity to efficiently simulate the dynamics of 1D systems which are inaccessible to exact calculation. Here we consider dynamics which are generated by varying the optical lattice depth $V_0(t)$ according to some ramping profile in time. The results of this is that the parameters $J(t)$ and $U(t)$ in the BHM Hamiltonian of Eq. (5.1) become time dependent. By appropriately choosing the range of values covered by the optical depth $V_0(t)$ it is possible to dynamically drive the system through the SF-MI transition. We shall consider such dynamics occurring on two different timescales. Firstly via a slow and smooth profile, and secondly as fast linear ramping. Our objective being in both cases to observe the nature and speed in which coherence is reestablished within the system.

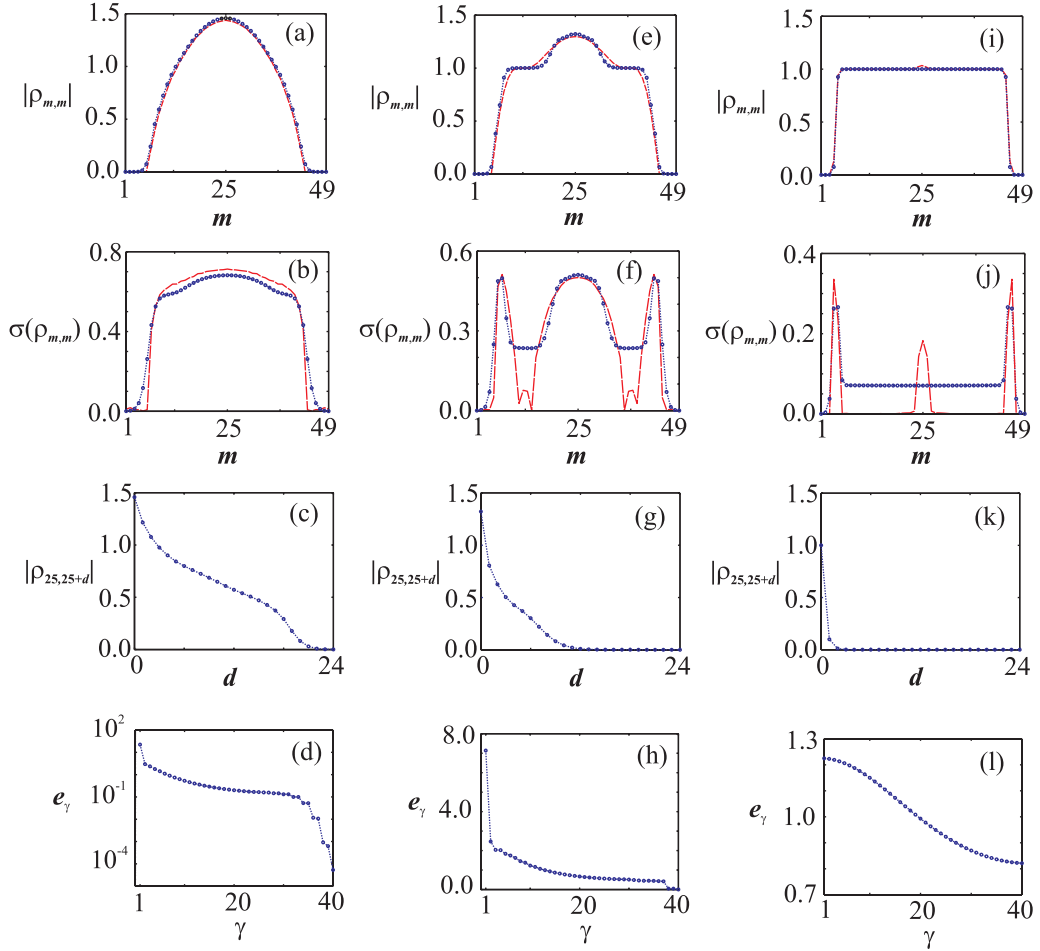


Figure 5.5. Specific plots for the three regimes. For $U/2J = 2$ there is (a) the site occupancy $|\rho_{m,m}|$, (b) the standard deviation of the site occupancy $\sigma(\rho_{m,m})$, both with the MF calculation shown as the dashed curve, (c) the spatial correlations from the central site $m = 25$, and (d) the spectrum e_γ of the one-particle density matrix, showing only the 40 non-zero eigenvalues. The same plots are presented for $U/2J = 6$ in (e)-(h), and for $U/2J = 20$ in (i)-(l).

5.4.1 Slow dynamics

Profile of slow dynamics

For the slow dynamical profile a smoothed ‘box’ function was used for the depth $V_0(t)$. Such a profile for the dynamics has been considered before for small systems [17]. It has the form

$$V_0(t) = V_{\text{SF}} + \mathcal{N} \frac{V_{\text{MI}} - V_{\text{SF}}}{1 + e^{((t-t_c)^2 - t_w^2)/t_s^2}}, \quad (5.12)$$

where t_c , t_w and t_s are time parameters specifying the center, width and step size of the profile respectively, whilst $\mathcal{N} = 1 + e^{-t_w^2/t_s^2}$ is the scaling factor required to ensure that the depth varies from V_{SF} to V_{MI} . The lattice depths V_{SF} and V_{MI} were chosen to be the depths equivalent to $U/2J = 2$ and $U/2J = 20$ respectively, in correspondence with the parameters used in the previous section for the SF and MI regime. The exact shape of the profile for $U/2J$ resulting from the ramping of $V_0(t)$ chosen is shown in Fig. 5.6(a). Large time parameters have been used in order to keep the time evolution of the system sufficiently adiabatic and to prevent excessive excitations.

Slow dynamics of the small system - $M = 7$

Firstly we consider the slow dynamics applied to the small system. This provides the opportunity to solve the BHM dynamics both numerically and exactly, allowing a direct comparison of the accuracy and a demonstration of the applicability of the algorithm to the dynamics of the BHM. The system was initially prepared in the SF ground state computed earlier in Sec. 5.3.1, and using $\chi = 5$ for the numerical calculations. The time evolution was then performed for a total time $t_{\text{tot}} = 2t_c$, with time t running over the interval $[0, t_{\text{tot}}]$. The spectrum e_γ of the one-particle density matrix $\rho_{m,n}(t)$ is plotted as a function of time in Fig. 5.6(b). For times t where $U/2J < u_c$ the spectrum is, as expected, dominated by one large eigenvalue whose value is of order of the number of atoms. As $U/2J$ crosses the MF critical value u_c the eigenvalues are found to converge around the region of 1. Indeed the state of the system given by the numerical calculation at the time $t = t_c$ in the dynamics, which corresponds to $U/2J = 20$, is found to have an infidelity with the numerical MI ground state computed earlier in Sec. 5.3.1 as $1 - F < 10^{-4}$. This confirms that for a small and homogeneous system the ramping is sufficiently adiabatic to ensure that the system has entered the MI regime as the ground state, and the one-particle density matrix is diagonal.

With decreasing optical depth, and in turn decreasing $U/2J$, the SF ground state is restored when $U/2J = 2$ is reached again at $t = 2t_c$. The infidelity between the initial numerical SF ground state and the final numerical SF state was found to be $1 - F < 10^{-3}$. In Fig. 5.6(c) the behavior of the fluctuations in the site occupancy is as expected, namely the standard deviation in site occupancy is suppressed with increasing lattice depth, and restored with its subsequent decrease.

To test the accuracy of the TEBD algorithm a number of comparisons to the exact calculation were made. The simplest of these was the maximum relative deviation between the exact and numerical results for the one-particle density matrix spectrum

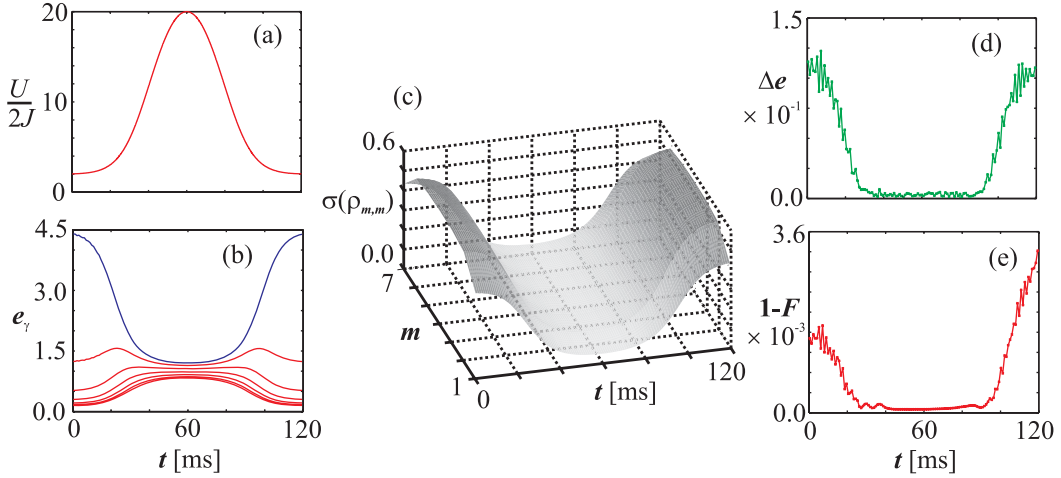


Figure 5.6. Slow dynamics of the small system: (a) the resulting ramping profile of the parameter $U/2J$ with time, where the time parameters for the $V_0(t)$ profile are $t_c = 60$ ms, $t_w = 24$ ms and $t_s = 18$ ms, (b) the spectrum of the one-particle density matrix e_γ with time obtained from the numerical calculation, (c) the standard deviation of the site occupancy $\sigma(\rho_{m,m})$ with time obtained from the numerical calculation, (d) the maximum deviation between the numerical and exact spectrum Δe with time, and (e) the infidelity $1 - F$ of the numerical many body state compared to the exact state with time.

$\Delta e = \max_\gamma(|1 - e_\gamma/e'_\gamma|)$, where e_γ and e'_γ are the numerical and exact results respectively. The time profile Δe is plotted in Fig. 5.6(d). It is found that over the whole time evolution the relative deviation is at most $\Delta e \approx 10^{-1}$. A similar relative deviation can be defined for the standard deviation of the occupancy as $\Delta\sigma = \max_m(|1 - \sigma_m/\sigma'_m|)$, where it is found that $\Delta\sigma \approx 10^{-2}$ at most during the time evolution.

The most conclusive comparison however is the infidelity $1 - F(t)$ of the exact and numerical many body states over the time evolution, shown in Fig. 5.6(e). It is clear from this that the infidelity is bounded as $1 - F(t) < 4 \times 10^{-3}$ over the whole evolution. The shape of the infidelity profile also gives important information about the TEBD method. Namely it fits the general observation made in Sec. 5.3.1 for the ground state calculations that for fixed numerical parameters χ and n_{\max} the simulation is more accurate in the intermediate and MI regimes than the SF regime. This behavior is precisely exhibited in the time dependence of the above comparisons where significant reductions in the deviations are seen when the system enters the MI regime.

Slow dynamics of the larger system - $M = 49$

The larger system presents many features which are essential characteristics of current experimental realisations of the SF-MI transition [1, 2]. In particular the inhomogeneous nature of the system caused by a trapping potential, and the larger number of both lattice sites, and atoms, as compared with the smaller system. With a linear size

of $M = 49$ sites the system considered is on the same scale as experiments already performed [1, 2]. The major difference is that the mean occupancy at the center of our system is $\langle n_c \rangle \approx 1.5$, roughly half that of most experiments, were it is usual to have $\langle n_c \rangle \approx 2.5$. Whilst the mean occupancy undoubtedly has an important influence in the dynamics, the system simulated here is sufficiently close that it can demonstrate much of the important physics.

The slow ramping profile Fig. 5.6(a) was performed identically on the larger inhomogeneous system using the ground state Fig. 5.4(a) computed earlier as the initial state and for a total time $t_{\text{tot}} = 3t_c$. The resulting spectrum e_γ of the one-particle density matrix is plotted as a function of time in Fig. 5.7. General features of this spectrum follow from the smaller homogeneous system, namely the trend for the eigenvalues to decrease as the bottom of the ramping is reached. Whilst most eigenvalues converge to unity, as with the smaller system, one in particular can be seen to remain much larger than this during the entire dynamics. This is a clear indicator of a significant SF region within the state as it is dynamically driven into the MI regime. For the larger inhomogeneous system we see that the slow ramping profile is not adiabatic enough to bring the system into the MI ground state shown in Fig. 5.4(c).

Indeed to examine the nature of the state generated by the dynamics additional plots of the one-particle density matrix are also shown in Fig. 5.7 for the two times indicated during the dynamics. These show that the state of the system remains close in form to that of the ground state for the intermediate regime shown in Fig. 5.4(b), where a large SF region exists at the center of the trap. However unlike that ground state we see that sizable correlations between the separated SF regions, which were alluded to earlier in Sec. 5.3.2, do exist and remain present even at the bottom of the profile for Fig. 5.7(ii) where $U/2J = 20$.

Another important difference between the spectra of the small and larger system is the more prominent excitations which have been induced during the transition. These are visible as the oscillatory behavior of the eigenvalues seen in the latter section of the profile in Fig. 5.7. Their presence is consistent with the fact that larger systems have more numerous and closely spaced low lying excitations, however despite this the oscillations have only a small amplitude and so do not destroy the SF obtained at the end of the transition.

In order to examine the speed at which coherence is reestablished in the system during the latter half ($t > t_c$) of the ramping profile the correlation length of the system must be computed over time. The correlation length is typically defined as the distance at which the off-diagonal elements of the one-particle density matrix become negligible [44]. For symmetrical systems, like those considered here, it is natural to measure this from the central site $m = 25$. However the inhomogeneity of the system, which results in the kind correlations between spatially separated SF regions just discussed for Fig. 5.7(i), makes the determination of the correlation length ambiguous. Instead we choose to examine a cut-off length ξ_c where the spatial correlations with the central site have a specific value $|\rho_{25,25+\xi_c}| = 1/e \approx 0.37$. This value is large enough that it corresponds to tracking a point on the central SF region and so can provide a relative measure of its size. The change in ξ_c over time is plotted in Fig. 5.8(a). The same

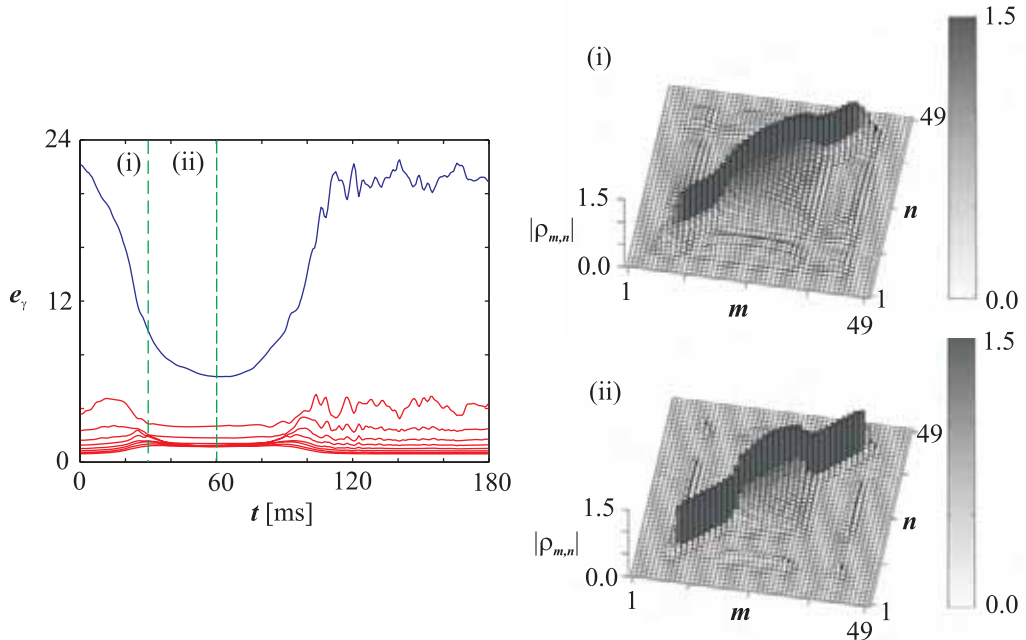


Figure 5.7. The spectrum of the one-particle density matrix e_γ for the slow dynamics of the larger inhomogeneous system, showing only the largest 10 eigenvalues. The dashed lines denote the two times (i) $t = t_c/2$ and (ii) $t = t_c$ for which the absolute value $|\rho_{m,n}|$ of the one-particle density matrix is plotted.

plot also shows the fitted curve whose function is that of a smooth ‘well’, which is the reflection of the smooth ‘box’ used earlier in Eq. (5.12) about the t -axis. The time parameters of this fit are very close to those of the resulting ‘well’ for $J(t)$ generated from the $V_0(t)$ profile. The variation in ξ_c over time demonstrates that it is capturing the essential changes in the central SF region, including the oscillations in its size at later times caused by excitations.

To investigate how much the presence of residual SF correlations effects the time dependence of ξ_c the latter half ($t > t_c$) of the same slow ramping profile was applied to the MI ground state of Fig. 5.4(c) found earlier for $U/2J = 20$. In contrast to the state which is dynamically driven to the MI regime this ground state has virtually no off-diagonal correlations for any site. The change in ξ_c of time for this case is shown in Fig. 5.8(b), and as before the fitted smooth ‘well’ function is also plotted. These show that despite ξ_c starting from a much smaller value for the MI ground state it still acquires the mean value of the final SF state on the same timescale as that of the dynamically driven state.

An important and experimentally motivated measure of the coherence of a state can be obtained from its momentum distribution function p_k . In experiments the interference pattern resulting from the state of the system is examined by allowing all the atoms within the lattice to expand freely for a short period of time, and then measure the absorption $I(x)$ at points x on a distant observation line. In the simplest

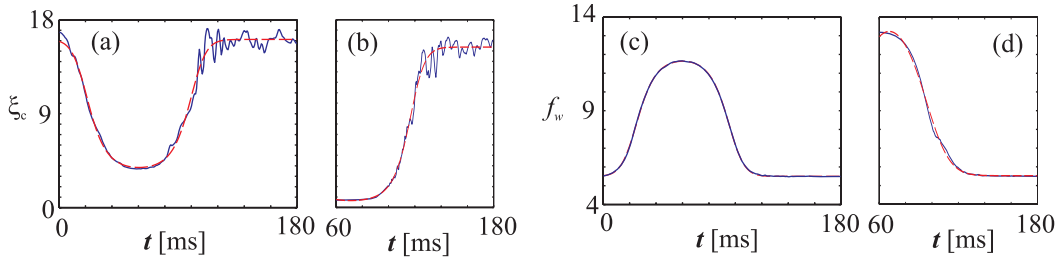


Figure 5.8. Slow dynamics of the larger inhomogeneous system with the variation in the correlation cut-off ξ_c , measured in lattice sites, for (a) the complete slow ramping profile starting from the SF ground state, and for (b) the MI ground state beginning at the bottom of the ramping. The momentum distribution width f_w , also measured in lattice sites, for the same situations is shown in (c) and (d) respectively. The dashed curves present in all plots are the fitted smooth ‘box’ or ‘well’ functions to the data.

model of this process one can neglect both the interactions between atoms during the expansion, and the spatial dependence of the interference caused by the freely evolved Wannier function envelopes $w(x - x_m)$ [45]. This gives the generic features of the interference pattern at an observation point x in terms of the path phases acquired by each site in a 1D lattice of phase coherent matter wave sources. In the far-field approximation the intensity $I(x)$ along the observation line is proportional to the momentum distribution $p_k \propto \sum_{m,n} \exp[ik(m - n)]\rho_{m,n}$ [45, 42].

The form of the momentum distribution is sufficiently well behaved that its width f_w can be determined most easily by taking its standard deviation. The variation of f_w in time for the full dynamics is shown in Fig. 5.8(c), along with the fitted smooth ‘box’ function. The time parameters of this fit are again very similar to those of $J(t)$. As expected it is seen that f_w increases in line with the decrease in off-diagonal correlations. The time profile of f_w for the half-ramping of the MI ground state is shown in Fig. 5.8(d) and again confirms that the momentum distribution width of the SF is re-established on approximately the same timescale as that of the dynamically driven state.

Finally we examine the speed at which the correlation cut-off length ξ_c increases with time over the latter half of the slow ramping. At any given time t the characteristic timescale at which single-atom hopping occurs is given by $\tau_{\text{tunnel}}(t) = \pi/2J(t)$ ². The simplest description of the growth of the central SF region is based on atoms at the edge of the system hopping towards the center. In this way correlations can be established over the whole lattice of M sites [1]. An estimate for the overall timescale for this

²We define the timescale $\tau_{\text{tunnel}} = \pi/2J$. This is physically motivated by considering the time required for one atom, within a double well potential, to hop from one well to another, given a tunnelling matrix element J .

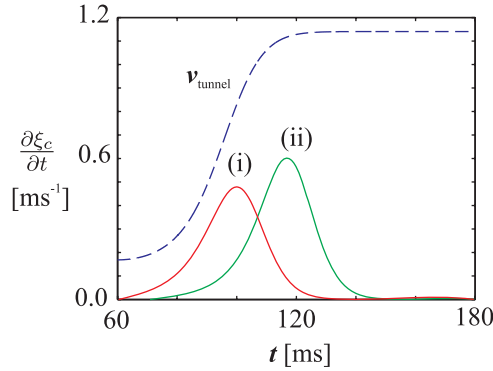


Figure 5.9. A comparison between the speeds at which the correlation cut-off length ξ_c changes in time for (i) the full slow ramping profile starting from the SF ground state, and (ii) the last half of the ramping profile starting from the MI ground state at the bottom of the ramping. The time profile for the single-atom hopping speed $v_{\text{tunnel}}(t)$ is also shown. All speeds are expressed in lattice sites per ms.

mechanism to occur is given by $t_{\text{restore}} = M\tau_{\text{tunnel}}/2$ ³, which for the system and depths used here has a value $t_{\text{restore}} \approx 23$ ms. In Fig. 5.9 the speed $\partial \xi_c / \partial t$ obtained from the function fitting is plotted for (i) the full dynamics of the ramping and (ii) the half ramping from the MI ground state. In line with the plots of ξ_c in Fig. 5.8(a)(b) we see that there is a time delay before there is a significant rate of change in ξ_c for the MI ground state ramping. Since the restoration of correlations occurs over the same total timescale in both cases the peak in the correlation speed is higher for the MI ground state. In addition to these curves the characteristic tunnelling speed $v_{\text{tunnel}}(t) = 1/\tau_{\text{tunnel}}(t)$ over the ramping is also shown, and most importantly we note that neither of the two correlation speeds (i) nor (ii) exceed this curve. This confirms that the ramping applied is sufficiently slow that the propagation of the SF is dominated by single atom hopping.

5.4.2 Fast dynamics

Profile for fast dynamics

The timescale over which the slow ramping occurs is of the order of 60 ms, and so greater than t_{restore} . Here we consider ramping occurring much more rapidly. Specifically we replace the latter part ($t > t_c$) of the slow ramping profile with a linear ramping of the optical depth $V_0(t)$ from V_{MI} to V_{SF} as

$$V_0(t) = V_{\text{MI}} - \frac{(V_{\text{MI}} - V_{\text{SF}})}{t_{\text{ramp}}} (t - t_c), \quad (5.13)$$

³To define a timescale for hopping across half the lattice, when J varies in time, some appropriate value must be chosen to represent its typical value during the ramping.

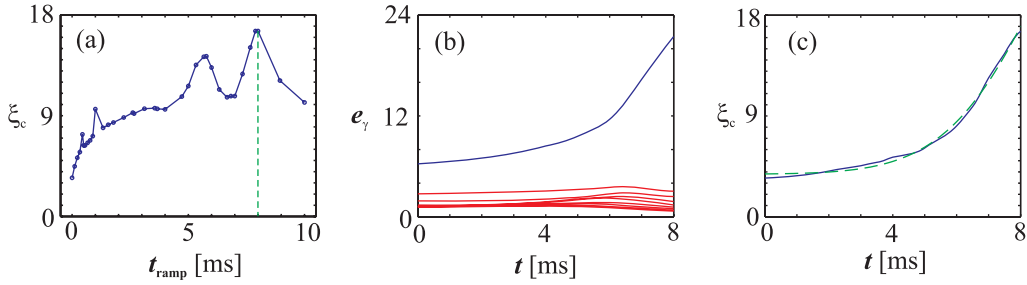


Figure 5.10. Results for rapid dynamics, (a) the final correlation cut-off length ξ_c obtained for different linear ramping times t_{ramp} , focussing on $t_{\text{ramp}} = 8$ ms we have (b) the spectrum of the one-particle density matrix e_γ showing only the largest 10 eigenvalues, and (c) the variation in ξ_c over the simulation run, along with a fitted smooth ‘box’ function shown as the dashed curve.

where t runs from t_c to $t_c + t_{\text{ramp}}$, and the total time of the ramping is t_{ramp} . This gives a total ramping profile similar to that studied experimentally by M. Greiner *et al* [1].

Fast dynamics of the larger system - $M = 49$

For the fast dynamics we restrict our attention to the state that is dynamically driven to the MI regime by the slow ramping profile at $t = t_c$. A number of simulation runs were performed for total ramping times t_{ramp} between 0.1 ms and 10 ms, along with $t_{\text{ramp}} = 0$ ms which is equivalent to the initial state. The value of ξ_c obtained at the end of each of the ramping times is plotted in Fig. 5.10(a). We see that there is a steady monotonic increase in the ξ_c for ramping times t_{ramp} , except where it is broken by peaks and troughs which are the expected manifestations of the trapping used. In particular the trough centered around $t_{\text{ramp}} \approx 7$ ms corresponds to the period of an oscillation with frequency 2ω , where ω is the trapping frequency introduced in Sec. 5.3.2. On a similar basis the spikes which appear around $t_{\text{ramp}} \approx 1$ ms can be seen to be a result of the excitation spectrum.

We take a special interest in the ramping time $t_{\text{ramp}} = 8$ ms where ξ_c obtains its maximum value approximately equal to that of the SF ground state. The variation in time of the spectrum e_γ of the one-particle density matrix and ξ_c during this particular ramping simulation is given in Fig. 5.10(b)(c). A well behaved monotonic increase in ξ_c is observed which can be accurately fitted over the interval [0,8] ms by a smooth ‘box’ function, as used earlier. This again provides the basis for computing the speed $\partial\xi_c/\partial t$ at which the correlation cut-off length ξ_c is increasing over the ramping, and is shown in Fig. 5.11(b) along with that of the characteristic tunnelling speed $v_{\text{tunnel}}(t)$ for the rapid ramping profile. Unlike the similar comparison for the slow dynamics we see here that after approximately 3 ms ξ_c is increasing in time much more rapidly than single-site tunnelling speed v_{tunnel} alone can account for. Indeed by the end of the ramping $\partial\xi_c/\partial t$ is almost three times that of the maximum tunnelling speed. This is a

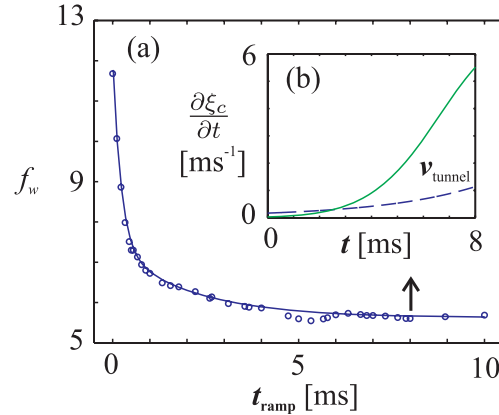


Figure 5.11. Rapid ramping of an optical lattice from the MI ($U/2J = 20$) to the SF ($U/2J = 2$) regime for $N = 40$ atoms in $M = 49$ lattice sites superimposed by a magnetic trapping potential. The width of the central interference fringe f_w as a function of the ramping time t_{ramp} is shown in (a). The solid curve is a fit using a double exponential decay ($\tau_1 = 0.22$ ms, $\tau_2 = 2.14$ ms) (cf. [1]). In (b) the rate of change of the correlation cut-off length ξ_c is shown for the ramping performed with $t_{\text{ramp}} = 8$ ms, along with the profile for the characteristic tunnelling speed $v_{\text{tunnel}}(t)$ for the ramping. Both are plotted in units of lattice sites per ms.

clear indication that single atom hopping is not adequate to describe the growth of the central SF region for such rapid dynamics. Instead the specific form and contributions of higher order correlation functions must play a crucial role.

To draw direct comparisons with the results of M. Greiner *et al.* [1] on the restoration of coherence we also plot the momentum distribution width f_w obtained from the one-particle density matrix at the end of each ramping in Fig. 5.11(a). The data points for this quantity show a pronounced trend, without any of the large scale variations seen in ξ_c caused by the trapping [42]. The decrease of f_w with increasing t_{ramp} fits well to a double exponential decay curve of the form

$$f_w(t_{\text{ramp}}) = A_1 e^{-t_{\text{ramp}}/\tau_1} + A_2 e^{-t_{\text{ramp}}/\tau_2} + C, \quad (5.14)$$

where τ_1, τ_2 are the characteristic decay times, A_1, A_2 are coefficients and C is a constant. Most notably the exact same functional form was found to fit the experimental data in [1]. Since their experiment was conducted for a 3D lattice, along with a larger mean occupancy and a deeper ramping profile, exact agreement for the time parameters of this fit is not expected. However we do note that the ratio of the decay times used for their fit and ours are both $\tau_2/\tau_1 \approx 10$. Similarly we can make the same observation as made in [1] that the momentum distribution width f_w has returned to its steady state value within a timescale approximately of order τ_{tunnel} . This is much shorter than the expected time t_{restore} required for coherence to spread over the whole lattice of M

sites via single atom hopping. This confirms that the restoration of coherence as seen in the experiment is accurately described by the BHM.

Validity of the simulation for fast dynamics

The simulations performed here assume that the dynamics of the atoms is described by the lowest Bloch band of the optical lattice. This assumption holds if the typical frequency $f \approx 1/t_{\text{ramp}}$ of the ramp in U and J obeys $f \ll \nu$, where $\nu = \sqrt{4E_R V_0}/2\pi$ is the harmonic approximation of the excitation frequency to the first excited Bloch band [15]. The shortest ramping time we considered is $t_{\text{ramp}} = 0.1$ ms, whilst $1/\nu = 0.05$ ms for the lattice on average over the ramping. Because the condition $f \ll \nu$ is not fulfilled we numerically calculated the probability of exciting a single particle, when initially prepared in the lowest Bloch band and located at the central site of the lattice, during the ramping above as a function of t_{ramp} . We find that the time evolution is well approximated by the adiabatic time evolution for $t_{\text{ramp}} > 0.05$ ms and that it changes to being sudden for $t_{\text{ramp}} < 0.005$ ms. Therefore we expect only a small influence to the form of the curve in Fig. 5.11(a) between the points at $t_{\text{ramp}} = 0$ ms and $t_{\text{ramp}} = 0.1$ ms due to higher band excitations which is not resolved in the experiments [1].

5.5 Conclusion

In these studies we have established the accuracy and applicability of the TEBD algorithm to the BHM, for both the computation of ground states and its dynamics. We have then applied this method to systems of a size equivalent to those studied in experiments and in the presence of a trapping potential. In particular we have examined the nature and speed in which coherence is reestablished within the system for both slow and rapid dynamics which cross the SF-MI transition. Our results indicate that for slow ramping of the lattice depth the SF growth is consistent with single atom hopping as might naively be expected. However for very rapid ramping of the lattice depth we find that the SF growth is much greater than can be explained by this mechanism alone, and so points to the importance of higher order correlation functions. We made direct comparisons between our simulation results for the momentum distribution width f_w during rapid ramping and the experimental results obtained by M. Greiner *et al.* [1] and found that the reduction in f_w with the ramping time follows precisely the same functional form as their data, despite a number of significant differences in the systems analysed. Perhaps most fundamentally we have shown that the results obtained in [1] for the rapid restoration of coherence are consistent and explicable within the BHM alone, and are present even in 1D systems. Finally, we note that a detailed knowledge of the correlations of atoms in different sites and the particle number fluctuations as provided by our numerical calculations are important for utilising the MI state in a number of applications [6, 7, 8, 9, 10, 11, 12, 13, 14].

References

- [1] M. Greiner, O. Mandel, T. Esslinger, T.W. Hänsch, I. Bloch, *Nature (London)* **415**, 39 (2002).
- [2] T. Stöferle, H. Moritz, C. Schori, M. Köhl, T. Esslinger, *Phys. Rev. Lett.* **92**, 130403 (2004).
- [3] S. Peil, J.V. Porto, B.L. Tolra, J.M. Obrecht, B.E. King, M. Subbotin, S.L. Rolston, W.D. Phillips, *Phys. Rev. A* **67**, 051603 (2003).
- [4] S.E. Sklarz, I. Friedler, D.J. Tannor, Y.B. Band, C.J. Williams, *Phys. Rev. A* **66**, 053620 (2002).
- [5] M.P.A. Fisher, P.B. Weichman, G. Grinstein, D.S. Fisher, *Phys. Rev. B* **40**, 546 (1989).
- [6] D. Jaksch, H.J. Briegel, J. I. Cirac, C. W. Gardiner, P. Zoller, *Phys. Rev. Lett.* **82**, 1975 (1999).
- [7] O. Mandel, M. Greiner, A. Widera, T. Rom, T.W. Hänsch, I. Bloch, *Nature (London)* **425**, 937 (2003).
- [8] U. Dorner, P. Fedichev, D. Jaksch, M. Lewenstein, P. Zoller, *Phys. Rev. Lett.* **91**, 073601 (2003).
- [9] J.K. Pachos and P.L. Knight, *Phys. Rev. Lett.* **91**, 107902 (2003).
- [10] G.K. Brennen, C.M. Caves, P.S. Jessen, I.H. Deutsch, *Phys. Rev. Lett.* **82**, 1060 (1999).
- [11] D. Jaksch, J. I. Cirac, P. Zoller, S.L. Rolston, R. Cote, and M.D. Lukin, *Phys. Rev. Lett.* **85**, 2208 (2000).
- [12] H.J. Briegel, T. Calarco, D. Jaksch, J. I. Cirac, P. Zoller, *J. Mod. Opt.* **47**, 415 (2000).
- [13] E. Jane, G. Vidal, W. Dür, P. Zoller, J.I. Cirac, *Quant. Inf. Comput.* **3**, 15 (2003).
- [14] A. Sørensen, K. Mølmer, *Phys. Rev. Lett.* **83**, 2274 (1999).
- [15] D. Jaksch, C. Bruder, J.I. Cirac, C.W. Gardiner, P. Zoller, *Phys. Rev. Lett.* **81**, 3108 (1998).
- [16] H.P. Büchler, G. Blatter, W. Zwerger, *Phys. Rev. Lett.* **90**, 130401 (2003).
- [17] D. Jaksch, V. Venturi, J.I. Cirac, C.J. Williams, P. Zoller, *Phys. Rev. Lett.* **89**, 040402 (2002).
- [18] K. Sheshadri, H.R. Krishnamurthy, R. Pandit, T.V. Ramakrishnan, *Europhys. Lett.* **22**, 257 (1993).
- [19] J.K. Freericks, H. Monien, *Europhys. Lett.* **26**, 545 (1994).
- [20] G. Vidal, *Phys. Rev. Lett.* **91**, 147902 (2003).
- [21] G. Vidal, *Phys. Rev. Lett.* **93**, 040502 (2004).

- [22] A.J. Daley, C. Kollath, U. Schollwöck, G. Vidal, *J. Stat. Mech.* P04005 (2004).
- [23] B. Paredes, A. Widera, V. Murg, O. Mandel, S. Fölling, J.I. Cirac, G. Shlyapnikov, T.W. Hänsch, I. Bloch, *Nature (London)* **429**, 277 (2004).
- [24] S.R. White, *Phys. Rev. Lett.* **69**, 2863 (1992).
- [25] S.R. White, *Phys. Rev. B* **48**, 10345 (1993).
- [26] E. Jeckelmann, *Phys. Rev. B* **66**, 045114 (2002).
- [27] M.A. Cazalilla, J.B. Marston, *Phys. Rev. Lett.* **88**, 256403 (2002); *ibid* *Phys. Rev. Lett.* **91**, 049702 (2003).
- [28] H.G. Luo, T. Xiang, X.Q. Wang, *Phys. Rev. Lett.* **91**, 049701 (2003).
- [29] S.R. White, A.E. Feiguin, *Phys. Rev. Lett.* **93**, 076401 (2004).
- [30] M. Fannes, B. Nachtergaele, R.F. Werner, *Comm. Math. Phys.* **144**, 3 (1992).
- [31] S. Östlund, S. Rommer, *Phys. Rev. Lett.* **75**, 3537 (1995).
- [32] W. Krauth, M. Caffarel, J.P. Bouchaud, *Phys. Rev. B* **45**, 3137 (1992).
- [33] D. van Oosten, P. van der Straten, H.T.C. Stoof, *Phys. Rev. A* **63**, 053601 (2001).
- [34] M. Suzuki, *Phys. Lett. A* **146**, 6 (1990); *ibid*, *J. Math. Phys.* **32**, 2 (1991).
- [35] M. Zwolak, G. Vidal, *Phys. Rev. Lett.* **93**, 207205 (2004).
- [36] F. Verstraete, J.J. Garia-Ripoll, J.I. Cirac, *Phys. Rev. Lett.* **93**, 207204 (2004).
- [37] C. Schroll, F. Marquardt, C. Bruder, *Phys. Rev. A* **70**, 053609 (2004).
- [38] G.G. Batrouni, V. Rousseau, R.T. Scalettar, M. Rigol, A. Muramatsu, P.J.H. Denteneer, M. Troyer, *Phys. Rev. Lett.* **89**, 117203 (2002).
- [39] S. Bergkvist, P. Henelius, A. Rosengren, *Phys. Rev. A* **70**, 053601 (2004).
- [40] C. Kollath, U. Schollwöck, J. von Delft, W. Zwerger, *Phys. Rev. A* **69**, 031601 (2004).
- [41] S. Wessel, F. Alet, M. Troyer, G.G. Batrouni, *Phys. Rev. A* **70**, 053615 (2004).
- [42] V.A. Kashurnikov, N.V. Prokof'ev, B.V. Svistunov, *Phys. Rev. A* **66**, 031601 (2002).
- [43] L. Pollet, S. Rombouts, K. Heyde, J. Dukelsky, *Phys. Rev. A* **69**, 043601 (2004).
- [44] L. Pitaevskii, S. Stringari, *Bose-Einstein Condensation* (Oxford Univ. Press, Oxford, 2003).
- [45] R. Roth, K. Burnett, *Phys. Rev. A* **67**, 031602(R) (2003).

CHAPTER 6

PUBLICATION

Signatures of the Superfluid to Mott-insulator transition in the excitation spectrum of ultracold atoms

S. R. Clark, and D. Jaksch

Clarendon Laboratory, University of Oxford, Parks Road, Oxford OX1 3PU, U.K.

New Journal of Physics **8**, 160 (2006)

We present a detailed analysis of the dynamical response of ultra-cold bosonic atoms in a one-dimensional optical lattice subjected to a periodic modulation of the lattice depth. Following the experimental realisation by Stöferle *et al* [Phys. Rev. Lett. **92**, 130403 (2004)] we study the excitation spectrum of the system as revealed by the response of the total energy as a function of the modulation frequency Ω . By using the Time Evolving Block Decimation algorithm, we are able to simulate one-dimensional systems comparable in size to those in the experiment, with harmonic trapping and across many lattice depths ranging from the Mott-insulator to the superfluid regime. Our results produce many of the features seen in the experiment, namely a broad response in the superfluid regime, and narrow discrete resonances in the Mott-insulator regime. We identify several signatures of the superfluid-Mott insulator transition that are manifested in the spectrum as it evolves from one limit to the other.

6.1 Introduction

The realisation of ultracold atoms confined in optical lattices has made a large range of fundamental equilibrium and dynamical phenomena of degenerate quantum gases experimentally accessible. The success of this approach stems from the fact that, in contrast to analogous condensed matter systems, optical lattices form a defect free lattice potential which can trap a dense cloud of atoms with long decoherence times and can be controlled rapidly with a great deal of flexibility. This has already enabled a seminal demonstration of the superfluid (SF) to Mott insulator (MI) transition by Greiner *et al* [1] that was predicted to occur for a clean realisation of the Bose-Hubbard model (BHM) [2, 3]. More recently, other themes of ultracold-atom research have been explored experimentally such as the purely one-dimensional (1D) Tonks-Girardeau limit [4, 5], the characterisation of the SF-MI transition via the excitation spectrum

through 1D - 3D dimensionality crossover [6, 7], and impurity effects caused by Bose-Fermi mixtures [8, 9].

Here we focus on features of the excitation spectrum from reference [6] which were revealed for a 1D BHM by periodic modulation of the lattice depth. The experimental accessibility of the excitation spectrum provides a rich source of additional information that can be compared with well studied quantities such as the dynamic structure factor [10, 11]. In addition to this the experiment demonstrates the transition through the evolution of the spectrum from discrete sharp resonances in the MI regime to a broad continuum of excitations in the SF regime. Changes in the structure of the excitation spectrum provide important evidence for the transition beyond the loss and revival of phase coherence when ramping the lattice [1], and can also be used to diagnose the temperature of the system [12, 13]. The 1D system is of particular interest for several reasons. Firstly, quantum fluctuations are expected to play a strong role there [14], and this is indeed found to be the case with the critical ratio of the on-site interaction to kinetic energy $(U/J)_c$, identified by the appearance of the discrete structure in the spectrum, being lower than that predicted by mean-field theory [6]. Secondly, the behavior found in the 1D experiment for the SF regime, specifically a large and broad non-zero response, most strikingly departs from standard theoretical predictions. Specifically, linear response using Bogoliubov theory for a Bose-Einstein condensate (BEC) in a shallow 1D optical lattice predicts that lattice modulation cannot excite the gas in the SF regime due to the phonon nature of the excitation spectrum [15]. Since the quantum depletion of the SF in the experiment was significant ($\approx 50\%$), it has been suggested that this was responsible for the response [16]. Indeed, it has been shown that only a small amount of seed depletion is required for non-linear effects like the parametric amplification of Bogoliubov modes to reproduce the SF response [17, 18]. More recently still, the use of the sine-Gordon model and bosonisation method has demonstrated that linear response is non-zero at low frequencies [19]. Lastly, the study of the 1D system permits the use of quasi-exact numerical methods, such as the Time Evolving Block Decimation (TEBD) algorithm, where the fully time-dependent dynamical evolution of the system can be computed efficiently for systems of equivalent size to those in the experiment.

In addition to the many-body physics perspective, understanding the excitation spectrum revealed in [6] is important for potential applications of the MI state. The zero particle number fluctuations for an ideal commensurate MI state make them attractive candidates for several applications, most notably as a quantum memory, a basis for quantum computing [20, 21, 22, 23, 24, 25], and quantum simulations of many-body quantum systems [26, 27]. A well understood excitation spectrum can give valuable information about the nature and stability of the experimental approximation of the ideal MI state to external perturbations.

In this paper we study the dynamics of the 1D BHM under lattice modulation and generate excitation spectra for box and harmonic trapping of a large system over numerous lattice depths ranging from the SF to MI regime. We find that much of the features of the box system can be understood from a small exact calculation. However, the large system calculations were crucial for the investigation of signatures in the

spectra which indicate the transition from MI to SF regime in both trappings. We find that for a harmonically trapped system with less than unit filling the spectra is similar to the commensurately filled box, but with the transition producing less pronounced signatures. Additional calculations progressing from the MI regime for a harmonically trapped system with a central filling greater than unity produces a spectra that has very good qualitatively agreement with the experiment. In this way our results are different but complementary to a very recent study of the same experiment by Kollath *et al* [28] where they discovered that excitation spectra can reveal information about the commensurateness of the system.

The structure of the paper is as follows: we give an overview of the physical setup for the 1D system in section 6.2.1 followed by a description of the excitation scheme in section 6.2.2. We then introduce the linear response formalism for this scheme in section 6.3.1, and in section 6.3.2 we give an overview of the literature describing the TEBD simulation method used here for the larger systems. The results are then presented in section 6.4, firstly for a small box system computed exactly in section 6.4.1, then for larger systems computed with the TEBD algorithm for box and harmonic trapping in section 6.4.2 and 6.4.3 respectively. We then end with the conclusions in section 6.5.

6.2 Probing the system

6.2.1 Optical lattices and the Bose-Hubbard model

In the experiment [6] effective 1D systems were formed from an anisotropic 3D optical lattice loaded with ultra-cold bosonic atoms [3]. This is done by adiabatically exposing a BEC to far-off resonance standing wave laser fields in three orthogonal directions forming a 3D optical lattice potential $V_{OL}(\mathbf{r}) = \sum_{d=1}^3 V_{d0} \sin^2(q_B r_d)$ where $q_B = 2\pi/\lambda$ and λ is the wavelength of the laser light yielding a lattice period $a = \lambda/2$ [29]. The height of the potential V_{d0} is proportional to the intensity of the d -th pair of laser beams, and is conveniently expressed in terms of the recoil energy $E_r = q_B^2/2m$ for atoms of mass m (taking $\hbar = 1$ throughout).

Effective 1D systems are then formed by making laser intensities in two of the directions $r_2 \equiv y$ and $r_3 \equiv z$ very large ($V_\perp \approx 30E_r$). The confinement is then sufficiently strong to inhibit any tunnelling or excitations in those directions on the energy scales we are concerned with. The result is an array of many isolated effective 1D systems in the $r_1 \equiv x$ direction [6, 30, 4, 5]. For the remaining lattice intensity $V_{10} \equiv V_0$ we consider much shallower depths, but always remain deep enough ($V_0 > 4E_r$) to ensure that there is an appreciable band-gap between the lowest and first excited Bloch band, given in the harmonic approximation by $\omega_{ho} = 2E_r \sqrt{V_0/E_r}$. Combined with the ultra-low temperatures of the atoms this is sufficient to ensure that the dynamics can be described by the lowest Bloch band of the lattice, and that the tight-binding approximation is applicable [3].

With the centre of lattice site j in one such 1D system given by $x_j = ja$ we can construct a complete and orthonormal set of localised mode functions $\phi_j(\mathbf{r}) = w(x - x_j)W(y)W(z)$ factorised as the product of Wannier functions w and W of the lowest

Bloch band for the shallow and deeply confined directions respectively. After expanding the bosonic field operator $\hat{\psi}(\mathbf{r})$ into these modes and restricting our consideration to one 1D system, the resulting Hamiltonian H reduces to the 1D BHM [3] composed of M sites

$$H = -J \sum_{j=1}^{M-1} (b_j^\dagger b_{j+1} + \text{h.c.}) + \sum_{j=1}^M v_j b_j^\dagger b_j + \frac{U}{2} \sum_{j=1}^M b_j^\dagger b_j^\dagger b_j b_j, \quad (6.1)$$

where the operators b_j (b_j^\dagger) are bosonic destruction (creation) operators for an atom in site j . The parameters of the BHM are functions of the lattice depth V_0 with the matrix elements for hopping between adjacent sites j and $j+1$ and on-site interaction strength given by [31]

$$\begin{aligned} J &= - \int dx w(x - x_j) \left(-\frac{\hbar^2}{2m} \frac{d^2}{dx^2} + V_0 \sin^2(q_B x) \right) w(x - x_{j+1}), \\ U &= 2a_s \omega_{ho} \int dx |w(x - x_j)|^4, \end{aligned} \quad (6.2)$$

where a_s is the s -wave scattering length, and a Gaussian ansatz has been used for the tightly confined Wannier states W . The trapping offset is well approximated as $v_j \approx V_T(x_j, y, z)$, where $V_T(\mathbf{r})$ describes an additional slowly varying trapping potential which could be due to magnetic trapping. In the case of [6] the axial potential of the 1D system was dominated by the Gaussian beam envelopes (with $1/e^2$ waists l) of the lasers for the strongly confined directions characterised by the trapping frequency $\omega_T = 2E_r \frac{\lambda}{\pi l} \sqrt{V_\perp/E_r}$ [30].

The physics of the BHM is governed by the ratio U/J . Competition between these two terms results in a transition at temperature $T = 0$ for a critical ratio $(U/J)_c$ from the SF to the MI regime [2, 32]. Mean-field theory for an infinite unit commensurately filled 1D system predicts that $(U/J)_c \approx 2 \times 5.8$. However, if the strong quantum fluctuations present in 1D are taken into account, the appearance of the SF regime is not predicted to occur until the critical ratio drops to $(U/J)_c \approx 3.85$ [33]. The presence of trapping and the finite size of a system modifies the nature of the transition, prohibiting it from being sharp and so in line with the experiment [6] we expect the transition to occur gradually somewhere in between these limits [34].

6.2.2 Lattice modulation excitation scheme

In the experiment [6] the 1D system was initially prepared in the groundstate for some depth V_0 , ranging from the SF to MI regime. The axial lattice depth was then subjected to a modulation of the form

$$V_{OL}(x, t) = V_0[1 + A \sin(\Omega t)] \sin^2(q_B x), \quad (6.3)$$

where A is the modulation amplitude as a fraction of the initial lattice depth, and Ω is the modulation frequency [6]. The modulation was applied for a fixed time $\tau = 30$ ms after which the energy deposited into the system was measured by time-of-flight

imaging of central momentum width averaged over the many 1D systems realised. The applied modulation frequency was taken to a maximum of $\Omega/2\pi = 6$ kHz which defines the relevant energy scale for the system and was well below the band-gap.

To compare with the experiment we take the wavelength of the light used to form the optical lattice as $\lambda = 826$ nm, and the atomic species trapped as ^{87}Rb , where $a_s = 5.1$ nm, in all numerical values quoted. For our calculations we initially computed the groundstate of the system over depths $U/J = 5, 6, \dots, 20$ for the large systems and slightly shallower depths $U/J = 2, 3, \dots, 20$ for the small system¹, all with fixed particle number N . We study a small and large system with box boundaries which are commensurately filled as $M = N = 7$ and $M = N = 41$ respectively. We also consider a harmonically trapped system where $v_j = m\omega_T^2 x_j^2/2$ for a slightly smaller system with $M = 25$ using $\omega_T/2\pi = 70$ Hz and $N = 15$, as well as $\omega_T/2\pi = 100$ Hz and $N = 30$. These trapping frequencies are close to that in the experiment [6, 30] where $\omega_T/2\pi \approx 85$ Hz, and where sufficient to eliminate any occupation at the box boundaries of the system. The modulation given in Eq. (6.3) was then applied to the system by computing time-dependent BHM parameters via Eq. (6.2). This includes an implicit assumption that the Wannier states describing atoms in the lattice adiabatically follow the variations in the lattice potential induced by the modulation. Given that the timescale of atomic motion in a lattice site is $\nu = \omega_{ho}/2\pi$ and that this is typically an order of magnitude greater than the modulation frequencies applied, the adiabatic assumption is reasonable. The response of the system was then measured via the total energy $\langle H_0 \rangle$, with respect to the unperturbed BHM, for different Ω . To demonstrate the evolution of the spectra at different depths we use the same fixed range for $\Omega/2\pi$ at all depths. This range is identical to the experiment and is likewise quoted in kHz while the energy absorbed is expressed in units of E_r .

6.3 Analysis

6.3.1 Linear response

We consider a straightforward linear response treatment of this excitation scheme which follows under the same assumption used for the numerical calculation that the system is described by the BHM with time-varying parameters $J[V_{OL}(t)]$ and $U[V_{OL}(t)]$. For perturbative calculations we make an additional assumption that the modulations are weak and approximate the variation of these functions about the initial depth V_0 linearly resulting in a harmonic perturbation [19]

$$H(t) = H_0 + AV_0 \sin(\Omega t) (\delta U H_0 - J_0 \{\delta J - \delta U\} H_J), \quad (6.4)$$

where $H_0 = -J_0 H_J + U_0 H_U$, $\delta U = \frac{d \ln U}{dV}|_{V_0}$, $\delta J = \frac{d \ln J}{dV}|_{V_0}$, $U_0 = U[V_0]$ and $J_0 = J[V_0]$. The perturbation is split into a part that is proportional to the unperturbed BHM

¹For the exact system we consider shallow depths which are strictly beyond the validity of the tight-binding lowest-band BHM. However, these still provide important information regarding the evolution of the excitation spectrum at shallow depths.

Hamiltonian H_0 and a part proportional to the hopping operator $H_J = \sum_{j=1}^{M-1} (b_j^\dagger b_{j+1} + \text{h.c.})$ under the proviso that $U_0 > J_0$. The first part cannot induce excitations and instead gives a small time-dependent shift to the unperturbed energies which can be ignored. As a result the excitation operator of this perturbation is just the hopping operator [19, 13] with coupling $\kappa = AV_0J_0(\delta J - \delta U)$. By acting over the whole system uniformly it creates excitations with zero quasimomentum as expected.

Let us label the eigenstates of the unperturbed BHM H_0 as $|n\rangle$ with energy ϵ_n . The principle quantities of interest are the excitation probabilities $P_{0\rightarrow n}(\tau, \Omega)$ for the transitions to the excited states $|n\rangle$ from the groundstate $|0\rangle$ due to this perturbation being applied for a time τ with a frequency Ω . In first-order time-dependent perturbation theory these are given by

$$P_{0\rightarrow n}^{(1)}(\tau, \Omega) = \left| t_{0\rightarrow n}^{(1)} \right|^2 = \kappa^2 \left| \langle n | H_J | 0 \rangle I_n^{(1)}(\tau, \Omega) \right|^2, \quad (6.5)$$

where $I_n^{(1)}(\tau, \Omega) = \int_0^\tau dt e^{i\omega_{n0}t} \sin(\Omega t)$ and $\omega_{n0} = (\epsilon_n - \epsilon_0)$. This result reduces under the rotating wave approximation and the limit $\tau \rightarrow \infty$ to the familiar Golden rule result. We also make use of the second-order result

$$P_{0\rightarrow n}^{(2)}(\tau, \Omega) = \left| t_{0\rightarrow n}^{(1)} - \kappa^2 \sum_m \langle n | H_J | m \rangle \langle m | H_J | 0 \rangle I_{nm}^{(2)}(\tau, \Omega) \right|^2, \quad (6.6)$$

where $I_{nm}^{(2)}(\tau, \Omega) = \int_0^\tau dt \int_0^t dt' e^{i\omega_{n0}t} e^{i\omega_{m0}t'} \sin(\Omega t) \sin(\Omega t')$. The total energy absorbed by the system, relative to H_0 , is then $E(\tau, \Omega) = \sum_n \epsilon_n P_{0\rightarrow n}(\tau, \Omega) - \epsilon_0$.

6.3.2 Numerical method

For the large systems investigated later in sections 6.4.2 and 6.4.3 exact integration of the many-body Schrödinger equation is not feasible. To compute these results we employed the TEBD algorithm [35, 36] which is a quasi-exact numerical method that allows the dynamical evolution of 1D quantum lattice systems with nearest-neighbor interactions to be computed efficiently and accurately. The algorithm has been successfully applied to numerous physical systems including the BHM [37, 38, 39, 40, 28, 41]. Not long after being proposed by Vidal it was recognised [38, 42] that TEBD shares some conceptual and formal similarities with the well established density matrix renormalisation group (DMRG) [43, 44] method enabling the development of a new adaptive time-dependent-DMRG algorithm which incorporates optimisations from both. A detailed analysis of the accuracy and error propagation of this method was given by Gobert *et al* [40] and applies quite generally to TEBD also. We do not describe the TEBD algorithm here, except to mention some specific issues, and instead refer the reader to the relevant articles above for more details.

The objective of the simulations in this paper were to map out the response of the system with the modulation frequency Ω and depths U/J which cross the SF-MI transition. For sufficient sampling this required in excess of 1000 simulations for

both the box and harmonically trapped systems presented here. Consequently we were limited for practical reasons to using a truncation parameter $\chi = 30$ (see [36] for an explanation of χ) for all simulations which was lower than that strictly necessary in order to achieve full convergence. Thus we cannot claim that our calculations are quasi-exact and would not expect the many-body state given by the simulation at the end to have a high fidelity with the true state of the system. Instead we treat our calculation as an approximation in the same spirit as the Gutzwiller ansatz [2, 45] (where $\chi = 1$), but with the important difference that since $\chi > 1$ we are permitting a non-negligible amount of quantum correlations. Given that we are only interested in the total energy, which is an observable composed of one- and two-particle correlations, we expect that this approximation should yield quantitative agreement for the system sizes and regimes considered here. Indeed, we have carried out more accurate calculations at specific points which reveal that the total energy is a robust observable with respect to truncation [46]. Consequently, the features of the energy spectrum do emerge, even with this relatively low χ , and the approximations made do not invalidate the results presented here. For simulations of the lattice modulation problem at some specific lattice depths with larger χ see the recent work by Kollath *et al* [28].

6.4 Results

6.4.1 Exact calculation for a small system

We begin by studying the exact dynamical evolution of the BHM under the lattice modulation for a small system composed of $M = 7$ sites and $N = 7$ atoms with box boundary conditions. This system is large enough to produce many of the essential physical features while still permitting the exact eigenstates to be computed [47]. In fact we find that much of what is learnt from the small system can be directly applied to the larger systems. We make use of this by computing the energy spectrum ϵ_n and perturbation matrix elements $\langle n | H_J | 0 \rangle$ for two lattice depths with $U/J = 4$ and $U/J = 20$ representing the SF and MI regimes respectively. In Fig. 6.1(a) the MI spectrum is shown with its characteristic gapped structure composed of Hubbard bands located around multiples of the dominant interaction energy U and spread by finite hopping J . In addition to the spectrum, the perturbation matrix elements $\langle n | H_J | 0 \rangle$ which are of order $\mathcal{O}(J/U)$ or above are shown as the vertical lines. For the MI the most numerous (and strongest) contributions are to the U -Hubbard band which is described by 1-particle-hole (1-ph) excitations like those depicted in Fig. 6.1(c)(i). The matrix elements to the $2U$ -Hubbard band, which is composed of two 1-ph excitations shown in Fig. 6.1(c)(ii), cancel to first order explaining the absence of lines for this manifold. However, there are a small number of matrix elements to first order connecting the groundstate to the $3U$ -Hubbard band via two 1-ph excitations with both particles on the same site as in Fig. 6.1(c)(iii), but not to three 1-ph excitations as in Fig. 6.1(c)(iv). In Fig. 6.1(b) the ‘gapless’ SF spectrum is shown. Here in contrast to the MI there are significant contributions to $\langle n | H_J | 0 \rangle$ stretching from below an energy of U to below $3U$. Separated from this there are contributions tightly distributed around $4U$.

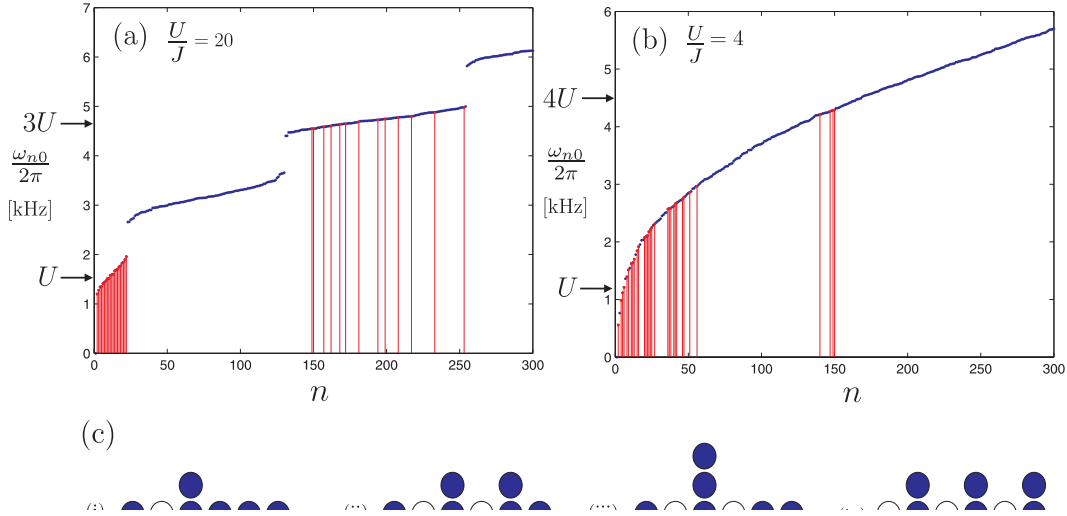


Figure 6.1. The energy spectra for the first 300 eigenstates n for (a) $U/J = 20$ MI regime, and (b) $U/J = 4$ SF regime. In both cases the vertical (red) lines denote the presence of a matrix element $|\langle n | H_J | 0 \rangle|$ connecting an excited state to the groundstate which is of order $\mathcal{O}(J/U)$ or above. In (c) a schematic depiction of the excitations which exist in the (i) U -, (ii) $2U$ - and (iii-iv) $3U$ -Hubbard bands of the MI regime in (a) is given.

Given the comparatively equal strengths of the hopping and interaction terms for the SF regime at $U/J = 4$ there is no simple picture of either the groundstate or the excitations related to these contributions as there was for the MI regime. Despite this the exact eigenstates for this small system do reveal two important details: firstly two 1-ph configurations like those in Fig. 6.1(c)(iii) have an average energy relative to the $U/J = 4$ groundstate which exceeds $4U$; and secondly these types of configurations are the dominant contributions in the relevant eigenstates around $4U$. This overlap in the nature of the excitations points to the possibility, which we shall shortly confirm, that a resonance to $3U$ excitations in the MI regime will evolve into a $4U$ resonance as the SF regime is entered.

We first consider the modulation scheme with a weak amplitude $A = 0.01$ where linear-response is applicable. In Fig. 6.2 (a) the total energy of the system ϵ is shown after the modulation as a function of Ω for the MI regime with $U/J = 20$. As expected from the matrix elements $\langle n | H_J | 0 \rangle$ in Fig. 6.1(a) there is strong response centred around U spread by the width of the U -Hubbard band which is approximately $10J \sim 0.8$ [kHz], and a smaller (barely visible) response at $3U$. The linear response predictions based on Eq. (6.5) are shown also and agree well. For the largest peak the growth of energy over the modulation time is shown in Fig. 6.2(b) and the slight overestimation of the energy by linear-response is evident at later times. The same calculation for the SF regime with $U/J = 4$ is shown in Fig. 6.2(b). Again the results of linear-response agree well and the structure follows that of perturbation matrix elements with a broader

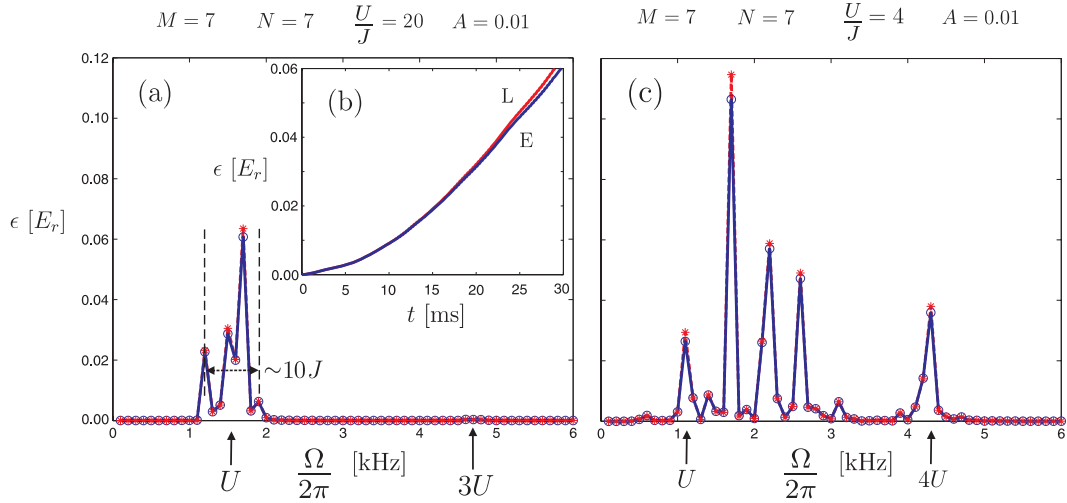


Figure 6.2. For a weak modulation of the small system we have (a) the total energy ϵ absorbed in the MI regime with $U/J = 20$ as a function of Ω , (b) ϵ over time for the largest MI peak at $\Omega/2\pi \sim 1.7$ [kHz] for the exact (E) and linear-response (L) calculations, and (c) ϵ against Ω for the SF regime with $U/J = 4$. In (a) and (c) the markers (o) and (*) denote the exact and linear response results respectively, while the lines are drawn to guide the eye.

response between U and $3U$ and an equivalent strength resonance at $4U$.

In line with the experiment [6] from this point on we consider much stronger modulations with $A = 0.2$. The result of these for the MI and SF regimes is given in Fig. 6.3. For the MI in Fig. 6.3(a) we see that the discrete resonances around U have now filled out into a single peak centred on U that is about 25% wider than the U -Hubbard band at ~ 1 [kHz], and that the stronger modulation has now increased height of the $3U$ peak relative to the U peak. In Fig. 6.3(a) we have also included both first- and second-order perturbation theory results. For such strong modulations the applicability of perturbation theory is highly questionable, especially for the long times considered here. This is exemplified by the gross overestimation of the central peak at U by both linear- and quadratic-response. In Fig. 6.3(b) curve (i) shows the saturation of energy absorption for the central peak at U and departure from linear response after a short time. In contrast for the peak at $3U$ Fig. 6.3(b) curve (ii) shows that linear-response underestimates the energy absorbed due to its neglect of the role these eigenstates play in the indirect processes to higher energies. However, the use of quadratic-response given by Eq. (6.6) provides some useful insight into the additional structure seen for the strong modulation which do not appear for weak modulations and is not predicted by linear-response. Specifically, the small satellite peaks either side of the dominant peak at U , which are located at $U/2$ and $3U/2$ respectively, only appear at second and higher order leading to their natural identification as the absorption of two quanta of energy Ω from the perturbation to reach to U - and $3U$ -Hubbard bands. We note also that even under strong modulations no resonance at $2U$ is seen in

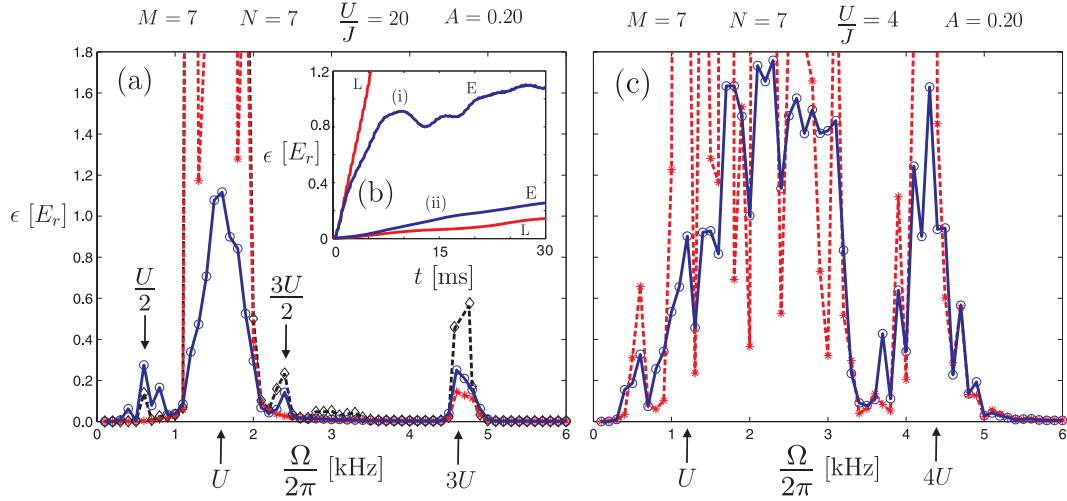


Figure 6.3. For a strong modulation of the small system we have (a) the total energy ϵ absorbed in the MI regime with $U/J = 20$ as a function of Ω , (b) ϵ over the time at the MI peaks (i) U and (ii) $3U$ for the exact (E) and linear-response (L) calculations, and (c) ϵ against Ω in the SF regime with $U/J = 4$. For (a) and (c) the markers (o), (*) denote the exact and linear-response results respectively, while in (a) (◊) denotes the quadratic-response. The lines are drawn to guide the eye.

agreement with recent findings [28] for commensurate systems. For the SF regime in Fig. 6.3(c) a broad response is seen spanning the region between U and $3U$ consistent with linear response, but higher-order effects have resulted in saturation and merging of linear response peaks. As with weaker modulations there is a separate resonance centred at $4U$ which is now as equivalent in strength and broader.

With the full exact calculation we have computed the response of the system for a sequence of depths $U/J = 2, 3, \dots, 20$ which are displayed in Fig. 6.4 (a) demonstrating the evolution of the MI spectrum in Fig. 6.3 (a) into SF spectrum in Fig. 6.3 (c) with decreasing lattice depth. By examining the accompanying colour-map in Fig. 6.4 (b) we can make a number of initial observations regarding the changing characteristics of the spectrum over the SF-MI transition. Firstly, as with the weak modulations, the MI peak at U is seen to broaden and shift upwards in energy into the SF response, and this change is most prominent after the depth is lower than $U/J \sim 12$. Secondly, it is now clear that the resonance at $3U$ for deep in the MI regime reduces only slightly in energy and ends up as the $4U$ resonance in the SF regime. Additionally, in line with weaker modulations in Fig. 6.2, the $4U$ peak is stronger than the $3U$ peak it evolves from, and signatures of this change are already visible in Fig. 6.4 (a). Finally, by progressing to slightly shallower depths ($U/J = 2, 3$) in Fig. 6.4 we see the broadening of the SF spectrum over the entire frequency range considered caused by the eventual merging of the U to $3U$ response with the $4U$ peak.

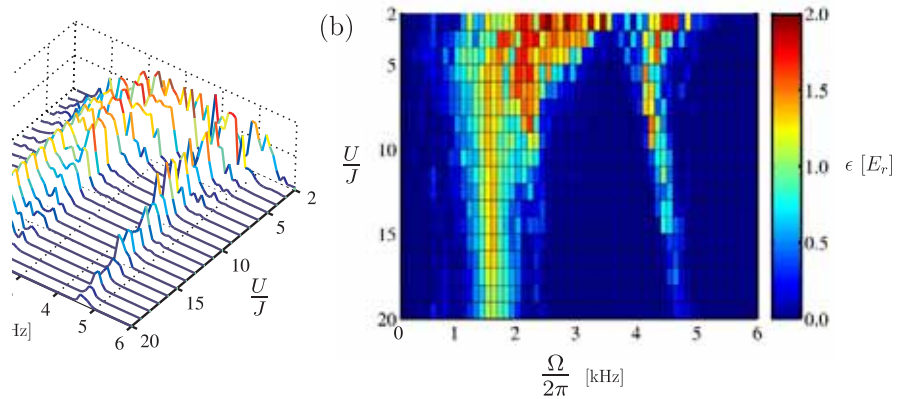


Figure 6.4. (a) The total energy ϵ absorbed by a small box system over a sequence of depths, ranging from the MI to SF regimes, as a function of Ω for strong modulations. (b) A colour-map of plot (a).

6.4.2 Large system in a box

To put some of the observations made in the previous section on a firmer footing we now examine a larger system with $M = 41$ and $N = 41$, again with box boundaries, under the same modulation scheme with $A = 0.2$. To compute the dynamical evolution for this system we resort to the TEBD algorithm using a lattice site dimension $d_s = 5$. In Fig. 6.5 the one-particle density matrix $\rho_{jk} = \langle b_j^\dagger b_k \rangle$ for the groundstate of (a) the MI with $U/J = 20$ and (b) the SF with $U/J = 5$ is plotted, along with the corresponding spectra obtained from these groundstates in (c) and (d) respectively. As might be expected the increase in the size of the system reduces finite size effects resulting in much smoother excitation profiles. However, the essential features of these plots still follow directly from our analysis of a small system in terms of both the position and width of the resonances. Specifically, the width of the U peak in Fig. 6.5(c) is again slightly larger than the width of the U -Hubbard band for this system given approximately by first order perturbation theory as $12J \sim 1$ [kHz]. The effects of saturation also appear to follow similarly with the maximum energy absorbed per particle being nearly identical for the two system sizes.

The absorption spectrum over a sequence of depths $U/J = 5, 6, \dots, 20$ ranging from the SF to MI regime are shown in Fig. 6.6. The increased size of the system permits us to investigate more conclusively some of the observations made earlier regarding the evolution of the absorption spectra with decreasing depth. Firstly, we focus on the maximum strength of the $3U \rightarrow 4U$ peak with U/J which is shown in Fig. 6.7 (a). The plot shows that the strength of this peak displays a distinct alteration in its behavior close to $U/J \sim 10$ where it jumps from an increasing to a decreasing curve. This behaviour is consistent with what was seen earlier for the small system and can be attributed to the increasing SF character with a strong $4U$ peak becoming dominant over the weaker $3U$ MI peak.

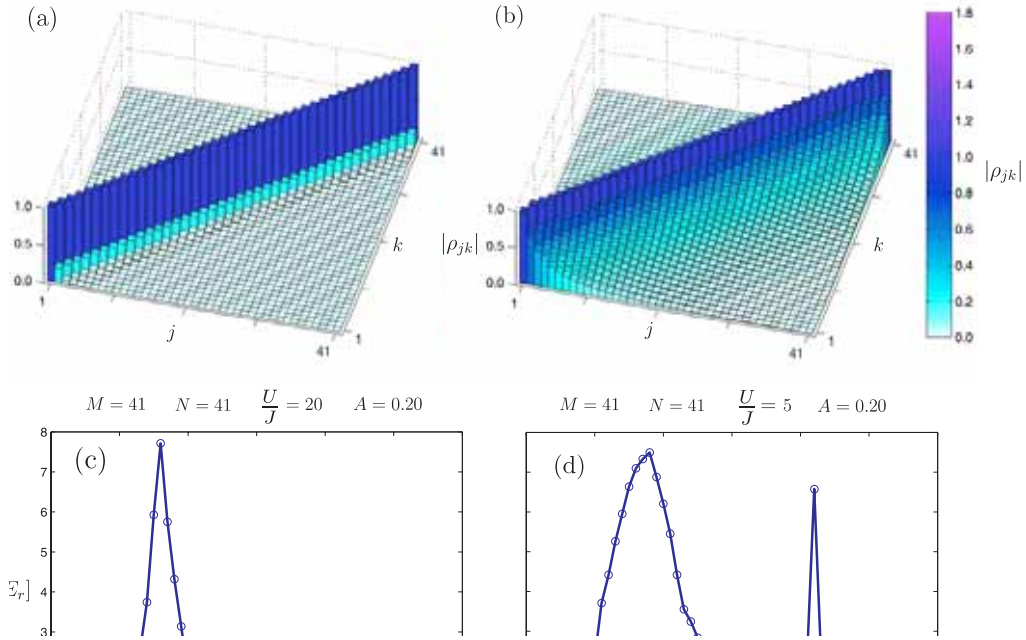


Figure 6.5. The one-particle density matrix ρ_{jk} of the groundstate for (a) the MI regime with $U/J = 20$ and (b) the SF regime with $U/J = 5$. The corresponding excitation spectra of the total energy ϵ against Ω for these groundstate is shown in (c) and (d) respectively.

To understand the changes exhibited by the resonance around U we fit this peak with a smoothed-box function of the form

$$\epsilon(\Omega) = \epsilon_{\min} + \mathcal{N} \frac{\epsilon_{\max} - \epsilon_{\min}}{1 + e^{[(\Omega - \Omega_c)^2 - w^2]/s^2}}, \quad (6.7)$$

where Ω_c , w and s are parameters specifying the center, top width and step size of the profile respectively, whilst $\mathcal{N} = 1 + e^{-w^2/s^2}$ is the scaling factor. The advantages of this function (which are even more apparent in the next section) is that it faithfully describes both the width and centre location of broad topped resonances. The centre Ω_c and the full-width-half-maximum Ω_w extracted from this fitting then characterises quantitatively the behaviour which is evident in Fig. 6.6 (b).

In Fig. 6.7 (b) we see that the centre Ω_c of the U peak remains relatively stationary until $U/J \sim 12$ where it then shifts more dramatically to higher energies. This is again a signature of increasing SF character consistent with the disappearance of the gap between the U - and $2U$ -Hubbard bands and the shifting of the strongest contributions

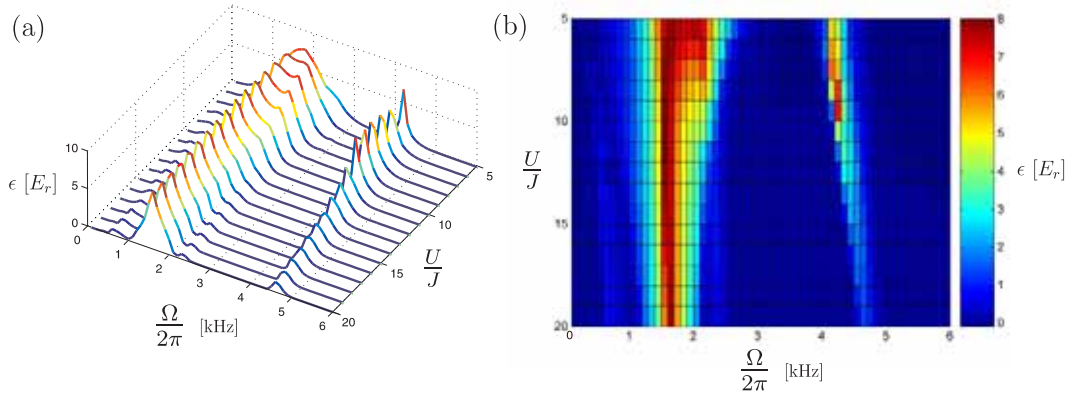


Figure 6.6. (a) The total energy ϵ absorbed by a large box system over a sequence of depths, ranging from the MI to SF regimes, as a function of Ω for strong modulations. (b) A colour-map of plot (a).

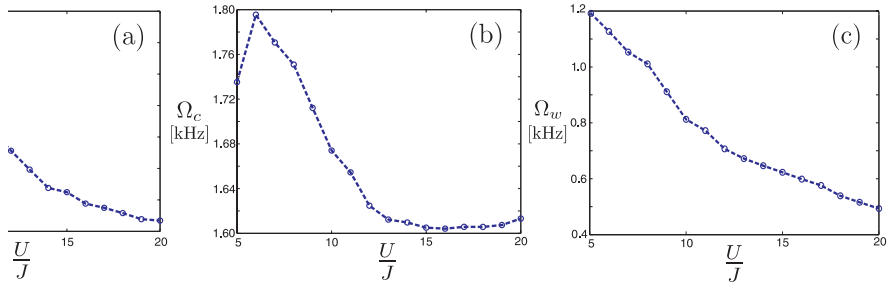


Figure 6.7. (a) The maximum energy ϵ absorbed for the $3U \rightarrow 4U$ peak with the lattice depth U/J . (b) The centre position Ω_c , and (c) width Ω_w of the U resonance with the lattice depth U/J . The dotted lines in all cases is drawn to guide the eye.

to $\langle n | H_J | 0 \rangle$ to higher frequency seen for the small system. The width Ω_w in Fig. 6.7 (c) instead displays a gradual increase without any pronounced changes.

It is clear from the structure of both the MI and SF spectra shown in Fig. 6.5(c) and (d) that the box system has some differences compared to the 1D spectra obtained in the experiment. These differences are not surprising given that the SF state of the box system at $U/J = 5$ exhibits significant quantum depletion of 75%, which is much larger than that in the experiment. Also, at all depths considered here the groundstate of the box has a near homogeneous density of 1 atom per site, as can be seen in Fig. 6.5(a) and (b), which is different from the harmonically trapped system in the experiment.

6.4.3 Large harmonically trapped system

To approach a setup closer to that of the experiment we now consider a system with $M = 25$ and $N = 15$ superimposed with harmonic trapping using $\omega_T/2\pi = 70$ Hz. A

significant difference is that at $U/J = 5$ the depletion of the SF state is reduced to 50% in line with the experiment for this setup. The one-particle density matrices for the MI and SF groundstates in this case are shown in Fig. 6.8(a) and (b) respectively. We now see that the MI state is composed of a central core with unit filling along with small SF lobes at the edges. This change in structure compared to Fig. 6.5(a) introduces additional types of excitations such as those caused by particles hopping into the vacuum surrounding the MI core. For the SF state there are now significantly greater off-diagonal correlations in ρ_{jk} compared to the box system. Despite these differences, however, the form of the spectrum shown in Fig. 6.8(c) and (d) remains very close to the box system displaying the same characteristic peaks as before. The effects of trapping manifest themselves in this case by flattening of the U peak, along with the broadening and shifting of the $4U$ peak. The maximum energy per particle again remains approximately equal to the previous cases considered, showing that the saturation effects are not significantly altered by the trapping.

In Fig. 6.9 we report the spectra for the system ranging over SF to MI regimes as before. Again, the essential features of this plot follow from our earlier discussion. Performing the same analysis on the evolution of the spectrum demonstrates that maximum strength of the $3U \rightarrow 4U$ peak has a maximum at $U/J \sim 8$ as shown in Fig. 6.10(a). The trapping is also seen to introduce peaks and troughs to this curve compared to the smooth behaviour of the box system. Also, in contrast to the box both the centre Ω_c and width Ω_w of the U resonance show a gradual change from the MI to SF character in Fig. 6.10(b) and (c). This reflects a difference in the evolution of U resonance, which for the box develops a two-peaked structure in Fig. 6.6(a), whereas in the harmonic trap this is washed out into a broader and flatter response in Fig. 6.9(a).

We have seen that the introduction of harmonic trapping for the case considered above has not lead to any new features in the spectrum beyond a small amount of shifting and broadening. One such feature which might be expected is the emergence of a resonance at $2U$. However, it is known that the relevant excitation processes for a $2U$ resonance require either excitations to already be present in the system due to finite temperature [13], or significant inhomogeneity in the density caused by a trap [28]. Since the system above is at $T = 0$ and has virtually no incommensurability in the MI, beyond the small SF lobes at the edges, the lack of a $2U$ resonance is consistent. In the experiment both finite-temperature and inhomogeneity are expected to make important contributions to the spectrum. Presently there are still open questions as to which is the most dominant and what interplay there might be between these effects. Future studies with the TEBD algorithm, exploiting recent developments which permit the simulation of master equation evolution of 1D finite-temperature and dissipative systems [48], could allow both these effects to be treated on an equal footing.

To demonstrate the contribution of inhomogeneity we have performed additional calculations again using $M = 25$ but with a larger occupancy of $N = 30$ and larger trapping frequency $\omega_T/2\pi = 100$ Hz. In Fig. 6.11(a) the one-particle density matrix of the MI groundstate at $U/J = 20$ is shown and displays the coexistence of significant MI and SF regions characteristic of trapped systems. Despite using a larger lattice site dimension $d_s = 6$ for this setup we found that truncation in on-site occupancy limited

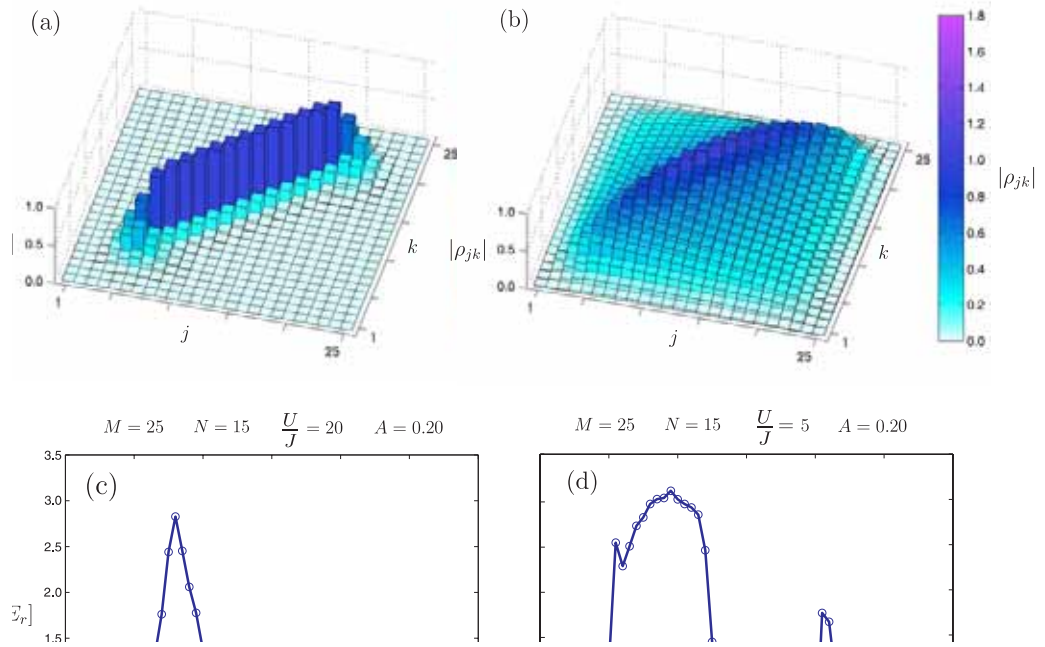


Figure 6.8. The one-particle density matrix ρ_{jk} of the groundstate for a trapped system with $\omega_T/2\pi = 70$ Hz for (a) the MI regime with $U/J = 20$ and (b) the SF regime with $U/J = 5$. The corresponding excitation spectra of the total energy ϵ against the modulation frequency Ω for these groundstate are shown in (c) and (d) respectively.

the smallest U/J from which we could reliably compute the spectrum to $U/J = 9$. The one-particle density matrix for the $U/J = 9$ groundstate is shown in Fig. 6.11(b) and appears to be dominated by a central SF region. The excitation spectra for these two groundstates are shown in Fig. 6.11(c) and (d) respectively. For the MI in Fig. 6.11(c) a pronounced $2U$ resonance is seen in addition to the peaks seen in previous MI spectra. The appearance of a $2U$ peak in the $T = 0$ case examined here arises predominantly from particles in the unit filled MI shell hopping into the doubly occupied region at the centre [28, 6] which is evident in the one-particle density matrix shown in Fig. 6.11(a). For the shallower depth $U/J = 9$ the spectrum in Fig. 6.11(d) exhibits the initial merging of the U and $4U$ peaks with this $2U$ peak. In Fig. 6.12 the evolution of the spectrum between these limits is shown. The form of these spectra is very reminiscent of that found in the experiment [6] and it is likely that a more detailed analysis of this setup to shallower lattice depths would reveal the broad SF resonance seen there.

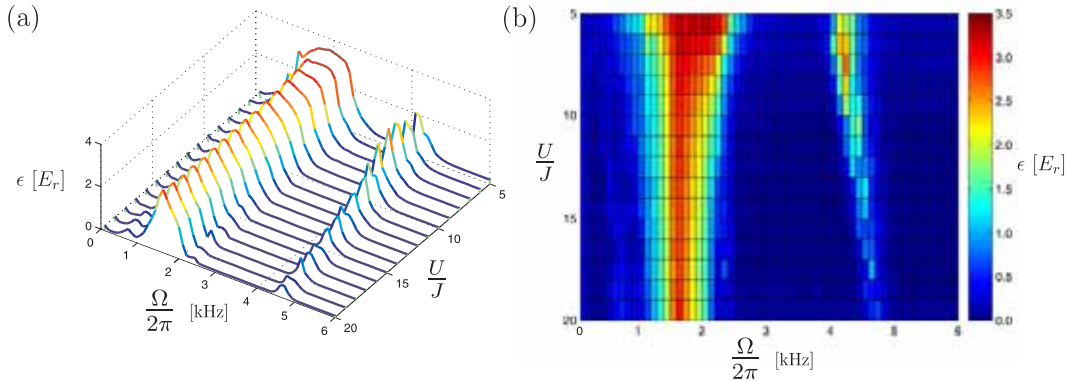


Figure 6.9. (a) The total energy ϵ absorbed by a $M = 25$ and $N = 15$ harmonically trapped system over a sequence of depths, ranging from the MI to SF regimes, as a function of Ω for strong modulations. (b) A colour-map of plot (a).

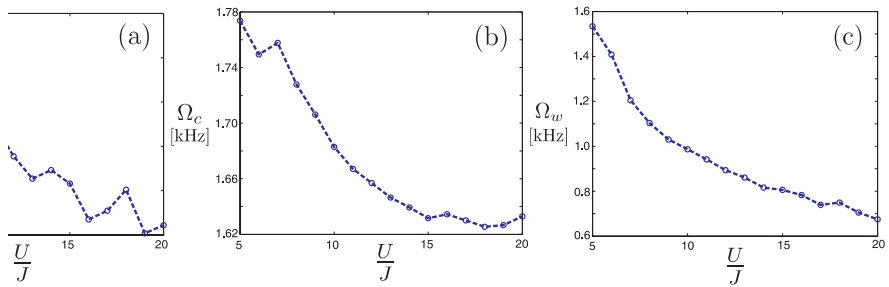


Figure 6.10. (a) The maximum energy ϵ absorbed for the $3U \rightarrow 4U$ peak with the lattice depth U/J . (b) The centre position Ω_c , and (c) width Ω_w of the U resonance with the lattice depth U/J . The dotted lines in all cases is drawn to guide the eye.

6.5 Conclusions

We have examined in detail the dynamical response at $T = 0$ of the ultracold atoms in an optical lattice subjected to lattice modulations. We have reported the evolution of the excitation spectrum with the lattice depth from the SF to MI regime for small and large box systems, and for large harmonically trapped systems. For the box system we identified two pronounced signatures of the transition from the MI to SF regime, specifically the strength of the $3U \rightarrow 4U$ peak and the centre of the U resonance. The introduction of trapping for the case considered here, where the occupancy remains less than or equal to unity, does not significantly alter the evolution of the spectrum compared to a box system. While we find that it does wash out any pronounced changes in the structure of the U resonance with depth, the strength of the $3U \rightarrow 4U$ peak still exhibits a signature of increasing SF character.

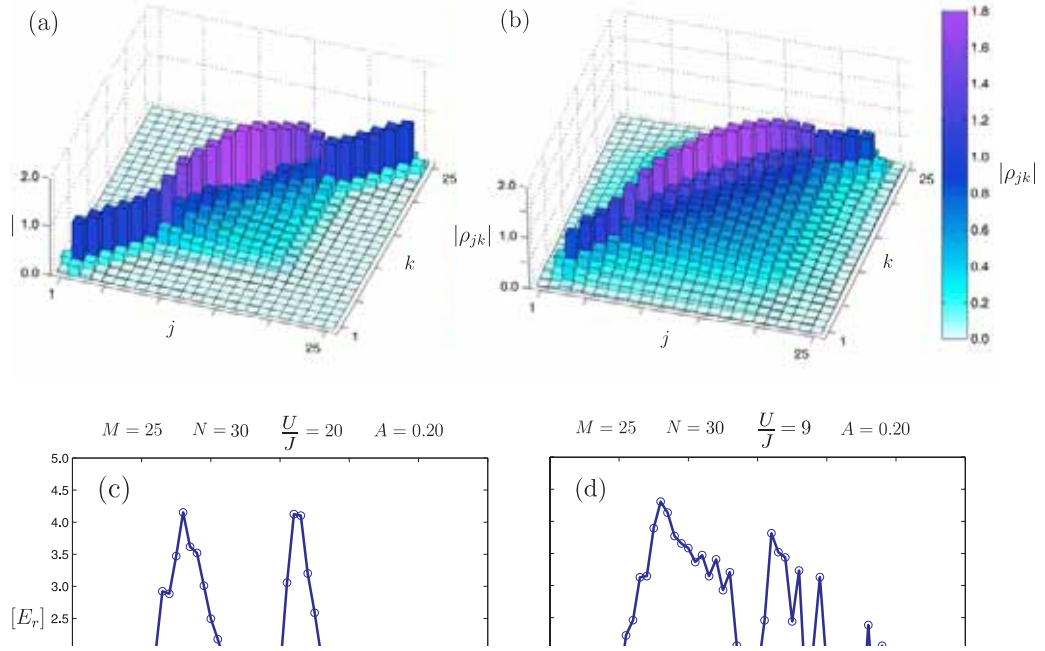


Figure 6.11. The one-particle density matrix ρ_{jk} of the groundstate for a trapped system with $\omega_T/2\pi = 100$ Hz for (a) the MI regime with $U/J = 20$ and (b) an intermediate regime with $U/J = 9$. The corresponding excitation spectra of the total energy ϵ against the modulation frequency Ω for these groundstate are shown in (c) and (d) respectively.

We also presented calculations showing spectra progressing from the MI regime for a harmonically trapped system which has a central region with greater than unit filling. We found that this changes the structure of the spectrum by introducing a $2U$ resonance and brings our results closer with the experiment. Direct comparison to the experiment [6], however, is difficult due to the 3D rethermalisation performed prior to measurement, which cannot be simulated with TEBD, and the fact that the measurement itself was an averaged result over many 1D systems in parallel with differing total particle number. Despite this our results point to that fact that the BHM is sufficient to explain all the features discovered in the experiment and that the experiment was a clean realisation of this model as expected.

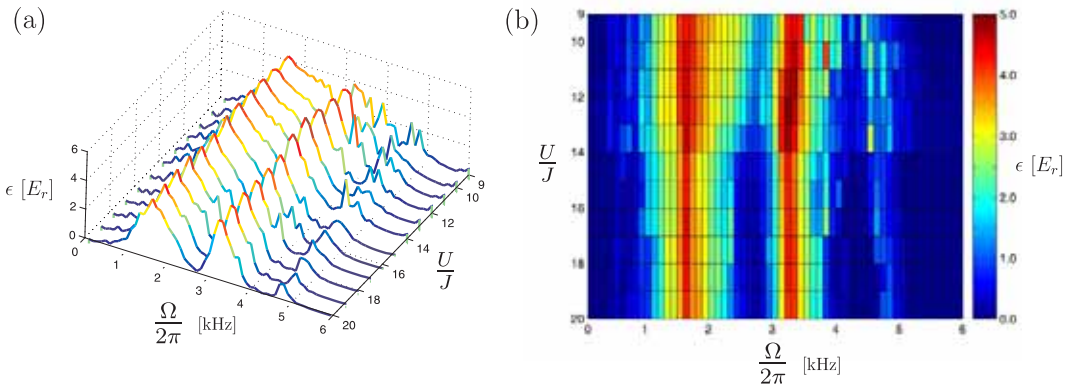


Figure 6.12. (a) The total energy ϵ absorbed by a $M = 25$, $N = 30$ harmonically trapped system over a sequence of depths, ranging from the MI to SF regimes, as a function of Ω for strong modulations. (b) A colour-map of plot (a).

References

- [1] M. Greiner, O. Mandel, T. Esslinger, T.W. Hänsch, I. Bloch, *Nature (London)* **415**, 39 (2002).
- [2] M.P.A. Fisher, P.B. Weichman, G. Grinstein, D.S. Fisher, *Phys. Rev. B* **40**, 546 (1989)
- [3] D. Jaksch, C. Bruder, J.I. Cirac, C.W. Gardiner, P. Zoller, *Phys. Rev. Lett.* **81**, 3108 (1998).
- [4] B. Paredes, A. Widera, V. Murg, O. Mandel, S. Fölling, J.I. Cirac, G.V. Shlyapnikov, T.W. Hänsch, I. Bloch, *Nature (London)* **429**, 277 (2004).
- [5] T. Kinoshita, T. Wenger, D.S. Weiss, *Science* **305**, 1125 (2004).
- [6] T. Stöferle, H. Moritz, C. Schori, M. Köhl, T. Esslinger, *Phys. Rev. Lett.* **92**, 130403 (2004).
- [7] M. Köhl, H. Moritz, T. Stöferle, C. Schori, T. Esslinger, *J. Low Temp. Phys.* **138**, 635 (2005).
- [8] K. Günter, T. Stöferle, H. Moritz, M. Köhl, T. Esslinger, *Phys. Rev. Lett.* **96**, 180402 (2006).
- [9] S. Ospelkaus, C. Ospelkaus, O. Wille, M. Succo, P. Ernst, K. Sengstock, K. Bongs, *Phys. Rev. Lett.* **96**, 180403 (2006).
- [10] R. Roth, K. Burnett, *J. Phys. B* **37**, 3893 (2004).
- [11] G.G. Batrouni, F.F. Assaad, R.T. Scalettar, P.J.H. Denteneer, *Phys. Rev. A* **72**, 031601(R) (2005).

- [12] A.M. Rey, P. Blakie Blair, G. Pupillo, C.J. Williams, C.W. Clark, *Phys. Rev. A* **72**, 023407 (2005).
- [13] A. Reischl, K.P. Schmidt, G.S. Uhrig, *Phys. Rev. A* **72**, 063609 (2005).
- [14] T. Giamarchi *Quantum Physics in One Dimension* (Oxford University Press, Oxford, 2004)
- [15] C. Menotti, M. Krämer, L. Pitaevskii, S. Stringari, *Phys. Rev. A* **67**, 053609 (2003).
- [16] H.P. Büchler, G. Blatter, [arXiv:cond-mat/0312526](https://arxiv.org/abs/cond-mat/0312526).
- [17] M. Krämer, C. Tozzo, F. Dalfovo, *Phys. Rev. A* **71** 061602(R) (2004).
- [18] C. Tozzo, M. Krämer, F. Dalfovo, *Phys. Rev. A* **72**, 023613 (2005).
- [19] A. Iucci, M.A. Cazilla, A.F. Ho, T. Giamarchi, *Phys. Rev. A* **73** 041608 (2006).
- [20] O. Mandel, M. Greiner, A. Widera, T. Rom, T.W. Hänsch, I. Bloch, *Nature (London)* **425**, 937 (2003).
- [21] D. Jaksch, H.-J. Briegel, J.I. Cirac, C.W. Gardiner, P. Zoller, *Phys. Rev. Lett.* **82**, 1975 (1999).
- [22] U. Dorner, P. Fedichev, D. Jaksch, M. Lewenstein, P. Zoller, *Phys. Rev. Lett.* **91** 073601 (2003).
- [23] J.K. Pachos, P.L. Knight, *Phys. Rev. Lett.* **91**, 107902 (2003).
- [24] G.K. Brennen, C.M. Caves, P.S. Jessen, I.H. Deutsch, *Phys. Rev. Lett.* **82** 1060 (1999).
- [25] S.R. Clark, C. Moura-Alves, D. Jaksch, *New J. Phys.* **7**, 124 (2005).
- [26] E. Jane, G. Vidal, W. Dür, P. Zoller, J.I. Cirac, *Quant. Inf. Comput.* **3**, 15 (2003).
- [27] A. Sørensen, K. Mølmer, *Phys. Rev. Lett.* **83**, 2274 (1999).
- [28] C. Kollath, A. Iucci, T. Giamarchi, W. Hofstetter, U. Schollwöck, *Phys. Rev. Lett.* **97**, 050402 (2006).
- [29] D. Jaksch, P. Zoller, *Ann. Phys. (N.Y.)* **315**, 52 (2004).
- [30] H. Moritz, T. Stöferle, M. Köhl, T. Esslinger, *Phys. Rev. Lett.* **91**, 250402 (2003).
- [31] W. Zwerger, *J. Opt. B* **5**, 9 (2003).
- [32] S. Sachdev, *Quantum Phase Transitions* (Cambridge Univ. Press, Cambridge, 2001).
- [33] T. Küchner, H. Monien, *Phys. Rev. B* **58**, R14741 (1998).
- [34] G.G. Batrouni, V. Rousseau, R.T. Scalettar, M. Rigol, A. Muramatsu, P.J.H. Denteneer, M. Troyer, *Phys. Rev. Lett.* **89**, 117203 (2002).
- [35] G. Vidal, *Phys. Rev. Lett.* **91**, 147902 (2003).
- [36] G. Vidal, *Phys. Rev. Lett.* **93**, 040502 (2004).
- [37] S.R. Clark, D. Jaksch, *Phys. Rev. A* **70**, 043612 (2004).

- [38] A.J. Daley, C. Kollath, U. Schollwöck, G. Vidal, *J. Stat. Mech.* P04005 (2004).
- [39] A.J. Daley, S.R. Clark, D. Jaksch, P. Zoller, *Phys. Rev. A* **72**, 043618 (2005).
- [40] D. Gobert, C. Kollath, U. Schollwoeck, G. Schuetz, *Phys. Rev. E* **71**, 036102 (2005).
- [41] C. Kollath, U. Schollwöck, J. von Delft, W. Zwerger, *Phys. Rev. A* **71**, 053606 (2005).
- [42] S.R. White, A.E. Feiguin, *Phys. Rev. Lett.* **93**, 076401 (2004).
- [43] S.R. White, *Phys. Rev. Lett.* **69**, 2863 (1992); *ibid Phys. Rev. B* **48**, 10345 (1993).
- [44] U. Schollwöck, *Rev. Mod. Phys.* **77**, 259 (2005).
- [45] W. Krauth, M. Caffarel, J.P. Bouchaud, *Phys. Rev. B* **45**, 3137 (1992).
- [46] M.C. Bañuls, R. Orús, J.I. Latorre, A. Pérez, P. Ruiz-Femenia, *Phys. Rev. A* **73**, 022344 (2006).
- [47] K. Braun-Munzinger, J.A. Dunningham, K. Burnett, *Phys. Rev. A* **69**, 053613 (2004).
- [48] M. Zwolak, G. Vidal, *Phys. Rev. Lett.* **93**, 207205 (2004).

Part III

Quantum State Engineering

CHAPTER 7

QUANTUM STATE ENGINEERING WITH OPTICAL LATTICES

Up to now we have been considering the dynamical behaviour of alkali atoms in optical lattices which were in a single fixed internal state $|g\rangle$ and whose dynamical behaviour was governed by the standard Bose-Hubbard model. In chapter 3 we detailed how the strength of the optical potential crucially depends on the atomic dipole transition matrix element between the internal states involved and the polarisation of light used. In this short chapter we shall outline how dipole selection rules for optical transitions can be exploited to create independent potentials for different internal states of the same atomic species. This novel feature then permits a much richer set of model Hamiltonians, involving effective spin-like degrees of freedom, to be engineered. We consider the simplest case here involving only two internal states¹. This situation then lends itself to quantum information processing involving qubits, or more specifically quantum state engineering in which precise knowledge and control of the system's state is required. As we shall describe, state-dependent optical lattices allow this to be achieved either by exploiting the near-perfect realisation of some model Hamiltonian or through the direct implementation of quantum gates via quantum optical manipulation.

7.1 State-dependent optical lattices

Our case of interest is an atom with the fine structure shown in figure Fig. 7.1(a), like that for ^{23}Na or ^{87}Rb commonly used in experiments [1, 2], which interacts with two circularly polarised laser beams σ^\pm . The right circularly polarised light σ^+ couples the level $S_{1/2}$ with $m_j = -\frac{1}{2}$ to the two excited levels $P_{1/2}$ and $P_{3/2}$ with $m_j = \frac{1}{2}$, which are separated from it by energies $\hbar\omega_1$ and $\hbar\omega_2$, respectively. The resulting optical potential is the sum of the two AC Stark shifts, and if the laser frequency ω is chosen so $\omega_1 < \omega < \omega_2$ the two contributions will have opposite detunings which gives rise to a point $\omega = \omega_c$ in which they cancel exactly, as depicted in Fig. 7.1(b). Thus at $\omega = \omega_c$ the state $S_{1/2}$ with $m_j = -\frac{1}{2}$ decouples from the σ^+ laser field. Since σ^+ light only couples the $S_{1/2}$ with $m_j = \frac{1}{2}$ state to the $P_{3/2}$ with $m_j = \frac{3}{2}$ state its AC Stark shift is non-zero and it will experience an optical potential [3]. At precisely frequency ω_c

¹Not to be confused with the two internal states $|g\rangle$ and $|e\rangle$ used earlier in chapter 3.

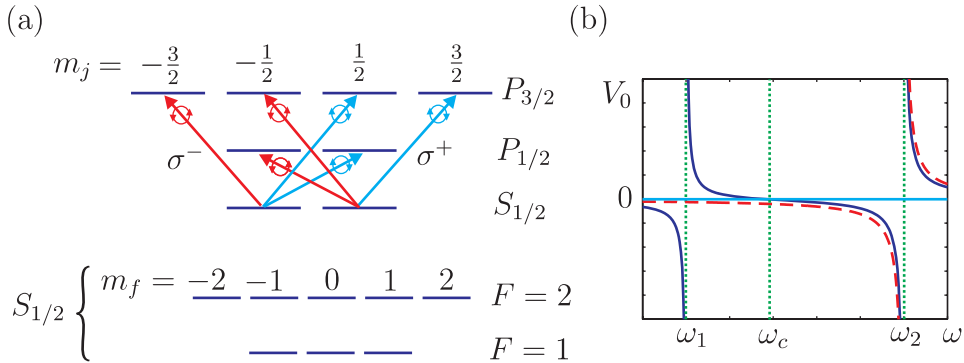


Figure 7.1. (a) The three lowest levels of the fine structure (top) and hyperfine structure (bottom) of the \$S_{1/2}\$ manifold for an atom with nuclear spin \$I = \frac{3}{2}\$, e.g. alkali atoms \$^{23}\text{Na}\$ or \$^{87}\text{Rb}\$. The arrows in the fine structure diagram indicate the electric dipole transitions induced by circularly polarised light \$\sigma^\pm\$ on the \$S_{1/2}\$ levels. Notice that for \$\sigma^+\$ light the \$m_j = -\frac{1}{2}\$ level has transitions to the \$P_{1/2}\$ and \$P_{3/2}\$ levels, whereas \$m_j = \frac{1}{2}\$ only couples to \$P_{3/2}\$. (b) A schematic plot of the AC Stark shift for the \$S_{1/2}\$ levels with \$m_j = -\frac{1}{2}\$ (solid lines) and \$m_j = \frac{1}{2}\$ (dashed lines) as a function of the laser frequency \$\omega\$ of \$\sigma^+\$ polarised light. By tuning \$\omega\$ to \$\omega_c\$, in between the two resonant frequencies \$\omega_1\$ and \$\omega_2\$ for the transitions to the \$P_{1/2}\$ and \$P_{3/2}\$ levels, the overall AC Stark shift for the \$m_j = -\frac{1}{2}\$ level can be made zero.

the same effect can be achieved with \$\sigma^-\$. Therefore at \$\omega = \omega_c\$ the AC Stark shifts of the \$m_j = \pm \frac{1}{2}\$ levels are purely due to \$\sigma^\pm\$ polarised light generating the potentials \$V_\pm(x)\$. The hyperfine states in the \$S_{1/2}\$ manifold is also shown in Fig. 7.1(a). Their corresponding level shifts \$V_{F,m_f}(x)\$ are related to the fine level shifts \$V_\pm(x)\$ by the Clebsch-Gordan coefficients. In particular, this gives [3]

$$\begin{aligned} V_{2,2}(x) &= V_+(x), & \text{for } & |F=2, m_f=2\rangle, \\ V_{1,1}(x) &= \frac{1}{4}V_+(x) + \frac{3}{4}V_-(x), & \text{for } & |F=1, m_f=1\rangle, \end{aligned} \quad (7.1)$$

which we will make use of very shortly.

The two standing waves with \$\sigma^\pm\$ polarisation can be produced by two linearly polarised counter-propagating running waves with the same intensity. More precisely, we consider the wave travelling with wave-vector \$\mathbf{k} = k \mathbf{e}_x\$ along the \$x\$-axis with an angle of \$2\theta\$ between their corresponding electric fields²

$$\begin{aligned} \mathbf{E}_1(\mathbf{r}, t) &= E [\cos(\theta)\mathbf{e}_y + \sin(\theta)\mathbf{e}_z] e^{i\mathbf{k}\cdot\mathbf{r}-i\omega t}, \\ \mathbf{E}_2(\mathbf{r}, t) &= E [\cos(\theta)\mathbf{e}_y - \sin(\theta)\mathbf{e}_z] e^{i\mathbf{k}\cdot\mathbf{r}-i\omega t}, \end{aligned}$$

²Following standard conventions the physical electric field is the real part of this complex quantity.

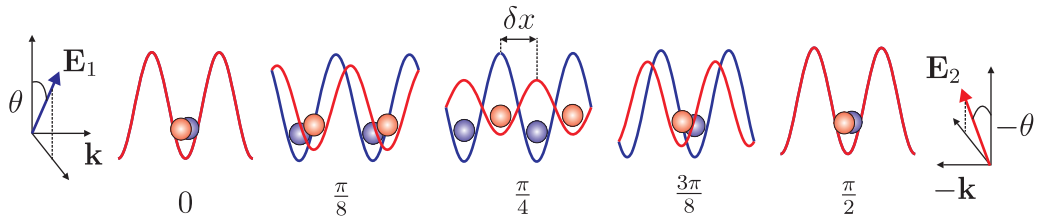


Figure 7.2. The laser configuration for a state dependent optical lattice. Two circularly polarised standing waves (with opposite helicity) are produced by two superimposed counter-propagating running waves with linear polarisations separated by an angle 2θ . The lattice potentials for two different hyperfine states, here $V_{2,2}(x)$ for $|F = 2, m_f = 2\rangle$ (blue) and $V_{1,1}(x)$ for $|F = 1, m_f = 1\rangle$ (red), are shifted with respect to one another spatially by a distance $\delta x = 2\theta/k$. The sequence of lattice potentials for $\theta = 0, \pi/8, \pi/4, 3\pi/8, \pi/2$ are shown. Notice that the depth of $V_{1,1}(x)$ is modulated during the sequence due to its form in Eq. (7.1), however this presents no particular practical issues.

where E is the amplitude and $\{\mathbf{e}_x, \mathbf{e}_y, \mathbf{e}_z\}$ are the standard Cartesian unit vectors. The total electric field $\mathbf{E}(\mathbf{r}, t) = \mathbf{E}_1(\mathbf{r}, t) + \mathbf{E}_2(\mathbf{r}, t)$ can then be expressed as a superposition of right and left circularly polarised standing waves [3]

$$\mathbf{E}(\mathbf{r}, t) = E [\cos(\mathbf{k} \cdot \mathbf{r} - \theta) \mathbf{e}_- + \cos(\mathbf{k} \cdot \mathbf{r} + \theta) \mathbf{e}_+] e^{-i\omega t},$$

where $\mathbf{e}_\pm = \mathbf{e}_z \pm i\mathbf{e}_y$. This then results in the optical potentials $V_\pm(x) \propto \cos^2(kx \pm \theta)$ along the x -axis. Importantly, it is possible to move the nodes of the two standing waves, and therefore the minima of the potentials, in opposite directions by changing the angle θ . After choosing $\omega = \omega_c$ the σ^\pm standing waves act as state-dependent potentials. Thus, by varying θ between 0 and $\pi/2$, as shown in Fig. 7.2, the lattice potentials in Eq. (7.1) for the hyperfine states $|a\rangle = |F = 2, m_f = 2\rangle$ and $|b\rangle = |F = 1, m_f = 1\rangle$ can be moved one site with respect to one another, see for example [4].

7.2 Entanglement generation

The ability to create state-dependent optical lattices and to shift them with respect to each other provides a direct means of implementing a two-qubit quantum gate, when combined with the collisional interactions of atoms [5, 6]. To illustrate this idea we follow the presentation given in reference [3]. We begin by considering two atoms in the states $|a\rangle$ and $|b\rangle$, respectively, each trapped in the ground state $\psi_0^{a,b}$ of a corresponding state-dependent potential well $V_{a,b}$. For concreteness will we assume that $V_{a,b}$ are harmonic potentials both with a frequency ω_{ho} and a ground state size a_{ho} . Initially at time $t = 0$, the two potential wells $V_{a,b}$ are centred at positions \bar{x}_a and \bar{x}_b which are sufficiently far apart that the atoms do not interact. We then suppose that the positions of the potentials are moved in opposite directions along the x -axis,

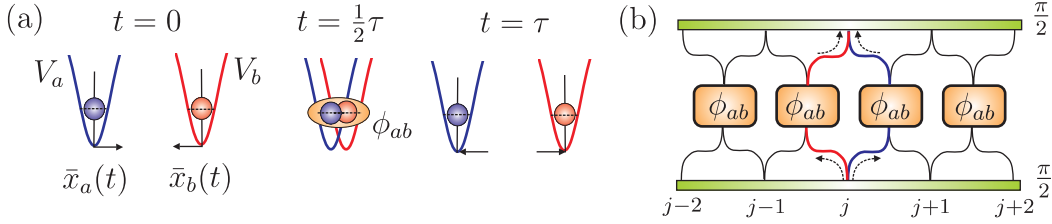


Figure 7.3. (a) Two atoms in different hyperfine states $|a\rangle$ (left) and $|b\rangle$ (right) are stored in state-dependent potential minima that are well separated at $t = 0$. The centre of these wells $\bar{x}_a(t)$ and $\bar{x}_b(t)$ are then moved along the x -axis until the two atoms collide and pick up a phase ϕ_{ab} . They are then returned to their initial positions by time $t = \tau$. (b) A schematic representation of the Ramsey-style interferometric creation of an N qubit entangled state using a state-dependent optical lattice (along one axis of a 3d lattice). After a $\frac{1}{2}\pi$ -pulse the $|a\rangle$ and $|b\rangle$ wave packets on site j are shifted by half a lattice spacing to the right and left, respectively. Collisions then occur between the $|a\rangle$ wave packet of site j and the $|b\rangle$ wave packet of site $j + 1$ for all sites j , before the lattice is shifted back to its original configuration and a further $\frac{1}{2}\pi$ -pulse is applied.

as $\bar{x}_a(t)$ (to the right) and $\bar{x}_b(t)$ (to the left), so that for a certain time the wave packets of the two atoms overlap resulting in a collisional interaction, before being returned to their initial positions at time $t = \tau$. This scenario is depicted in Fig. 7.3(a).

Ideally, we want this process to implement a transformation of the form

$$\psi_0^a(x_a - \bar{x}_a)\psi_0^b(x_b - \bar{x}_b) \mapsto e^{i\phi}\psi_0^a(x_a - \bar{x}_a)\psi_0^b(x_b - \bar{x}_b), \quad (7.2)$$

so each atom remains in the ground state of its trapping potential and preserves its internal state [3]. The phase $\phi = \phi_a + \phi_b + \phi_{ab}$ will contain a contribution ϕ_{ab} from the collisional interaction and trivial single particle kinematic phases ϕ_a and ϕ_b . If this is the case then the collisional phase shift is given by $\phi_{ab} = \int_0^\tau dt \Delta E(t)/\hbar$, where

$$\Delta E(t) = \frac{4\pi\hbar^2 a_s}{m} \int dx |\psi_0^a(x - \bar{x}_a(t))|^2 |\psi_0^b(x - \bar{x}_b(t))|^2.$$

with a_s being the s -wave scattering length for the interaction between the two hyperfine states $|a\rangle$ and $|b\rangle$. A detailed analysis of this scenario reveals that the transformation Eq. (7.2) can be realised in the adiabatic limit [7, 5, 6]. The full consistency of this scheme then requires that (i) $|\Delta E(t)| \ll \hbar\omega_{ho}$ so that the interaction cannot induce any *sloshing* motion; (ii) $|\dot{x}^{a,b}(t)| \ll v_{ho} = a_{ho}\omega_{ho}$ which is the adiabatic condition with v_{ho} being the rms velocity of the atoms in the ground state; and (iii) that v_{ho} is sufficiently small for the s -wave scattering approximation used above to be valid. In practise these conditions can be readily fulfilled [2].

Let us now generalise slightly to the case where the state dependent potentials $V_{a,b}$

are composed of two deep harmonic wells and initially overlap perfectly. The single atom in either of the wells can now be in an arbitrary superposition of the states $|a\rangle$ and $|b\rangle$ and remain trapped. We now implement the shifts of these potentials, as above, which moves the two V_b wells to the right and the two V_a wells to the left. In this way the wave function of each atomic qubit is split up in space according to its internal state and only the wave function of the left atom in state $|a\rangle$ will overlap with the position of the right atom in state $|b\rangle$ and interact. All other combinations of internal states never overlap and so never acquire a collisional phase. Under the conditions outlined the motional states of the atoms will remain unchanged while their internal states will transform as

$$\begin{aligned} |a\rangle_1|a\rangle_2 &= e^{2i\phi_a}|a\rangle_1|a\rangle_2, \\ |a\rangle_1|b\rangle_2 &= e^{i(\phi_a+\phi_b+\phi_{ab})}|a\rangle_1|b\rangle_2, \\ |b\rangle_1|a\rangle_2 &= e^{i(\phi_a+\phi_b)}|b\rangle_1|a\rangle_2, \\ |b\rangle_1|b\rangle_2 &= e^{2i\phi_b}|b\rangle_1|b\rangle_2. \end{aligned}$$

The appearance of the collision phase ϕ_{ab} conditional on the internal states of the two atoms makes this transformation equivalent to an entangling two-qubit gate [5]. From this point on we shall absorb the single-particle phases into our definition of $|a\rangle$ and $|b\rangle$.

The process of colliding atoms *by hand* outlined above can be realised using a state-dependent optical lattice described in section 7.1 along one axes of a 3d optical lattice. Here we consider the situation where a sufficiently deep and densely filled optical lattice has been prepared in the Mott insulating state with one atom per site in the hyperfine state $|a\rangle$. When perfectly filled with the lattice deep enough to suppress on-site number fluctuations this initial state represents an ideal quantum register of N qubits. Single qubit rotations are then equivalent to the coherent transfer of population between the two hyperfine states $|a\rangle$ and $|b\rangle$. This can be achieved either through magnetic dipole transitions driven by an additional oscillating microwave field, or with a Raman laser setup in which two laser beams couple the two hyperfine states via a far detuned excited state. In both cases a Hamiltonian of the form $H_R = \frac{1}{2}\hbar(\Omega_R|a\rangle\langle b| + \Omega_R^*|b\rangle\langle a|) + \delta_R|b\rangle\langle b|$ is implemented, with Ω_R the Rabi frequency and δ_R the detuning [3]. Since the achievable timescales of such a process are several orders of magnitude faster than the characteristic timescales of the atomic motion we may take H_R as the only Hamiltonian acting on the atoms for the duration of a pulse. When resonant ($\delta_R = 0$) the dynamical evolution of H_R for a time $t = \pi/\Omega_R$ (a so-called π -pulse) results in the perfect transfer (or Rabi-flop) of the population between $|a\rangle$ and $|b\rangle$.

With this setup in mind we will consider a Ramsey-type interferometric process for entangling a line of N atoms [5] in one operational step. It begins by performing a $\frac{1}{2}\pi$ -pulse³ in which the initial state $|a\rangle$ of each atom, in every lattice site, is placed into the equal superposition $|+\rangle = (|a\rangle + |b\rangle)/\sqrt{2}$. We then perform a shift operation

³This pulse is applied globally to all atoms in the lattice.

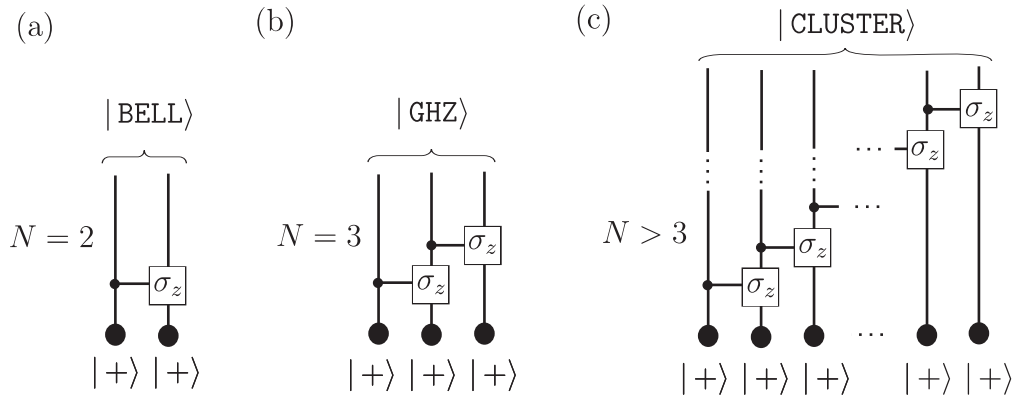


Figure 7.4. After an initial $\frac{1}{2}\pi$ -pulse all the atomic qubits are in the $|+\rangle$ state. When $\phi_{ab} = \pi$ the proceeding collisional interaction is locally equivalent to a controlled- σ_z gate between each nearest-neighbour along the chain. (a) For $N = 2$ this gives a state locally equivalent to $|\text{BELL}\rangle$. (b) For $N = 3$ it gives a state locally equivalent to $|\text{GHZ}\rangle$, whereas for (c) $N > 3$ the resulting state is a 1D cluster state $|\text{CLUSTER}\rangle$.

on the state-dependent lattices, V_a and V_b , so that the spatial wave-packets of the two internal states, $|a\rangle$ and $|b\rangle$, are moved half a lattice spacing to the right and left, respectively. The wave packets of neighbouring sites with differing internal states are then brought into contact and held for a certain time so they acquire a collisional phase ϕ_{ab} , as shown in Fig. 7.3(b). These collisions are locally equivalent to controlled- σ_z gates applied between all nearest-neighbouring qubits in the chain. They are then shifted back to their original locations and finally have another $\frac{1}{2}\pi$ -pulse applied to them. For the simplest case of $N = 2$ sites this operations performs the mapping

$$|a\rangle|a\rangle \mapsto \frac{1 + e^{i\phi_{ab}}}{2}|a\rangle|a\rangle + \frac{1 - e^{i\phi_{ab}}}{2}|\text{BELL}\rangle,$$

where we define $|\text{BELL}\rangle = (|a\rangle|+> - |b\rangle|->)/\sqrt{2}$ which is locally equivalent⁴ to the usual maximally entangled state of two-qubits [6]. For $N = 3$ we obtain

$$|a\rangle|a\rangle|a\rangle \mapsto \frac{1 + e^{i\phi_{ab}}}{2}|a\rangle|a\rangle|a\rangle + \frac{1 - e^{i\phi_{ab}}}{2}|\text{GHZ}\rangle,$$

where we define $|\text{GHZ}\rangle = (|a\rangle|+>|b\rangle - |b\rangle|->|a\rangle)/\sqrt{2}$, which is similarly a state that is locally equivalent to the so-called maximally entangled Greenberger-Horne-Zeilinger

⁴By locally equivalent we mean that it may be transformed into another type of state by applying appropriate single-qubit rotations.

(GHZ) state [6]. For $N > 3$ we obtain a

$$|a\rangle \cdots |a\rangle \mapsto \frac{1 + e^{i\phi_{ab}}}{2} |a\rangle \cdots |a\rangle + \frac{1 - e^{i\phi_{ab}}}{2} |\text{CLUSTER}\rangle,$$

where $|\text{CLUSTER}\rangle$ is locally equivalent to the 1D cluster state for N qubits [8]. This method has been implemented experimentally in [2] where the disappearance and revival of interference fringes provided indicative evidence that an array of 1D cluster states was created. Repeating this procedure along the other axes of the 3d optical lattice creates higher dimensional cluster states. In contrast to the 1D case 2D/3D cluster states are a universal resource for one-way quantum computing.

7.3 Engineering spin chains Hamiltonians

In this section we consider an anisotropic 3d optical lattice configuration, like that described in chapter 2, of the form

$$V(\mathbf{r}) = \sum_{\eta=\{x,y,z\}} \sum_{\nu=\{a,b\}} V_{\eta}^{\nu} \sin^2(\mathbf{k}_{\eta} \cdot \mathbf{r}),$$

where \mathbf{k}_{η} is the wave-vector of the laser along the η direction (with $|\mathbf{k}_{\eta}| = k$) and $E_R = \hbar^2 k^2 / 2m$ is the recoil energy. By using the state-dependent techniques described in section 7.1 this optical lattice traps two hyperfine states $|a\rangle$ and $|b\rangle$ of bosonic atoms. We further assume that the lattice is very deep along the y - and z -axes for both species, as $V_y^{\nu} = V_z^{\nu} \gg E_R$, for $\nu = a, b$, which creates effective isolated two-species 1D lattice systems along the x -axis. For sufficiently low temperatures and deep lattices the atoms become restricted to the lowest Bloch band of their respective lattice and their dynamical evolution over a system of M sites is described by a two-species generalisation of the BHM introduced in chapter 2. Along one of these 1D lattices the Hamiltonian will be [9, 10]

$$\begin{aligned} \hat{H} = & \sum_{j=1}^M \left[\frac{U^a}{2} \hat{n}_j^a (\hat{n}_j^a - 1) + \frac{U^b}{2} \hat{n}_j^b (\hat{n}_j^b - 1) + U^{ab} \hat{n}_j^a \hat{n}_j^b \right] \\ & - \sum_{j=1}^{M-1} \left(J^a \hat{a}_j^{\dagger} \hat{a}_{j+1} + J^b \hat{b}_j^{\dagger} \hat{b}_{j+1} + \text{H.c.} \right), \end{aligned} \quad (7.3)$$

where $\hat{a}_j (\hat{b}_j)$ is the bosonic destruction operator for an $a(b)$ -atom in site j and $\hat{n}_j^a (\hat{n}_j^b)$ is the corresponding number operator. Note that in Eq. (7.3) we have neglected the overall energy shifts for each site j since this can easily be compensated by a homogeneous external magnetic field applied along the z -axis. Much like the conventional single-species BHM implemented in an optical lattice the parameters of this Hamiltonian are controlled by the corresponding depths V_{η}^{ν} which are proportional to the laser intensities. The state-dependent tunnellings can be approximated from the 1D

Mathieu equation as

$$J^\nu \approx \frac{4}{\sqrt{\pi}} \left(\frac{V_x^\nu}{E_R} \right)^{3/4} \exp \left[-2 \left(\frac{V_x^\nu}{E_R} \right)^{1/2} \right] E_R,$$

while the on-site interaction energies in the harmonic approximation are

$$\begin{aligned} U^\nu &\approx \sqrt{8\pi} \frac{a_s^\nu}{a} (V_x^\nu V_y^\nu V_z^\nu E_R)^{1/4}, \\ U^{ab} &\approx \sqrt{8\pi} \frac{a_s^{ab}}{a} (\bar{V}_x^{ab} \bar{V}_y^{ab} \bar{V}_z^{ab} E_R)^{1/4}, \end{aligned}$$

where a_s^ν and a_s^{ab} are the intra- and inter-species s -wave scattering lengths, and

$$\bar{V}_\eta^{ab} = \frac{4V_\eta^a V_\eta^b}{(\sqrt{V_\eta^a} + \sqrt{V_\eta^b})^2},$$

is the average two-species potential in each direction η . From these expressions we observe that J^ν depends exponentially on the depths V_x^ν , while the interactions U^ν and U^{ab} exhibit only a weak dependence. Thus state-dependent tunnelling can be activated or suppressed by controlling the intensity of the x -axis lasers [9, 10, 11]. Additionally and independent of this, the interaction energies can be varied within a broad range by tuning the ratio of the scattering lengths a_s^{ab} and a_s^ν via an external magnetic field sweeping through a Feshbach resonance [12]. The interaction energies may also be reduced by shifting the lattice trapping each species by some fraction of a lattice spacing reducing the overlap of the atomic wave functions.

The versatility of an optical lattice realisation of the two-species BHM in Eq. (7.3) can be used to engineer a wide class of spin chain Hamiltonians. To do so we firstly restrict our attention to the regime where $U^a, U^b, U^{ab} \gg J^a, J^b$, (which we generically denote as $U/J \gg 1$) in which multiple occupancies of any site are energetically suppressed. Secondly, we consider the system as being commensurately filled, where $\langle \hat{n}_j^a \rangle + \langle \hat{n}_j^b \rangle = 1$, corresponding to an insulating phase. In this limit the kinetic terms in Eq. (7.3) can be treated as a perturbation. To proceed we note that the Hilbert space of this system is spanned by the two-species Fock states $| (n_1^a, n_1^b)(n_2^a, n_2^b) \cdots (n_M^a, n_M^b) \rangle$, where (n_j^a, n_j^b) are the occupancies of the a and b hyperfine states at site j , and with the constraint $\sum_j \sum_\nu n_j^\nu = M$. Of particular relevance is the subspace \mathcal{H}_s spanned by the 2^M states where the occupancy pairs $(n_j^a, n_j^b) = \{(1, 0), (0, 1)\}$ exclusively for all sites j , and therefore excludes all double occupancies. States outside \mathcal{H}_s represent a distinct subspace \mathcal{H}_e separated from \mathcal{H}_s by a large energy in the insulating limit. For this reason these states are expected to have a negligible amplitude in the overall state of the system at low (or in our case zero) temperatures. Our approach is then to derive an effective Hamiltonian in the subspace \mathcal{H}_s alone by using the projection method [13, 10, 11] already introduced in chapter 2 (also a Schrieffer-Wolf transformation can be used [9]). The kinetic terms in Eq. (7.3) couple states in \mathcal{H}_s and \mathcal{H}_e with

each other, and do not induce any direct transitions in \mathcal{H}_s . However, it does induce indirect transitions via ‘virtual’ second-order hopping processes to and from a doubly occupied state in \mathcal{H}_e . These then introduce terms in the effective Hamiltonian which possess a characteristic J^2/U -type coupling. The effective Hamiltonian, to lowest order in J/U , is then found to be [9, 10, 11]

$$\hat{H}_s = \sum_{j=1}^{M-1} \lambda^{zz} \sigma_j^z \sigma_{j+1}^z - \lambda^{xy} (\sigma_j^x \sigma_{j+1}^x + \sigma_j^y \sigma_{j+1}^y) + \sum_{j=1}^M \lambda^z \sigma_j^z. \quad (7.4)$$

Thus we obtain the anisotropic Heisenberg (XXZ) spin- $\frac{1}{2}$ model with the equivalence $|a\rangle \equiv |\uparrow\rangle$ and $|b\rangle \equiv |\downarrow\rangle$ at each site. The corresponding Pauli operators are then given by $\sigma_j^z = \hat{a}_j^\dagger \hat{a}_j - \hat{b}_j^\dagger \hat{b}_j$, $\sigma_j^x = \hat{a}_j^\dagger \hat{b}_j + \hat{b}_j^\dagger \hat{a}_j$ and $\sigma_j^y = -i(\hat{a}_j^\dagger \hat{b}_j - \hat{b}_j^\dagger \hat{a}_j)$ acting exclusively on the subspace \mathcal{H}_s . The couplings in Eq. (7.4) are then given by [9, 10, 11]

$$\begin{aligned} \lambda^{zz} &= \frac{(J^a)^2 + (J^b)^2}{2U^{ab}} - \frac{(J^a)^2}{U^a} - \frac{(J^b)^2}{U^b}, \\ \lambda^{xy} &= \frac{J^a J^b}{U^{ab}}, \\ \lambda^z &= 4 \left[\frac{(J^a)^2}{U^a} - \frac{(J^b)^2}{U^b} \right]. \end{aligned}$$

We note that by engineering a spatially dependent laser intensity profile along the axis of the chain these couplings can likewise be made spatially dependent. Given its sensitivity to the lattice depth this will predominately manifest itself as spatially dependent tunnellings $J^a \mapsto J_j^a$ and $J^b \mapsto J_j^b$.

For typical optical lattice experiments the tunnelling rate J/h can be chosen from zero to a few 100Hz, while the on-site interactions are approximately 1-2kHz at zero magnetic field, but can be much larger near a Feshbach resonance. As a conservative example we consider a setup with ^{87}Rb using $V_y^\nu = V_z^\nu = 40E_R$ and a moderately shallow depth⁵ $V_x^\nu = 4E_R$ along the chain giving $J/h \approx 0.3\text{ kHz}$, while $U/h \approx 2\text{ kHz}$ is attainable with the help of a Feshbach resonance. The energy scale for the magnetic interaction is then $J^2/hU \approx 50\text{ Hz}$, corresponding to a time scale of approximately 20ms, and next order corrections to the effective Hamiltonian are proportional to $(J/U)^2 \approx 0.03$. These values are compatible with current experimental setups which are able to maintain coherence for time scales on the order of 1s [1, 2].

A simple example of this approach is to set $V_x^b \gg V_x^a$ so J^b becomes negligible, while J^a remains finite. In this case the Hamiltonian Eq. (7.4) reduces to an Ising spin chain $H_{\text{Is}} = \sum_j \lambda^{zz} \sigma_j^z \sigma_{j+1}^z$ with $\lambda^{zz} = (J^a)^2(1/2U^{ab} - 1/U^a)$. Following our earlier discussion on the generation of cluster states the implementation of this Hamiltonian provides another route. Specifically, we exploit the fact that the Ising interaction λ^{zz} can be turned on and off by controlling the depth V_x^a . To begin we again initialise the atoms in the state $|+\rangle$ and then lower V_x^a for a time $\tau_{\text{is}} = \pi/4\lambda^{zz}$ [9, 8]. The resulting

⁵This is perhaps the shallowest depth at which we may safely use the BHM - see chapter 2.

state is locally equivalent to a 1D cluster state spanning the chain. By creating a higher dimensional Ising model within the optical lattice a corresponding 2D or 3D cluster state can be produced. In contrast to the cold-collision scheme this methods exploits the dynamical properties of a specific many-body Hamiltonian engineered within the lattice. In chapter 8 we shall describe an entanglement generation scheme in which some (non-entangling) operations are performed by hand, like the cold collision scheme, while the non-trivial entangling operations are performed using the always-on dynamics of a specific spin-chain Hamiltonian realised with the above method.

7.4 Two-atom manipulation

In this final section we will discuss the recent progress in experimentally controlling the coherent collisional spin⁶ dynamics of atoms in an optical lattice [14, 15, 16]. The setup of interest is composed of a 3d optical lattice filled with approximately 10^5 atoms and an overall harmonic trapping which is adjusted so that a significant proportion (usually near one half) of the sites at the centre of the trap are doubly occupied. By making the lattice potential sufficiently deep, atoms can neither leave a lattice site by tunnelling nor be excited via interactions to a higher vibrational state. Consequently, the system forms Mott insulating shells (see discussion at the end of chapter 3) in which the motional dynamics of the atoms is frozen.

For doubly occupied sites the atoms will undergo spin changing collisions in which an initial (unsymmetrised) spin state $|F, m_1\rangle |F, m_2\rangle$ is transferred to $|F, m_3\rangle |F, m_4\rangle$. For binary collisions between alkali atoms the total spin projection on the quantisation axis is conserved so $m_1 + m_2 = m_3 + m_4$ [14, 15, 16]. This limits the number of accessible final states to those that have the same total magnetisation as the initial ones. Thus by using a Mott insulating state the ensuing dynamics is confined to the spin degrees of freedom of only two atoms within one lattice site.

We shall focus on one particular experimental setup where only the $F = 1$ level is used and all atoms are prepared in the $m_f = 0$ hyperfine state. In this case the initial state⁷ of an atom pair $|0, 0\rangle$ can access only one other final state $| -1, +1\rangle$ while conserving the total magnetisation, as shown in Fig. 7.5(a). As a result the spin-dynamics of an atom pair behaves like a two-level system undergoing Rabi-like oscillations between $|0, 0\rangle$ and $| -1, +1\rangle$ [14, 15, 16]. It should be noted, however, that this is quite different from the usual Rabi-model coupling a pair of *single-particle* states under the influence of an external field. Instead, we have a coherent coupling between a pair of *two-particle* states induced by direct atomic interactions. The probability of finding the atom pair in the state $| -1, +1\rangle$ is given by the usual form

$$P_{-1,1} = \frac{\Omega_0^2}{2\Omega_{\text{eff}}^2} [1 - \cos(\Omega_{\text{eff}} t)],$$

⁶Following the experimentalists convention we shall call the two $S_{1/2}$ hyperfine manifolds of an Alkali atoms spin-1 and spin-2 particles, and the corresponding hyperfine states spin states.

⁷Where we abbreviate the spin states for this case as $|m_1, m_2\rangle = |F = 1, m_1\rangle |F = 1, m_2\rangle$.

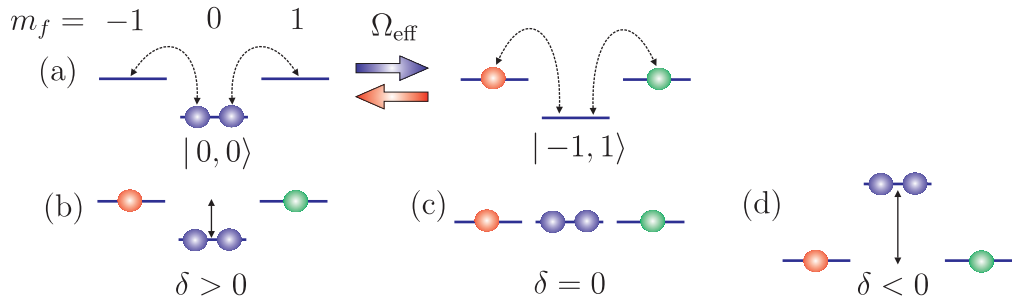


Figure 7.5. (a) The collisional interaction between two alkali atoms conserves the total magnetisation of the atom pair. Thus for the $F = 1$ hyperfine levels with two atoms in the $m_f = 0$ state ($|0,0\rangle$) there is only one other accessible final state from the interaction where the two atoms are in $m_f = -1$ and $m_f = 1$ states ($|-1,1\rangle$). This results in coherent spin oscillations between the two-particle state $|0,0\rangle$ and $|-1,1\rangle$ like an effective Rabi-model system with frequency Ω_{eff} . (b) When there is zero or weak microwave field there is an intrinsic energy mismatch, or detuning, $\delta > 0$ between the two-particle states caused by the interaction. (c) By properly tuning the microwave field this detuning can be compensated and a full resonance, $\delta = 0$, can be achieved. (d) For larger intensities the detuning can be overcompensated, $\delta < 0$, causing the suppression of spin-changing oscillations.

where $\Omega_{\text{eff}} = \sqrt{\Omega_0^2 + \delta^2}$ is the effective Rabi frequency. Here $\Omega_0 = 2\sqrt{2}U_s$ is the coupling strength that is proportional to the spin-dependent interaction energy U_s , and δ is the detuning. Since δ is dependent on the second-order Zeeman shift an external magnetic field can be used to control Ω_{eff} . However, magnetic fields alone cannot enforce a fully resonant oscillation and additional microwave fields are needed to shift the energies of the two states making $\delta = 0$ [15], as depicted in Fig. 7.5(b)-(d). This then permits the near-unit conversion of atom pairs in the single-species state $|0,0\rangle$ to the two-species state $|-1,1\rangle$.

These methods have already proven to be very useful for measuring the spin-dependent interaction strengths of alkali atoms [16]. Beyond this it provides a promising method for quantum state detection, preparation and manipulation. In particular, by exploiting the distinguishing feature between doubly-occupied and singly-occupied sites, namely that the former undergo the spin dynamics whereas the latter do not, a scheme has been proposed for filtering the system [15]. This filtration allows homogeneous (flat) Mott insulators to be created with either singly or doubly occupied sites, from an initially inhomogeneous system where both coexist. A purely doubly occupied Mott insulator has proven useful for the coherent creation of long-lived diatomic molecules in an optical lattice [17]. More generally, the use of coherent transformations between two-particle states is also of obvious benefit for quantum state engineering. In chapter 9 we consider the adiabatic quantum melting of the doubly occupied MI in the state $|-1,1\rangle$ and show that the resulting two-species superfluid could permit Heisen-

berg limited interferometry. We also briefly investigate the intriguing initial state that is obtained by applying a single-particle $\frac{1}{2}\pi$ -pulse to $| -1, 1 \rangle$ which transforms the atom pair state into

$$| \psi_{\text{ent}} \rangle = \frac{1}{\sqrt{2}}(| -1, -1 \rangle + | 1, 1 \rangle).$$

This represents a maximally entangled Bell-like state on each site. The quantum melting of this state, which from the offset has quantum correlations on every site, appears to have a rich, albeit more complicated, structure and is the subject of current work [18].

References

- [1] M. Greiner, O. Mandel, T. Esslinger, T.W. Hänsch, I. Bloch, *Nature (London)* **415**, 39 (2002).
- [2] O. Mandel, M. Greiner, A. Widera, T. Rom, T.W. Hänsch, I. Bloch, *Nature (London)* **425**, 937 (2003).
- [3] D. Jaksch, P. Zoller, *Ann. Phys. (N.Y.)* **315**, 52 (2005).
- [4] O. Mandel, M. Greiner, A. Widera, T. Rom, T.W. Hänsch, I. Bloch, *Phys. Rev. Lett.* **91**, 010407 (2003).
- [5] D. Jaksch, H.-J. Briegel, J.I. Cirac, C.W. Gardiner, P. Zoller, *Phys. Rev. Lett.* **82**, 1975 (1999).
- [6] H.-J. Briegel, T. Calarco, D. Jaksch, J.I. Cirac, P. Zoller, *J. Mod. Opt.* **47**, 415 (2000).
- [7] D. Jaksch, *Bose-Einstein Condensation and Applications* (PhD. Thesis, Leopold-Franzens-Univ., Innsbruck, 1999).
- [8] H.-J. Briegel, R. Raussendorf, *Phys. Rev. Lett.* **86**, 910 (2001).
- [9] L.M. Duan, E. Demler, M.D. Lukin, *Phys. Rev. Lett.* **91**, 090402 (2003).
- [10] J.J Garcia-Ripoll, J.I. Cirac, *New J. Phys.* **5**, 76 (2003).
- [11] A.B. Kuklov, B.V. Svistunov, *Phys. Rev. Lett.* **90**, 100401 (2003).
- [12] E.A. Donley, N.R. Claussen, S.T. Thompson, C.E. Wieman, *Nature (London)* **417**, 529 (2002).
- [13] C. Cohen-Tannoudji, J. Dupont-Roc, G. Grynberg, *Atom-Photon Interactions* (John Wiley & Sons, New York, 1998).
- [14] A. Widera, F. Gerbier, T. Gericke, S. Fölling, O. Mandel, I. Bloch, *Phys. Rev. Lett.* **95**, 190405 (2005).
- [15] F. Gerbier, A. Widera, S. Fölling, O. Mandel, I. Bloch, *Phys. Rev. A* **73**, 041602(R) (2006).

- [16] A. Widera, F. Gerbier, T. Gericke, S. Fölling, O. Mandel, I. Bloch, *New J. Phys.* **8**, 152 (2006).
- [17] G. Thalhammer, K. Winkler, F. Lang, S. Schmid, R. Grimm, J. Hecker Denschlag, *Phys. Rev. Lett.* **96**, 050402 (2006).
- [18] M. Rodriguez, S.R. Clark, D. Jaksch, *manuscript in preparation*, (2007).

CHAPTER 8

PUBLICATION

Efficient generation of Graph states for quantum computation

S. R. Clark, C. Moura-Alves and D. Jaksch

Clarendon Laboratory, University of Oxford, Parks Road, Oxford OX1 3PU, U.K.

New Journal of Physics **7**, 124 (2005)

We present an entanglement generation scheme which allows arbitrary graph states to be efficiently created in a linear quantum register via an auxiliary entangling bus. The dynamics of the entangling bus is described by an effective non-interacting fermionic system undergoing mirror-inversion in which qubits, encoded as local fermionic modes, become entangled purely by Fermi statistics. We discuss a possible implementation using two species of neutral atoms stored in an optical lattice and find that the scheme is realistic in its requirements even in the presence of noise.

8.1 Introduction

Bipartite entanglement has long been recognised as a useful physical resource for tasks such as quantum cryptography and quantum teleportation. Similarly, multipartite entanglement is an essential ingredient for more complex quantum information processing (QIP) tasks, and interest in this resource has grown since its controlled generation was demonstrated in several physical systems [1, 2, 3, 4, 5]. An important class of multipartite entangled states are graph states. By using vertices in a graph to represent qubits, and edges to represent an Ising type interaction that has taken place between two qubits, the graph formalism gives an intuitive characterisation of entanglement by the presence of edges [6]. As a result a graph represents a preparation procedure for a state. Additionally graph theory allows some properties of these states, such as the effects of local Pauli operations and the persistence of entanglement after local Pauli measurements, to be computed exactly, and others, such as the Schmidt measure, which is computationally intractable for general states, to be bounded from above and below [6, 7]. The class of graph states includes many well studied states such as GHZ states, and special instances of graph states are the resource used in quantum error correcting codes [8, 9] and in one-way quantum computing [10, 11].

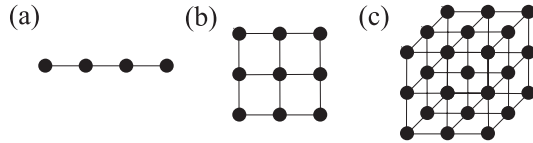


Figure 8.1. Examples of (a) 1D, (b) 2D and (c) 3D cluster states. States (b) and (c) (and larger versions thereof) are a universal resource for one-way quantum computing.

Initial proposals for the generation of graph states in physical systems have focussed on qubit lattices of fixed geometry, where each qubit interacts only with its nearest-neighbors [6, 7, 11]. Such a scheme has been experimentally implemented in a three-dimensional (3D) optical lattice of neutral atoms via controlled collisions [1] along one axis of the lattice. The graph states generated with this method follow the geometry of the lattice, and so for collisions along one-axis an array of 1D cluster states, similar to Fig. 8.1(a), should be obtained. In the experiment [1] interference measurements provided indicative evidence that this was indeed achieved. Extending this process to all axes of 2D and 3D square lattices would then generate cluster states of the form Fig. 8.1(b) and Fig. 8.1(c), respectively. These both constitute, together with single qubit measurements, a universal resource for quantum computation [10]. Despite the 1D cluster states of the type shown in Fig. 8.1(a) not being a universal resource they are still a useful resource for specific computational tasks, as emphasised by the recent use of the four-qubit 1D cluster state to implement the two-qubit Grover search algorithm with photons [3]. More generally wider classes of graph states also represent specific resources for certain QIP tasks, and this builds upon the notion that entanglement is an algorithmic resource [11]. The direct generation of arbitrary graphs, where the set of edges does not translate into a regular arrangement of the underlying qubits, e.g. the quantum Fourier transform graph state [6], requires the ability to pre-engineer a complicated geometry of the qubit interactions. A simple scheme in which any graph state can be created in a set of qubits with a regular fixed geometry is therefore highly desirable. Some progress has been made towards this with non-deterministic linear optical protocols, where proposals have been made for graph state generation in photon [12] and solid-state qubits [13].

In this paper we propose a deterministic scheme for efficiently generating arbitrary graph states within a linear quantum register. We consider a general setup in which there is an auxiliary system, denoted as an entangling bus (EB), running parallel and along the length of the register. All entanglement within the register is generated via the EB by performing local swaps between subsets of register qubits and the EB and allowing the EB to evolve for a fixed time. More specifically the EB is an ‘always on’ 1D system whose dynamical evolution over a fixed time generates a specific entangling operation \mathcal{C} composed of controlled- σ_z ($c\sigma_z$) gates between all pairs of the transferred qubits in one step. After local swaps back to the register this operation can generate GHZ-type graph states [6] within this subset of register qubits. Repeated use of this

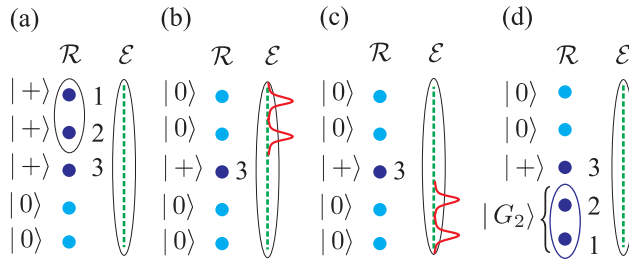


Figure 8.2. (a) Consider a quantum register \mathcal{R} which has 3 graph qubits in a state $|+\rangle$. (b) Two of them are transferred to the EB \mathcal{E} where their state is mapped into local fermionic modes. (c) \mathcal{E} evolves via H_f for time τ , which results in the mirror-inversion of the two qubits. (d) The qubits at the mirror-inverted location are transferred back to \mathcal{R} , yielding a graph state with 2 vertices $|G_2\rangle$. Repeating this procedure with different qubits allows any 3-qubit graph state to be generated in \mathcal{R} .

entangling operation then allows arbitrary graph states to be generated in the register, as depicted for the simplest case with two qubit in Fig. 8.2. This setup is motivated by the following three results.

Our first result is a construction of the EB using a system which *maps* to a 1D non-interacting fermionic lattice. Within this mapping qubits from the register become encoded as local fermionic modes (LFMs) [14]. We begin in section 8.2 by showing that for an engineered lattice with a specific spatially varying hopping profile the dynamical evolution over some fixed time results in the complete mirror inversion of the LFMs. This inversion is then shown to generate robust phases within the fermionic state purely as a consequence of Fermi statistics which are equivalent to entanglement between the LFM qubits resulting from an effective entangling operation \mathcal{C} .

Our second result described in section 8.3 is then a scheme which utilises the availability of the entangling operation \mathcal{C} through the EB to efficiently generate arbitrary graph states within the register. Specifically we show that any graph state of n vertices can be generated in at most $O(2n)$ EB steps representing an improvement over the $O(n^2)$ steps required in a network model composed of two-qubit gates.

In section 8.4 we present our third result which is a proposal for the implementation of this scheme in an optical lattice of neutral atoms. We begin by examining how an effective XY spin chain can be engineered within an optical lattice. Two adjacent spin chains then form the basis of the register and EB. We investigate how imperfections in the mapping of the optical lattice to an XY spin chain alter the fidelity of the EB dynamics. Finally, we briefly note some other viable alternatives for implementing this scheme, and conclude in section 8.5.

8.2 Non-interacting fermionic system

8.2.1 Mirror inversion on a lattice

The construction of the fermionic EB relies on the fermionic system being mapped from another underlying system. The specific example we consider is a XY spin chain composed of N spins which is described by the Hamiltonian

$$H_{\text{xy}} = \sum_{n=1}^N \lambda_n^z \sigma_n^z - \sum_{n=1}^{N-1} \lambda_n^{xy} (\sigma_n^x \sigma_{n+1}^x + \sigma_n^y \sigma_{n+1}^y), \quad (8.1)$$

where λ_n^{xy} are the spatially varying XY couplings and λ_n^z is the contribution of an external field taken to be uniform as $\lambda_n^z = B/2$. It is well known that the Jordan Wigner transformation (JWT) [15] maps the XY spin chain to a non-interacting fermionic Hamiltonian

$$H_f = \sum_{n=1}^N u_n c_n^\dagger c_n - \sum_{n=1}^{N-1} j_n (c_n^\dagger c_{n+1} + c_{n+1}^\dagger c_n), \quad (8.2)$$

where $j_n = 2\lambda_n^{xy}$, $u_n = B$, and c_n is a fermionic destruction operator for the n th site obeying the usual anticommutation relations. We are particularly interested in the *angular momentum* hopping profile [16] given by $j_n = (J/2)\sqrt{n(N-n)}$, with J a constant. We choose to write this as $j_n = W\alpha_n$ with

$$\alpha_n = 2\sqrt{\frac{n}{N} \left(1 - \frac{n}{N}\right)}, \quad (8.3)$$

and $W = JN/4$. In this way the spatial dependence of the hopping j_n is contained entirely in the profile α_n obeying $0 < \alpha_n \leq 1$, and the overall scaling is given by the constant W such that $\max(j_n) \leq W$. With this hopping profile the projection of H_f onto the single fermion subspace of the lattice, \mathcal{H}_1 , results in a Hamiltonian equivalent to $H_1 = -JS_x + B\mathbb{1}$, where S_x is the x -angular momentum operator for an ‘effective’ spin- \mathcal{S} particle, with $\mathcal{S} = (N-1)/2$. The single-fermion states $\{|n\rangle = c_n^\dagger |\text{vac}\rangle\}$ then correspond to the z -angular momentum eigenstates $\{|\mathcal{S}, l\rangle_z\}$ of the spin- \mathcal{S} particle, with $|1\rangle = |\mathcal{S}, -\mathcal{S}\rangle_z, \dots, |N\rangle = |\mathcal{S}, \mathcal{S}\rangle_z$. The dynamics generated in \mathcal{H}_1 , when H_1 is applied for a fixed time $\tau = \pi/J$, result in the time-evolution unitary $U_1(\tau) = \exp(i\phi_B) \exp(i\pi S_x)$ composed of an overall phase $\phi_B = -B\pi/J$ for \mathcal{H}_1 and a rotation of the spin- \mathcal{S} particle about the x -axis by π . This leads directly to perfect state transfer over the lattice [16].

The action of $U_1(\tau)$ on the single-particle basis follows from its equivalence to the z -angular momentum states where $\exp(i\pi S_x)|\mathcal{S}, l\rangle_z = \exp(i\pi\mathcal{S})|\mathcal{S}, -l\rangle_z$. Thus we find that $U_1(\tau)|n\rangle = \exp(i\phi_1)|\bar{n}\rangle$, with the phase $\phi_1 = \pi\mathcal{S} + \phi_B$ and mirror-conjugate location $\bar{n} = N - n + 1$. The choice $B = \mathcal{S}J$ then ensures that the single-particle phase ϕ_1 vanishes. The evolution of the fermionic modes c_n^\dagger can then immediately be seen to satisfy $U c_n^\dagger U^\dagger = c_{\bar{n}}^\dagger$, where $U = \exp(-iH_f\tau)$, with respect to the full Hamiltonian H_f , and the dynamics of the system describes the complete mirror-inversion of the LFM.

Typically implementations of this effective fermionic system will have a maximum obtainable value for the overall scaling W of the hopping which prevents J from being arbitrarily increased, and so once it is maximised we must pay a linear cost in the inversion time τ with the increasing size of the system N .

8.2.2 Entanglement of fermionic modes

Under the JWT the N qubit (or spin) states $|q_1, \dots, q_N\rangle$, with $q_n \in \{0, 1\}$, of the chain are mapped to Fock states of the LFM as $|q_1, \dots, q_N\rangle = (c_1^\dagger)^{q_1} \dots (c_N^\dagger)^{q_N} |\text{vac}\rangle$ (where operators are ordered according to the lattice) which describe the occupancy of the system by quasi-fermions. The use of fermionic mode occupancy as a basis for quantum computation has been proposed before [14]. An immediate difficulty with a direct implementation of this approach using massive and/or charged fermions is the constraint caused by *superselection* rules which prohibits the superposition of states with different mass/charge eigenvalues [17, 18]. Such superpositions are essential for encoding qubits as LFM. In [14] the accessibility of the Fock space is widened by including an interaction with a superconducting reservoir that relaxes particle number conservation to modulo 2 via the exchange of Cooper pairs. Also, in contrast to bosons, the Fock space of fermions does not have a natural tensor product structure permitting independent operations on each mode [19]. This intrinsically nonlocal behavior of fermions adds a significant degree of complexity to quantum computing with LFM qubits in [14]. Here, in contrast, we have focussed on a physical system which maps to a non-interacting fermionic system. As a result the quasi-Fock space is fully accessible, thus enabling superpositions of states with different numbers of quasi-fermions, which are essential for encoding qubits.

For systems of identical fermions a bilinear fermionic Hamiltonian such as H_f suffices to generate mode entanglement, despite describing a non-interacting system [20]. This is a natural consequence of the nonlocal character of fermions. The entanglement generated by mirror-inversion then follows straightforwardly from Fermi statistics through its action on Fock states as

$$e^{-iH_f\tau} |q_1, \dots, q_N\rangle = e^{-i\pi\Sigma_Q} |q_N, \dots, q_1\rangle, \quad (8.4)$$

where Σ_Q is the number of anti-commutations of the operators c_n^\dagger required to reestablish a Fock state. Specifically $\Sigma_Q = Q(Q - 1)/2$, where Q is the number of fermions, i.e. $Q = \sum_{n=1}^N c_n^\dagger c_n = \sum_{n=1}^N q_n$, and so phases are only acquired between subspaces with different Q . Since Eq. (8.4) is written in terms of Fock states, the inverse-JWT removes the implicit antisymmetry when mapping back to qubits, while leaving the phases acquired between fermion-number (or total magnetisation) subspaces untouched. Thus the evolution of the EB after a fixed time τ is equivalent to a quantum circuit $\mathcal{C}(N)$ composed of $c\sigma_z$ gates between all distinct pairs of N qubits followed by the inversion operator R , as shown in Fig. 8.3(a) for $N = 5$. Usefully, if any $N - q$ qubits of the system are in the state $|0\rangle$, then this circuit reduces to $\mathcal{C}(q)$ between the remaining q qubits, independent of their locations, followed by the full inversion R of all qubits.

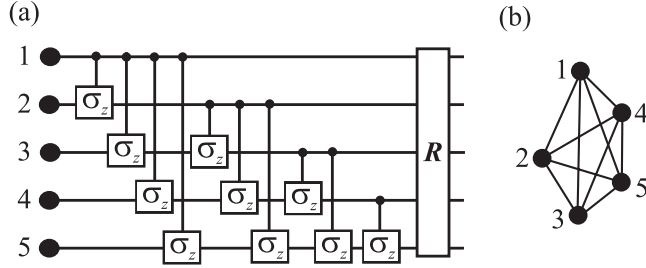


Figure 8.3. For 5 qubits we have (a) the quantum circuit $\mathcal{C}(5)$ equivalent to the dynamics of H_f for a time τ , and (b) the fully connected graph state $|G_5\rangle$ with 5 vertices generated by this circuit if all the qubits are initialised in the $|+\rangle$ state. Both the circuit and the resulting graph state generalise in an obvious way for more qubits.

8.2.3 Generalisations

In passing we note that the above results apply to more general settings. Suppose we partition the fermionic lattice into M equal blocks, each labelled by their central site k , and composed of sites $m(k)$. Within each block k we consider an extended fermionic mode $f_k^\dagger = \sum_{n \in m(k)} \phi_n^k c_n^\dagger$, defined by a single-particle state ϕ_n^k contained entirely within the block k and symmetrical about its center. The dynamics of the EB over some fixed time will be equivalent to $\mathcal{C}(M) R$ as long as j_n and u_n are chosen such that the dynamics of H_f performs mirror-inversion with respect to the modes f_k^\dagger [21, 22]. We can equally consider partitioning a 1D continuous fermionic system, described by field operators $\hat{\psi}^\dagger(x)$, and defining extended LFM analogously as $f_k^\dagger = \int_{m(k)} dx \phi^k(x) \hat{\psi}^\dagger(x)$, via a single-particle wavefunction $\phi^k(x) = 0, \forall x \notin m(k)$. In this case harmonic trapping $V(x) = m\omega^2 x^2/2$ and Gaussian wavefunctions $\phi^k(x)$ centered on a block are sufficient for mirror-inversion over a time $\tau = \pi/\omega$. Such an arrangement could potentially be implemented using effective bosonic Fock states of arrays of atomic quantum dots [23] following conceptually similar lines to the 1D cold-collision proposal in [24], but with the difference that the Tonks-Girardeau limit [25] of the bosons is exploited to yield robust phases from an effective non-interacting fermionic system.

8.3 Entanglement generation scheme

To generate arbitrary graph states within a linear register of N storage qubits we utilise the entangling operation \mathcal{C} implemented by the EB repeatedly. As with other such schemes each qubit in the register is assumed to be individually manipulable and measurable. This includes the ability for each qubit to be selected to undergo a transfer process which maps its state into a LFM encoded qubit in the EB via $\sigma_n^+ \mapsto c_n^\dagger$, where σ_n^+ is the Pauli ladder operator on the register. Since the register is a distinct commuting physical system to the EB the transfer process allows certain sets of qubits to be temporarily endowed with fermionic character and subsequently

become entangled as a result of the mirror-inversion of the fermionic modes.

The register and the EB are taken to be initialised in the states $\otimes_i^N |0\rangle_i$ and $|\text{vac}\rangle$ respectively. The scheme begins by choosing a set of register qubits Γ to be the graph vertices, and applying a Hadamard transformation to each of them: $|0\rangle \rightarrow |+\rangle = (|0\rangle + |1\rangle)/\sqrt{2}$, as in Fig. 8.2(a) for qubits 1 – 3. A subset Σ of m of these qubits is then transferred to the EB and allowed to evolve for a time τ , as shown (for $m = 2$) in Fig. 8.2(b) and Fig. 8.2(c) for qubits 1 and 2. The qubits encoded by LFM_s at the corresponding mirror-inverted locations $\bar{\Sigma}$ of the EB are then transferred back to the register, yielding a fully connected graph state $|G_m\rangle$ between these m vertices, as in Fig. 8.2(d). Such a state is locally equivalent to a m -qubit GHZ state, as depicted in Fig. 8.3(b) for $m = 5$. Overlap between EB and register graph qubits after inversion can be avoided by choosing $|\Gamma| = \lceil N/2 \rceil$ with locations in the first half of the register.

This setup can generate any graph state of n vertices in at most $O(n^2)$ steps by utilising only the two-qubit interaction of the EB to establish each edge individually, mimicking a network model of two-qubit gates. However, by exploiting the multi-qubit circuit \mathcal{C} implemented by the EB dynamics over the same time τ , as in Fig. 8.3(a), our scheme can improve this upper bound. Specifically, we proceed iteratively, starting with $g = 1$, by :

1. transferring the g th graph qubit, and all graph qubits $g_c > g$ which will connect to g , into the EB;
2. allowing them to evolve for a time τ creating a complete set of connections between these vertices, c.f. Fig. 8.3(b);
3. then transferring qubit g back to the register while leaving the qubits g_c to evolve for one cycle longer in the EB, subsequently removing all the connections between them;
4. finally transferring the qubits g_c back to the register and repeating step (i) with $g \mapsto g + 1$.

Thus, any graph of $g = n$ vertices can be generated in at most $O(2n)$ uses of the EB.

8.4 Implementations

8.4.1 Optical lattice realisation

The physical basis for the implementation of this scheme which we focus on is an optical lattice of ultracold bosonic atoms [26]. In an optical lattice neutral atoms are trapped due to the optical dipole force in the intensity maxima (or minima) of a far-off resonance standing wave light-field formed from counter-propagating lasers. We consider atoms possessing two long-lived internal (hyperfine) states $|a\rangle$ and $|b\rangle$ which are trapped by two such optical lattices of different polarisations. For sufficiently low temperatures and deep lattices the atoms become restricted to the lowest Bloch band

and their dynamical evolution over a system of N sites is described by a two-species Bose-Hubbard model (BHM) given by [27]

$$\begin{aligned} H = & \sum_{n=1}^N \left(\frac{U_n^a}{2} a_n^{\dagger 2} a_n^2 + \frac{U_n^b}{2} b_n^{\dagger 2} b_n^2 + U_n^{ab} a_n^\dagger a_n b_n^\dagger b_n \right) \\ & - \sum_{n=1}^{N-1} (t_n^a a_n^\dagger a_{n+1} + t_n^b b_n^\dagger b_{n+1} + \text{H.c.}) + H_B, \end{aligned} \quad (8.5)$$

where $a_n(b_n)$ is the bosonic destruction operator for an $a(b)$ -atom in the n th site, and $H_B = (B/2) \sum_n (a_n^\dagger a_n - b_n^\dagger b_n)$ is the contribution of an external field which we assume to be uniform over the system. The parameters $t^{a(b)}$ and $U^{a(b)}$, U^{ab} are the laser-intensity-dependent hopping matrix elements and on-site interactions for atoms in states $|a\rangle$ ($|b\rangle$) respectively. These parameters will in general have a spatial profile across the lattice. The dynamic controllability and long decoherence times of this system have made it of considerable interest for QIP [28, 29] and for realising spin models [27, 30].

As outlined in section 8.3 the scheme requires an initial state with one atom per site (each in a state $|a\rangle$) and single site addressability for manipulations. While the preparation of a high-fidelity initial state could be achieved using the techniques described in [31, 32], single site addressability remains a challenging technical limitation in optical lattices. However, there are theoretical proposals which offer the potential to overcome this by using ideas such as marker atoms to localise global operations [33], as well as increasing technical improvements in experiments. Hence it does not seem unrealistic to assume that single-site addressability will become possible in the near future.

Initially we take the lattice as being sufficiently deep to prohibit hopping in all directions. A chain of sites from the commensurately filled lattice is then selected to be the register of non-interacting qubits, and an adjacent chain becomes the EB. Addressability is exploited to engineer a spatially dependent intensity profile along the EB chain which activates hopping exclusively along this chain. The transfer process between the register and EB is accomplished by again using addressability to localise Raman induced hopping [26] between two adjacent register and EB sites and implement a swap gate, as described in detail in [28], on a timescale sufficiently faster than τ .

For the non-zero hopping within the EB chain we focus on the two-species BHM in the limit of large interactions, $U^a, U^b, U^{ab} \gg t^a, t^b$, which energetically prohibit the multiple occupancy of any site. The hopping can be then treated perturbatively and to lowest order, for an initial Mott insulating state with commensurate filling of one atom per lattice site, the effective Hamiltonian is found to be [27]

$$H_s = \sum_{n=1}^{N-1} \lambda_n^{zz} \sigma_n^z \sigma_{n+1}^z - \lambda_n^{xy} (\sigma_n^x \sigma_{n+1}^x + \sigma_n^y \sigma_{n+1}^y) + \sum_{n=1}^N \lambda_n^z \sigma_n^z. \quad (8.6)$$

Hence we obtain the anisotropic Heisenberg spin model in the optical lattice, with

the correspondence $|a\rangle \equiv |\uparrow\rangle$ and $|b\rangle \equiv |\downarrow\rangle$ at each site. The corresponding Pauli operators are then $\sigma_n^z = a_n^\dagger a_n - b_n^\dagger b_n$, $\sigma_n^x = a_n^\dagger b_n + b_n^\dagger a_n$, $\sigma_n^y = -i(a_n^\dagger b_n - b_n^\dagger a_n)$, while the couplings are given by

$$\begin{aligned}\lambda_n^{zz} &= \frac{t_n^{a2} + t_n^{b2}}{2U_n^{ab}} - \frac{t_n^{a2}}{U_n^a} - \frac{t_n^{b2}}{U_n^b} \\ \lambda_n^{xy} &= \frac{t_n^a t_n^b}{U_n^{ab}} \\ \lambda_n^z &= 4\left(\frac{t_n^{a2}}{U_n^a} - \frac{t_n^{b2}}{U_n^b}\right) + \frac{B}{2}.\end{aligned}\quad (8.7)$$

The construction of the EB requires the optical lattice parameters to be engineered such that $U_n^a = U_n^b = 2U_n^{ab}$ and $t_n^a = t_n^b$, thereby ensuring that $\lambda_n^{zz} = 0$, $\lambda_n^z = B/2$, and that H_s reduces to the pure XY spin chain Hamiltonian H_{xy} .

The spatial dependence of the two-species BHM model parameters arises due to some appropriately configured laser-intensity profile along the system. Since the on-site interactions have a weak dependence on the laser-intensity, in contrast to hopping matrix elements which have an exponential dependence [26], only hopping is assumed to be spatially dependent over the system. Specifically, we take $t_n^a = t_n^b = T\sqrt{\alpha_n}$, where the spatial dependence is again contained in the profile α_n , and the overall scaling is given by a constant T such that $\max(t_n^{a(b)}) \leq T$. The interaction energies are constant over the system and defined as $U^a = U^b = 2U^{ab} = U$. To first order in T/U the dynamics of the optical lattice reduces to an XY spin chain with couplings $\lambda_n^{xy} = (2T^2/U)\alpha_n$. The profile α_n must then have the spatial dependence introduced earlier in section 8.2 enabling the effective non-interacting fermionic lattice resulting from this XY spin chain to undergo mirror-inversion. This dynamical evolution will proceed exactly in the ideal limit where $U/T \gg 1$. The graph states generated with this implementation could then be used for one-way quantum computation if single site imaging was available, or alternatively the multi-qubit entanglement could be diagnosed with the procedure described in [34].

8.4.2 Optical lattice imperfections

We have considered some dominant sources of imperfections within the optical lattice implementation of the EB. In particular, we investigate the fidelity of the two-species BHM to spin-chain mapping introduced earlier, for finite U/T . For a system of size $N = 6$ initialised in a product state $|+\rangle \otimes |0\rangle^{\otimes 4} \otimes |+\rangle$, and we compute the exact time-evolution of the two-species BHM, using the time-evolving block decimation (TEBD) algorithm [35, 36], for varying U/T over the appropriate inversion time τ . Using the effective two-spin density matrix for the end sites, the fidelity F was computed with the state $|G_2\rangle$ obtained from a perfectly implemented XY chain. The simulation results in Fig. 8.4(a) demonstrate that, as expected, the fidelity increases with U/T . Given that $\tau = UN\pi/16T^2$ the increasing fidelity, induced by deepening the lattice, comes at the cost of longer inversion times. However, Fig. 8.4(b) shows that $F > 0.99$ even at a

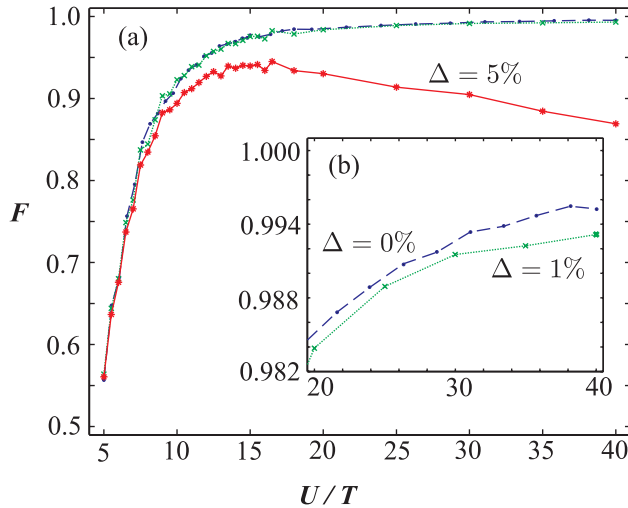


Figure 8.4. (a) The fidelity F of the effective XY spin-chain implemented by the 2-species BHM with the ratio U/T , for no noise $\Delta = 0\%$ (·), $\Delta = 1\%$ (×) and $\Delta = 5\%$ (*). (b) A close-up of (a). The solid, dashed and dotted lines are drawn to guide the eye.

moderate ratio of $U/T = 26$, and we found this curve to be largely independent of N for $N \sim O(10)$ tested. At this depth a $\lambda = 514$ nm optical lattice of ^{23}Na atoms has $\tau = 9.3$ ms, while a $\lambda = 826$ nm optical lattice of ^{87}Rb atoms has $\tau = 79$ ms. These are fast enough for multiple EB inversions to occur within the decoherence time of the system, which is typically of order of a second [37, 38].

We also investigate the effect of jitter in the lattice laser intensities. For ^{87}Rb the laser intensities I_a and I_b of the a and b lattices were taken as varying independently according to some Wiener noise $dW_{a(b)}(t)$ with variance Δ^2 : $I_{a(b)}(t) = I_0 + dW_{a(b)}(t)$, where I_0 is the ideal laser intensity. Such laser fluctuations are then nonlinearly related to the corresponding fluctuations in the hopping $t_n^{a(b)}$ and on-site interaction $U^{a(b)}, U^{ab}$ matrix elements of the 2-species BHM [26]. We assume a simplified version of this noise in which the intensity fluctuations alter, according to these nonlinear relations, the hopping and interaction scalings T and U contained within the overall scaling $W = 4T^2/U$ of j_n , but not the spatial profile α_n . Despite this restriction, this noise causes fluctuations in the inversion time τ during the dynamics, and also breaks the symmetry required to ensure that no $\sigma_n^z \sigma_{n+1}^z$ or spatially-varying σ_n^z contributions occur. In Fig. 8.4(a) the fidelity curves are plotted for $\Delta = 1\%$ and $\Delta = 5\%$ of I_0 . For $\Delta = 5\%$ the fidelity is seen to drop off in deeper lattices due to the cumulative effect of noise over longer inversion times. Crucially, the fidelity curve suffers only a minimal reduction due to $\Delta = 1\%$ noise, as in Fig. 8.4(b), and this represents a realistic value for the experimental stabilisation of the laser intensity.

8.4.3 Alternative implementations

Finally, we note that the scheme described in section 8.3 could be implemented in any physical system where the entangling operation \mathcal{C} is available. Specifically the architecture composed of a register and EB considered here could in principle be implemented wherever two adjacent engineered spin-chains are realisable. This requirement is particularly well suited to solid state systems such as arrays of quantum dots with one electron per dot in an external magnetic field [39, 40]. Here the qubit is encoded in the spin degree of freedom of the electron and the dynamics are described by a standard Heisenberg Hamiltonian. The presence of $\sigma_n^z\sigma_{n+1}^z$ terms in this Hamiltonian can be compensated by an appropriate spatially varying external magnetic field [16], while the angular momentum coupling profile can then be produced by controlling the external voltage applied to the gates defining the tunnelling barriers between the dots. However, such an implementation is currently limited by the small numbers of solid-state qubits realisable.

Another possibility is trapped ions [41]. A scheme for generating GHZ-type states over a chain of many ions has been proposed [42] and experimentally realised for four-qubits [4]. Although implemented by different means the entangling procedure in [42] is locally equivalent to the entangling operation \mathcal{C} when it is applied globally to the entire register. Permitting single-ion addressability, which has also been experimentally demonstrated [43], allows universal two-qubit quantum gates to be implemented by the same method [44], and additionally by addressing many ions \mathcal{C} can be applied to any subset of qubits. Thus the entangling operation constructed above for optical lattices via the EB is also realisable in ion trap systems via the collective vibrational degrees of freedom of the ions.

8.5 Conclusions

We have shown how arbitrary graph states can be generated efficiently by using an EB whose dynamics correspond to a non-interacting fermionic system undergoing mirror-inversion. By utilising an EB which is fixed and always on the dynamical control required for QIP tasks can be reduced to single qubit operations. Here an implementation of this scheme using an optical lattice of neutral atoms was considered in detail. The fidelity of the optical lattice proposal was examined not only for the depth ratio U/T , but also in the presence of noise, and found to be both realistic and robust. We have also briefly noted the suitability of the scheme to other physical systems.

References

- [1] O. Mandel, M. Greiner, A. Widera, T. Rom, T.W. Hänsch, I. Bloch, *Nature (London)* **425**, 937 (2003).
- [2] P. Walther, J.W. Pan, M. Aspelmeyer, R. Ursin, S. Gasparoni, A. Zeilinger, *Nature (London)* **429**, 158 (2004).

- [3] P. Walther, K.J. Resch, T. Rudolph, E. Schenck, H. Weinfurter, V. Vedral, M. Aspelmeyer, A. Zeilinger, *Nature (London)* **434**, 169 (2005).
- [4] C.A. Sackett, D. Kielpinski, B.E. King, C. Langer, V. Meyer, C.J. Myatt, M. Rowe, Q.A. Turchette, W.M. Itano, D.J. Wineland, C. Monroe, *Nature (London)* **404**, 256 (2000).
- [5] A. Rauschenbeutel, G. Nogues, S. Osnaghi, P. Bertet, M. Brune, J.M. Raimond, S. Haroche, *Science* **288**, 2024 (2000).
- [6] M. Hein, J. Eisert, H.-J. Briegel, *Phys. Rev. A* **69**, 062311 (2004).
- [7] H.-J. Briegel, R. Raussendorf, *Phys. Rev. Lett.* **86**, 910 (2001).
- [8] D. Gottesman, *Ph.D thesis* (CalTech, Pasadena, 1997).
- [9] A.M. Steane, *Phys. Rev. Lett.* **77**, 793 (1996).
- [10] R. Raussendorf, H.-J. Briegel, *Phys. Rev. Lett.* **86**, 5188 (2001).
- [11] R. Raussendorf, D.E. Browne, H.-J. Briegel, *Phys. Rev. A* **68**, 022312 (2003).
- [12] D.E. Browne, T. Rudolph, *Phys. Rev. Lett.* **95**, 010501 (2005).
- [13] S.D. Barrett, P. Kok, *Phys. Rev. A* **71**, 060310(R) (2005).
- [14] S.B. Bravyi, A.Y. Kitaev, *Ann. Phys. (N.Y.)* **298**, 210 (2002).
- [15] S. Sachdev, *Quantum Phase Transitions* (Cambridge Univ. Press, Cambridge, 2001).
- [16] M. Christandl, N. Datta, A.K. Ekert, A.J. Landahl, *Phys. Rev. Lett.* **92** 187902 (2004).
- [17] P. Zanardi, *Phys. Rev. A* **65**, 042101 (2002).
- [18] P. Zanardi, X. Wang, *J. Phys. A* **35**, 7947 (2002).
- [19] L.A. Wu, D.A. Lidar, *J. Math. Phys.* **43**, 4506 (2002).
- [20] V. Vedral, *Central Eur. J. Phys.* **1**, 289 (2003).
- [21] M.H. Yung, S. Bose, *Quant. Inf. Comput.* **4**, 174 (2004).
- [22] M.H. Yung, S. Bose, *Phys. Rev. A* **71**, 032310 (2005).
- [23] A. Recati, P.O. Fedichev, W. Zwerger, J. von Delft, P. Zoller, *Phys. Rev. Lett.* **94**, 040404 (2005).
- [24] T. Calarco, E.A. Hinds, D. Jaksch, J. Schmiedmayer, J.I. Cirac, P. Zoller, *Fortschritte der Physik* **48**, 945 (2000).
- [25] B. Paredes, A. Widera, V. Murg, O. Mandel, S. Fölling, J.I. Cirac, G.V. Shlyapnikov, T.W. Hänsch, I. Bloch, *Nature (London)* **429**, 277 (2004).
- [26] D. Jaksch, C. Bruder, J.I. Cirac, C.W. Gardiner, P. Zoller, *Phys. Rev. Lett.* **81**, 3108 (1998).
- [27] L.M. Duan, E. Demler, M.D. Lukin, *Phys. Rev. Lett.* **91**, 090402 (2003).
- [28] J.K. Pachos, P.L. Knight, *Phys. Rev. Lett.* **91**, 107902 (2003).

- [29] D. Jaksch, P. Zoller, *Ann. Phys. (N.Y.)* **315**, 52 (2005).
- [30] J.J. Garcia-Ripoll, J.I. Cirac, *New J. Phys.* **5**, 76 (2003).
- [31] A. Griessner, A.J. Daley, D. Jaksch, P. Zoller, *Phys. Rev. A* **72**, 032332 (2005).
- [32] P. Rabl, A.J. Daley, P.O. Fedichev, J.I. Cirac, P. Zoller, *Phys. Rev. Lett.* **91**, 110403 (2003).
- [33] T. Calarco, U. Dorner, P. Julienne, C. Williams, P. Zoller, *Phys. Rev. A* **70**, 012306 (2004).
- [34] C. Moura Alves, D. Jaksch, *Phys. Rev. Lett.* **93**, 110501 (2004).
- [35] G. Vidal, *Phys. Rev. Lett.* **91**, 147902 (2003).
- [36] G. Vidal, *Phys. Rev. Lett.* **93**, 040502 (2004).
- [37] M. Greiner, O. Mandel, T. Esslinger, T.W. Hänsch, I. Bloch, *Nature (London)* **415**, 39 (2002).
- [38] W.K. Hensinger, H. Häffner, A. Browaeys, N.R. Heckenberg, K. Helmerson, C. McKenzie, G.J. Milburn, W.D. Phillips, S.L. Rolston, H. Rubinsztein-Dunlop, B/ Upcroft, *Nature (London)* **412**, 52 (2001).
- [39] V.N. Golovach, D. Loss, *Semicond. Sci. Technol.* **17**, 355 (2002).
- [40] Y.A. Pashkin, T. Yamamoto, O. Astafiev, Y. Nakamura, D.V. Averin, J.S. Tsai, *Nature (London)* **421**, 823 (2003).
- [41] J.I. Cirac, P. Zoller, *Phys. Rev. Lett.* **74**, 4091 (1995).
- [42] K. Mølmer, S. Sørensen, *Phys. Rev. Lett.* **82**, 1835 (1999).
- [43] C. Roos, M. Riebe, H. Häffner, W. Hänsel, J. Benhelm, G.P.T. Lancaster, C. Becher, F. Schmidt-Kaler, R. Blatt, *Science* **304**, 1478 (2004).
- [44] S. Sørensen, K. Mølmer, *Phys. Rev. Lett.* **82**, 1971 (1999).

CHAPTER 9

PUBLICATION

Generation of twin-Fock states via two-component Mott insulating to Superfluid transition

M. Rodriguez, S. R. Clark¹, and D. Jaksch

Clarendon Laboratory, University of Oxford, Parks Road, Oxford OX1 3PU, U.K.

Physical Review A **75**, 011601(R) (2007)

We propose the dynamical creation of twin-Fock states, which exhibit Heisenberg limited interferometric phase sensitivities, in an optical lattice. In our scheme a two-component Mott insulator with two bosonic atoms per lattice site is melted into a superfluid. This process transforms local correlations between hyperfine states of atom pairs into multi-particle correlations extending over the whole system. The melting time does not scale with the system size which makes our scheme experimentally feasible.

Degenerate atomic Bose- and Fermi-gases [1] provide an excellent starting point for engineering almost-pure many-particle quantum states which are an essential resource for novel quantum technologies. This is illustrated by the realisation of a Mott insulator (MI) [2, 3, 4] in the lowest Bloch band of an optical lattice which can serve as a quantum memory [5]. However, new methods are necessary for attaining some of the most important N -particle states, in particular those which allow a sensitivity enhancement from the standard quantum limit $\propto 1/\sqrt{N}$ to the Heisenberg limit $\propto 1/N$ in quantum metrology [6]. Here we propose a method for engineering twin-Fock states [7, 8] starting from a two component MI with two bosonic atoms per site in an optical lattice [5, 9, 10, 11]. Our scheme manipulates the hyperfine states a and b of atom pairs pinned to single lattice sites and decoupled from one another in the MI regime. In this limit the dynamics is reduced to a set of identical two particle problems and correlations between states a and b are accurately induced using Raman laser pulses or microwaves and collisional interactions controlled via Feshbach resonances [12, 13, 14]. These local *two-particle* correlations are then transformed into *multi-particle* correlations extending over the whole system by melting the MI into a superfluid (SF). This quantum melting can be experimentally implemented by adiabatically ramping down the depth of the lattice potential [2, 3, 4, 15] as shown in Fig. 9.1(a). By an appropriate choice of correlations created in the MI phase a twin-Fock state emerges in the resulting two component superfluid. Using this state in a Mach-Zehnder interferometer (MZI), shown in Fig. 9.1(b), one can approach sensitivities scaling as $1/N$.

¹The present author was a joint first author of this paper

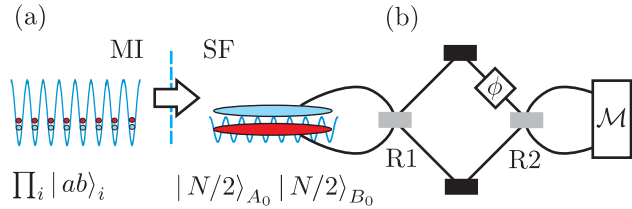


Figure 9.1. (a) Melting of a two-component two-atom MI into a SF. (b) The internal states a and b represent the arms of an interferometer with rotations $R1$, $R2$ and phase-shift ϕ induced by a Ramsey pulse sequence; ϕ is measured by \mathcal{M} .

Our method is motivated by theoretical and experimental evidence [2, 3, 4, 15, 16] that long range correlations build up quickly when melting a MI to a SF. Almost adiabatic melting can be achieved with ramping times t_r on the order of a few tens of N/MJ_0 where J_0 is the typical tunneling amplitude between lattice sites during the melting process and M is the number of lattice sites [16]. Importantly, in our scheme $M \propto N$ thus preventing t_r from scaling with N . The achievement of sensitivities at the Heisenberg limit relies acutely on the relative number of atoms entering each port of the interferometer. This stringent requirement rules out simple schemes involving either a $\pi/2$ rotation into a two-component Bose-Einstein condensate (BEC) or a rapid splitting of a single-component BEC in a double-well potential, since both result in a binomial relative number distribution. While number squeezing to a twin-Fock state could be achieved in the latter case by an adiabatic splitting, since $M = 2$ is fixed this timescale $t_r \propto N$ [17, 16]. In contrast, the smaller t_r for our scheme is less demanding on the suppression of dissipation which is known to degrade the achievable sensitivities [18, 19, 20]. We note another promising route to generating a twin-Fock state is through the coherent dissociation of a molecular BEC as suggested in [21].

Our starting point is a MI with two atoms in each lattice site i given by $|\Psi_{ab}\rangle = \prod_i |ab\rangle_i$ [9, 10, 11, 22, 23]. This state, with exactly the same number of a and b atoms, can be created by collisional interactions involving an auxiliary state c as experimentally demonstrated in [9, 10, 11]. We analyse the melting of $|\Psi_{ab}\rangle$, and also of the superposition state $|\Psi_{aa+bb}\rangle = \prod_i (|aa\rangle_i + |bb\rangle_i)/\sqrt{2}$ obtainable from $|\Psi_{ab}\rangle$ by applying a $\pi/2$ -Raman pulse. For this we use the two component Bose-Hubbard model describing the dynamics of atoms trapped in the lowest Bloch band of a sufficiently deep optical lattice. The corresponding Hamiltonian is ($\hbar = 1$) [2, 3, 4]

$$\begin{aligned} \hat{H} = & - \sum_{\langle i,j \rangle} (J_a \hat{a}_i^\dagger \hat{a}_j + J_b \hat{b}_i^\dagger \hat{b}_j) + U \sum_i \hat{n}_i^a \hat{n}_i^b \\ & + \frac{V_a}{2} \sum_i \hat{n}_i^a (\hat{n}_i^a - 1) + \frac{V_b}{2} \sum_i \hat{n}_i^b (\hat{n}_i^b - 1), \end{aligned} \quad (9.1)$$

where $\hat{a}_i(\hat{b}_i)$ is the bosonic destruction operator for an $a(b)$ -atom localised in lattice site i , $\hat{n}_i^a = \hat{a}_i^\dagger \hat{a}_i$ and $\hat{n}_i^b = \hat{b}_i^\dagger \hat{b}_i$, while $\langle i, j \rangle$ denotes summation over nearest-neighbors. The parameter $J_{a(b)}$ is the tunneling matrix element for atoms in state $a(b)$; $V_{a(b)}$ and U are the on-site intra- and inter-species interaction matrix elements respectively. For simplicity we only consider the symmetric case with $J_{a(b)} = J$, $V_{a(b)} = V$. The ratio between the matrix elements is determined by the lattice depth [2, 4] and additionally U, V can be controlled via Feshbach resonances [12, 13, 14] or by shifting the a and b atoms away from each other using state-dependent lattices [5]. We denote the total number of atoms in state $a(b)$ as $\hat{N}_{a(b)} = \sum_i \hat{n}_i^{a(b)}$ and introduce Schwinger boson operators $\hat{J}_x = \sum_i (\hat{a}_i^\dagger \hat{b}_i + \hat{b}_i^\dagger \hat{a}_i)/2$, $\hat{J}_y = \sum_i (\hat{a}_i^\dagger \hat{b}_i - \hat{a}_i^\dagger \hat{b}_i)/2i$, $\hat{J}_z = (\hat{N}^a - \hat{N}^b)/2$ and $\hat{\mathbf{J}} = (\hat{J}_x, \hat{J}_y, \hat{J}_z)$.

We illustrate the outcome of melting two-component MI ground states with fixed total particle number $N = 2M$ assuming adiabatic evolution in an M -site system with periodic boundary conditions. The melting starts deep in the MI regime, where J can be neglected. For $U < V$ the nondegenerate MI ground state is $|\Psi_{ab}\rangle$ and this adiabatically melts into the nondegenerate SF ground state $|\Psi_{\text{tf}}\rangle = |N/2\rangle_{A_0} |N/2\rangle_{B_0} \propto (\hat{A}_0^\dagger)^{N/2} (\hat{B}_0^\dagger)^{N/2} |\text{vac}\rangle$ for $V/J \rightarrow 0$. Here all $N/2$ a -atoms are in the same delocalised symmetric mode $\hat{A}_0 \propto \sum_i \hat{a}_i$, all $N/2$ b -atoms are in mode $\hat{B}_0 \propto \sum_i \hat{b}_i$ and $|\text{vac}\rangle$ is the vacuum state. Thus, adiabatic melting of $|\Psi_{ab}\rangle$ provides a direct means of obtaining a twin-Fock state $|\Psi_{\text{tf}}\rangle$ with zero relative atom number difference.

In the opposite case $U > V$ the system exhibits spatial separation of the a and b components and has a large number of degenerate ground states. For an even number N_a of a -atoms this degeneracy is lifted by completely connected hopping [24] and the state $|\Psi_{\text{sep}}^{N_a}\rangle = \$\{\prod_{(i \leq N_a/2)} |aa\rangle_i \prod_{(N_a/2 < j \leq N)} |bb\rangle_j\}$ is adiabatically connected to the nondegenerate SF ground state $|N_a\rangle_{A_0} |N - N_a\rangle_{B_0}$, where $\$$ denotes symmetrisation over lattice site configurations. Our second initial state $|\Psi_{aa+bb}\rangle$ is a binomial superposition of ground states $|\Psi_{\text{sep}}^{N_a}\rangle$ and therefore results in the melted state

$$|\Psi_{\text{mac}}\rangle = \frac{1}{\sqrt{2^{N/2}}} \sum_{m=0}^{N/2} \binom{N/2}{m}^{1/2} |2m\rangle_{A_0} |N - 2m\rangle_{B_0}.$$

After rotation, the overlap of this state with the macroscopic superposition state [25] $|\Psi_{\text{max}}\rangle = (|N\rangle_{A_0} |0\rangle_{B_0} + |0\rangle_{A_0} |N\rangle_{B_0})/\sqrt{2}$ is found to be $\mathcal{O} = |\langle\Psi_{\text{max}}|\exp(i\pi\hat{J}_y/2)|\Psi_{\text{mac}}\rangle| = \sqrt[4]{8/9} > 0.97$ for $N \rightarrow \infty$ and this limit is monotonically attained with $\mathcal{O} > 0.97$ for $N > 20$.

We can use either of the final states obtained by adiabatic melting to realise sensitivities $\propto 1/N$ in the MZI setup shown in Fig. 9.1(b). For the twin-Fock state $|\Psi_{\text{tf}}\rangle$ R1 implements the conventional beam-splitter operation $\exp(i\pi\hat{J}_x/2)$. In the case of $|\Psi_{\text{mac}}\rangle$ R1 rotates the state according to $\exp(i\pi\hat{J}_y/2)$ as discussed above. Then a relative phase ϕ is induced in one of the arms of the MZI. The operation R1 can be implemented by rapid resonant $\pi/2$ -Raman pulses, while the relative phase ϕ could be induced by an appropriate off-resonant pulse. The achievable phase sensitivity inside the interferometer (after R1) can be computed from the relative phase probability dis-

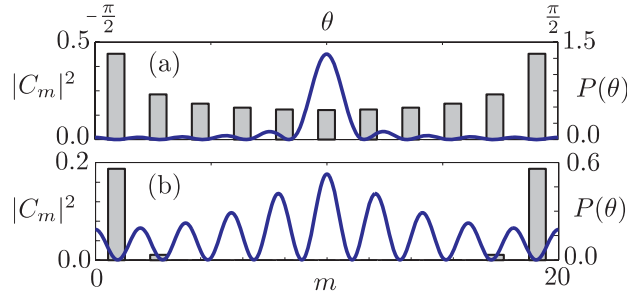


Figure 9.2. The amplitudes $|C_m|^2$ (left-bottom axes) and corresponding relative phase probability distribution $P(\theta)$ (right-top axes) after the rotation R1 of (a) $|\Psi_{\text{tf}}\rangle$ and (b) $|\Psi_{\text{mac}}\rangle$ with $N = 20$.

tribution $P(\theta)$. For a given state $|\psi\rangle = \sum_{m=0}^N C_m |m\rangle_{A_0} |N-m\rangle_{B_0}$ this is computed as $P_s(\Delta\theta) = |\sum_{m=0}^N C_m \exp(-im\Delta\theta)|^2/(s+1)$ where $\Delta\theta$ is a multiple of $2\pi/(s+1)$. The distribution $P(\theta)$ is obtained by multiplying $P_s(\Delta\theta)$ with $(s+1)/2\pi$ and taking the limit $s \rightarrow \infty$ [18, 19]. As shown in Fig. 9.2(a) $P(\theta)$ is sharply peaked for the rotated $|\Psi_{\text{tf}}\rangle$ and Fig. 9.2(b) displays the oscillatory behavior of $P(\theta)$ for the rotated $|\Psi_{\text{mac}}\rangle$. The sensitivity $\delta\phi$ of each state is quantified by the half width at half maximum (HWHM) of $P(\theta)$ around some fixed phase typically taken as $\theta = 0$. From this definition it can be shown for both states that $\delta\phi \propto 1/N$ and so scale at the Heisenberg limit [18, 19, 7, 8, 25]. The final step in the MZI consists of rotation R_2 and measurement \mathcal{M} of a phase dependent quantity which exhibits this Heisenberg limited phase resolution. For instance the measurement of parity as discussed in [26, 27] or \hat{J}_z^2 as proposed in [28, 29] can achieve this. These methods exploit nonlinearities caused by atomic collisions and are thus realisable in our setup.

We now analyse the achievable sensitivity for incomplete melting at finite (residual) values of V/J before considering experimental imperfections arising from non-adiabatic ramping and particle loss. We restrict our considerations to the measurement of \hat{J}_z^2 and to the twin-Fock state due to its greater experimental feasibility. We study these effects in terms of the noise $\Delta\phi$ on the ϕ dependent observable \hat{J}_z^2 . Error propagation theory gives $\Delta\phi = \Delta\hat{J}_z^2/|\partial\langle\hat{J}_z^2\rangle/\partial\phi|$ where $\langle\hat{J}_z^2\rangle$ and $\Delta\hat{J}_z^2$ are the average and the spread respectively. For states which are zero eigenvectors of \hat{J}_z , such as $|\Psi_{\text{tf}}\rangle$, this gives

$$\Delta\phi^2 = \frac{\sin^2\phi(\langle\hat{J}_x^4\rangle - \langle\hat{J}_x^2\rangle^2) + \cos^2\phi\langle\hat{J}_x\hat{J}_z^2\hat{J}_x\rangle}{4\cos^2\phi\langle\hat{J}_x^2\rangle^2}. \quad (9.2)$$

At $\phi = 0$ the sensitivity reduces to $\Delta\phi(0) = \frac{1}{2}\langle\hat{J}_x^2\rangle^{-1/2}$ which can be expressed entirely in terms of the one-particle density matrices $\rho_{ij}^a = \langle\hat{a}_i^\dagger\hat{a}_j\rangle$ and $\rho_{ij}^b = \langle\hat{b}_i^\dagger\hat{b}_j\rangle$ using $\langle\hat{J}_x^2\rangle = [\sum_i(\rho_{ii}^a + \rho_{ii}^b) + \sum_{i,j}(\rho_{ij}^a\rho_{ji}^b + \text{h.c.})]/4$. The initial MI state $|\Psi_{ab}\rangle$ with no off-diagonal correlations $\rho_{ij}^a = \rho_{ij}^b = \delta_{ij}$ yields the standard quantum limit $\Delta\phi = 1/\sqrt{2N}$ (cf. Fig. 9.3(a) at $V/J \gg 1$). The final SF $|\Psi_{\text{sf}}\rangle$ with long-range correlations $\rho_{ij}^a = \rho_{ij}^b =$

1 asymptotically recovers the Heisenberg limit $\Delta\phi = 1/\sqrt{N^2/2 + N}$ (cf. Fig. 9.3(a) at $V/J = 0$). Thus the scaling $\Delta\phi \propto N^{-\alpha}$ changes from $\alpha = 1/2$ to $\alpha = 1$ during the melting.

The presence of a residual intra-species interaction V results in quantum depletion of the populations in the A_0 and B_0 modes which reduces the attainable sensitivity. We consider this effect for $U = 0$, achieved for example by fully separating the sites of a spin-dependent lattice. In the SF regime $J \gg V$ a translationally invariant system is well described by the N -conserving Bogoliubov wavefunction

$$|\psi_{\text{bog}}\rangle \sim (\hat{\Lambda}_a)^{N/2} (\hat{\Lambda}_b)^{N/2} |\text{vac}\rangle, \quad (9.3)$$

where $\hat{\Lambda}_a = (\hat{A}_0^{\dagger 2} - \sum_{\mathbf{q} \neq 0} c_{\mathbf{q}} \hat{A}_{\mathbf{q}}^\dagger \hat{A}_{-\mathbf{q}}^\dagger)$ with $\hat{A}_{\mathbf{q}}$ the \mathbf{q} quasi-momentum modes for a , and similarly $\hat{\Lambda}_b$ is defined in terms of $\hat{B}_{\mathbf{q}}$ for component b . Within this ansatz the depletion is identical for both components and is given by $\zeta = \sum_{\mathbf{q} \neq 0} n_{\mathbf{q}} = c_{\mathbf{q}}^2/(1 - c_{\mathbf{q}}^2)$ where $n_{\mathbf{q}} = \langle \hat{A}_{\mathbf{q}}^\dagger \hat{A}_{\mathbf{q}} \rangle = \langle \hat{B}_{\mathbf{q}}^\dagger \hat{B}_{\mathbf{q}} \rangle$ and the amplitudes $c_{\mathbf{q}} \ll 1$ can be solved in terms of V/J and are given in [30, 31, 32]. The sensitivity is then $\Delta\phi(0) = 1/[N^2(1 - \zeta)^2/2 + N + 2 \sum_{\mathbf{q} \neq 0} n_{\mathbf{q}}^2]^{1/2}$. For a three dimensional (3D) optical lattice the depletion $\zeta = (V/J)^{3/2}/3\pi^2\sqrt{2}$ and the sum $\sum_{\mathbf{q} \neq 0} n_{\mathbf{q}}^2 = (V/J)^{3/2}(3\pi - 8)/12\sqrt{2}$ are constant in N . Within the region of validity of the Bogoliubov ansatz there will thus be no degradation of the sensitivity scaling α . Similarly we find no decrease of α in 2D within the Bogoliubov ansatz. In contrast, for a 1D system the depletion increases with N since there is no true condensate for non-zero V and long-range correlations decay algebraically. Consequently the scaling α decreases with increasing V/J as shown in Fig. 9.3(a) for a finite number of particles.

We explore the sensitivity scaling between the SF and MI limit in 1D numerically using the Time-Evolving-Block-Decimation algorithm [33, 34]. For specific values of N we compute the ground states of the Hamiltonian Eq. (9.1) over a range of V/J and $U = 0$ and calculate their sensitivities. The result for $N = 60$ in Fig. 9.3(b) shows a smooth transition between the ideal SF and MI results and agrees with the Bogoliubov result for $V/J \leq 2$. By repeating this calculation for different N we extract the sensitivity scaling α . For all values of V/J the numerical results are well approximated by a power-law $\Delta\phi \sim N^{-\alpha}$ as shown for the extreme cases in Fig. 9.3(c). We combine these results in Fig. 9.3(a) which displays the scaling α as a function of V/J . The value of α decreases smoothly from the Heisenberg limit in the SF regime to the standard quantum limit in the MI regime. As also shown in Fig. 9.3(a) the 1D-Bogoliubov ansatz Eq. (9.3) is consistent with the numerics for $V/J \leq 2$ and the values of N used here. In the MI regime a number conserving particle-hole ansatz [35] underestimates long-range correlations and therefore does not predict an increase of α from $1/2$ at finite V/J . This emphasises the importance of the growth of long range correlations for increasing α above the standard quantum limit. While our numerical calculations are performed for sizes of 1D optical lattices currently used in experiments [2, 3, 5] we expect the scaling α to drop from $\alpha = 1$ to $\alpha = 1/2$ at vanishingly small V/J when $N \rightarrow \infty$ because of the lack of true long range correlations. In 2D and 3D this reduction is instead expected to occur at finite V/J close to the phase transition

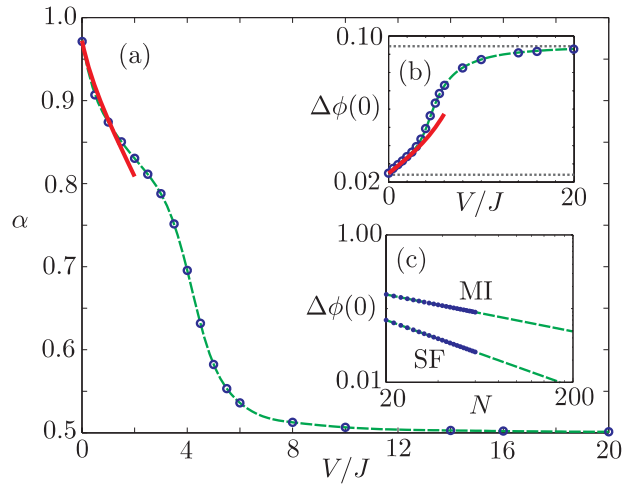


Figure 9.3. (a) Scaling α in $\Delta\phi \sim N^{-\alpha}$ against V/J of ground states of \hat{H} with $U = 0$. The scaling was obtained from calculations with $N = 20$ up to $N = 60$ with $M = N/2$ for both the 1D numerical results (\circ) in a box system and the N -conserving Bogoliubov results (solid line). (b) Sensitivity $\Delta\phi$ as a function of V/J for $N = 60$. The dotted lines show exact results for the twin Fock SF (bottom) and the MI (top) states, while the thick solid line shows the Bogoliubov result. (c) $\Delta\phi$ as a function of N for $V/J = 20$ (MI) and $V/J = 1/2$ (SF) giving α of the corresponding points in (a). In all cases the dashed lines are to guide the eye.

point $(V/J)_{\text{crit}}$ below which long range correlations exist at large N .

In experiments the ramping time t_r will be finite and so the melting is never perfectly adiabatic. We numerically compute the dynamical ramping of V/J for the Hamiltonian Eq. (9.1) with $U = 0$ from the MI ground state. In Fig. 9.4(a) the energy difference per atom between the final ramped state $|\Psi(t_r)\rangle$ and the SF ground state $|\Psi_0\rangle$ is shown as a function of the ramping time t_r , along with the corresponding many-body overlap $|\langle\Psi(t_r)|\Psi_0\rangle|$. For the infinite Bose-Hubbard-model it has been shown [16] that $t_r \gg V_{\max}/J^2$ guarantees adiabatic evolution. Our numerics of a finite-sized system agree with this result giving a near-unit overlap and small energy differences for ramping times of $t_r \sim 3V_0/J^2$ with V_0 the initial interaction strength in the MI.

Given that the ramping time t_r is much longer than the time required to implement the MZI in Fig. 9.1(b) we consider the influence of atom loss over a time t_r . The build-up of long range correlations during the melting process has been found to be robust to atom loss processes [2, 3]. However, atom loss will cause uncertainty in the relative number of a and b atoms in the final state $|\Psi_{\text{tf}}\rangle$. We use the model introduced in [18, 19] to calculate the sensitivity scaling α assuming the state $|\Psi_{\text{tf}}\rangle$ is subject to atom loss at a rate κ for time t_r . As shown in Fig. 9.4(b) we find that $\alpha \approx 1$ for $\kappa t_r \ll 0.1$. In combination with the adiabaticity condition on t_r Heisenberg limited sensitivities can thus be achieved for $\kappa \ll J^2/30V_0$. This condition is within the reach

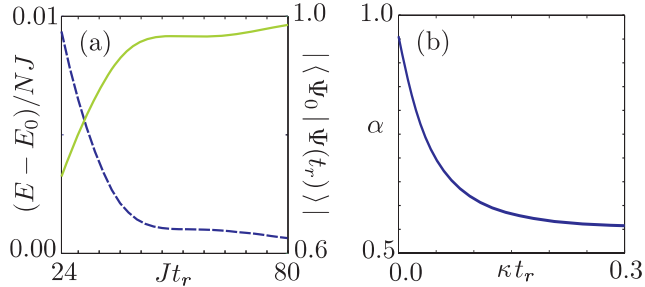


Figure 9.4. (a) Energy difference per atom $(E - E_0)/NJ$ between $|\Psi(t_r)\rangle$ and the final SF ground state $|\Psi_0\rangle$ (left axis, dashed lines) and overlap $|\langle \Psi(t_r) | \Psi_0 \rangle|$ (right axis, solid line) as a function of the ramping time t_r . Starting from the MI ground state at $V_0/J = 20$ we ramped $V(t)$ down to a final $V_{t_r}/J = 1/2$ using different ramping times t_r and $U = 0$, $N = 50$ and $M = 25$. (b) Scaling α of $\delta\phi$ with N for $|\Psi_{tf}\rangle$ under the presence of atom-loss at a rate κ obtained from results for $N = 20$ up to $N = 60$. Note that α does not reach unity because of the finite N used.

of current optical lattice technology where tunneling amplitudes J of a few hundred Hz and loss rates on the order of Hz can be achieved [2, 3, 5]. Furthermore, additional fluctuations in the overall particle number N which occur from shot to shot do not affect the scaling α [28, 29]. In the experiment a harmonic trapping potential is likely to be present and causes an outer shell of singly occupied lattice sites with atoms in the auxiliary state c . Additionally, an imperfect Raman transition during the creation of the initial MI state may leave a c atom pair within the $|\Psi_{ab}\rangle$ state. In both cases the presence of a small number of c -atom impurities will not destroy the coherence of the final SF state, as seen in recent experiments [36, 37]. Also these atoms will remain in state c throughout the whole process and thus not contribute to the particle number fluctuations [9, 10, 11].

In summary we have shown that quantum melting of a two-component MI in an optical lattice provides a viable route to engineer twin-Fock on timescales t_r smaller than current experimental atom-loss times. In particular the creation time t_r does not scale with N . Our scheme also exploits the accurate controllability of two-atoms in a single lattice sites to minimise fluctuations in the relative numbers of a and b atoms which is crucial for achieving Heisenberg limited sensitivities $\propto 1/N$.

References

- [1] L. Pitaevskii, S. Stringari, *Bose-Einstein Condensation* (Oxford Univ. Press, Oxford, 2003).
- [2] M. Greiner, O. Mandel, T. Esslinger, T.W. Hänsch, I. Bloch, *Nature (London)* **415**, 39 (2002).

- [3] T. Stöferle, H. Moritz, C. Schori, M. Köhl, T. Esslinger, *Phys. Rev. Lett.* **92**, 130403 (2004).
- [4] D. Jaksch, C. Bruder, J.I. Cirac, C.W. Gardiner, P. Zoller, *Phys. Rev. Lett.* **81**, 3108 (1998).
- [5] O. Mandel, M. Greiner, A. Widera, T. Rom, T.W. Hänsch, I. Bloch, *Nature (London)* **425**, 937 (2003)..
- [6] V. Giovannetti, S. Lloyd, L. Maccone, *Science* **306**, 1330 (2004) and references therein.
- [7] M.J. Holland, K. Burnett, *Phys. Rev. Lett.* , **71**, 1355 (1993);
- [8] P. Bouyer, M.A. Kasevich, *Phys. Rev. A* **56**, 1083(R) (1997).
- [9] A. Widera, F. Gerbier, T. Gericke, S. Fölling, O. Mandel, I. Bloch, *Phys. Rev. Lett.* **95**, 190405 (2005).
- [10] F. Gerbier, A. Widera, S. Fölling, O. Mandel, I. Bloch, *Phys. Rev. A* **73**, 041602(R) (2006).
- [11] G. Thalhammer, K. Winkler, F. Lang, S. Schmid, R. Grimm, J. Hecker Denschlag, *Phys. Rev. Lett.* **96**, 050402 (2006).
- [12] E.A. Donley, N.R. Claussen, S.T. Thompson, C.E. Wieman, *Nature (London)* **417**, 529 (2002).
- [13] A. Marte, T. Volz, J. Schuster, S. Dürr, G. Rempe, E.G.M. van Kempen, B.J. Verhaar, *Phys. Rev. Lett.* **89**, 283202 (2002);
- [14] M. Theis, G. Thalhammer, K. Winkler, M. Hellwig, G. Ruff, R. Grimm, J. Hecker Denschlag, *Phys. Rev. Lett.* **93**, 123001 (2004).
- [15] S.R. Clark, D. Jaksch, *Phys. Rev. A* **70**, 043612 (2004).
- [16] J. Dziarmaga, A. Smerzi, W.H. Zurek, A.R. Bishop, *Phys. Rev. Lett.* **88**, 167001 (2002).
- [17] Y. Shin, M. Saba, T.A. Pasquini, W. Ketterle, D.E. Pritchard, A.E. Leanhardt, *Phys. Rev. Lett.* **92**, 050405 (2004) and references therein.
- [18] J.A. Dunningham, K. Burnett, S.M. Barnett, *Phys. Rev. Lett.* **89**, 150401 (2002);
- [19] S.M. Barnett, D.T. Pegg, *Phys. Rev. A* **42**, 6713 (1990).
- [20] S.F. Huelga, C. Machiavello, T. Pellizzari, A.K. Ekert, M.B. Plenio, J.I. Cirac, *Phys. Rev. Lett.* **79**, 3865 (1997).
- [21] K.V. Kheruntsyan, P.D. Drummond, *Phys. Rev. A* **66**, 031602 (2002).
- [22] P. Rabl, A.J. Daley, P.O. Fedichev, J.I. Cirac, P. Zoller, *Phys. Rev. Lett.* **91**, 110403 (2003).
- [23] M. Popp, J.J. Garcia-Ripoll, K.G.H. Vollbrecht, J.I. Cirac, *Phys. Rev. A* **74**, 013622 (2006).

- [24] M.P.A. Fisher, P.B. Weichman, G. Grinstein, D.S. Fisher, *Phys. Rev. B* **40**, 546 (1989).
- [25] J.J. Bollinger, W.M. Itano, D.J. Wineland, D.J. Heinzen, *Phys. Rev. A* **54**, R4649 (1996).
- [26] R.A. Campos, C.C. Gerry, A. Benmoussa, *Phys. Rev. A* **68**, 023810 (2003);
- [27] C.C. Gerry, R.A. Campos, *Phys. Rev. A* **68**, 025602 (2003).
- [28] J.A. Dunningham, K. Burnett, *Phys. Rev. A* **70**, 033601 (2004);
- [29] T. Kim, Y. Ha, J. Shin, H. Kim, G. Park, K. Kim, T.-G. Noh, C.K. Hong, *Phys. Rev. A* **60**, 708 (1999).
- [30] A.J. Leggett, *Rev. Mod. Phys.* **73**, 307 (2001);
- [31] M. Girardeau and R. Arnowitt, *Phys. Rev.* **113**, 755 (1959);
- [32] C.W. Gardiner, *Phys. Rev. A* **56**, 1414 (1997).
- [33] G. Vidal, *Phys. Rev. Lett.* **93** 040502 (2004);
- [34] F. Verstraete, J.J. Garcia-Ripoll, J.I. Cirac, *Phys. Rev. Lett.* **93**, 207204 (2004).
- [35] F.M. Cucchietti, B. Damski, J. Dziarmaga, W.H. Zurek, *Phys. Rev. A* **75**, 023603 (2007).
- [36] K. Günter, T. Stöferle, H. Moritz, M. Köhl, T. Esslinger, *Phys. Rev. Lett.* **96** 180402 (2006).
- [37] S. Ospelkaus, C. Ospelkaus, O. Wille, M. Succo, P. Ernst, K. Sengstock, K. Bongs, *Phys. Rev. Lett.* **96**, 180403 (2006).

CHAPTER 10

SUMMARY AND CONCLUSIONS

Throughout this thesis we have emphasised the abilities of optical lattices for creating coherent, controllable, strongly-correlated systems many times. With this capability, however, comes considerable theoretical challenges in understanding not only the results produced by such experiments, but also in devising new applications for these systems. For 1D systems this thesis has addressed these issues by employing available analytical methods and the recently developed time-evolving-block-decimation (TEBD) algorithm. In the following I am going to summarise what I consider to be the most relevant contributions of this work.

- In part II of this thesis we analysed several open questions raised by two seminal experiments with optical lattices. Specifically, we investigated the rapid emergence of single-particle coherence when dynamically melting a Mott insulating state, and the surprisingly broad superfluid excitation spectrum. Our simulations revealed that the Bose-Hubbard model (BHM) is sufficient to describe these features and therefore represents an excellent model for the dynamics of cold atoms in optical lattices. In addition to this we have determined limits on the applicability of the adiabatic approximation to quantum melting, and quantified the stability of the Mott insulator via its excitation spectrum, both of which are essential requirements for its uses in part III.
- In part III of this thesis we devised two schemes for engineering useful quantum states of a two-component system. In the first scheme our aim was to generate arbitrary graph states by utilising the special dynamical properties of a mirror-inverting spin-chain. Our analytical investigation of mirror inversion revealed that for a given fixed time the evolution of the spin-chain implements a useful entangling quantum circuit. By using TEBD we found that the implementation of this scheme with an insulating phase of the two-component BHM is robust. In the second scheme we demonstrated how dynamically melting a two-component Mott insulator, with two atoms per lattice site, into a superfluid provides a means of reliably creating twin-Fock states. Furthermore, our earlier work in part II suggests that near-adiabatic melting can be achieved with a melting time that does not scale with the system size.
- From a computational perspective the calculations in this thesis were some of the first to actually test the applicability of the TEBD method beyond the simple

exactly solved Ising model. In this sense they have collectively demonstrated its accuracy and scalability to realistic sized problems in optical lattices.

To end I would like to outline some future directions of this work. We have noted that many of the calculations presented here were only possible due to the spectacular advances in numerical methods for 1D systems. Further adaptations of the TEBD algorithm that have recently been developed give several promising avenues to explore. These include the ability to simulate finite-temperature and dissipative 1D systems according to a master equation evolution [1]. We have already exploited this method with success in recent work [2] where we analysed the robustness of the graph state generation scheme outlined in chapter 8. Additionally by adopting a more sophisticated treatment of symmetries [3, 4] in TEBD further, more demanding calculations involving the two-component systems could be pursued which would be of direct relevance to Bose-Fermi mixture experiments. An interesting recent development for TEBD is the ability for it to handle infinite translationally-invariant systems¹ [5]. This method may well provide some fundamental insight into the dynamical and stationary properties of 1D systems. For example, this might include the proliferation of “defects” during a non-adiabatic transition and the determination of extremely accurate phase diagrams for various systems. Applying all of these developments to $1\frac{1}{2}$ D ladder systems may also reveal new interesting physics.

Beyond TEBD there have been a number of new algorithms proposed very recently which, by further utilising tools from quantum information theory, could potentially open up higher dimensional systems to the same level of numerical scrutiny. Among the first of these was the projected entangled pairs (PEPS) [6]. In 1D this method is equivalent to the matrix product states (MPS) construction used in TEBD, but unlike MPS the PEPS construction can be readily generalised to higher dimensional systems. This method has now been used to investigate an 11×11 hard-core boson system in 2D [7] and has also been reformulated to handle translationally-invariant systems (iPEPS) [8]. Another very promising method is the multi-scale entanglement renormalisation Ansatz (MERA) [9, 10]. This method relies on a special hierarchically structured quantum network whose purpose is to “disentangle”, as best as it can, a given many-body ground state. Extracting correlation functions can be done efficiently due to this network possessing a bounded causal cone [10]. Very recently such a quantum network has been generalised to include other structures [11] showing that this quantum computing approach to many body systems may well be very fruitful. An alternative approach is the so-called weighted-graph state ansatz [12, 13]. This method is based on exploiting a slightly extended form of graph states in order to describe many-body ground states by a small set of parameters. This type of states possess a number of important properties. Firstly, they can possess an unbounded amount of entanglement; secondly they are adaptable to any geometry; and thirdly expectation values of local observables, such as terms contributing to a Hamiltonian, can be evaluated efficiently. As a result such states are a potentially powerful basis for variational calculations of strongly-correlated ground states. At the time of writing much work is

¹This method is called iTEBD following the popular “i...” à la iPOD naming convention [5].

needed to determine which of these methods (or hybrid combinations of them) is best suited to particular physical problems. Moreover, large scale implementations still need to be developed if they are to truly reveal new physics in higher dimensional systems. Future research in this direction could well follow a similar line to the work in this thesis and is clearly of benefit for future and current optical lattice experiments.

References

- [1] M. Zwolak, G. Vidal, *Phys. Rev. Lett.* **93**, 207205 (2004).
- [2] S.R. Clark, A. Klein, M. Bruderer, D. Jaksch, *New J. Phys.* **9**, 202 (2007).
- [3] S. Singh, H.-Q. Zhou, G. Vidal, [arXiv:cond-mat/0701427](https://arxiv.org/abs/cond-mat/0701427).
- [4] I.P. McCulloch, *J. Stat. Mech.* P10014 (2007).
- [5] G. Vidal, *Phys. Rev. Lett.* **98**, 070201 (2007).
- [6] F. Verstraete, J. I. Cirac, [arxiv:cond-mat/0407066](https://arxiv.org/abs/cond-mat/0407066).
- [7] V. Murg, F. Verstraete, J.I. Cirac, *Phys. Rev. A* **75**, 033605 (2007).
- [8] J. Jordan, R. Orus, G. Vidal, F. Verstraete, J.I. Cirac, [arXiv:cond-mat/0703788](https://arxiv.org/abs/cond-mat/0703788).
- [9] G. Vidal, *Phys. Rev. Lett.* **99**, 220405 (2007).
- [10] G. Vidal, [arXiv:quant-ph/0610099](https://arxiv.org/abs/quant-ph/0610099).
- [11] C.M. Dawson, J. Eisert, T.J. Osborne, [arXiv:0705.3456](https://arxiv.org/abs/0705.3456).
- [12] S. Ander, M.B. Plenio, W. Dür, F. Verstraete, H.-J. Briegel, *Phys. Rev. Lett.* **97**, 107206 (2006).
- [13] S. Anders, H.-J. Briegel, W. Dür, *New J. Phys.* **9**, 361 (2007).